frontiers | Research Topics

The challenge and opportunity of CCUS in the development of unconventional resource

Edited by
Yibo Li, Shuang Zheng, Daoyi Zhu, Shuai Zhao and Yu Peng

Published in
Frontiers in Energy Research

ISSN 1664-8714
ISBN 978-2-83252-171-7
DOI 10.3389/978-2-83252-171-7

About Frontiers

Frontiers is more than just an open access publisher of scholarly articles: it is a pioneering approach to the world of academia, radically improving the way scholarly research is managed. The grand vision of Frontiers is a world where all people have an equal opportunity to seek, share and generate knowledge. Frontiers provides immediate and permanent online open access to all its publications, but this alone is not enough to realize our grand goals.

Frontiers journal series

The Frontiers journal series is a multi-tier and interdisciplinary set of open-access, online journals, promising a paradigm shift from the current review, selection and dissemination processes in academic publishing. All Frontiers journals are driven by researchers for researchers; therefore, they constitute a service to the scholarly community. At the same time, the *Frontiers journal series* operates on a revolutionary invention, the tiered publishing system, initially addressing specific communities of scholars, and gradually climbing up to broader public understanding, thus serving the interests of the lay society, too.

Dedication to quality

Each Frontiers article is a landmark of the highest quality, thanks to genuinely collaborative interactions between authors and review editors, who include some of the world's best academicians. Research must be certified by peers before entering a stream of knowledge that may eventually reach the public - and shape society; therefore, Frontiers only applies the most rigorous and unbiased reviews. Frontiers revolutionizes research publishing by freely delivering the most outstanding research, evaluated with no bias from both the academic and social point of view. By applying the most advanced information technologies, Frontiers is catapulting scholarly publishing into a new generation.

What are Frontiers Research Topics?

Frontiers Research Topics are very popular trademarks of the *Frontiers journals series*: they are collections of at least ten articles, all centered on a particular subject. With their unique mix of varied contributions from Original Research to Review Articles, Frontiers Research Topics unify the most influential researchers, the latest key findings and historical advances in a hot research area.

Find out more on how to host your own Frontiers Research Topic or contribute to one as an author by contacting the Frontiers editorial office: frontiersin.org/about/contact

The challenge and opportunity of CCUS in the development of unconventional resource

Topic editors

Yibo Li — Southwest Petroleum University, China
Shuang Zheng — Aramco Services Company, United States
Daoyi Zhu — China University of Petroleum, Beijing, China
Shuai Zhao — Southwest Petroleum University, China
Yu Peng — Southwest Petroleum University, China

Citation

Li, Y., Zheng, S., Zhu, D., Zhao, S., Peng, Y., eds. (2023). *The challenge and opportunity of CCUS in the development of unconventional resource*. Lausanne: Frontiers Media SA. doi: 10.3389/978-2-83252-171-7

Table of contents

frontiers | Frontiers in Energy Research

TYPE Editorial
PUBLISHED 30 March 2023
DOI 10.3389/fenrg.2023.1153929

OPEN ACCESS

EDITED BY
Aliakbar Hassanpouryouzband,
University of Edinburgh, United Kingdom

REVIEWED BY
Yang Xiao,
Xi'an University of Science and Technology, China

*CORRESPONDENCE
Yi-Bo Li,
liyibo@swpu.edu.cn

SPECIALTY SECTION
This article was submitted to Advanced Clean Fuel Technologies, a section of the journal Frontiers in Energy Research

RECEIVED 30 January 2023
ACCEPTED 21 March 2023
PUBLISHED 30 March 2023

CITATION
Li Y-B (2023), Editorial: The challenge and opportunity of CCUS in the development of unconventional resource.
Front. Energy Res. 11:1153929.
doi: 10.3389/fenrg.2023.1153929

Editorial: The challenge and opportunity of CCUS in the development of unconventional resource

Yi-Bo Li*

State Key Laboratory of Oil and Gas Reservoir Geology and Exploitation, Southwest Petroleum University, Chengdu, Sichuan, China

KEYWORDS

CCUS, CO_2, unconventional resource, EOR, hydraulic fracture

Editorial on the Research Topic
The challenge and opportunity of CCUS in the development of unconventional resource

1 Introduction

The decline in conventional oil production and the rise in costs for exploitation have led to a shift in global interest towards unconventional resources. To address environmental issues, the development of unconventional resources aims to increase oil and gas production without increasing emissions (Li et al., 2017a; Li et al., 2021). The use of low-carbon technologies, which emit low or zero CO_2 emissions, is crucial in reducing CO_2 emissions and promoting carbon neutrality. Key to this is the application of low-carbon technology in the development process to reduce emissions and increase CO_2 utilization and storage (Li et al., 2014; Li et al., 2017b; Li et al., 2020).

This Research Topic, which accompanies the Research Topic of Frontiers in Energy Research, places an emphasis on the fundamental innovations and compiles 11 current publications on original applications of *the challenge and opportunity of CCUS in the development of unconventional resource*.

2 Review of the research presented in this Research Topic

The works presented in this section focus on different aspects of unconventional hydrocarbon reservoirs, including hydraulic fracturing operations, acid fracturing techniques, non-aqueous fracturing techniques, CO_2 flooding, casing deformation, micro-scale reservoir properties, interplay mechanisms for enhanced oil recovery, geological-engineering integration, and natural gas pipeline leaks.

Chen's presented two novel models for predicting the Drag Reduction (DR) in hydraulic fracturing operations with slickwater, based on dynamic similarity and offering reliable

predictions with deviations ranging from −10% to 10% and −6%–6% for models 1 and 2, respectively (Chen et al.).

In Liu's research, the acid rock reaction and acid-etched fracture conductivity experiments of Qixia Fm tight carbonate are investigated to optimize the main acid type and acid frac technique. In addition, the feasibility of open-hole packer and sliding sleeve staged acid fracturing is discussed, and the staged acid frac tool string is optimized (Liu et al.).

In Peng's study, Supercritical CO_2 has been found to be a promising non-aqueous fracturing technique for low-pressure tight sandstone, with reduced formation sensitivity damage observed in tight sandstone cores from the Jinqiu Gas field in the Sichuan Basin after interaction with supercritical CO_2 (Peng et al.; Peng et al.).

In Wang's Research, CO_2 flooding and burial efficiency in the Daqing Oilfield can be improved by using multiple linear regression to establish a screening standard for suitable CO_2 flooding reservoirs. A total of 15 factors are used as independent variables and the results are consistent with the oilfield's production history, with over 70% of well groups having an evaluation value greater than 0.50 and an annual oil exchange ratio above 40%. This provides effective guidance for the development of the Daqing Oilfield (Wang et al., 2022).

In Shen's paper, the casing deformation (CD) prediction model was established for 105 gas wells in the Luzhou shale gas area to analyze the impact of CD on shale gas fracturing progress and stimulation effect using the fracture operation curve diagnosis method (Shen et al.).

In Guo's research, a digital core reconstruction method was applied to study the fluid distribution and pore structure of the Xujiahe Formation in Yuanba. Results showed that water residues could reduce pore sizes and affect their connectivity. This study provides an applicable method to understand micro-scale reservoir properties and fluid distribution mechanisms in tight sandstone gas reservoirs (Guo et al.).

Li's work presented a model that simulates the impact of hydraulic fracturing and shut-in period on pore pressure and water saturation in shale gas wells, which are key factors in well production. The model uses an efficient simulation technique (EDFM) and accounts for the fracture propagation and matrix flow (Li et al.; Li et al.).

In Hao's work, the interplay mechanisms for enhanced oil recovery were studied using laboratory and numerical models, which showed that CO_2 injection at the lower well can move upward to the higher well and increase oil recovery. Pilot tests in China showed a 2.27×104 m^3 crude oil recovery with a high oil/CO_2 exchange ratio of 3.92. The well-to-well interplay is a promising approach for EOR with better CO_2 utilization efficiency (Hao et al.).

Zeng established a geological-engineering integration model to optimize the development of tight sandstone gas reservoirs in Jinqiu Gas field with low porosity and permeability, leading to increased well productivity from 50,500 to 434,300 cubic meters per day through customized stimulation strategies (Zeng et al.).

In Nie's work, both laboratory tests and reservoir simulation were done to study the feasibility and benefits of associated gas injection. The experiments and simulation showed that oil recovery was increased by 16.8% compared to depletion development by natural energy through the optimization of depletion development and gas injection development strategy (Xu et al.).

Xu presented a leakage diffusion model and simulation scheme for exposed natural gas pipeline leaks in mountainous areas, providing insight into the diffusion pattern and influence range of leaks under different factors, helping to form emergency response strategies and provide a theoretical basis for risk analysis in these areas (Xu et al.).

The works presented here offer valuable insights into different aspects of unconventional hydrocarbon reservoirs, and their findings can be applied to improve the efficiency and effectiveness of hydrocarbon extraction operations. The studies also highlight the importance of continued research into unconventional reservoirs, particularly in the face of increasing global energy demands and environmental concerns. Additionally, gas hydrates, another unconventional hydrocarbon reservoir, also offer significant potential for energy production, but further research is needed to better understand their properties and develop efficient extraction techniques.

3 Conclusion

In conclusion, this Research Topic of Frontiers in Energy Research has provided valuable contributions to the development of unconventional hydrocarbon reservoirs. The studies have explored various techniques and approaches, ranging from hydraulic fracturing operations to non-aqueous fracturing techniques, CO_2 flooding, casing deformation, micro-scale reservoir properties, interplay mechanisms for enhanced oil recovery, geological-engineering integration, and natural gas pipeline leaks. These findings are significant for improving the efficiency and effectiveness of hydrocarbon extraction operations, while also addressing environmental concerns through the use of low-carbon technologies. Moreover, this research highlights the importance of continued investigation into unconventional reservoirs, as they offer significant potential for energy production to meet increasing global demands. The application of these studies will be instrumental in achieving carbon neutrality, and their fundamental innovations will guide future research towards a sustainable energy future.

Author contributions

The author confirms being the sole contributor of this work and has approved it for publication.

Funding

The authors wish to recognize financial support from the National Natural Science Foundation of China (52174034) and the Sichuan Science and Technology Program (2021YFH0081).

Conflict of interest

The author declares that the research was conducted in the absence of any commercial or financial relationships that could be construed as a potential conflict of interest.

Publisher's note

References

Li, Y. B., Chen, Y. F., Pu, W. F., Dong, H., Gao, H., Jin, F. Y., et al. (2017). Low temperature oxidation characteristics analysis of ultra-heavy oil by thermal methods. *J. industrial Eng. Chem.* 48, 249–258. doi:10.1016/j.jiec.2017.01.017

Li, Y. B., Chen, Y., Pu, W. F., Gao, H., and Bai, B. (2017). Experimental investigation into the oxidative characteristics of Tahe heavy crude oil. *Fuel* 209, 194–202. doi:10.1016/j.fuel.2017.07.029

Li, Y. B., Luo, C., Lin, X., Li, K., Xiao, Z. R., Wang, Z. Q., et al. (2020). Characteristics and properties of coke formed by low-temperature oxidation and thermal pyrolysis during *in situ* combustion. *Industrial Eng. Chem. Res.* 59 (5), 2171–2180. doi:10.1021/acs.iecr.9b05635

Li, Y. B., Wang, Z. Q., Hu, Z. Q., Xu, B., and Pu, W. (2021). A review of *in situ* upgrading technology for heavy crude oil. *Petroleum* 7 (2), 117–122. doi:10.1016/j.petlm.2020.09.004

Li, Y. B., Zhao, J. Z., Pu, W. F., Peng, H., Zhong, D., Hu, Z. W., et al. (2014). A method based on the Harcourt and Esson equation to estimate the catalytic effect of metallic additives on light crude oil. *J. alloys Compd.* 585, 7–13. doi:10.1016/j.jallcom.2013.09.062

Wang, Z., Hou, J., Hao, H., Ke, J., and Zhang, B. Y. (2022). AK098656: A new biomarker of coronary stenosis severity in hypertensive and coronary heart disease patients. *Front. ENERGY Res.* 14, 10. doi:10.1186/s13098-022-00783-3

frontiers | Frontiers in Energy Research

ORIGINAL RESEARCH
published: 24 May 2022
doi: 10.3389/fenrg.2022.905187

Prediction of Drag Reduction in Slickwater Fracturing by Two General Models

Pengfei Chen, Honggang Chang, Yongqiang Fu, Yongfan Tang, Xuesong Huang and Weichu Yu*

Research Institute of Natural Gas Technology, PetroChina Southwest Oil and Gas Field Company, Chengdu, China

Drag reduction (DR) is critical to the success of hydraulic fracturing operations with slickwater, and it is a challenge to accurately predict DR due to the problem of high injection rates. Although a practical pipe diameter model is frequently used to predict the field DR based on laboratory experimental data, there exist many limitations. This study, on account of dynamic similarity, shows two novel general models for the prediction of field DR, and such two models can give reliable predictions when the laboratory and field Reynolds numbers (*Re*) are the same. For general model 1, the DR can be predicted by using the laboratory volumetric flow rate, pipe diameter and pressure drop, and the field volumetric flow rate, with a deviation ranging from −10 to 10%. For general model 2, it is simpler than general model 1, and the DR can be predicted by using the laboratory pipe diameter and the field volumetric flow rate, with a deviation ranging from −6 to 6%. The two novel general models can be used for more scenarios than the existing reported ones.

Keywords: drag reduction prediction, Reynolds criterion, slickwater fracturing, slickwater, general model

OPEN ACCESS

Edited by:
Yu Peng,
Southwest Petroleum University, China

Reviewed by:
Guandong Su,
National University of Singapore, Singapore
Liu Lu,
Southwest Petroleum University, China

****Correspondence:***
Pengfei Chen
chenpengfei@petrochina.com.cn

Specialty section:
This article was submitted to Advanced Clean Fuel Technologies, a section of the journal Frontiers in Energy Research

Received: *26 March 2022*
Accepted: *19 April 2022*
Published: *24 May 2022*

Citation:
Chen P, Chang H, Fu Y, Tang Y, Huang X and Yu W (2022) Prediction of Drag Reduction in Slickwater Fracturing by Two General Models. Front. Energy Res. 10:905187. doi: 10.3389/fenrg.2022.905187

INTRODUCTION

As a widely distributed clean and efficient energy source, shale gas has been highly valued by the international energy market and various countries (Peng et al., 2019a). Since the early 21st century, the boom in shale gas development in the United States has significantly advanced the global shale gas development. Since then, the energy landscape in the world has changed gradually (Yuan et al., 2015; Shi et al., 2020). As far as we know, China has abundant shale gas resources and an increasing demand for natural gas. Therefore, a large-scale commercialized development (Ma et al., 2018; Pang, 2018) of hydraulic fracturing shale reservoirs can be expected. Hydraulic fracturing is a necessary technology for developing shale gas (Yu et al., 2020). During the hydraulic fracturing process, the proppant-carrying fracturing fluid is injected into a well at a high pressure and rate to fracture the reservoir rocks. To reduce the friction loss due to tubular roughness, slickwater with drag reducers is often used since it has desirable hydraulic features (Barbot et al., 2013; Shaffer et al., 2013; Al-Muntasheri, 2014; Engle and Rowan, 2014). Numerous studies have focused on various parameters affecting drag reduction (Gallego and Shah, 2009; Chai et al., 2019). Four main parameters can affect the drag reduction of slickwater, including the drag-reducing agent concentration, fluid flow Reynolds number (*Re*), relative pipe roughness, and water quality (Yang et al., 2019). Meanwhile, two main underlying mechanisms of drag reduction have been identified (Habibpour and Clark, 2017; Habibpour et al., 2017). The first mechanism introduced by Lumley is based on the elongation of coiled polymer molecules, hence increasing the thickness of the viscous sublayer; the other mechanism is the elastic properties of polymers.

Although we have known a lot of the slickwater parameters affecting drag reduction, accurate prediction of drag reduction still remains a challenge. Allahdadi Mehrabadi and Sadeghy (2008) obtained a good drag reduction prediction model called the κ-ε turbulence model for low Reynolds numbers. Al-Sarkhi et al. (2011) developed two correlations to predict the effect of drag-reducing polymers on the friction factor of the two-phase flow for any pipe diameter. Karami and Mowla (2013) presented a general model for predicting drag reduction in crude oil pipelines. Recently, Zhou et al. (2011) proposed a practical pipe diameter model by introducing an effective pipe radius (r_{eff}) which is defined as follows:

$$r_{eff} = \frac{v_f \rho}{\mu},$$

where ρ is the fluid density, μ is the fluid viscosity, and v_f is the flow velocity calculated as $(d\Delta p/4\rho l)^{1/2}$. To upscale the laboratory experimental results of the drag reduction of slickwater to the field application, two conditions must be met: first, the r_{eff} value of the field pipe (tubing/casing) must be in the same range as the laboratory pipe; second, the slope of r_{eff} versus v of the field must match the laboratory setup, where v is the average fluid velocity. We found that as long as the slopes of effective pipe radius versus velocity from the laboratory pipe and the field pipe are numerically close, field drag reduction can be predicted by a modified correlation between DR and velocity established in the laboratory (Zhao et al., 2018; Chen et al., 2021). In this study, two novel general models are proposed using the Reynolds criterion to simplify the prediction condition.

THEORETICAL BASIS

The models presented in this study are based on the similarity principle so as to upscale the laboratory experimental results to the field application. Due to laboratory setting constraints that are different from those in the field application, the experimental results can be upscaled to the field application only under some specific conditions. The laboratory measurements can accurately represent the flow dynamics of the corresponding prototype. Therefore, the similarity between the model and the prototype must be satisfied. There are three types of similarity principles: geometric similarity, kinematic similarity, and dynamic similarity. It is relatively easy to achieve the geometric and kinematic similarities, while the dynamic similarity requires an equal ratio of forces acting on the two systems. Usually, dynamic similarity can be achieved by equating such flow dynamic dimensionless variables as Froude number and Reynolds number. In this study, we chose the Reynolds number as the inherent parameter because it can be easily measured in both the laboratory condition and the field application condition. Reynolds number (*Re*) is a dimensionless number that is commonly used to characterize flow patterns in different fluid flow situations (Peng et al., 2019b). Because of the similarity of flow viscosity between the prototype and the model, the Reynolds number of the field fracturing flow model should be equal to that

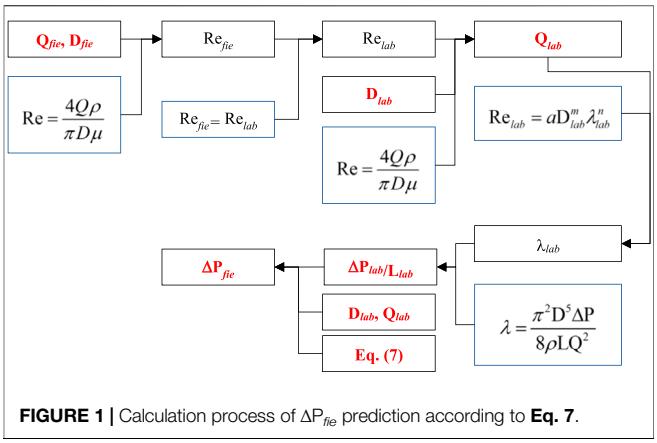

FIGURE 1 | Calculation process of ΔP_{fie} prediction according to **Eq. 7**.

of the lab drag reduction experiment model, according to the similarity of flow dynamics.

In previous studies, we have developed a modified Virk's correlation to accurately characterize the friction factor (λ) under different Reynolds numbers in the turbulent flow pattern for the polyacrylamide polymer drag-reducing agent using laboratory data. The unified model is shown in **Eq. 1**.

$$\frac{1}{\sqrt{\lambda}} = \alpha D^{\beta} \lg\left(Re\sqrt{\lambda}\right) + \gamma D^{\theta}. \tag{1}$$

This equation can be changed to **Eq. 2**.

$$Re_{lab} = aD_{lab}^{m}\lambda_{lab}^{n}, \tag{2}$$

where Re_{lab} is the Reynolds number based on the laboratory data, D_{lab} is the lab pipe diameter, and λ_{lab} is the friction factor from the laboratory data. For a given pipe diameter in the field, a similar relationship between the field Re (Re_{fie}) and the field λ (λ_{fie}) can be obtained by **Eq. 3**.

$$Re_{fie} = b\lambda_{fie}^{n}. \tag{3}$$

The Reynolds numbers of the lab and field can be equated by **Eq. 4**:

$$\lambda_{fie} = \left(\frac{aD_{lab}^{m}}{b}\right)^{1/n} \lambda_{lab}. \tag{4}$$

For a slickwater solution, the λ_{lab} and λ_{fie} can be determined by the Hagen–Poiseuille equation, respectively, as follows:

$$\lambda_{lab} = \frac{\pi^2 D_{lab}^5 \Delta P_{lab}}{8\rho L_{lab} Q_{lab}^2}, \tag{5}$$

$$\lambda_{fie} = \frac{\pi^2 D_{fie}^5 \Delta P_{fie}}{8\rho L_{fie} Q_{fie}^2}, \tag{6}$$

where ΔP_{lab} is the pressure drop in the laboratory experiment, ρ is the density of slickwater, L_{lab} is the pipe length in the laboratory experiment, Q_{lab} is the volumetric flow rate in the laboratory experiment, ΔP_{sie} is the field friction of slickwater, L_{fie} is the well depth, and Q_{fie} is the field volumetric flow rate.

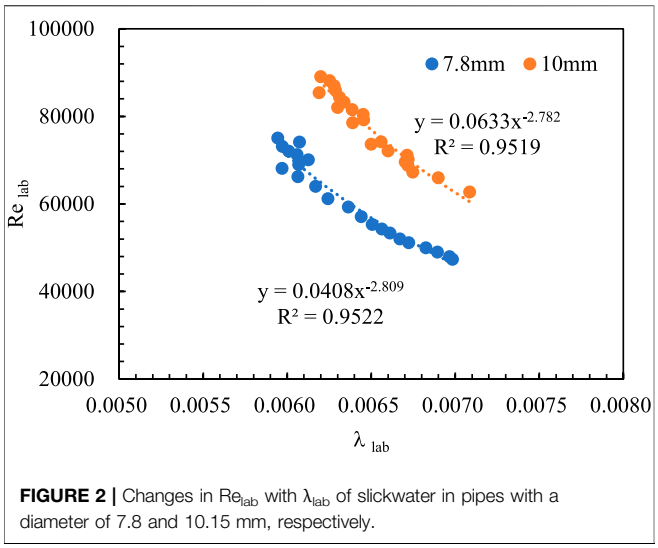

FIGURE 2 | Changes in Re_{lab} with λ_{lab} of slickwater in pipes with a diameter of 7.8 and 10.15 mm, respectively.

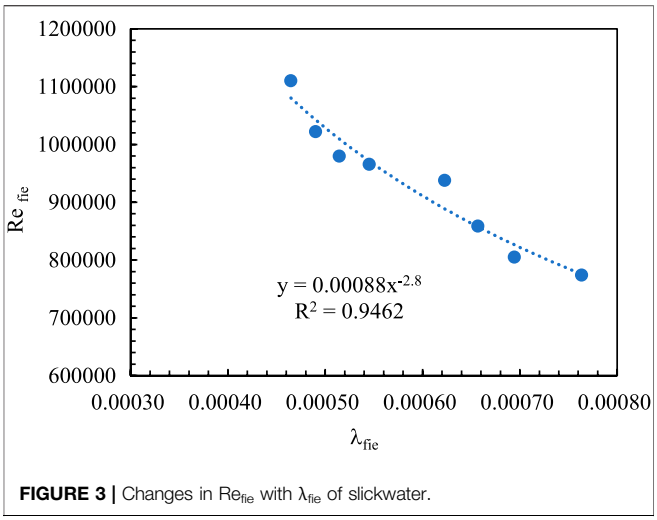

FIGURE 3 | Changes in Re_{fie} with λ_{fie} of slickwater.

Eq. 5 and **6** are substituted into **Eq. 4** to get the predicted ΔP_{fie} by **Eq. 7**:

$$\Delta P_{fie} = \left(\frac{a}{b} D_{lab}^{m}\right)^{1/n} \frac{D_{lab}^{5} \Delta P_{lab} L_{fie} Q_{fie}^{2}}{L_{lab} Q_{lab}^{2} D_{fie}^{5}}. \quad (7)$$

For the given L_{fie}, Q_{fie}, and D_{fie}, ΔP_{fie} can be calculated according to the process shown in **Figure 1**.

The field friction of pure water (ΔP_{pw}) can be calculated by **Eq. 8**, which is obtained by the friction-gradient flow rate diagram of water, as shown in Supplementary Figure S1 in Supporting Information.

$$\Delta P_{pw} = 1.385 \times 10^{6} D_{fie}^{-4.8} Q_{fie}^{1.8} L_{fie}. \quad (8)$$

The drag reduction (DR) is defined as follows:

$$DR = 100 - \frac{\Delta P_{fie}}{\Delta P_{pw}} \times 100. \quad (9)$$

Eq. 7 and **8** are substituted into **Eq. 9** to get the DR:

$$DR = 100 - 7.22 \times 10^{-5} \left(\frac{a}{b} D_{lab}^{m}\right)^{1/n} \frac{D_{lab}^{5} \Delta P_{lab} Q_{fie}^{0.2}}{L_{lab} Q_{lab}^{2} D_{fie}^{-9.8}} \times 100. \quad (10)$$

EXPERIMENT

Materials

The drag-reducing agent, having an average molecular weight of 1.05×10^{7} and a hydrolysis degree of 21.5%, was provided by Chengdu Ringt Technology Development Co., Ltd. In the laboratory experiment, an aqueous solution of 0.1 wt% drag-reducing agent and deionized water as the solvent were used. The experimental setup used to study the drag reduction performance is shown in Supplementary Figure S2 in Supporting Information. The laboratory flow loop was composed of a mixing tank (20 L), a cavity progressive pump (XBY, model: G FG 25-2, range: 0–2 m^3h^{-1}), a steel pipe (relative roughness: 3.2), a heater, and a flow meter (SINCERITY, model: DMF-1-M, range: 0–35 kg min^{-1}, accuracy: 0.10–0.20% relative error of the flow meter). It also had two pressure sensors (Sailsors Instruments Ltd., model: V4Db7E, range: -700 to 700 kPa, output: 4–20 mA DC, accuracy: ±0.5% full scale).

Drag Reduction Experiments in the Laboratory

The drag reduction experiments in the laboratory were conducted, following the procedures detailed in the literature (Zhao et al., 2018).

1) Drag-reducing agent and experimental equipment

The drag-reducing agent used in the experiment was the high molecular weight polyacrylamide emulsion prepared by inverse emulsion polymerization. It was a linear polymer with a molecular weight of 1.05×10^{7} and a concentration of 31.2 wt%. The dosage of the linear polymer was 0.1wt%. All experiments were carried out at room temperature. The loop included a 50-L container, and it can circulate at different rates up to 50 L/min under the action of the pump. First, the liquid flowed from the mixing tank through the flow meter having a maximum capacity of 10 t/h and an accuracy of ±0.1%. Then, the liquid flowed through the pipeline, and the pressure was measured by using the pressure sensors with a range of 0–14 MPa. A 30-m long pipe with a diameter of 0.08 m was used in the system. A 50-L container was used to prepare the drag-reducing agent solution, and the solution can be recycled. Then, experiments were conducted at different flow rates.

2) Experimental procedures

1) The water was added to a mixing tank and allowed to circulate for 5 min, followed by filling the pipeline with water and

TABLE 1 | Predicted DRs and deviations obtained by using general model 1.

Field data					Predicted ΔP_{fie} (MPa)		Predicted DR (%) and deviation (%)			
Well	Number of fracturing section	ΔP_{fie} (MPa)	DR (%)	Average velocity (m/s)	7.8 mm	10 mm	7.8 mm		10 mm	
							DR	Deviation	DR	Deviation
W1	1	25.24	69.40	22.84	23.28	25.15	71.77	3.30	69.51	0.16
	2	29.62	63.55	22.81	22.87	24.70	71.86	11.56	69.60	8.70
	3	23.86	65.20	20.23	17.71	19.12	74.18	12.10	72.11	9.58
	4	29.79	66.95	24.39	25.37	27.40	71.85	6.82	69.60	3.81
	5	30.49	67.31	26.02	28.47	30.75	69.48	3.12	67.04	−0.41
	10	25.9	70.17	26.13	26.71	28.85	69.23	−1.35	66.77	−5.09
	11	25.01	70.77	26.02	26.10	28.19	69.49	−1.84	67.05	−5.55
	12	28.96	65.67	26.02	25.74	27.80	69.48	5.49	67.04	2.04
	13	27.97	66.54	26.09	25.65	27.70	69.31	4.00	66.86	0.48
	14	28.16	65.58	26.02	24.97	26.96	69.49	5.62	67.04	2.18
	15	22.81	71.67	26.01	24.56	26.52	69.50	−3.13	67.06	−6.88
	16	22.81	71.20	26.07	24.26	26.20	69.38	−2.64	66.93	−6.39
	17	28.45	63.47	26.00	23.73	25.63	69.52	8.71	67.09	5.39
	18	24.44	68.06	26.04	23.39	25.27	69.42	1.97	66.98	−1.61
	19	22.98	69.42	26.01	22.93	24.76	69.49	0.10	67.05	−3.53
W2	1	30.75	63.24	22.80	23.52	25.40	71.88	12.03	69.63	9.19
	2	28.24	70.11	24.47	26.79	28.93	71.65	2.14	69.38	−1.05
	3	26.91	67.02	22.83	23.01	24.85	71.80	6.66	69.54	3.63
	4	24.43	74.68	26.08	29.58	31.95	69.34	−7.70	66.89	−11.65
	5	27.94	70.64	26.10	29.22	31.56	69.29	−1.94	66.83	−5.69
	6	27.96	70.19	26.09	28.79	31.09	69.31	−1.27	66.85	−4.99
	7	28.62	67.49	24.40	24.82	26.80	71.81	6.01	69.56	2.97
	10	25.7	64.99	22.78	20.61	22.26	71.92	9.64	69.68	6.72
	11	25.62	70.46	26.07	26.56	28.69	69.37	−1.57	66.92	−5.29
	12	28.58	64.89	24.30	22.74	24.56	72.06	9.95	69.83	7.07
	13	25.22	64.06	22.78	19.70	21.28	71.92	10.93	69.68	8.06
	14	23.5	71.62	26.01	25.24	27.26	69.52	−3.02	67.08	−6.77
	15	26.83	60.36	22.79	19.01	20.53	71.91	16.07	69.66	13.36
	16	22.74	70.07	24.48	21.55	23.27	71.64	2.19	69.37	−1.01
	17	28.66	63.49	26.01	23.94	25.86	69.50	8.65	67.06	5.33
	18	25.13	67.47	26.00	23.55	25.43	69.52	2.95	67.09	−0.58
	19	23.43	69.19	26.04	23.24	25.10	69.44	0.36	66.99	−3.28
	20	20.38	72.76	26.04	22.87	24.70	69.43	−4.80	66.98	−8.63
	21	18.85	74.39	26.06	22.53	24.33	69.39	−7.21	66.94	−11.13
	22	16.18	73.15	22.75	16.88	18.23	72.00	−1.60	69.76	−4.87
	23	19.67	72.32	26.01	21.67	23.40	69.50	−4.05	67.06	−7.84

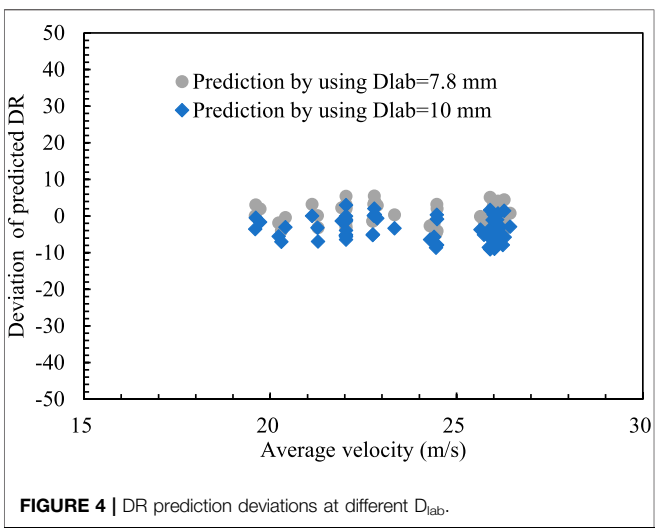

FIGURE 4 | DR prediction deviations at different D_{lab}.

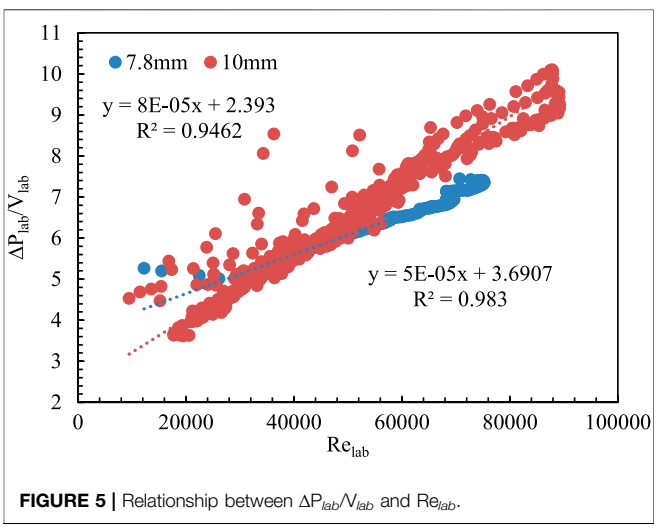

FIGURE 5 | Relationship between $\Delta P_{lab}/V_{lab}$ and Re_{lab}.

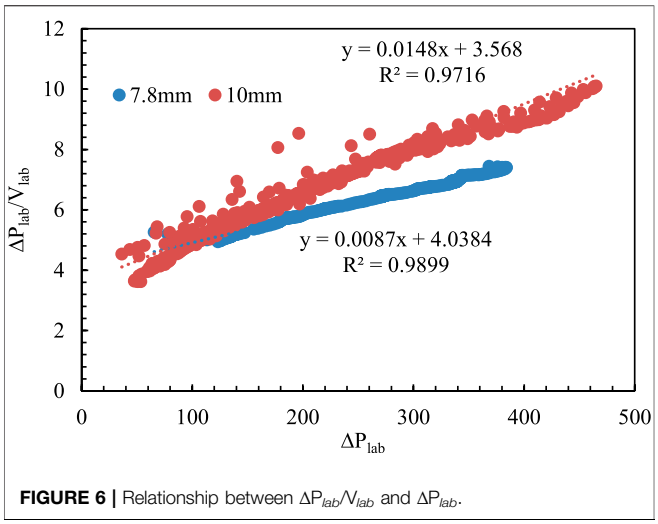

FIGURE 6 | Relationship between $\Delta P_{lab}/V_{lab}$ and ΔP_{lab}.

checking the flow meter and pressure sensor to ensure proper and stable range.

2) The water was circulated for 5 min, and the pressure difference (ΔP_0) per second and the flow rate were recorded.
3) A drag-reducing agent was added to the water and allowed to circulate for 5 min, followed by recording the pressure difference (ΔP_1) per second and the flow rate.
4) The system was cleaned with water.
5) The drag reduction was calculated.
6) The drag reduction performance was evaluated by Reynolds number, shear rate, friction coefficient, and average velocity.

RESULTS AND DISCUSSION

Construction and Validation of General Model 1

Figure 2 shows the changes of Re_{lab} with λ_{lab} of slickwater in pipes with a diameter of 7.8 and 10.15 mm, respectively. We applied numerical regression to the experimental data and obtained the correlation **Eq. 11** with coefficients of $a = 0.0011$, $m = 1.76$, and $n = -2.8$.

$$Re_{lab} = 1.1 \times 10^{-3} D_{lab}^{1.76} \lambda_{lab}^{-2.8}. \tag{11}$$

Figure 3 shows the changes of Re_{fie} with λ_{fie} of slickwater in the pipe with a diameter of 114.3 mm. For this pipe, the correlation was obtained by **Eq. 12**.

$$Re_{fie} = 8.8 \times 10^{-4} \lambda_{fie}^{-2.8}. \tag{12}$$

Eq. 11 and **12** should be substituted into **Eq. 7** and **10** to obtain the predicted ΔP_{fie} and drag reduction (by general model 1), respectively, by **Eq. 13** and **14**:

$$\Delta P_{fie} = \frac{0.66}{D_{lab}^{0.55}} \frac{D_{lab}^5}{D_{fie}^5} \frac{L_{fie}}{3} \frac{Q_{fie}^2}{(Q_{lab}/60 \times 1000)^2} \Delta P_{lab}, \tag{13}$$

$$DR = 100 - 7.22 \times 10^{-5} \left(1.25 D_{lab}^{1.76}\right)^{-0.36} \frac{D_{lab}^5 \Delta P_{lab} Q_{fie}^{0.2}}{L_{lab} Q_{lab}^2 D_{fie}^{-9.8}} \times 100. \tag{14}$$

For the pipe with a diameter of 114.3 mm, the field data, predicted ΔP_{fie}, and predicted DR are listed in **Table 1**. Since ΔP_{fie} predicted using D_{lab} of 10 mm was higher than that of D_{lab} of 7.8 mm, the DR predicted using D_{lab} of 10 mm was lower than that of D_{lab} of 7.8 mm. **Figure 4** shows the DR prediction deviations. In general, the prediction deviation produced by using D_{lab} of 7.8 mm was lower than that of D_{lab} of 10 mm, and the deviation was -10–10%.

Construction and Validation of General Model 2

As shown in **Figure 1** and **Eq. 10**, the DR prediction using general model 1 is very complicated. Many parameters in the model cannot be measured directly. Therefore, general model 1 should be further simplified. When L_{fie} and D_{fie} are known, ΔP_{fie} is a function of Re_{lab}, D_{lab}, and V_{fie}, as shown in **Eq. 7**. Therefore, **Eq. 10** can be changed to **Eq. 15**as follows:

TABLE 2 | Data used for parameter determination.

D_{fie} (mm)	Q_{fie} (m^3/min)	V_{fie} (m/s)	D_{lab} = 7.8 mm		D_{lab} = 10 mm	
			d (ΔP_{lab}/V)/d (ΔP_{lab})	Calculated DR	d (ΔP_{lab}/V)/dΔp_{lab}	Calculated DR
114.3	1	1.63	0.0087	60.32	0.0147	60.43
114.3	2	3.25	0.0087	63.99	0.0147	64.09
114.3	3	4.88	0.0087	65.98	0.0147	66.07
114.3	4	6.50	0.0087	67.32	0.0147	67.41
114.3	5	8.13	0.0087	68.33	0.0147	68.41
114.3	7	11.38	0.0087	69.79	0.0147	69.87
114.3	9	14.63	0.0087	70.83	0.0147	70.91
114.3	10	16.25	0.0087	71.26	0.0147	71.34
114.3	12	19.50	0.0087	71.98	0.0147	72.06
114.3	14	22.75	0.0087	72.58	0.0147	72.65
114.3	16	26.00	0.0087	73.09	0.0147	73.16
114.3	18	29.25	0.0087	73.53	0.0147	73.60
114.3	20	32.50	0.0087	73.92	0.0147	73.99

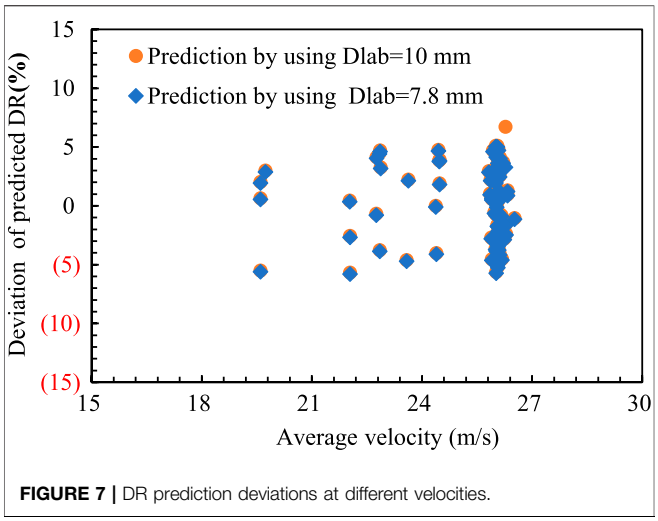

FIGURE 7 | DR prediction deviations at different velocities.

$$DR = 100 - x\mathrm{Re}_{lab}^{y} D_{lab}^{z} V_{fie}^{q}. \quad (15)$$

Re_{lab} is also a parameter that cannot be measured directly. Our laboratory experimental results showed that there was a linear relationship between $\Delta P_{lab}/V_{lab}$ and Re_{lab} (**Figure 5**) within our experiment range. In addition, we also found that there was a linear relationship between $\Delta P_{lab}/V_{lab}$ and ΔP_{lab} (see **Figure 6**). As shown in **Figure 5** and **Figure 6**, Re_{lab} and ΔP_{lab} also have a linear relationship. In other words, d $(\Delta P_{lab}/V)$/d (ΔP_{lab}) and Re_{lab} have multiple relationships. As a result, **Eq. 15** can be converted to **Eq. 16**as follows:

$$DR = 100 - x' \times \left[\frac{\mathrm{d}(\Delta P_{lab}/V_{lab})}{\mathrm{d}(\Delta P_{lab})}\right]^{y'} \times D_{lab}^{z} V_{fie}^{q}. \quad (16)$$

When V_{fie} is changed from 1.63 m/s to 32.5 m/s, the DR was calculated for different pipe diameters by adjusting the parameters in **Eq. 16**. The data used for parameter determination are shown in **Table 2**. Using numerical regression, we obtained general model 2, as shown in **Eq. 17**.

$$DR = 100 - 56 \times \left[\frac{\mathrm{d}(\Delta P_{lab}/V_{lab})}{\mathrm{d}(\Delta P_{lab})}\right]^{0.028} \times D_{lab}^{-0.07} \times V_{fie}^{-0.14}. \quad (17)$$

When the pipe diameter was 114.3 mm, the field data and the predicted ΔP_{fie} and DR were obtained using general model 2. **Figure 7** shows the DR prediction with a deviation ranging from -6 to 6%.

Deviation Analysis

This study presents models from regression and upscaling laboratory data to predict the field performance of slickwater. The potential deviation from the developed model comes from three different sources: 1) uncertainties of the laboratory measurements and their propagation to the regression correlation. To overcome the system deviation of measurement, multiple measurements on rates, diameters, and pressures were conducted, and the averaged values were used in the laboratory experimental results; 2) numerical regression on a laboratory experiment. To obtain the quantitative relationships between measured quantities and overcome the potential deviations, we applied weighted least squares with data uncertainties determined from experiments; 3) propagation of deviation during upscaling laboratory data to field applications. In this upscaling, we did not consider the potential impact of other differences such as different water quality and changes in fluid flow dynamics or thermodynamic properties, and all of them can contribute to the increased inaccuracy in the upscaling process.

Additionally, **Eq. 16** shows that the friction resistance value predicted for the field is related to the linear relationship between the ratio of pressure difference to linear velocity and the differential pressure measured in the laboratory experiment, hydrodynamic radius, and linear velocity designed in the field. The calibration of the hydrodynamic radius is based on the water experiment, and the friction coefficient of water conforms to the Prandtl–Karman law in the hydraulic smooth area, which requires the accurate measurement of the stable pressure difference at different linear velocities under laboratory experimental conditions. Similarly, to establish an accurate linear relationship between the ratio of pressure difference to linear velocity and differential pressure, it is necessary to measure the stable pressure difference of the drag-reducing agent at different linear velocities. Therefore, the most important factor for accurate prediction of field friction is to obtain the stable pressure difference between water and drag-reducing agent solution at different linear velocities under laboratory experimental conditions.

CONCLUSION

Two novel general models are established to predict the field drag reduction using laboratory experimental data based on the dynamic similarity theory. When the laboratory and field Reynolds numbers are the same and the laboratory and field volumetric flow rates and pipe diameters are known, general model 1 can be used. When the field volumetric flow rates and the laboratory pipe diameter are known, general model 2 can be used. The two proposed mathematical models for field drag reduction prediction are validated by 42 data points. The validation results showed that both models can give high-accuracy predictions, with a deviation ranging from −10 to 10% using general model 1 and a deviation ranging from −6 to 6% using general model 2.

DATA AVAILABILITY STATEMENT

The original contributions presented in the study are included in the article/Supplementary Material; further inquiries can be directed to the corresponding author.

AUTHOR CONTRIBUTIONS

All authors listed have made a substantial, direct, and intellectual contribution to the work and approved it for publication.

FUNDING

This research was partially funded by one of the National Key Technology R&D Programs—Research and Application of Generic Technologies for National Quality Infrastructure (2018YFF0213800), specifically research on key technical standards of coalbed methane, shale gas and modern coal chemical industry and that on key technical standards of shale gas resource exploration, geological evaluation and development process.

REFERENCES

Al-Muntasheri, G. (2014). A Critical Review of Hydraulic-Fracturing Fluids for Moderateto Ultralow-Permeability Formations over the Last Decade. *SPE Prod. Operations* 29, 1–18. doi:10.2118/169552-pa

Al-Sarkhi, A., Nakla, M. E., and Ahmed, W. H. (2011). Friction Factor Correlations for Gas-Liquid/liquid-Liquid Flows with Drag-Reducing Polymers in Horizontal Pipes. *Int. J. Multiph. Flow* 37 (5), 501–506. doi:10.1016/j.ijmultiphaseflow.2011.01.005

Allahdadi Mehrabadi, M., and Sadeghy, K. (2008). Simulating Drag Reduction Phenomenon in Turbulent Pipe Flows. *Mech. Res. Commun.* 35 (8), 609–613. doi:10.1016/j.mechrescom.2008.06.003

Barbot, E., Vidic, N. S., Gregory, K. B., and Vidic, R. D. (2013). Spatial and Temporal Correlation of Water Quality Parameters of Produced Waters from Devonian-Age Shale Following Hydraulic Fracturing. *Environ. Sci. Technol.* 47, 2562–2569. doi:10.1021/es304638h

Chai, Y., Li, X., Geng, J., Pan, J., Huang, Y., and Jing, D. (2019). Mechanistic Study of Drag Reduction in Turbulent Pipeline Flow over Anionic Polymer and Surfactant Mixtures. *Colloid Polym. Sci.* 297, 1025–1035. doi:10.1007/s00396-019-04525-2

Chen, P. F., Chang, H. G., Peng, T., Tang, Y. F., Liu, Y. Q., and Xiang, C. (2021). Synthesis and Performance Evaluation of a New Drag Reducer Based on Acrylamide/12-Allyloxydodecyl Acid Sodium. *J. Appl. Polym. Sci.* 138, e50314. doi:10.1002/app.50314

Engle, M. A., and Rowan, E. L. (2014). Geochemical Evolution of Produced Waters from Hydraulic Fracturing of the Marcellus Shale, Northern Appalachian Basin: a Multivariate Compositional Data Analysis Approach. *Int. J. Coal Geol.* 126, 45–56. doi:10.1016/j.coal.2013.11.010

Gallego, F., and Shah, S. N. (2009). Friction Pressure Correlations for Turbulent Flow of Drag Reducing Polymer Solutions in Straight and Coiled Tubing. *J. Petroleum Sci. Eng.* 65, 147–161. doi:10.1016/j.petrol.2008.12.013

Habibpour, M., and Clark, P. E. (2017). Drag Reduction Behavior of Hydrolyzed Polyacrylamide/xanthan Gum Mixed Polymer Solutions. *Pet. Sci.* 14, 412–423. doi:10.1007/s12182-017-0152-7

Habibpour, M., Koteeswaran, S., and Clark, P. E. (2017). Drag Reduction Behavior of Hydrolyzed Polyacrylamide/polysaccharide Mixed Polymer Solutions-Effect of Solution Salinity and Polymer Concentration. *Rheol. Acta* 56, 7–8. doi:10.1007/s00397-017-1024-1

Karami, H. R., and Mowla, D. (2013). A General Model for Predicting Drag Reduction in Crude Oil Pipelines. *J. Petroleum Sci. Eng.* 111 (21), 78–86. doi:10.1016/j.petrol.2013.08.041

Ma, Y. S., Cai, X. Y., and Zhao, P. R. (2018). China's Shale Gas Exploration and Development: Understanding and Practice. *Petroleum Explor. Dev.* 45, 561–574. doi:10.1016/s1876-3804(18)30065-x

Pang, W. (2018). A Method for Determining the Contribution of Adsorption Gas to the Production of Shale Gas Wells. *Pet. Drill. Technol.* 46, 86–92.

Peng, Y., Zhao, J., Sepehrnoori, K., Li, Y., Yu, W., and Zeng, J. (2019). Study of the Heat Transfer in Wellbore during Acid/Hydraulic Fracturing Based on Semi-analytical Transient Model [J]. *SPE J.* 24 (2), 877–890. doi:10.2118/194206-pa

Peng, Y., Zhao, J., Sepehrnoori, K., Li, Z., and Xu, F. (2019). Study of Delayed Creep Fracture Initiation and Propagation Based on Semi-analytical Fractional Model. *Appl. Math. Model.* 72, 700–715. doi:10.1016/j.apm.2019.03.034

Shaffer, D. L., Arias Chavez, L. H., Ben-Sasson, M., Romero-Vargas Castrillón, S., Yip, N. Y., and Elimelech, M. (2013). Desalination and Reuse of High-Salinity Shale Gas Produced Water: Drivers, Technologies, and Future Directions. *Environ. Sci. Technol.* 47, 9569–9583. doi:10.1021/es401966e

Shi, W., Wang, X., Guo, M., Shi, Y., Feng, A., Liang, R., et al. (2020). Water Use for Shale Gas Development in China's Fuling Shale Gas Field. *J. Clean. Prod.* 256, 120680. doi:10.1016/j.jclepro.2020.120680

Yang, B., Zhao, J., Mao, J., Tan, H., Zhang, Y., and Song, Z. (2019). Review of Friction Reducers Used in Slickwater Fracturing Fluids for Shale Gas Reservoirs. *J. Nat. Gas Sci. Eng.* 62, 302–313. doi:10.1016/j.jngse.2018.12.016

Yu, P., Zhao, J., Sepehrnoori, K., and Li, Z. (2020). Fractional Model for Simulating the Viscoelastic Behavior of Artificial Fracture in Shale Gas[J]. *Eng. Fract. Mech.* 228, 106892. doi:10.1016/j.engfracmech.2020.106892

Yuan, J., Luo, D., and Feng, L. (2015). A Review of the Technical and Economic Evaluation Techniques for Shale Gas Development. *Appl. Energy* 148, 49–65. doi:10.1016/j.apenergy.2015.03.040

Zhao, J., Chen, P., Liu, Y., Zhao, W., and Mao, J. (2018). Prediction of Field Drag Reduction by a Modified Practical Pipe Diameter Model. *Chem. Eng. Technol.* 41, 1417–1424. doi:10.1002/ceat.201600570

Zhou, J., Sun, H., Stevens, R., Qu, Q., and Bai, B. (2011). "Bridging the Gap between Laboratory Characterization and Field Applications of Friction Reducers," in SPE Production and Operations symposium. doi:10.2118/140942-ms

Conflict of Interest: Authors PC, HC, YF, YT, XH and WY were employed by PetroChina Southwest Oil and Gas Field Company.

Publisher's Note: All claims expressed in this article are solely those of the authors and do not necessarily represent those of their affiliated organizations, or those of the publisher, the editors, and the reviewers. Any product that may be evaluated in this article, or claim that may be made by its manufacturer, is not guaranteed or endorsed by the publisher.

NOMENCLATURE

Λ: friction factor, dimensionless;

Re: Reynolds numbers, dimensionless;

Re_{lab}: recalculated by using laboratory data, dimensionless;

D_{lab}: pipe diameter in the laboratory experiment, mm;

D_{fie}: pipe diameter in the field application, mm;

λ_{lab}: λ calculated by using laboratory data, dimensionless;

ΔP_{lab}: pressure drop in the laboratory experiment, MPa;

ρ: density of slickwater, g/cm^3;

L_{lab}: pipe length in the laboratory experiment, mm;

Q_{lab}: volumetric flow rate in the laboratory experiment, m^3/min;

ΔP_{fie}: field friction of slickwater, MPa;

L_{fie}: well depth, m;

Q_{fie}: field volumetric flow rate, m^3/min;

V_{fie}: linear velocity, m/s.

frontiers | Frontiers in Energy Research

ORIGINAL RESEARCH
published: 08 June 2022
doi: 10.3389/fenrg.2022.922941

Influence of Supercritical CO_2 on the Formation Sensitivity of Tight Sandstone

Huan Peng[1,2], Lang Zhou[3], Jian Yang[1,2], Junliang Peng[1,2], Huifen Han[1,2], Xinghao Gou[1,2] and Zhouyang Wang[1,2]*

[1]Engineering Technology Research Institute of Southwest Oil and Gas Field Company, PetroChina, Chengdu, China, [2]Key Laboratory of Oil and Gas Well Stimulation Technology of Southwest Oil and Gas Field Company, Chengdu, China, [3]Southwest Oil and Gas Field Company, PetroChina, Chengdu, China

It is challenging to get water-based fracture fluid to flow back into low-pressure gas reservoirs. In order to solve the problem, supercritical CO_2 is a novel type of non-aqueous fracturing technique with a wide range of applications prospect in low-pressure tight sandstone. In order to determine whether supercritical CO_2 fracturing with low-pressure tight sandstone is feasible tight sandstone cores from the Jinqiu Gas field in the Sichuan Basin were used to evaluate the influence of supercritical CO_2 on the formation sensitivity of sandstone reservoirs. Supercritical CO_2 was used to interact with tight sandstone samples under formation conditions, and then the changes in velocity sensitivity, water sensitivity, salinity sensitivity, alkaline sensitivity, acid sensitivity, and stress sensitivity of tight sandstone were observed. Velocity sensitivity damage decreased by 5.4%, water sensitivity damage decreased by 13.3%, salinity sensitivity damage decreased by 16.6%, alkaline sensitivity damage decreased by 2%, acid sensitivity damage decreased by 14.4%, and stress sensitivity damage increased by 8% after the interaction between tight sandstone and supercritical CO_2. This finding provides a quantitative assessment of the impact of supercritical CO_2 on formation sensitivity, and it can be used to build a supercritical CO_2 fracturing scheme for low-pressure water-sensitive tight sandstone.

Keywords: supercritical CO_2, tight sandstone, formation sensitivity, fracturing technology, experimental evaluation

OPEN ACCESS

Edited by:
Yibo Li,
Southwest Petroleum University, China

Reviewed by:
Zhezhi Liu,
Chongqing University of Science and Technology, China
Xingguang Xu,
China University of Geosciences Wuhan, China

****Correspondence:***
Huan Peng
282600120@qq.com
orcid.org/0000-0002-5307-0307

Specialty section:
This article was submitted to Advanced Clean Fuel Technologies, a section of the journal Frontiers in Energy Research

Received: *18 April 2022*
Accepted: *02 May 2022*
Published: *08 June 2022*

Citation:
Peng H, Zhou L, Yang J, Peng J, Han H, Gou X and Wang Z (2022) Influence of Supercritical CO_2 on the Formation Sensitivity of Tight Sandstone. Front. Energy Res. 10:922941. doi: 10.3389/fenrg.2022.922941

INTRODUCTION

With the accelerated development of the world economy and the increasing problem of energy shortage, the efficient development of unconventional oil and gas resources is the main means to effectively alleviate the energy crisis. However, the porosity, permeability, and formation pressure of unconventional oil and gas reservoirs are very low (Jiao, 2019; Peng et al., 2019). In order to obtain industrial production, it is usually necessary to carry out hydraulic fracturing for unconventional oil and gas reservoirs, inject high-pressure fluid with proppant into the formation, break the reservoir rock, and form artificial fractures. After the construction is completed, the high-pressure fluid is discharged back to the ground, and the proppant is left in the formation to avoid the re-closure of artificial fractures as a channel for oil and gas flow so as to improve the production of unconventional oil and gas reservoirs (Zhao et al., 2017; Dong et al., 2018; Peng et al., 2020).

At present, with the world economy's rapid growth and the growing problem of energy scarcity, the efficient development of unconventional oil and gas resources is the most effective means of effectively alleviating the energy crisis (Umar et al., 2022). Unconventional oil and gas reservoirs, on

the contrary, have relatively low porosity, permeability, and formation pressure (Jiao, 2019; Peng et al., 2019). Hydraulic fracturing for unconventional oil and gas reservoirs, which involves injecting high-pressure fluid with proppant into the formation, breaking the reservoir rock, and forming artificial fractures, is normally required to achieve industrial production. The high-pressure fluid is a flow back to the ground when the construction is completed, and the proppant is left in the formation to prevent the re-closure of artificial fractures as a channel for oil and gas flow, thereby improving the production of unconventional oil and gas reservoirs (Zhao et al., 2017; Dong et al., 2018; Peng et al., 2020).

For a long period, water-based fracturing fluid was the primary fluid used in fracturing. It is widely used in the fracturing construction of tight sandstone because of its simple formula, low cost, and ease of access (Peng et al., 2016). However, as reservoir stimulation technology advances and post-fracturing evaluation methods improve, it has been discovered that water-based fluids can affect the treatment of fracturing stimulation to tight sandstone gas reservoirs. It has also been discovered that water-based fracturing fluid has some drawbacks; for example, hydraulic fracturing cannot be widely used in places where water resources are scarce (Akrad et al., 2011; Gupta, 2011; Liu et al., 2014; Jia et al., 2018; Wang et al., 2018). These factors limit the widespread use and use of hydraulic fracturing in tight sandstone. River sands of the Shaximiao formation tight sandstone of Jinqiu gas reservoirs, for example, are extensively spread and rich in oil and gas resources in the Sichuan Basin. Water-based fracture fluid is difficult to flow back in low-pressure gas reservoirs of Jinqiu gas field, Sichuan Basin, because the tight sandstone reservoir pressure coefficient is 0.45–1.05 and the pressure coefficient of some sand bodies is too low (Zheng et al., 2021). As a result, in order to effectively improve gas recovery from low-pressure tight sandstone reservoirs, new stimulation technical approaches are urgently needed (Cao et al., 2017; Hazarika and Boruah, 2022).

CO_2 is a type of non-aqueous fracturing fluid that is sensitive to temperature and pressure. When the temperature and pressure of the reservoir exceed CO_2's critical temperature (31.1°C) and critical pressure (7.39 MPa), CO_2 is in a supercritical state (Nikolai et al., 2019; Mouahid et al., 2022). Supercritical CO_2 has a high density, low viscosity, low surface tension, and a high diffusion coefficient, allowing it to move heat and mass efficiently (Cabeza et al., 2017). The use of this fracturing fluid has no negative effects on the reservoir (Day et al., 2008; Lin et al., 2008), and it may effectively avoid formation blockage around the well, safeguard the oil and gas reservoir, and increase reservoir permeability, with supercritical CO_2 flowing back extremely easily. Supercritical CO_2 fracturing, which has unparalleled benefits over conventional hydraulic fracturing, has been proven in studies conducted both at home and abroad to be the key to the development of unconventional natural gas resources. Many research accomplishments have been accumulated in the interaction mechanism between supercritical CO_2 and rock (Zhou et al., 2019; Lin et al., 2022), physics structure (Gathitu et al., 2009; Ao et al., 2017), microstructure (Jiang et al., 2016), and replacement mechanism (Chen et al., 2022; Memon et al., 2022), and so on. Because the adsorption capacity of methane in shale is lower than that of supercritical CO_2, supercritical CO_2 can be used to substitute methane in shale reservoirs, allowing more shale gas to be recovered and more CO_2 to be stored *in situ* (Zhou et al., 2018; Memon et al., 2022). As a result, supercritical CO_2 fracturing has some advantages in reservoirs, particularly for water-sensitive formations, low-pressure reservoirs, and water-stressed areas, making it one of the most environmentally benign fracturing techniques.

The reservoir holding clay minerals, carbonate minerals, and iron-bearing minerals will come into contact with external fluids and solid particles at every construction link of oil and gas exploration and development, causing precipitation owing to incompatibility (Moghadasi et al., 2004; Xu et al., 2016). It either causes clay mineral expansion or reservoir particle migration, obstructing the pore throat and lowering reservoir permeability, disrupting the oil and gas flow channel, limiting the stimulation effect, and lowering the oil and gas final recovery ratio. As a result, prior to the development of an oil or gas field, a potential reservoir sensitivity assessment should be carried out to establish the type and extent of potential reservoir damage so that appropriate preventive countermeasures can be taken (Wilson et al., 2014; Fang et al., 2016).

Reservoir sensitivity refers to the nature of changes in reservoir pore structure and permeability caused by various physical or chemical interactions between reservoir and external fluids. In oil and gas field exploration and production, general reservoir sensitivity encompasses velocity sensitivity, water sensitivity, salinity sensitivity, acid sensitivity, alkali sensitivity, and stress sensitivity (Reinicke et al., 2010; Al-Yaseri et al., 2015; Zhang et al., 2019). The combination of internal potential harm components and external conditions causes reservoir sensitivity damage. Understanding the mechanism of reservoir sensitivity generation can aid in the development of tailored exploiting strategies for various reservoirs. Internal potential damage factors include lithology, physical properties, pore structure, sensitivity, and fluid properties, whereas external conditions include various external factors that cause reservoir damage, such as changes in reservoir pore structure and physical properties during the construction process, with the former changing as the latter changes (Bahrami et al., 2012; Zhou et al., 2022). As a result, analyzing the formation sensitivity of supercritical CO_2 fracturing in low-pressure tight sandstone reservoirs is crucial; unfortunately, no relevant reports have been published so far.

This study was conducted to discuss the implications of supercritical CO_2 fracturing on reservoir development. The effect of supercritical CO_2 on the formation sensitivity of sandstone reservoirs is investigated. Tight sandstone cores were taken from the Jinqiu Gas field in Sichuan Basin, and different tight sandstone samples were treated with supercritical CO_2, evaluating changes in microstructure, velocity sensitivity, water sensitivity, salinity sensitivity, alkaline sensitivity, acid sensitivity, and stress sensitivity. Furthermore, the effect of supercritical CO_2 on the formation sensitivity of tight sandstone is quantified, and the interaction

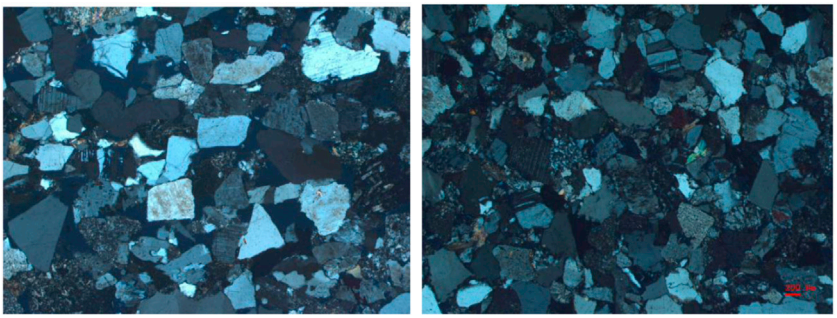

FIGURE 1 | Analysis of Shaximiao Formation rock slice in Jinqiu gas field.

mechanism between supercritical CO_2 and low-pressure tight sandstone is optimized. This finding provides a quantitative assessment of the impact of supercritical CO_2 on formation sensitivity, and it can be used to build a supercritical CO_2 fracturing scheme for low-pressure water-sensitive tight sandstone.

MATERIALS AND METHODS

Core Sample

The Jinqiu gas field's Shaximiao formation is a delta-lake sedimentary formation. The estuary dam and distributary channels overlap, generating a large-scale thick-layer mesh sand group with a sand body thickness of about 15~30 m, which is an important channel and area for natural gas storage and flow. The Shaximiao formation is made up of a variety of rock types, including conglomerate, sandstone, and mudstone. The main rock type is dark purple mudstone, followed by fine sandstone. Quartz has the highest mineral content, followed by feldspar, and debris has the lowest. **Figure 1** shows that sorting is good, the roundness is subcircular and subangular, and the particle contact is points and lines. Sandstone has a low compositional maturity and a medium structural maturity and developed intergranular pores, reservoir porosity of 8.0~16.0%, average porosity of 10.4%, and permeability of 0.01~1 mD. It has poor porosity and permeability overall. Residual intergranular pore and feldspar dissolved pore make up the majority of the reservoir space, and the reservoir type is pore type (Zhang et al., 2022). The thick reservoir is dispersed along the favorable sedimentary microfacies region in a continuous pattern. The pressure coefficient of the same sand group in different periods and different rivers in the same era varies (0.4~1.3), demonstrating the "one reservoir for one river" characteristics. The pressure coefficient of some sand bodies is low. The pressure coefficient of the sand body 7#, for example, is just approximately 0.47, so the pressure outlet cannot flow back freely because there is no gas or liquid there, necessitating gas lifting for gas testing.

First, underground cores with a diameter of 10 cm and a length of 5~15 cm were chosen from reasonably undeveloped cracks and bedding in the perforated interval, upper and lower portions, based on sample processing requirements. Then, using a core drilling machine, cylindrical core samples of 2.5 cm in diameter were drilled in the direction of the reservoir fluid. Following that, core samples with uneven ends were removed with a core cutter to get cylindrical core samples with a diameter of 2.5 cm and a length of 5.5 cm. Finally, a lapping machine was used to flatten the two ends of core samples so that they could be used in tests. **Figure 2** depicts the core processing flow. The core diameter is 2.5 cm, and the length must be at least 1.5 times the diameter. Core samples should have flat end surfaces and cylindrical surfaces, and the end surface should be perpendicular to the cylindrical surface with no flaws such as missing angles. In order to avoid mistakes, the same depth section of a well's core samples was chosen, and the processed core samples with a permeability of 1~10 mD were manually screened for the experiment.

Core samples of about 1 cm knocked off from underground cores of 10 cm in diameter were selected for microscopic experimental evaluation.

Apparatus

Visualization equipment for interaction between supercritical CO_2 and rock is shown in **Figure 3**, and it includes a CO_2 gas cylinder, CO_2 storage tank, cold bath, CO_2 booster pump, visual reactor, heating jacket, and control systems. The pressure bearing capacity of the whole unit is 50 MPa, the temperature range is from −5°C to 150°C, the volume of the visual reactor is 500 ml, and the volume of the CO_2 storage tank is 5 L. By using the control system and changing the parameters of the heating jacket and CO_2 booster pump, the interaction process between supercritical CO_2 and rock at different temperatures, pressures, and times can be realized. The experimental system key core component is visual reactor, and the interaction process between supercritical CO_2 and rock can be observed in real time through the visual reactor with sapphire glass.

The scanning electron microscope equipment is shown in **Figure 4**, and it is mainly composed of an electron microscope, electron gun filament, vacuum system, automatic sample, and image acquisition and processing system. It can quickly obtain high-quality images with rich surface features, which can be used to analyze sub-micron or nano-scale samples because the highest magnification is 150,000 times, and the resolution is better than 10 nm. The purpose

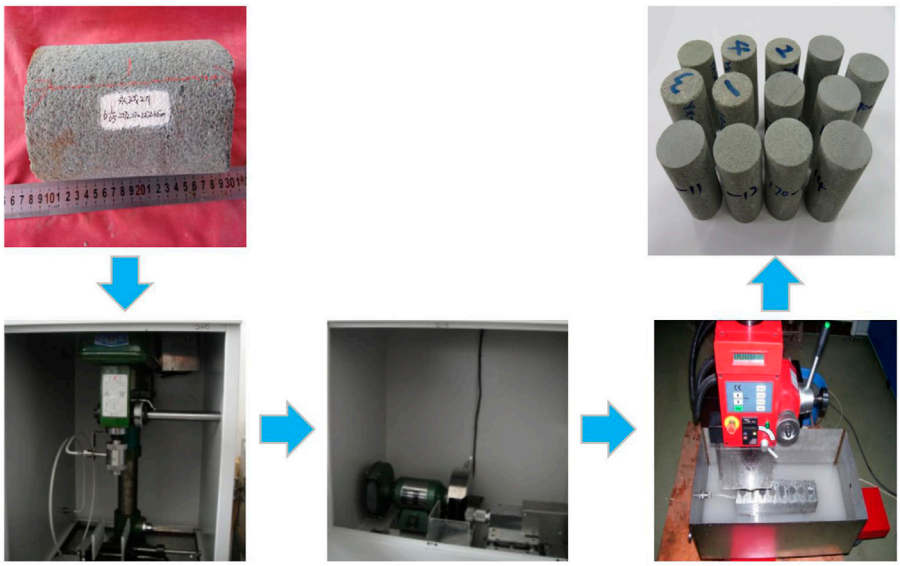

FIGURE 2 | Tight sandstone cores sample process flow.

FIGURE 3 | Visualization device for interaction between supercritical CO_2 and rock.

of SEM is to examine and determine the type, shape, occurrence, and distribution of clay minerals and other types of cement, examine the rock pore structure, particularly the size, morphology, and wall characteristics of the throat, and comprehend the spatial relationship between pore structure and various types of cement, fillings, and debris particles. SEM can see the expansion properties before and after clay mineral hydration, in addition to the aforementioned conventional findings. It is used to investigate the interaction of supercritical CO_2 with rock, examine the trends in reservoir physical parameters such as porosity, permeability, and mineral composition, and provide a foundation for sensitivity analysis.

The core displacement equipment is shown in **Figure 5**. It consists of a liquid injection pump, intermediate container for storing standard saline water and acid fluid, core holder, confining pressure pump, flow meter, constant temperature oven, back pressure valve, data collection and processing system, and core displacement equipment flowchart as shown in **Figure 6**. Equipment parameters: maximum injection pressure 70 MPa, core size Φ25 mm × L40~80 mm, maximum temperature 150°C, fluid logging permeability 0.0001~1,000 mD, constant speed constant pressure pump flow 0.01~40 ml/min. Simulation of a high-temperature environment by a constant temperature oven and simulation of actual formation pressure by a back pressure valve can restore the seepage environment of cores under formation conditions, simulate oil and gas well development and production processes, and then evaluate the effect of various development schemes and processes on improving reservoir permeability and oil and gas productivity, such as reservoir sensitivity research and relative permeability curve determination.

FIGURE 4 | Scanning electron microscope equipment.

The Experiment of Liquid

Standard saline water having the same salinity as formation water, namely, 8% (mass ratio NaCl: $CaCl_2$: $MgCl_2{\cdot}6H_2O$ = 7: 0.6:0.4) was used in the velocity sensitivity, water sensitivity, and salinity sensitive experiments.

The acid sensitivity experiment used formation water or normal saline water with the same salinity as formation water, namely, 8% (mass ratio NaCl: $CaCl_2$: $MgCl_2{\cdot}6H_2O$ = 7:0.6:0.4) and a 15% HCl acid fluid.

The water used in the alkali sensitivity study was standard saline water with the same salinity as formation water, namely, 8%.

Methods

The sensitivity of a reservoir is evaluated as follows. First, from the standpoint of petrographic analysis, the sensitive mineral

FIGURE 5 | Core displacement equipment.

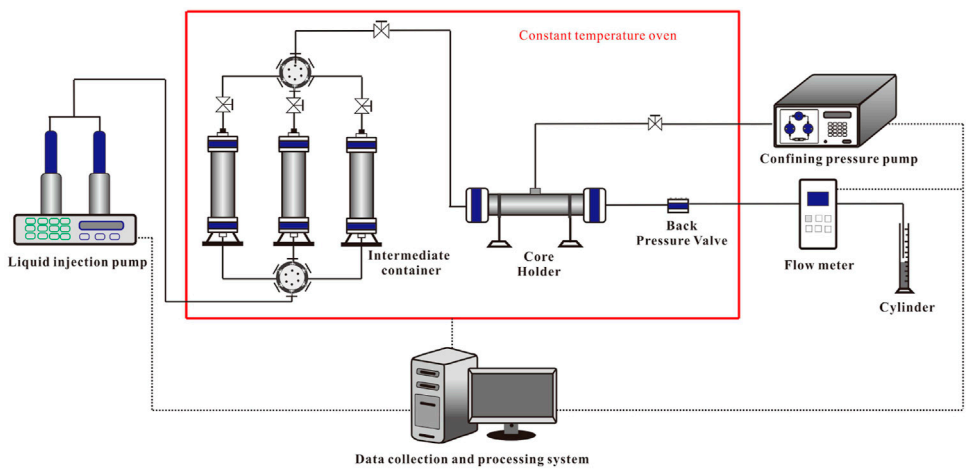

FIGURE 6 | Core displacement equipment flowchart.

properties were examined, and the potential damage factors of the reservoir were investigated. Second, representative samples were chosen for a sensitivity experiment that measured the permeability of rock before and after contact with various external fluids to assess the damage caused by external fluids to the reservoir.

Various liquids related to formation damage were injected under experimental conditions, or seepage conditions (net confining pressure, etc.) were changed to determine the permeability of core samples in order to judge the damage of critical parameters, experimental fluids, and seepage conditions to core sample permeability, in accordance with Darcy's law.

SEM and sensitivity experiments were conducted on core samples before and after contact between supercritical CO_2 and tight sandstone core samples to quantify the influence of supercritical CO_2 on tight sandstone sensitivity.

The following are the primary experimental steps, which are based on the People's Republic of China's petroleum and natural gas industry standard, SY/T 5358-2010 formation damage evaluation.

1) Tight sandstone core samples were evaluated for their original microstructure.
2) In the velocity sensitivity experiment, simulated formation water was injected into samples at various constant flow velocities to evaluate the liquid permeability of simulated formation water passing through cores and the critical velocity and velocity sensitivity damage of samples.
3) In the water sensitivity experiment, simulated formation water, saline water with half the salinity of simulated formation water, and distilled water were injected at a velocity lower than critical velocity as the initial test fluid, intermediate test fluid, and final test fluid, respectively, to measure the permeability of samples and determine water sensitivity damage.
4) In the salinity sensitivity experiment, saline water of various salinities was prepared and injected into samples in the order of high to low salinity (salinity was reduced by half) to determine the permeability of saline water of various salinities passing through core samples to determine the salinity sensitivity damage of samples.
5) To examine the acid sensitivity of samples, the initial permeability was tested with standard saline water, then 15% HCl solution was introduced into samples for saturation for 2 h, and lastly, the acidified permeability was measured with standard saline water.
6) In the alkali sensitivity experiment, saline water of various pH levels was used to test the permeability of samples to determine their alkali sensitivity damage.
7) In the stress sensitivity experiment, the difference between confining pressure and injection pressure was gradually increased from 2.5 to 20 MPa and then gradually dropped to 2.5 MPa to determine sample permeability and stress sensitivity damage.
8) The samples were placed in a visualization equipment visual reactor to see how supercritical CO_2 interacts with rock. Inject CO_2 into the visual reactor and configure the pressure and temperature to keep CO_2 supercritical for a specific amount of time. After 24 h of interaction at 15 MPa and 60°C, the pressure in the visual reactor was reduced to ambient, and tight sandstone core samples were allowed to cool naturally.
9) After the interaction between supercritical CO_2 and tight sandstone core samples, referring to 1–7, the microstructure, velocity sensitivity, water sensitivity, salinity sensitivity, acid sensitivity, alkali sensitivity, and stress sensitivity of tight sandstone core samples were investigated.

RESULTS AND DISCUSSION

Effect of Supercritical CO_2 on Microstructure of Tight Sandstone

Reservoir sensitivity is generally caused by sensitivity minerals in the reservoir, which are susceptible to physical, chemical, or physicochemical reactions with external fluids, resulting in a significant reduction in permeability. The sandstone contains sensitive minerals in the debris particles, matrixes, and cement. They have a small particle size (<20 μm) and a large specific surface area and are commonly dispersed on the pore surface and throat, where they are most likely to come into touch with external fluids.

SEM was used to examine the microstructure of tight sandstone core samples before and after supercritical CO_2 action at magnifications of ×1200. **Figure 7** depicts the experimental results of the microstructure.

The tight sandstone core's original surface was rather level, and the pores were very small. Residual intergranular pores, intergranular pores, dissolution holes, and microfractures are the most common types of primary pores.

During interaction with tight sandstone, supercritical CO_2 will somewhat dissolve feldspar, quartz, and clay particles, according to researchers. The SEM results revealed that after 48 h of interaction between tight sandstone and supercritical CO_2 at 60°C and 10 MPa, weak dissolution of feldspar and clay minerals occurred, forming a curved dissolution fracture of about 40 microns in length with irregular pores of about 10 microns and multiple small holes of 1–3 microns in diameter. A tiny quantity of irregular mineral precipitation with a diameter of 1–2 microns also formed, plugging the original pores (**Figures 7A,B**). In general, corrosion and dissolution of quartz, feldspar, and clay minerals enhanced the porosity and permeability of samples following interaction with supercritical CO_2, but precipitation of produced calcite and other minerals at the pore lowered the porosity and permeability of samples.

Effect of Supercritical CO_2 on Velocity Sensitivity

Changes in the velocity or pressure of external or reservoir fluids cause the initiation and plugging of pore throats of particles in the reservoir. The phenomenon of reservoir permeability reductions due to pore throat plugging by reservoir particle migration caused by velocity changes of external fluids or reservoir fluids is known as reservoir velocity sensitivity.

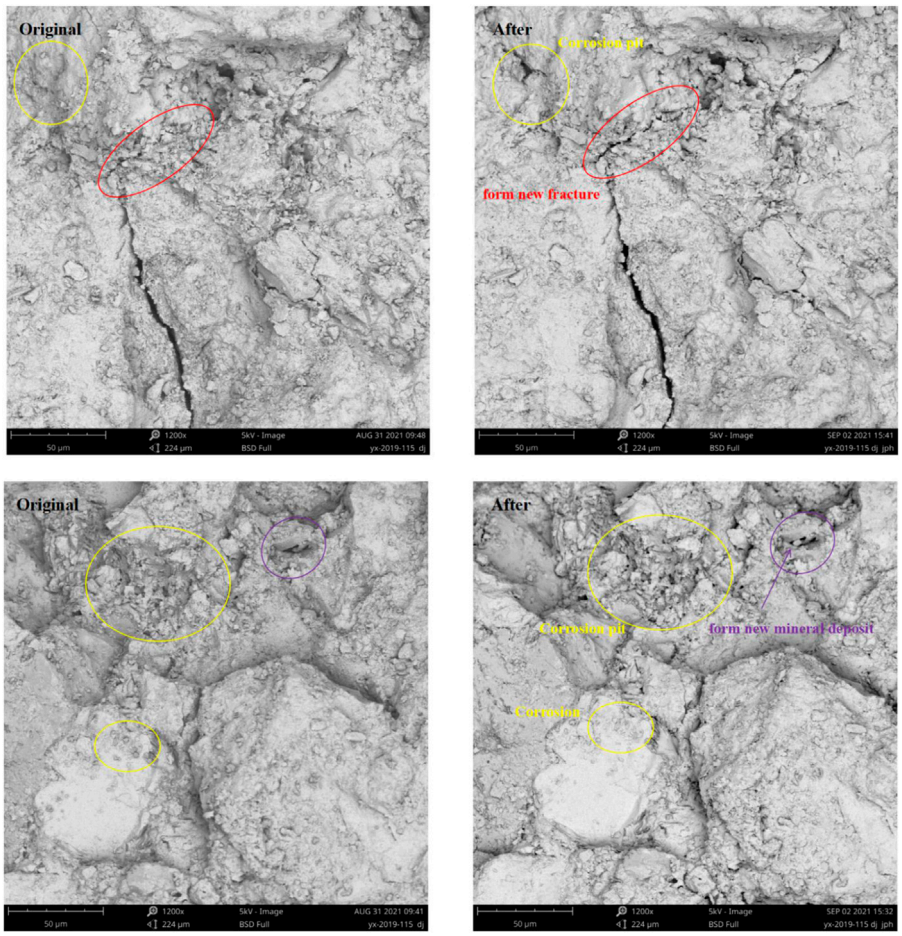

FIGURE 7 | Effect of supercritical CO_2 on microstructure.

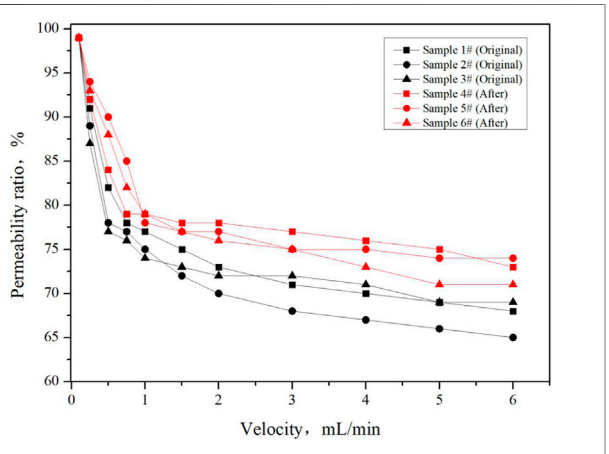

FIGURE 8 | Effect of supercritical CO_2 on velocity sensitivity.

After 24 h of interaction between supercritical CO_2 and tight sandstone core samples at 60°C and 15 MPa, simulated formation water at various constant flow velocities was injected into the samples to evaluate the velocity sensitivity of the samples before and after supercritical CO_2 action at room temperature using core displacement equipment. **Figure 8** depicts the experimental results of sample velocity sensitivity.

Small particles are always present in the reservoir, either strongly cemented, semi-consolidated, or even loosely distributed between the pore wall and large particles. When the flow velocity of external fluids or reservoir fluids was increased from 0.1 to 6.0 ml/min, particles migrated into the pore and plugged the pore throat, decreasing reservoir permeability. As shown in **Figure 8**, at the flow velocity of 0.5 ml/min, the permeability of Samples 2# and 3# decreased by 22% and 23%, respectively, causing flow velocity sensitivity, with a critical velocity of 0.25 ml/min; at the flow velocity of 0.75 ml/min, the permeability of Samples 1# and 4# decreased by 22% and 21%, respectively, causing flow velocity sensitivity, with a critical velocity of 0.50 ml/min; at the flow velocity of 1 ml/min, the permeability of Samples 5# and 6# decreased by 22% and 21%, respectively, causing flow velocity sensitivity, with a critical velocity of 0.75 ml/min. This revealed that after interacting with supercritical CO_2 and tight sandstone core samples,

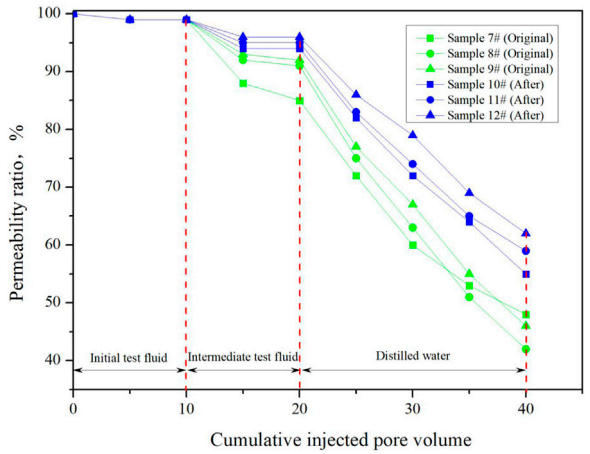

FIGURE 9 | Effect of supercritical CO_2 on water sensitivity.

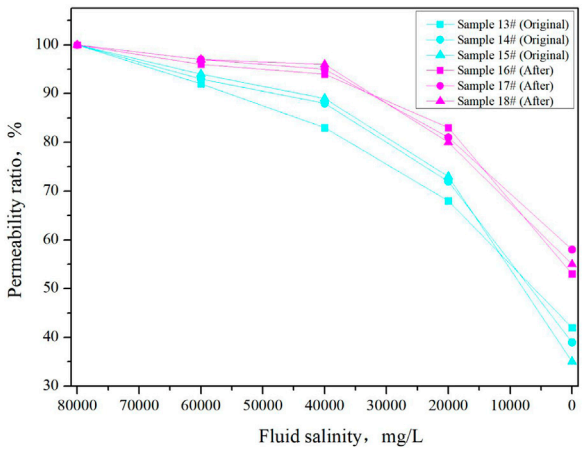

FIGURE 10 | Effect of supercritical CO_2 on salinity sensitivity.

corrosion and dissolution of quartz, feldspar, and clay minerals increased sample porosity and permeability, while precipitation of formed calcite and other minerals at the pore decreased sample porosity and permeability but had little effect on sample velocity sensitivity. The ultimate permeability rate increased from 67.3% to 72.7%, and the velocity sensitivity damage rate dropped by 5.4% as the average critical velocity of samples increased from 0.31 to 0.67 ml/min.

Effect of Supercritical CO_2 on Water Sensitivity

The phenomenon of reservoir permeability decreases due to hydration, expansion, dispersion, and migration of clay minerals due to their incompatibility with external fluids, which is dependent on the type and content of clay minerals in the reservoir, is referred to as reservoir water sensitivity. The purpose of the water sensitivity experiment is to find out how the reservoir expands, disperses, and migrates and how much the permeability of the reservoir decreases.

In order to evaluate the water sensitivity of samples before and after supercritical CO_2 action at a velocity lower than critical velocity using core displacement equipment, simulated formation water, saline water with salinity half that of simulated formation water, and distilled water were injected as initial test fluid, intermediate test fluid, and final test fluid, respectively. **Figure 9** depicts the experimental results of the water sensitivity of samples.

Clay minerals in the reservoir can balance with any natural reservoir fluid through cation exchange as the cumulative injected fluid increases. External fluid, on the contrary, changes the properties of pore fluid and breaks the balance during drilling, completion, and stimulation. The expandable clay will hydrate, expand, further disperse, fall off, and migrate in the presence of low salinity external fluid (such as distilled water), lowering and even blocking the pore throat, reducing reservoir permeability, and causing reservoir damage. As shown in **Figure 9**, when simulated formation water was injected as the initial test fluid, the permeability of six samples did not change significantly; when saline water with salinity half the simulated formation water was injected as intermediate test fluid, the permeability of six samples decreased, 8~15% for Samples 7#–9#, and 4~6% for Samples 10#–12#; and when distilled water was injected as final test fluid, the permeability of six samples further decreased, 52~58% for Samples 7#–9#, and 38%~45% for Samples 10#–12#. After interacting with supercritical CO_2 and tight sandstone core samples, corrosion and dissolution of quartz, feldspar, and clay minerals increased sample porosity and permeability, while the dissolution of water sensitivity minerals reduced the effect of salinity on sample permeability. The water sensitivity went from moderately high to moderately weak, and the water sensitivity damage rate went down by 13.3%.

Effect of Supercritical CO_2 on Salinity Sensitivity

Reservoir salinity sensitivity is a measure of the reservoir's ability to tolerate low-salinity fluids, with critical salinity as the mass index. It refers to the phenomenon of reservoir permeability decreases owing to hydration and expansion of clay minerals in saline water with varied salinities. When fluids of varying salinity flow through a clay-containing reservoir, the permeability of core samples changes little at first as the salinity decreases; however, when the salinity reaches a critical value, the permeability decreases dramatically as the salinity continues to decrease, and the salinity at this point is referred to as critical salinity.

After 24 h of interaction between supercritical CO_2 and tight sandstone core samples at 60°C and 15 MPa, saline water with various salinities was prepared and injected into samples in the order of high to low salinity (salinity was reduced by half) to measure the permeability of saline water with various salinities passing through core samples to evaluate the salinity sensitivity of samples before and after supercritical CO_2 action at a velocity lower than critical velocity. **Figure 10** depicts the experimental results of the salinity sensitivity of samples.

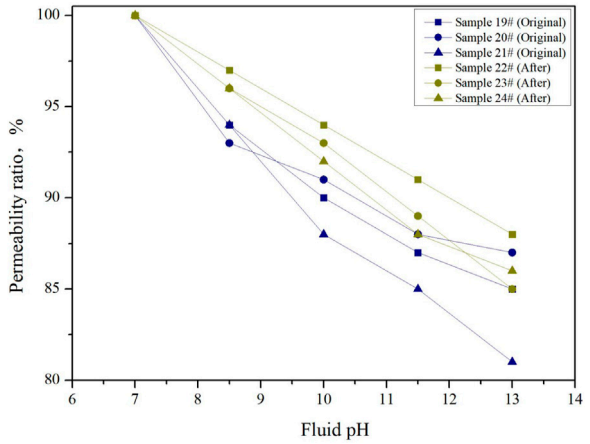

FIGURE 11 | Effect of supercritical CO_2 on alkali sensitivity.

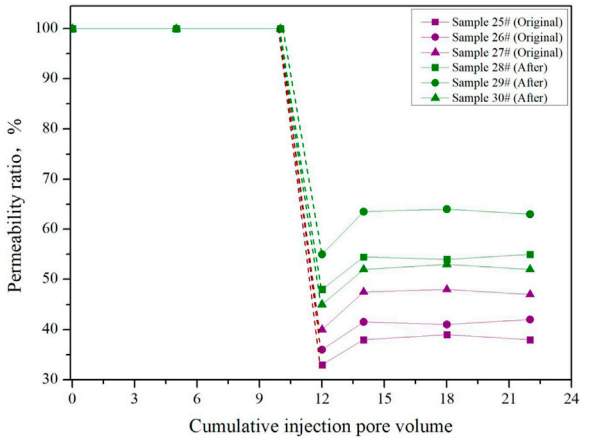

FIGURE 12 | Effect of supercritical CO_2 on acid sensitivity.

The clay particles became unstable, dropped off, and plugged the pore throat as salinity declined in sequence, resulting in a decrease in reservoir permeability. **Figure 10** shows that when simulated formation water was injected as the initial test fluid, the permeability of six samples did not change significantly; when saline water with a salinity of 60,000 mg/L was injected as test fluid, the permeability of six samples decreased, 6~8% for Samples 13#–15# and 3~4% for Samples 16#–18#; when saline water with a salinity of 40,000 mg/L was injected as test fluid, the permeability of six samples decreased, 11~17% for Samples 13#–15# and 4~6% for Samples 16#–18#; when saline water with a salinity of 20,000 mg/L was injected as test fluid, the permeability of six samples decreased, 27~32% for Samples 13#–15# and 17~20% for Samples 16#–18#; and when distilled water was injected as final test fluid, the permeability of six samples further decreased, 58~65% for Samples 13#–15# and 42~47% for Samples 16#–18#. Therefore, the critical salinity was 40,000 mg/L for Samples 13#–15# and 20,000 mg/L for Samples 16#–18#. This indicated that after interacting with supercritical CO_2 and tight sandstone core samples, the porosity and permeability of the samples increased due to corrosion and dissolution of quartz, feldspar, and clay minerals. The effect of salinity on permeability was reduced by the breakdown of water-sensitive minerals, and low-salinity liquid had a smaller effect on permeability. The critical salinity of the samples was reduced from 40,000 to 20,000 mg/L, and the salinity sensitivity damage rate was reduced by 16.6%.

Effect of Supercritical CO_2 on Alkaline Sensitivity

Alkali sensitivity is the phenomenon in which reservoir permeability decreases as a result of precipitation caused by alkaline fluids (pH > 7) reacting with reservoir rock or fluid. Although the reaction between alkaline fluid and formation rock is much weaker than that between acid fluid and formation rock, due to the long contact duration, the effect of alkaline fluid on reservoir permeability is still significant.

After 24 h of interaction between supercritical CO_2 and tight sandstone core samples at 60°C and 15 MPa, saline water with different pH was prepared to evaluate sample permeability and determine alkali sensitivity damage before and after supercritical CO_2 action at a velocity lower than critical velocity using core displacement equipment. **Figure 11** depicts the experimental results of alkali sensitivity of samples.

With the increase in pH, the formation of minerals and alkaline fluid exchanged ions to form water sensitivity minerals or directly generated precipitation materials to block the pore, so clay particles became unstable, fell off, and plugged the pore throat, resulting in a decrease in reservoir permeability. The permeability damage under five pH values was evaluated in the experiment. As can be seen from **Figure 11**, at pH = 7, the permeability of six samples did not change significantly; at pH = 8.5, the permeability of six samples decreased, 6~7% for Samples 19#–21# and 3~4% for Samples 22#–24#; at pH = 10, the permeability of six samples decreased, 9~12% for Samples 19#–21# and 6~8% for Samples 22#–24#; at pH = 11.5, the permeability of six samples decreased, 12~15% for Samples 19#–21# and 9~12% for Samples 22#–24#; and at pH = 13, the permeability of six samples decreased, 13~19% for Samples 19#–21# and 12~14% for Samples 22#–24#. The permeability of samples slightly decreased as pH increased, but there was no alkali sensitivity damage. Although the mineral composition and microstructure of the samples changed as a result of the interaction between supercritical CO_2 and tight sandstone core samples, the sensitivity of the alkaline fluid remained relatively unchanged. The rate of alkali sensitivity damage was lowered by only 2%.

Effect of Supercritical CO_2 on Acid Sensitivity

Acid sensitivity is the phenomenon in which reservoir permeability decreases as a result of precipitate or particles produced by acid fluids reacting with acid sensitivity minerals and fluids in the reservoir. Acid sensitivity causes two types of reservoir damage: one causes chemical precipitation, and the other causes the original rock structure to be destroyed, causing or aggravating velocity

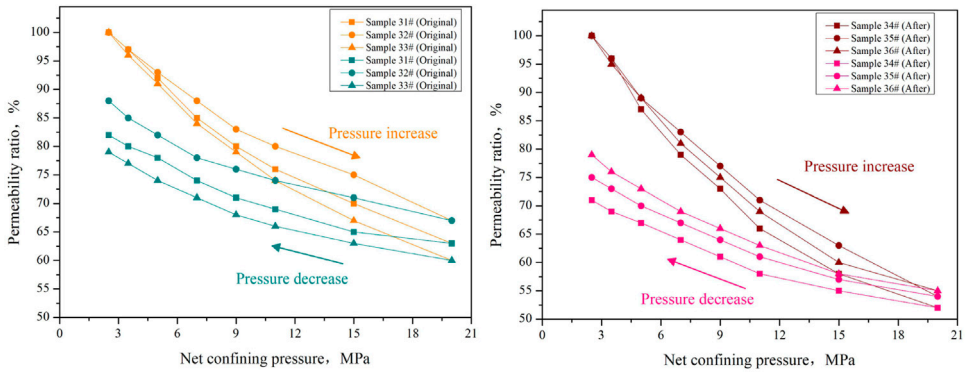

FIGURE 13 | Effect of supercritical CO_2 on stress sensitivity.

sensitivity. The most complicated category of reservoir sensitivities is acid sensitivity. The goal of the acid sensitivity evaluation experiment is to investigate whether and how much the acid prepared for the reservoir will damage the formation so that the acid fluid formula may be improved and more effective acid fluid types and treatment methods can be sought.

After 24 h of interaction between supercritical CO_2 and tight sandstone core samples at 60°C and 15 MPa, the initial permeability was tested with standard saline water, then 15% HCl solution was injected for saturation for 2 h, and finally, the acidified permeability was measured with standard saline water to evaluate the acid sensitivity of samples before and after supercritical CO_2 action at a velocity lower than critical velocity using core displacement equipment. **Figure 12** depicts the experimental results of acid sensitivity of samples.

Acid sensitivity minerals cause permeability to decrease by forming chemical precipitate or releasing particles when they react with acid fluid in the reservoir. Acid sensitivity minerals for hydrochloric acid are mainly minerals with high iron content, such as chlorite, chlorite- montmorillonite mixed-layer minerals, ankerite, and pyrite, with which hydrochloric acid reacts without producing direct precipitation, but the reaction products react again to produce an insoluble or insoluble secondary precipitation, such as silicate, aluminum silicate, hydroxide, or sulfide. Meanwhile, acid-released particles may plug the pore throat. As can be seen from **Figure 12**, when 15%HCl was injected, the permeability of six samples decreased significantly, 53~62% for Samples 25#–27# and 37~48% for Samples 28#–30#. This revealed that after interacting with supercritical CO_2 and tight sandstone core samples, corrosion and dissolution of quartz, feldspar, and clay minerals increased sample porosity and permeability. In contrast, the dissolution of acid-sensitive minerals reduced the influence of acid on sample permeability. Acid sensitivity dropped from fairly strong to moderately weak, and the rate of acid sensitivity damage dropped by 14.4%.

Effect of Supercritical CO_2 on Stress Sensitivity

The pore pressure decreases with the output of fluid inside the reservoir during the exploitation of oil and gas reservoirs and the original state of force balance of reservoir rock changes. As a result, the interaction of rock deformation and fluid seepage results in a change in reservoir permeability induced by net stress changes in the rock. The goal of the stress sensitivity evaluation experiment is to determine how much the throat deforms, closes, or opens as the net overlaying pressure changes and how much the rock seepage capability changes.

Standard saline water was used after 24 h of interaction between supercritical CO_2 and tight sandstone core samples at 60°C and 15 MPa, and the difference between confining pressure and injection pressure was gradually increased from 2.5 to 20 MPa and then decreased to 2.5 MPa to evaluate the stress sensitivity of samples before and after supercritical CO_2 action at a velocity lower than critical velocity using core displacement equipment. **Figure 13** depicts the experimental results of sample stress sensitivity.

According to rock mechanics theory, a change in stress state will eventually result in rock compression or expansion, that is, elastic or plastic deformation of rock, which will inevitably change the pore structure and pore volume of rock, affecting fluid seepage. As shown in **Figure 13**, after the increase in net confining pressure from 2.5 to 20 MPa, the permeability of Samples 31#–32# and Samples 33#–36# decreased by 33~40% and 45~48%, respectively, with average critical stress of 9 and 6.3 MPa corresponding to a 20% permeability decrease, respectively. After the decrease in net confining pressure from 20 to 2.5 MPa, the permeability of Sample 31#–32# and Sample 33#–36# was recovered to 79%~82% and 71%~79% of the initial core permeability, respectively. This showed that after interaction between supercritical CO_2 and tight sandstone core samples, corrosion and dissolution of quartz, feldspar, and clay minerals increased the porosity and permeability of samples, and the pore structure and volume of rock changed more under stress conditions. The rate of stress sensitivity damage increased by 8%.

SUMMARY AND CONCLUSION

1) Water-based fracture fluid is difficult to flow back in low-pressure gas reservoirs of Jinqiu gas field, Sichuan Basin, because the tight sandstone reservoir pressure coefficient is 0.45–1.05 and the pressure coefficient of some sand bodies is

too low. Supercritical CO_2 fracturing has some advantages in reservoirs, particularly for water-sensitive formations, low-pressure reservoirs, and water-stressed areas, making it one of the most environmentally benign fracturing techniques.

2) After interacting with supercritical CO_2, Jinqiu Gas field tight sandstone weak dissolution of feldspar and clay minerals occurred, forming a curved dissolution fracture, a tiny quantity of irregular mineral precipitation also formed, plugging the original pore velocity, and sensitivity damage decreased by 5.4%, water sensitivity damage decreased by 13.3%, salinity sensitivity damage decreased by 16.6%, alkaline sensitivity damage decreased by 2%, acid sensitivity damage decreased by 14.4%, and stress sensitivity damage increased by 8%.
3) Quantify the effect of supercritical CO_2 on tight sandstone formation sensitivity, and improve the interaction mechanism between supercritical CO_2 and low-pressure tight sandstone. This finding provides a quantitative evaluation of the effects of supercritical CO_2 on formation sensitivity, and it can be used to build a supercritical CO_2 fracturing scheme for low-pressure water-sensitive tight sandstone.

DATA AVAILABILITY STATEMENT

The original contributions presented in the study are included in the article/supplementary material. Further inquiries can be directed to the corresponding author.

AUTHOR CONTRIBUTIONS

HP is responsible for the overall structure and revision. LZ, JY, and HH help evaluate and improve the paper. JP, XG, and ZW help in setting up the device test, writing, and the experiment.

FUNDING

This work was funded by the Scientific Research and Technology Development Project of Southwest Oil and Gas Field Company, PetroChina, Project No. 20210302-05.

REFERENCES

Akrad, O., Miskimins, J., and Manika, P. (2011). "The Effects of Fracturing Fluids on Shale Rock Mechanical Properties and Proppant Embedment," in Paper Presented at the SPE Annual Technical Conference and Exhibition, Denver, CO, October 2011 (OnePetro). doi:10.2118/146658-MS

Al-Yaseri, A. Z., Lebedev, M., Vogt, S. J., Johns, M. L., Barifcani, A., and Iglauer, S. (2015). Pore-Scale Analysis of Formation Damage in Bentheimer Sandstone with *In-Situ* NMR and Micro-Computed Tomography Experiments. *J. Pet. Sci. Eng.* 129, 48–57. doi:10.1016/j.petrol.2015.01.018

Ao, X., Lu, Y., Tang, J., Chen, Y., and Li, H. (2017). Investigation on the Physics Structure and Chemical Properties of the Shale Treated by Supercritical CO_2. *J. CO2 Util.* 20, 274–281. doi:10.1016/j.jcou.2017.05.028

Bahrami, H., Rezaee, R., and Clennell, B. (2012). Water Blocking Damage in Hydraulically Fractured Tight Sand Gas Reservoirs: An Example from Perth Basin, Western Australia. *J. Pet. Sci. Eng.* 88-89, 100–106. doi:10.1016/j.petrol.2012.04.002

Cabeza, L. F., de Gracia, A., Fernández, A. I., and Farid, M. M. (2017). Supercritical CO_2 as Heat Transfer Fluid: A Review. *Appl. Therm. Eng.* 125, 799–810. doi:10.1016/j.applthermaleng.2017.07.049

Cao, Y., Zhang, J., Zhai, H., Fu, G., Tian, L., and Liu, S. (2017). CO_2 Gas Fracturing: A Novel Reservoir Stimulation Technology in Low Permeability Gassy Coal Seams. *Fuel* 203, 197–207. doi:10.1016/j.fuel.2017.04.053

Chen, K., Liu, X., Nie, B., Zhang, C., Song, D., Wang, L., et al. (2022). Mineral Dissolution and Pore Alteration of Coal Induced by Interactions with Supercritical CO2. *Energy* 248, 123627. doi:10.1016/j.energy.2022.123627

Day, S., Fry, R., and Sakurovs, R. (2008). Swelling of Australian Coals in Supercritical CO_2. *Int. J. Coal Geol.* 74 (1), 41–52. doi:10.1016/j.coal.2007.09.006

Dong, Z., Tang, S., Ranjith, P. G., and Lang, Y. (2018). A Theoretical Model for Hydraulic Fracturing through a Single Radial Perforation Emanating from a Borehole. *Eng. Fract. Mech.* 196, 28–42. doi:10.1016/j.engfracmech.2018.04.029

Fang, W., Jiang, H., Li, J., Li, W., Li, J., Zhao, L., et al. (2016). A New Experimental Methodology to Investigate Formation Damage in Clay-Bearing Reservoirs. *J. Petroleum Sci. Eng.* 143, 226–234. doi:10.1016/j.petrol.2016.02.023

Gathitu, B. B., Chen, W.-Y., and McClure, M. (2009). Effects of Coal Interaction with Supercritical CO_2: Physical Structure. *Ind. Eng. Chem. Res.* 48 (10), 5024–5034. doi:10.1021/ie9000162

Gupta, S. (2011). "Unconventional Fracturing Fluids: What, Where and Why," in Technical Workshops for the Hydraulic Fracturing Study, Arlington, VA, February 2011 (US EPA).

Hazarika, S., and Boruah, A. (2022). Supercritical CO_2 (SCO_2) as Alternative to Water for Shale Reservoir Fracturing. *Mater. Today Proc.* 50, 1754–1757. doi:10.1016/j.matpr.2021.09.187

Jia, Y., Lu, Y., Elsworth, D., Fang, Y., and Tang, J. (2018). Surface Characteristics and Permeability Enhancement of Shale Fractures Due to Water and Supercritical Carbon Dioxide Fracturing. *J. Pet. Sci. Eng.* 165, 284–297. doi:10.1016/j.petrol.2018.02.018

Jiang, Y., Luo, Y., Lu, Y., Qin, C., and Liu, H. (2016). Effects of Supercritical CO_2 Treatment Time, Pressure, and Temperature on Microstructure of Shale. *Energy* 97, 173–181. doi:10.1016/j.energy.2015.12.124

Jiao, F. (2019). Re-Recognition of "Unconventional" in Unconventional Oil and Gas. *Pet. Explor. Dev.* 46 (5), 847–855. doi:10.1016/s1876-3804(19)60244-2

Lin, H., Fujii, T., Takisawa, R., Takahashi, T., and Hashida, T. (2008). Experimental Evaluation of Interactions in Supercritical CO_2/Water/Rock Minerals System under Geologic CO_2 Sequestration Conditions. *J. Mater Sci.* 43 (7), 2307–2315. doi:10.1007/s10853-007-2029-4

Lin, R., Yu, Z., Zhao, J., Dai, C., Sun, Y., Ren, L., et al. (2022). Experimental Evaluation of Tight Sandstones Reservoir Flow Characteristics under CO_2–Brine–Rock Multiphase Interactions: A Case Study in the Chang 6 Layer, Ordos Basin, China. *Fuel* 309, 122167. doi:10.1016/j.fuel.2021.122167

Liu, H., Wang, F., Zhang, J., Meng, S., and Duan, Y. (2014). Fracturing with Carbon Dioxide: Application Status and Development Trend. *Pet. Explor. Dev.* 41 (4), 513–519. doi:10.1016/s1876-3804(14)60060-4

Memon, S., Feng, R., Ali, M., Bhatti, M. A., Giwelli, A., Keshavarz, A., et al. (2022). Supercritical CO_2-Shale Interaction Induced Natural Fracture Closure: Implications for $scCO_2$ Hydraulic Fracturing in Shales. *Fuel* 313, 122682. doi:10.1016/j.fuel.2021.122682

Moghadasi, J., Müller-Steinhagen, H., and Jamialahmadi, M. (2004). Model Study on the Kinetics of Oil Field Formation Damage Due to Salt Precipitation from Injection. *J. Pet. Sci. Eng.* 43 (3-4), 201–217. doi:10.1016/j.petrol.2004.02.014

Mouahid, A., Claeys-Bruno, M., Bombarda, I., Amat, S., Ciavarella, A., Myotte, E., et al. (2022). Supercritical CO_2 Extraction of Oil from Moroccan Unroasted Argan Kernels: Effects of Process Parameters to Produce Cosmetic Oil. *J. CO2 Util.* 59, 101952. doi:10.1016/j.jcou.2022.101952

Nikolai, P., Rabiyat, B., Aslan, A., and Ilmutdin, A. (2019). Supercritical CO_2: Properties and Technological Applications-A Review. *J. Therm. Sci.* 28 (3), 394–430. doi:10.1007/s11630-019-1118-4

Peng, Y., Li, Y., and Zhao, J. (2016). A Novel Approach to Simulate the Stress and Displacement Fields Induced by Hydraulic Fractures under Arbitrarily Distributed Inner Pressure. *J. Nat. Gas Sci. Eng.* 35, 1079–1087. doi:10.1016/j.jngse.2016.09.054

Peng, Y., Zhao, J., Sepehrnoori, K., Li, Y., and Li, Z. (2020). The Influences of Stress Level, Temperature, and Water Content on the Fitted Fractional Orders of Geomaterials. *Mech. Time-Depend Mater* 24 (2), 221–232. doi:10.1007/s11043-019-09417-0

Peng, Y., Zhao, J., Sepehrnoori, K., Li, Z., and Xu, F. (2019). Study of Delayed Creep Fracture Initiation and Propagation Based on Semi-analytical Fractional Model. *Appl. Math. Model.* 72, 700–715. doi:10.1016/j.apm.2019.03.034

Reinicke, A., Rybacki, E., Stanchits, S., Huenges, E., and Dresen, G. (2010). Hydraulic Fracturing Stimulation Techniques and Formation Damage Mechanisms-Implications from Laboratory Testing of Tight Sandstone-Proppant Systems. *Geochemistry* 70, 107–117. doi:10.1016/j.chemer.2010.05.016

Umar, M., Farid, S., and Naeem, M. A. (2022). Time-Frequency Connectedness Among Clean-Energy Stocks and Fossil Fuel Markets: Comparison between Financial, Oil and Pandemic Crisis. *Energy* 240, 122702. doi:10.1016/j.energy.2021.122702

Wang, J., Elsworth, D., Wu, Y., Liu, J., Zhu, W., and Liu, Y. (2018). The Influence of Fracturing Fluids on Fracturing Processes: A Comparison between Water, Oil and SC-CO_2. *Rock Mech. Rock Eng.* 51 (1), 299–313. doi:10.1007/s00603-017-1326-8

Wilson, M. J., Wilson, L., and Patey, I. (2014). The Influence of Individual Clay Minerals on Formation Damage of Reservoir Sandstones: A Critical Review with Some New Insights. *Clay Min.* 49 (2), 147–164. doi:10.1180/claymin.2014.049.2.02

Xu, C., Kang, Y., You, Z., and Chen, M. (2016). Review on Formation Damage Mechanisms and Processes in Shale Gas Reservoir: Known and to Be Known. *J. Nat. Gas Sci. Eng.* 36, 1208–1219. doi:10.1016/j.jngse.2016.03.096

Zhang, B. J., Pan, K., and Wu, C. J. (2022). Compound Gas Accumulation Mechanism and Model of Jurassic Shaximiao Formation Multistage Sandstone Formations in Jinqiu Gas Field of the Sichuan Basin. *Nat. Gas. Ind.* 42 (1), 51–61. doi:10.3787/j.issn.10000976.2022.01.005

Zhang, L., Zhou, F., Zhang, S., Wang, Y., Wang, J., and Wang, J. (2019). Investigation of Water-Sensitivity Damage for Tight Low-Permeability Sandstone Reservoirs. *ACS Omega* 4 (6), 11197–11204. doi:10.1021/acsomega.9b01286

Zhao, J., Peng, Y., Li, Y., and Tian, Z. (2017). Applicable Conditions and Analytical Corrections of Plane Strain Assumption in the Simulation of Hydraulic Fracturing. *Pet. Explor. Dev.* 44 (3), 454–461. doi:10.1016/s1876-3804(17)30052-6

Zheng, Y., Han, X., Zeng, J., Zhou, C., Zhou, L., and Chen, W. (2021). Practice of High-Intensity Volume Fracturing in the Shaximiao Formation Tight Sandstone Gas Reservoirs of the Qiulin Block, Central Sichuan Basin. *Nat. Gas. Ind. B* 8 (4), 367–375. doi:10.1016/j.ngib.2021.07.007

Zhou, D., Zhang, G., Prasad, M., and Wang, P. (2019). The Effects of Temperature on Supercritical CO_2 Induced Fracture: An Experimental Study. *Fuel* 247, 126–134. doi:10.1016/j.fuel.2019.02.099

Zhou, J., Xie, S., Jiang, Y., Xian, X., Liu, Q., Lu, Z., et al. (2018). Influence of Supercritical CO_2 Exposure on CH4 and CO_2 Adsorption Behaviors of Shale: Implications for CO_2 Sequestration. *Energy Fuels* 32 (5), 6073–6089. doi:10.1021/acs.energyfuels.8b00551

Zhou, Y., Yang, W., and Yin, D. (2022). Experimental Investigation on Reservoir Damage Caused by Clay Minerals after Water Injection in Low Permeability Sandstone Reservoirs. *J. Pet. Explor Prod. Technol.* 12 (4), 915–924. doi:10.1007/s13202-021-01356-2

Conflict of Interest: HP, JY, JP, HH, XG, and ZW were employed by the company Engineering Technology Research Institute of Southwest Oil and Gas Field Company, PetroChina, and Key Laboratory of Oil and Gas Well Stimulation Technology of Southwest Oil and Gas Field Company. LZ was employed by the company Southwest Oil and Gas Field Company, PetroChina

frontiers | Frontiers in Energy Research

METHODS
published: 30 June 2022
doi: 10.3389/fenrg.2022.929606

Using the Multiple Linear Regression Method for CO_2 Flooding Evaluation in the Daqing Oilfield

Zhenhua Wang[1,2], *Jirui Hou*[1,2]*, *Hongda Hao*[3], *Cheng Wang*[1,2] *and Likun Wang*[1,2]

[1]*Enhanced Oil Recovery Institute, China University of Petroleum, Beijing, China,* [2]*Basic Theory Laboratory of Improving Oil Recovery in Low Permeability Oilfields, Tertiary Oil Recovery Key Laboratory, CNPC, Beijing, China,* [3]*School of Petroleum Engineering, Changzhou University, Changzhou, China*

CO_2 flooding and burial efficiency can be improved by establishing a standard for screening suitable CO_2 flooding reservoirs for the Daqing Oilfield. Moreover, the influencing factors of CO_2 flooding can be classified into geological factors, fluid properties, and development factors. An evaluation index system and hierarchical structure are created based on the importance of multiple factors. The subjective analysis error of human beings is quite large when establishing the evaluation index system, especially in the fitting curves that are drawn by different analysts. Based on the geological characteristics of block Bei14 in the Daqing Oilfield, a typical CMG model is presented in this article. A total of 15 factors in the 72 models are used as independent variables, and the recovery factor is used as a dependent variable for multiple linear regression calculations. In addition to sensitivity tests based on how much significance is indicated by the *t* value in the results, a unique result can be calculated using standard statistical methods when analyzing the calculation results of the multiple linear regression model. The results of the screening standard evaluation system are consistent with the production history of the oilfield based on the mathematical understanding of multiple factors of CO_2 flooding. Around the high-score well group, oil saturation decreases significantly, and the cumulative production is generally higher than that of the low-score well group. The calculation results of block Bei 14 show that 74% of well groups have an evaluation value greater than 0.50, and 72% of well groups have an annual oil exchange ratio above 40%, which means that over 70% of well groups can benefit from CO_2 flooding. Thus, CO_2 flooding can be applied in the Daqing Oilfield, and multiple linear regression can provide effective guidance for the Daqing Oilfield's development.

Keywords: CO_2 flooding evaluation, Daqing Oilfield, numerical simulation, mathematical simulation, multiple linear regression

OPEN ACCESS

Edited by:
Yibo Li,
Southwest Petroleum University, China

Reviewed by:
Junyu You,
Chongqing University of Science and Technology, China
May Ali Alsaffar,
University of Technology, Iraq
Hao Gao,
Southwest Petroleum University, China

***Correspondence:**
Jirui Hou
houjirui@126.com

Specialty section:
This article was submitted to Advanced Clean Fuel Technologies, a section of the journal Frontiers in Energy Research

Received: *27 April 2022*
Accepted: *19 May 2022*
Published: *30 June 2022*

Citation:
Wang Z, Hou J, Hao H, Wang C and Wang L (2022) Using the Multiple Linear Regression Method for CO_2 Flooding Evaluation in the Daqing Oilfield. Front. Energy Res. 10:929606. doi: 10.3389/fenrg.2022.929606

1 INTRODUCTION

In the past few decades, greenhouse gas emissions have become increasingly serious, and a solution to the carbon dioxide problem is imminent with the use of fossil fuels (Zandalinas et al., 2021). Many countries and regions have proposed policies to address carbon emissions, including initiatives such as gasoline taxes, new energy sources, and emission subsidies (Finke et al., 2021). China still faces the

challenge of reaching peak total CO_2 emissions by 2030 and achieving 21 carbon neutrality by 2060 (Liu et al., 2021). China has also proposed solutions for its own energy structure, including green energy saving and emission reduction, carbon capture, carbon burial, and other technological innovation directions (Li, 2021). Low-permeability and extra-low-permeability reservoirs make up a large proportion of the reservoirs in China, so water-driven mining is easy to encounter the situation of not being able to inject and recover oil, and the recovery rate of water-driven mining is generally low compared with that of CO_2-driven technology (Li et al., 2021; Yu et al., 2021). CO_2 flooding technology can improve recovery while storing greenhouse gases in the ground, responding to today's carbon neutrality policy (Jiang and Ashworth, 2021; Xu et al., 2021). However, in CO_2 flooding, the effect of formation development is not understood, which leads to the lack of obvious effects of CO_2 flooding to improve recovery. Moreover, the influence of temperature, formation inclination, development method, and other factors on the effect of CO_2 flooding is not fully recognized (Feng et al., 2016; Xiaolong et al., 2021). For this reason, it is necessary to evaluate CO_2 flooding blocks and establish a complete selection index to provide a basis for the gas injection and extraction plan (DaneshFar et al., 2021; Angarita et al., 2022).

The change in recovery is frequently affected by various essential aspects in the research of practical problems, such as effective temperature, viscosity, and permeability. For example, oil reservoirs extracted at high temperatures can result in lower crude oil viscosity, which leads to less resistance of the subsurface fluid when driven by CO_2, and under the condition of low permeability, CO_2 is easily retained in the rock micropore throat, resulting in a poor CO_2 oil production effect (Zhou et al., 2019; Pu et al., 2022). At this point, two or more factors must be used as independent variables to explain the change in recovery. Nevertheless, the error of subjective analysis is relatively large when determining the impact of multiple factors on recovery (Mellor, 1965; Colclough, 1987). This is because while analyzing the experimental results of multi-factor CO_2 flooding-enhanced recovery, some individuals will focus on temperature, while others will focus on permeability, demonstrating that various people have different perspectives on experimental data. With the multiple linear regression method, this problem can be effectively solved as long as the data and model are identical, and a unique result can be calculated by using standard statistical methods (Etemadi and Khashei, 2021; Maaouane et al., 2021; Piekutowska et al., 2021). In order to establish the screening standard of CO_2 flooding reservoirs in the Daqing Oilfield more scientifically, after using the multiple linear regression method to judge the sensitivity, according to the influence of various factors on oil recovery, it is divided into multi-factor categories, and the effect indicators of CO_2 flooding are divided into three categories: geological factors, fluid properties, and development indicators. According to the importance of sorting, the evaluation index system is established, and the hierarchical structure is constructed. The screening standard of CO_2 flooding reservoirs in low-permeability reservoirs in the Daqing Oilfield is established (Chai et al., 2021; Pokoradi et al., 2021; Sun, 2021). When calculating the evaluation value of enhanced oil recovery by CO_2 flooding, because the reservoir data are complex and the units of different factors are different, the geological data of the field should be normalized (Gao et al., 2021; Moreira et al., 2021). According to the normalized data, the reservoir suitability evaluation of CO_2 flooding is calculated. This method can be used in all blocks of the whole Daqing Oilfield, and the evaluation value of all blocks will be calculated (Bhatti et al., 2019; Foukerdi et al., 2021; Zheng et al., 2022).

This article mainly focuses on the multi-factor experiment of CO_2 miscible flooding numerical simulation in ultra-low-permeability reservoirs on the basis of calculation results, typical model design of reservoir engineering numerical simulation, and the multi-factor screening criteria. With the sensitivity of experimental results by the multiple linear regression method, screening criteria are established by the analytic hierarchy process (AHP), and the CO_2 gas drive well groups in ultra-low-permeability reservoirs of the Daqing Oilfield are evaluated and divided. The purpose is to establish a screening index and provide technical support for field test demonstration zones for enhanced oil recovery in the Daqing Oilfield (Yu et al., 2021; Zhou, 2021). The novelty of this study is to apply the regression equation to the gas injection evaluation of ultra-low-permeability reservoirs. While calculating the suitability of well groups for CO_2 flooding, it can provide suggestions on readjusting for the gas injection wells with various evaluation values.

2 CO_2 FLOODING SENSITIVITY EVALUATION MODELING

2.1 Model Building

The Bei14 block, with an area of about 4.5 km^2, is located in the western Sudeerte tectonic belt of the Hailar Basin. The main oil-bearing reservoirs are fan delta front subfacies with formation temperatures ranging from 45.7 to 72.0°C and burial depths ranging from 1775 to 1820 m. This block's rock types are mostly tuffaceous sandstone with a few conglomerates that mostly exist in the form of a bottom conglomerate.

As formation water in the Xinganling formation in the Bei14 block is not well developed, the CMG-GEM simulator was used to create a typical reservoir model without marginal bottom water (**Figure 1**). The typical model has a crude oil density of 0.8389 g/cm^3 under surface conditions and an average rock compression coefficient of 13.74×10^4 MPa^{-1} and uses typical oil–water and oil–gas relative permeability curves for low-permeability reservoirs (**Figure 2**). Based on well testing and production data, the model reservoir temperature is set as 65 °C, the original formation pressure is set as 17.60 MPa, and the average oil saturation is set as 44%. According to the porosity and permeability distribution of different well test depths in the Bei14 block, the average

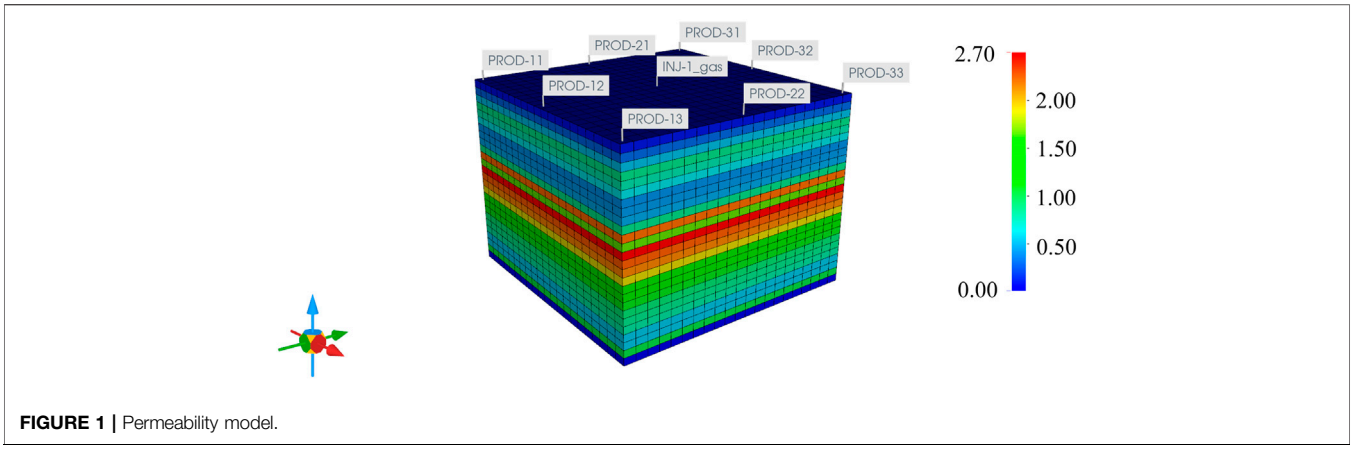

FIGURE 1 | Permeability model.

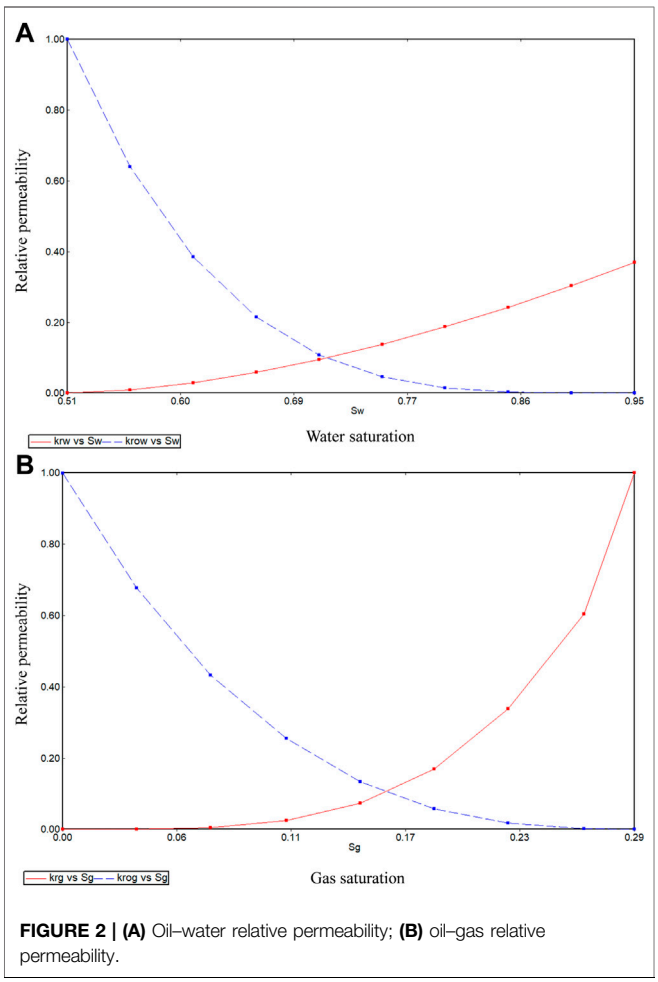

FIGURE 2 | (A) Oil–water relative permeability; **(B)** oil–gas relative permeability.

TABLE 1 | Modeled permeability and porosity.

Layer	Permeability (mD)	Porosity (%)
1	0.27	11
2	0.48	12
3	0.70	15
4	1.03	15
5	0.95	16
6	0.80	16
7	0.58	15
8	0.60	14
9	0.64	15
10	1.03	15
11	2.36	16
12	1.84	15
13	2.67	14
14	2.40	15
15	2.30	14
16	2.07	13
17	1.76	13
18	1.74	13
19	1.25	12
20	1.08	11
21	1.03	11
22	0.98	11
23	0.72	10
24	0.72	9
25	1.18	9
26	0.18	8

porosity of the model is set to 13%, and the average permeability is set to 1.2 mD (**Table1**). The typical model is divided vertically into 26 small layers, each with a thickness of 1 m and a uniform thickness in the plane. An orthogonal grid system is used to construct the typical model, which has a size of 410 m × 350 m × 15 m, grids of 41 × 35 × 26 = 37,310, a depth of 1815 m in the center, a height of 1830 m at the oil–water interface, a dip angle of 0° for the formation, and a geological reserve of 25.69×10^4 t. INJ-1, the gas injection well, is located in the models center, and the production mode of the production well is consistent with that of the oilfield site. Eight production wells are distributed by the nine-point method, and the well spacing is set to 300 m.

2.2 Phase Matching

In order to improve the prediction accuracy of oil reservoir fluid properties, well fluid components are combined into seven components according to the principle of similar component properties without affecting the simulation results. CMG-

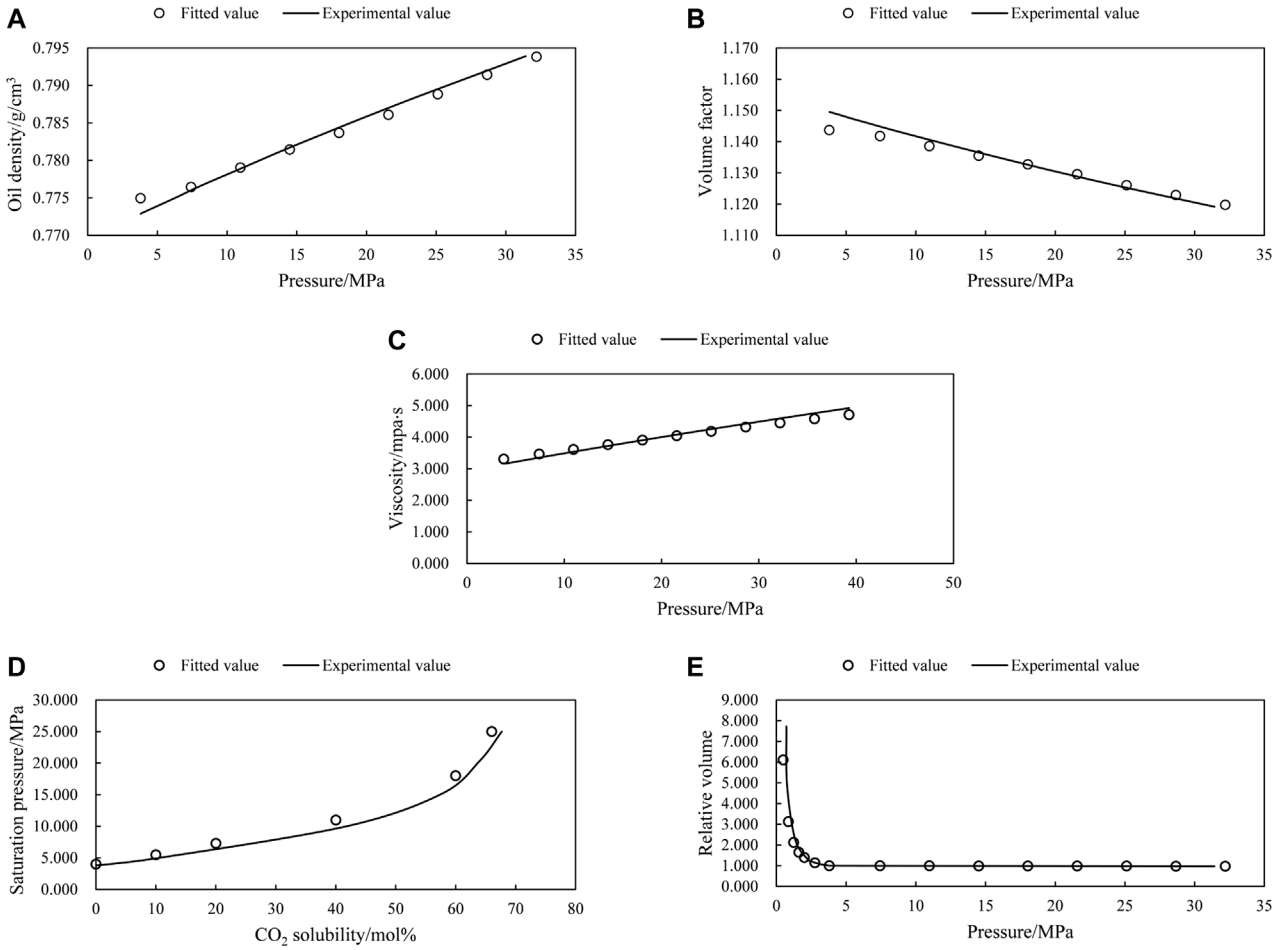

FIGURE 3 | (A) Oil density fitting; **(B)** volume factor fitting; **(C)** viscosity fitting; **(D)** saturation pressure fitting; **(E)** relative volume fitting.

Winprop software is used to fit the relative volumes, oil density, and oil viscosity at different pressures by adjusting more than 10 component critical state parameters of each component (**Figure 3**). Repeated trial calculations of the constant component expansion experimental data with high accuracy, within 5% of the fitting accuracy, are performed. The results of the component fitting show 'CO_2' for 0, 'C1′ for 0.086144, 'C2+' for 0.054421, 'C4+' for 0.030105, 'C6+' for 0.22996, 'C9+' for 0.28357, and 'C11+' for 0.3158.

After setting the corresponding components in the initial typical model, the resultant operations can be performed. When the production gas–oil ratio reaches 1000 m^3/m^3, the cumulative production is 4.705 × 10^4 t, which corresponds to an oil recovery rate of 18.32%.

2.3 Dynamic Model

A total of 72 reservoir models are designed to determine CO_2 flooding screening criteria for the Daqing Oilfield based on 17 factors, including formation pressure (5–20 MPa), formation temperature (35–45°C), effective thickness (6–56 m), average permeability (0.1–50 mD), and well spacing (100–500 m) (**Table2**).

3 SENSITIVITY ANALYSIS

3.1 Model Calculation Results

In terms of the calculation results of 72 models, it is known that in the geological factors, oil saturation and thickness of the oil reservoir have the most obvious influence on the enhanced oil in place. A thicker effective thickness and a steeper dip angle are detrimental to the recovery rate, but the effect of oil saturation on the recovery rate is the opposite with the recovery rate increasing from 19.40 to 32.68% with an increase from 44 to 74%. The recovery of the heterogeneity model is significantly lower when there is CO_2 flooding in the layer due to the vertical heterogeneity of multilayer reservoirs, which results in notable interlayer interference. Since increases in temperature and pressure lead to lower crude oil viscosity and increased CO_2 solubility in crude oil, it is easier to induce a miscible phase and thus increase the recovery rate. An inflection point occurs in the oil recovery ratio at around 1.2 mD, which is due to the theory that high gas flow rates at high permeability lead to high recovery rates that are not suitable for CO_2 flooding processes; when the permeability is too large, the CO_2 breakthrough time is too early and the contact time with oil is too

TABLE 2 | Model factor design.

Number	Factors	Factor Design
1	Dip angle (o)	0°, 5°, 10°, 15°
2	Depth (km)	1.312, 1.155, 0.984, 0.656, 0.328
3	Pressure (MPa)	20, 17.6, 15, 10, 5
4	Temperature (°C)	35, 45, 55, 65
5	Thickness (m)	6, 16, 26, 36, 46, 56
6	Average permeability (mD)	0.1, 0.8, 1.2, 10, 50
7	Formation development (K_V/K_H)	0.001, 0.01, 0.1, 0.3, 0.5
8	Oil saturation (%)	0.74, 0.64, 0.54, 0.44, 0.24
9	Permeability direction development (K_Y/K_X)	5, 10, 20, 50, 100
10	Well spacing (m)	100 m, 200 m, 300 m, 400 m, 500 m
11	Well pattern (spot)	5, 7, negative-7, 9, negative-9
12	Viscosity (mPa.s)	1,270, 64, 3.88, 1.2, 0.76
13	Density (kg/m^3)	798, 796, 782, 753, 700
14	Permeability variation coefficient	0.1, 0.2, 0.35, 0.6, 0.7
15	Injection volume (10^4 t/year)	0.2, 0.8, 1, 1.4, 1.6
16	Sedimentary rhythm	positive, negative, compound
17	Yield (m^3/d)	2, 5, 10, 20, 50

short, all of which prevent gas flooding from making full use of its advantages (**Figures 4A–J**). In the fluid properties, viscosity and density of the oil play a similar role in enhanced oil recovery of CO_2 flooding because the decrease of oil viscosity and density leads to the decrease of seepage resistance of CO_2 flooding and the increase of oil displacement efficiency (**Figures 4M,N**. In the development index, the inverse 9-point well pattern has higher cumulative oil production and a higher burial rate than the 5-point well pattern and inverse 7-point well pattern; a smaller distance between wells leads to the larger driving area of CO_2 flooding. In the process of gas flooding, CO_2 tends to advance rapidly along the upper part of the reservoir, the negative rhyme accelerates the trend with the worst recovery effect, and the positive rhyme slows down the trend with the best recovery effect, while in the compound rhyme, the superposition of the two rhymes has the middle effect on the recovery improvement (**Figures 4K**, **5**). Due to the higher sweeping volume, greater gas injection facilitates better oil displacement performance, which is advantageous for the daily oil production of well groups (**Figures 4L,O**).

Based on the data obtained in the factor sensitivity analysis, multiple linear regression is performed by integrating pressure and depth as one-factor consideration, viscosity and density as one-factor consideration, and 15 factors from the 72 models as independent variables with recovery rate as the dependent variable. The reason for combining some of them into one variable, such as pressure and depth, and viscosity and density, in this article is the extreme similarity of their effects on recovery, in order to avoid the multi-collinearity that arises in regression analysis (Gunst and Webster, 1975; Montgomery and Voth, 1994). Let y be the dependent variable and x_k be the independent variable, and when the relationship between the independent variable and the dependent variable is linear, the multiple linear regression model is as follows:

$$y = t_0 + t_1 x_1 + t_2 x_2 + \ldots e \tag{1}$$

In **Eq. 1**, y is the recovery factor, x_k is the formation dip angle, formation pressure, formation temperature, and other independent variables. The t value is calculated to represent the mathematical degree of sensitivity of each parameter to the recovery rate when considering the correlation between the independent variables. Based on a multiple linear regression model, the standard set of equations for solving the regression parameters is as follows:

$$\begin{bmatrix} t_0 \\ t_1 \\ t_2 \\ \vdots \end{bmatrix} = \begin{bmatrix} n & \sum x_1 & \sum x_2 \\ \sum x_1 & \sum x_1^2 & \sum x_1 x_2 \\ \sum x_2 & \sum x_1 x_2 & \sum x_2^2 \\ \vdots & \vdots & \vdots \end{bmatrix}^{-1} \times \begin{bmatrix} \sum y \\ \sum x_1 y \\ \sum x_2 y \\ \vdots \end{bmatrix} \tag{2}$$

Equation 2 is a matrix solution equation, where it is possible to solve for the value of t through the interactive effects among those parameters and the recovery rate y. The regression analysis has a prerequisite that the variables are independent of each other and also satisfy multi-collinearity. Therefore, the independence verification in the results is as follows. The results of the calculation are shown in **Table 3**; the more the " F" value converges to 1, the better the independence of the sample. For more details, please see the equations shown below:

$$\mathrm{R}^2 = \frac{\sum (\hat{y} - \bar{y})^2}{\sum (y - \bar{y})^2} \tag{3}$$

$$F = \frac{R^2/k}{(1 - R^2)/n - k - 1} \tag{4}$$

In **Eqs. 3** and **4**, y is the actual value, $\overline{y}$ is the mean value, $\hat{y}$ is the estimated value, and F is the multi-collinearity value of the K_{th} reservoir model. The formula for calculating the apparent value t_i of the regression equation is as follows:

$$t_i = \frac{b_i}{s_{\mathrm{bi}}} \tag{5}$$

In **Eq. 5**, b_i is the regression coefficient and s_{bi} is the standard deviation of the regression coefficient. According to the

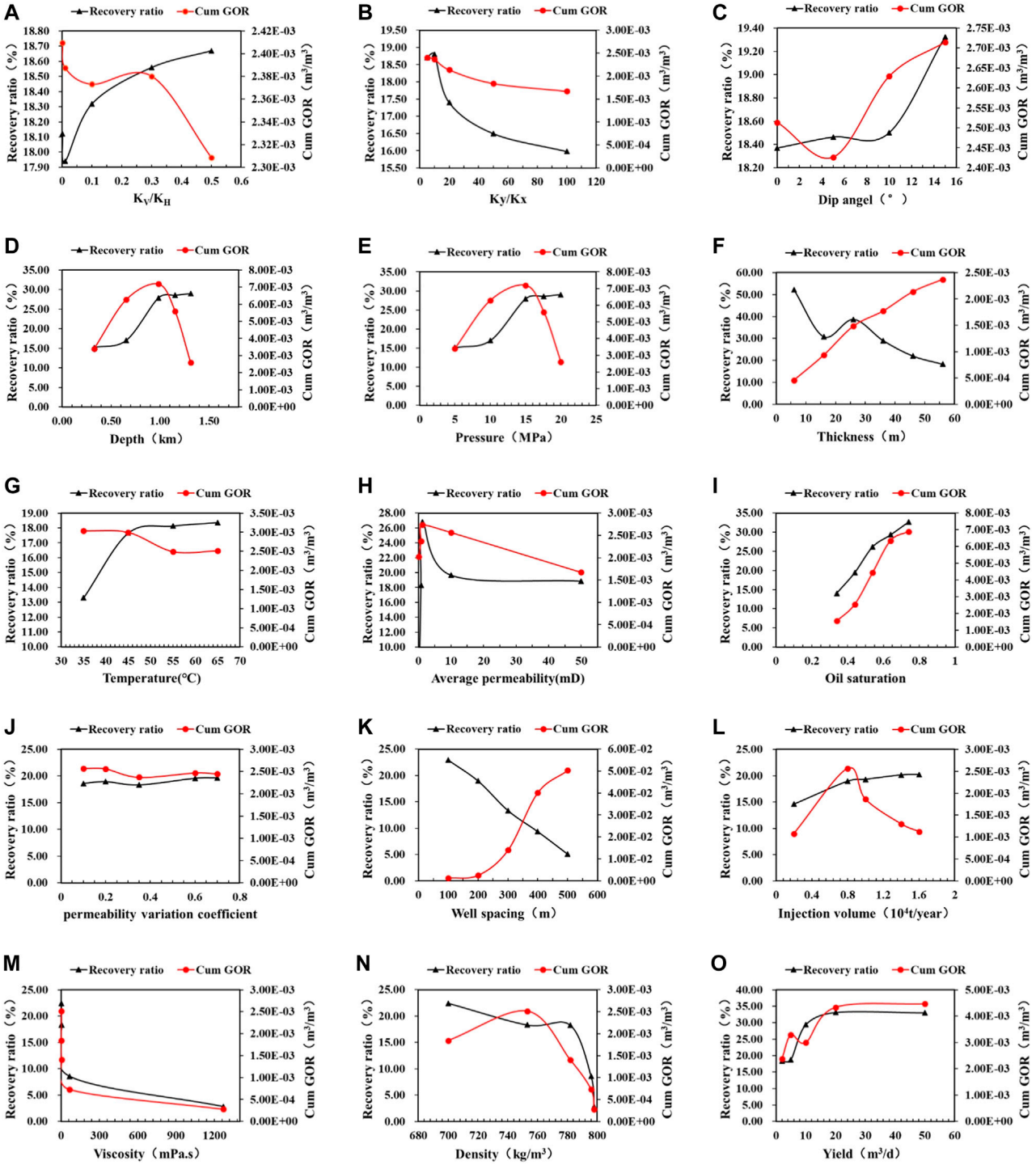

FIGURE 4 | (A) Effect of KV/KH; **(B)** effect of Ky/Kx; **(C)** effect of dip angle; **(D)** effect of depth; **(E)** effect of pressure; **(F)** effect of thickness; **(G)** effect of temperature; **(H)** effect of average permeability; **(I)** effect of oil saturation; **(J)** effect of permeability variation coefficient; **(K)** effect of well spacing; **(L)** effect of injection volume; **(M)** effect of viscosity; **(N)** effect of density; **(O)** effect of yield on oil recovery ratio and cumulative gas–oil ratio.

calculation result, the *t* value is positive, which proves that the influence of this factor on the recovery rate is positive feedback, and the larger the value is, the stronger the influence is. The *t* value is negative, which proves that the influence of this factor on the recovery rate is negative feedback. Various factors such as the trend of recovery rate change and cumulative gas–oil ratio,

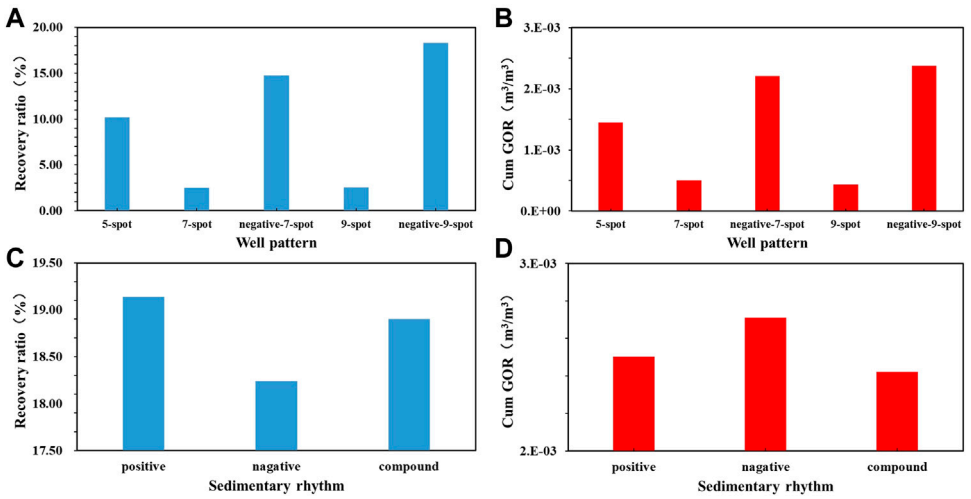

FIGURE 5 | (A) Effect of well pattern on recovery ratio; **(B)** effect of well pattern on cumulative gas–oil ratio; **(C)** effect of sedimentary rhythm on recovery ratio; **(D)** effect of sedimentary rhythm on cumulative gas–oil ratio.

TABLE 3 | Multiple linear regression table for CO_2 flooding in the Daqing low-permeability reservoir.

Factors	B	Standard error	Beta	t	Tolerances	F
Constants	19.93	9.96		2.002		
Dip angle	−2.51	5.13	−0.045	−0.489	0.983	1.017
Depth, Pressure	6.72	6.29	0.098	1.067	0.988	1.013
Temperature	6.80	5.13	0.122	1.326	0.983	1.017
Thickness	−18.44	7.19	−0.234	−2.565	0.997	1.003
Average permeability	−1.79	6.34	−0.026	−0.282	0.991	1.009
Formation development	−1.83	6.73	−0.025	−0.272	0.994	1.006
Oil saturation	17.21	6.55	0.241	2.626	0.989	1.012
Permeability direction development	−6.17	5.61	−0.101	−1.1	0.983	1.018
Well spacing	−21.31	6.55	−0.299	−3.252	0.989	1.012
5-spot	−10.69	6.30	−0.155	−1.696	0.993	1.007
7-spot	−18.34	6.30	−0.267	−2.91	0.993	1.007
Negative-7-spot	−6.09	6.30	−0.088	−0.966	0.993	1.007
9-spot	−18.31	6.30	−0.266	−2.905	0.993	1.007
Viscosity, Density	−22.60	6.92	−0.299	−3.266	0.995	1.005
Permeability variation coefficient	−2.10	7.24	−0.026	−0.289	0.999	1.001
Compound rhythm	−2.00	6.36	−0.029	−0.315	0.992	1.008
Positive rhythm	−1.72	6.30	−0.025	−0.273	0.993	1.007
Negitive rhythm	−2.62	6.30	−0.038	−0.415	0.993	1.007
Injection volume	5.49	7.96	0.063	0.689	1.000	1.000
Yield	13.33	4.76	0.259	2.802	0.979	1.022

combined with the magnitude of the absolute value of t in the multiple linear regression, are considered (**Table 3**). Some understandings applicable to CO_2 flooding reservoir screening in low-permeability reservoirs of the Daqing Oilfield can be obtained, as shown in **Table 4**.

3.2 CO_2 Flooding Reservoir Suitability Ranking in the Daqing Oilfield

All the indicators affecting the effect of CO_2 flooding are divided into three categories: geological factors, fluid properties, and development indicators. According to the importance of the ranking, the evaluation index system is established, and the hierarchical structure is constructed. Using the principle of hierarchical analysis, the calculation can be derived from the weights of indicators at all levels as shown in **Table 5**. The better indicators in the given reservoir geological data are the effective thickness of the oil layer, depth pressure of the oil layer, average permeability of the reservoir, oil saturation, single-well injection of CO_2, and single-well production of recovery wells. Therefore, the indicator weights need to be proportionally assigned to these six indicators, and the final weights of each indicator after the assignment are shown in **Table 6**.

TABLE 4 | Sensitivity judgment.

Number	Factors	Sensitivity Judgment
1	Dip angle	Relatively insensitive
2	Depth, Pressure	Sensitive
3	Temperature	Sensitive
4	Thickness	Extremely sensitive
5	Average permeability	Relatively insensitive
6	Formation development	Relatively insensitive
7	Oil saturation	Extremely sensitive
8	Permeability direction development	Sensitive
9	Well spacing	Extremely sensitive
10	Well pattern	Extremely sensitive
11	Viscosity, Density	Extremely sensitive
12	Permeability variation coefficient	Relatively insensitive
13	Sedimentary rhythm	Relatively insensitive
14	Injection volume	Sensitive
15	Yield	Extremely sensitive

The reservoir geological data are normalized, assuming that there are *l* reservoirs and *m* indicators that can be obtained for each reservoir, and the value of the *j* indicator of the *k* reservoir is $X'_{k,j}$.

$$X_{k,j} = \frac{\left|X'_{k,\bar{J}} - X'_{w,j}\right|}{\left|X^{\star}_{o,j} - X^{\star}_{w,j}\right|} \tag{6}$$

In **Eq. 1**, the optimal value $Y^{*}_{o,j} = Y^{*}_{n,j}$, the corresponding indicator takes the value $X^{*}_{o,j} = X^{*}_{n,j}$, the worst value $Y^{*}_{w,j} = Y^{*}_{1,j}$, and the corresponding indicator takes the value $X^{*}_{w,j} = X^{*}_{1,j}$. Considering that the cumulative gas–oil ratio does not touch the economic limit value of 0.2 for various values of the six indicators, the recovery rate is used as the main reference standard to determine the optimal and worst values in the normalization formula. The recovery rate and cumulative gas–oil ratio are only evaluated comprehensively in the case of a very insensitive recovery rate. The optimal and worst values used for the normalization of each index are shown in **Table 6**.

TABLE 6 | CO_2-driven reservoir screening index weighting values and best values/worst values used for reservoir index normalization in the Daqing Oilfield.

Factors	Weights	Worst Value	Optimum Value
Thickness	0.219	56	1
Depth, Pressure	0.127	328	1,312
Average permeability	0.069	0.1/50	1.2
Oil saturation	0.219	0.34	0.74
Injection volume	0.114	0.2	10
Yield	0.254	2	20

$$T_k = \sum X_{k,j} \times P_j \tag{7}$$

In **Eq. 2**, $X_{k,j}$ denotes the normalized reservoir geological data and P_j is the weight value of the j index calculated by the hierarchical analysis. T_k is the evaluation value of the block. Using the above theory and the obtained results, the evaluation of CO_2 flooding reservoir suitability can be calculated for all blocks in the whole Daqing Oilfield. The evaluation scores of all the calculated blocks are ranked, and the CO_2 flooding potential of the Daqing Oilfield can be evaluated by statistics with the evaluation value of 0.50 as the limit. Specific evaluation results are shown in **Table 7**.

3.3 Production Effect Evaluation of the Daqing Oilfield

In order to facilitate fine management in the production process of the Daqing Oilfield, block Bei14 of the Daqing Oilfield is divided into four sub-blocks, and the formation pressure of four sub-blocks can reach the minimum miscibility pressure of 16.6 MPa. Block SU12 has accumulated gas injection for about 10 years since February 2022, and blocks B1, B2, and B3 have accumulated gas injection for about 6 years since October 2016. The maximum reservoir capacity of block SU12 is 330×10^4 t, followed by block B3 is 292×10^4 t, and the reservoir capacity of blocks B1 and B2 is about 150×10^4 t. Statistics of the annual production of major well groups in the Bei14 block in **Table 8**

TABLE 5 | CO_2-driven reservoir screening index weighting values for the Daqing Oilfield.

First Indicators	Weights	Secondary Indicators	Weights
Geological factors	0.46	Sedimentary rhythm	0.05
		Oil saturation	0.19
		Thickness	0.19
		Depth, Pressure	0.11
		Average permeability	0.06
		Formation development	0.06
		Permeability direction development	0.06
		Dip angle	0.06
		Permeability variation coefficient	0.11
		Temperature	0.11
Fluid properties	0.19	Density	0.50
		Viscosity	0.50
Development Factors	0.35	Well pattern	0.29
		Well spacing	0.29
		Injection volume	0.13
		Yield	0.29

TABLE 7 | CO_2 flooding scoring for low-permeability reservoirs in the Daqing Oilfield.

Well group name	Injection volume (×10^4 t/year)	Evaluation score
Su12-X54-54	0.79	0.53
Su12-X54-58	0.87	0.49
Su12-X58-54	1.14	0.50
Su12-X58-58	1.07	0.76
Su12-X62-56	0.91	0.56
Su12-X62-60	1.31	0.69
Su12-X64-54	1.02	0.50
Su12-X66-56	1.23	0.59
Su12-X66-60	0.63	0.53
B1-X50-46	0.82	0.59
B1-X52-48	0.83	0.54
B1-X52-50	0.78	0.56
B1-X56-48	0.79	0.56
B2-X42-52	0.31	0.55
B2-X43-49	0.16	0.47
B2-X44-53	0.11	0.48
B2-X46-55	0.24	0.54
B2-X48-53	0.25	0.49
B3-X66-64	0.87	0.48
B3-X68-66	1.11	0.63
B3-X70-68	1.59	0.62
B3-X72-66	1.30	0.60
B3-X74-68	0.76	0.51
B3-X75-70	0.72	0.47
B3-XX73-68	0.83	0.61

shows that the average annual gas injection volume is 0.81×10^4 t, the average annual oil production volume is 0.30×10^4 t, the average annual oil change rate of well groups is about 41%, and the reservoir development effect is splendid.

According to the historical production data of the Bei14 block in the Daqing Oilfield, it can be seen that in the development process of the SU12 block, taking the oil saturation of the 16th simulated layer of SU12 as an example, the development spread area is mainly in the middle part of the oil group, and the spread range of the second half is large. Among them, the central part of the field is centered on the X58-58 well group with 0.62×10^4 t/year and bordered by the surrounding well groups with 0.30×10^4 t/year, forming a CO_2 flooding belt through the SU12 block. Taking the oil saturation of the 20th simulation layer in the B1 block as an example, the development-affected area is mainly in the middle of the oil group, and the edge angle affected is less. The development effect of the X56-48 well group and X50-46 well group is the best with the production of 0.30×10^4 t/year and 0.38×10^4 t/year, respectively; the oil saturation is centered on the gas injection well and decreases in the surrounding area (**Figure 6**). Taking the oil saturation of the 23rd simulation layer in the B2 block as an example, the development-affected area is mainly in the middle of the oil group, and the edge angle affected is less. The oil saturation around the X42-52 well group decreases most obviously with the production of 0.14×10^4 t/year. Taking the oil saturation of the 17th simulated layer in Block B3 as an example, the development area is mainly in the upper half of the oil group, and the lower half is less affected. The oilfield development is mainly centered on the X68-66 well group, X66-64 well group, and X70-68 well group with the production of about 0.50×10^4 t/year (**Figure 7**). In the multiple linear regression screening evaluation system of the Daqing Oilfield, the corresponding high-score well groups are 0.76 points in X58-58, 0.63 points in X68-66, 0.59 points in X50-46, and 0.54 points in X42-52, and the corresponding annual oil

TABLE 8 | Daqing Oilfield well group production data.

Well group name	Injection (×10^4 t/year)	Production (×10^4 t/year)	Oil Exchange ratio (year)
S (%)u12-X54-54	0.79	0.29	37
Su12-X54-58	0.87	0.31	36
Su12-X58-54	1.14	0.38	34
Su12-X58-58	1.07	0.62	58
Su12-X62-56	0.91	0.33	36
Su12-X62-60	1.31	0.46	35
Su12-X64-54	1.02	0.35	35
Su12-X66-56	1.23	0.42	34
Su12-X66-60	0.63	0.25	40
B1-X50-46	0.82	0.38	46
B1-X52-48	0.83	0.31	37
B1-X52-50	0.78	0.30	38
B1-X56-48	0.79	0.30	38
B2-X42-52	0.31	0.14	45
B2-X43-49	0.16	0.10	63
B2-X44-53	0.11	0.05	45
B2-X46-55	0.24	0.14	60
B2-X48-53	0.25	0.14	56
B3-X66-64	0.87	0.31	35
B3-X68-66	1.11	0.57	51
B3-X70-68	1.59	0.53	33
B3-X72-66	1.30	0.44	34
B3-X74-68	0.76	0.28	37
B3-X75-70	0.72	0.27	37
B3-XX73-68	0.83	0.32	38

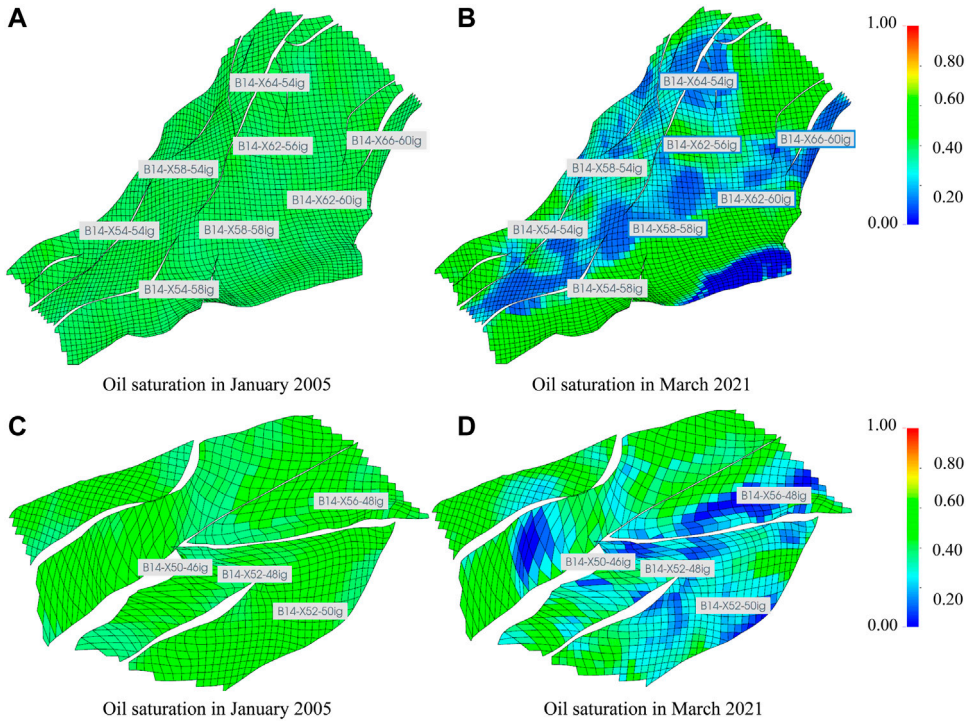

FIGURE 6 | (A,B) Oil saturation of simulated layer 16 in SU12; **(C,D)** oil saturation of simulated layer 20 in B1.

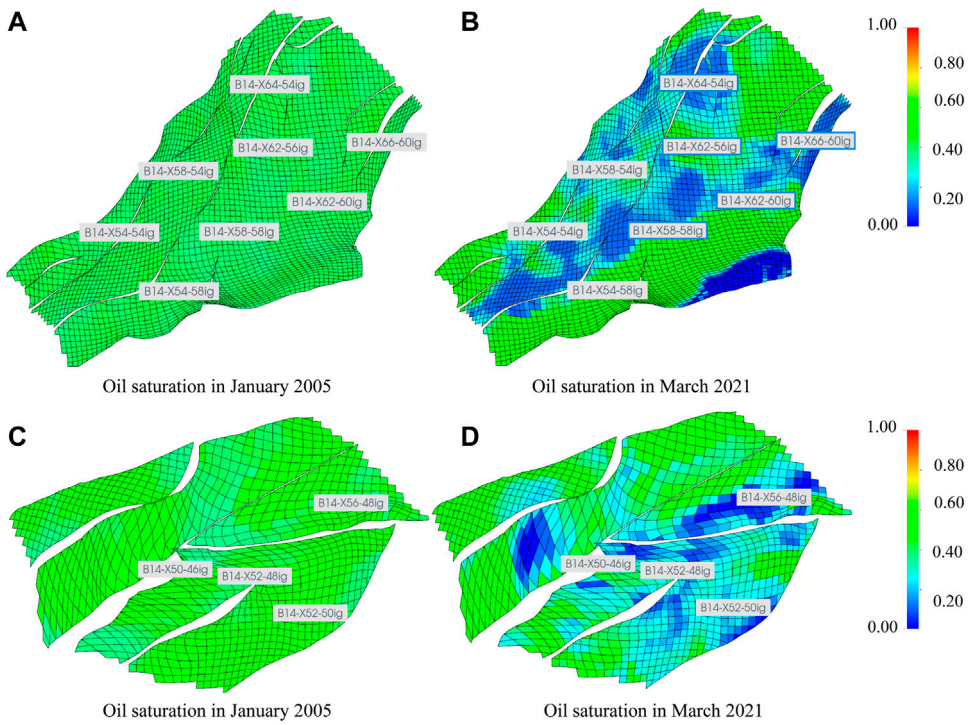

FIGURE 7 | (A,B) Oil saturation of simulated layer 23 in B2; **(C,D)** oil saturation of simulated layer 17 in B3.

exchange rates are 58% in X58-58, 51% in X68-66, 46% in X50-46, and 45% in X42-52. Thus, using the multiple linear regression method in the Daqing Oilfield development process can provide guidance, suggestions, and a dynamic development analysis basis.

4 CONCLUSION

Multiple linear regression equations are used to perform the suitability evaluation of CO_2 flooding reservoirs based on CMG numerical simulation results. The recovery rate can be considerably promoted by optimizing the well selection and gas injection scheme in block Bei14 (Enab and Ertekin, 2021; Olabode et al., 2021). As a proof, for well groups with an annual oil exchange ratio of 50% or more and evaluation values of 0.55 or more, later CO_2 injection mining can be considered to increase the amount of gas injection for groups with a smaller amount of gas injection. For well groups with an annual oil exchange ratio between 40 and 50% and evaluation values between 0.55 and 0.50 and producing well groups that do not see gas, it is rationed with stable gas injection; for well groups with an annual oil exchange ratio between 30 and 40% and evaluation values of 0.50 or less, gas injection is reduced to control the gas–oil ratio for producing well groups that have already seen gas. Block Bei14 calculation results show that 76% of the well groups have an evaluation value above 0.50, and the annual oil exchange ratio of 72% of the well groups is about 40%; more than 70% of the well groups are suitable for CO_2 flooding to increase oil recovery. Thus, CO_2 flooding can be a good application prospect in the Daqing Oilfield and brings great economic benefits.

DATA AVAILABILITY STATEMENT

The original contributions presented in the study are included in the article/**Supplementary Material**; further inquiries can be directed to the corresponding author.

AUTHOR CONTRIBUTIONS

ZW: Conceptualization, methodology, and writing—Original draft preparation. JH: Writing—reviewing and editing. HH: Supervision. CW: Visualization and investigation. LW: Software and validation.

FUNDING

This project was supported by the China Petroleum Major Strategic Project (ZLZX 2020-01-04). The authors would like to acknowledge all the involved colleagues of Changzhou University, China University of Petroleum (Beijing), and Petro China Daqing Oilfield Limited Company.

SUPPLEMENTARY MATERIAL

The Supplementary Material for this article can be found online at: https://www.frontiersin.org/articles/10.3389/fenrg.2022.929606/full#supplementary-material

REFERENCES

Bhatti, A. A., Raza, A., Mahmood, S. M., and Gholami, R. (2019). Assessing the Application of Miscible CO_2 Flooding in Oil Reservoirs: a Case Study from pakistan. *J. Pet. Explor Prod. Technol.* 9, 685–701. doi:10.1007/s13202-018-0504-x

Chai, X., Tian, L., Wang, G., Zhang, K., Wang, H., Peng, L., et al. (2021). Integrated Hierarchy-Correlation Model for Evaluating Water-Driven Oil Reservoirs. *ACS omega* 6, 34460–34469. doi:10.1021/acsomega.1c04631

Colclough, A. R. (1987). Two Theories of Experimental Error. *J. Res. Natl. Bur. Stan.* 92, 167. doi:10.6028/jres.092.016

DaneshFar, J., Nnamdi, D., Moghanloo, R., and Ochie, K. (2021). "Economic Evaluation of CO_2 Capture, Transportation, and Storage Potentials in Oklahoma," in SPE Annual Technical Conference and Exhibition, Dubai, United Arab Emirates, September, 2021 (OnePetro).

Enab, K., and Ertekin, T. (2021). Screening and Optimization of CO_2-wag Injection and Fish-Bone Well Structures in Low Permeability Reservoirs Using Artificial Neural Network. *J. Petroleum Sci. Eng.* 200, 108268. doi:10.1016/j.petrol.2020.108268

Etemadi, S., and Khashei, M. (2021). Etemadi Multiple Linear Regression. *Measurement* 186, 110080. doi:10.1016/j.measurement.2021.110080

Feng, H., Haidong, H., Yanqing, W., Jianfeng, R., Liang, Z., Bo, R., et al. (2016). Assessment of Miscibility Effect for CO_2 Flooding EOR in a Low Permeability Reservoir. *J. Petroleum Sci. Eng.* 145, 328–335. doi:10.1016/j.petrol.2016.05.040

Finke, C. E., Leandri, H. F., Karumb, E. T., Zheng, D., Hoffmann, M. R., and Fromer, N. A. (2021). Economically Advantageous Pathways for Reducing Greenhouse Gas Emissions from Industrial Hydrogen under Common, Current Economic Conditions. *Energy Environ. Sci.* 14, 1517–1529. doi:10.1039/d0ee03768k

Foukerdi, A., Esmaeili, S., and Shahrabadi, A. (2021). A Hybrid Fahp-Mcgp Approach to Sustainable Assessment of Candidate Eor Methods for a Given Oil Reservoir. *J. Petroleum Sci. Eng.* 207, 109143.. doi:10.1016/j.petrol.2021.109143

Gao, S.-H., Han, Q., Li, D., Cheng, M.-M., and Peng, P. (2021). "Representative Batch Normalization with Feature Calibration," in Proceedings of the IEEE/CVF Conference on Computer Vision and Pattern Recognition, Nashville, TN, June 20–25, 2021, 8669–8679. doi:10.1109/cvpr46437.2021.00856

Gunst, R. F., and Webster, J. T. (1975). Regression Analysis and Problems of Multicollinearity. *Commun. Statistics* 4, 277–292. doi:10.1080/03610927308827246

Jiang, K., and Ashworth, P. (2021). The Development of Carbon Capture Utilization and Storage (Ccus) Research in china: A Bibliometric Perspective. *Renew. Sustain. Energy Rev.* 138, 110521. doi:10.1016/j.rser.2020.110521

Li, H.-B., Yang, Z.-M., Li, R.-S., Zhou, T.-Y., Guo, H.-K., Liu, X.-W., et al. (2021). Mechanism of CO_2 Enhanced Oil Recovery in Shale Reservoirs. *Petroleum Sci.* 18, 1788–1796. doi:10.1016/j.petsci.2021.09.040

Li, Q. (2021). The View of Technological Innovation in Coal Industry under the Vision of Carbon Neutralization. *Int. J. Coal Sci. Technol.* 8, 1197–1207. doi:10.1007/s40789-021-00458-w

Liu, Z., Deng, Z., He, G., Wang, H., Zhang, X., Lin, J., et al. (2021). Challenges and Opportunities for Carbon Neutrality in china. *Nat. Rev. Earth Environ.* 3, 1–15. doi:10.1038/s43017-021-00244-x

Maaouane, M., Zouggar, S., Krajacõic´, G., and Zahboune, H. (2021). Modelling Industry Energy Demand Using Multiple Linear Regression Analysis Based on Consumed Quantity of Goods. *Energy* 225, 120270doi:10.1016/j.energy.2021.120270

Mellor, D. H. (1965). Experimental Error and Deducibility. *Philos. Sci.* 32, 105–122. doi:10.1086/288031

Montgomery, D. C., and Voth, S. R. (1994). Multicollinearity and Leverage in Mixture Experiments. *J. Qual. Technol.* 26, 96–108. doi:10.1080/00224065.1994.11979510

Moreira, L. L., de Brito, M. M., and Kobiyama, M. (2021). Effects of Different Normalization, Aggregation, and Classification Methods on the Construction of Flood Vulnerability Indexes. *Water* 13, 98. doi:10.3390/w13010098

Olabode, O., Isehunwa, S., Orodu, O., and Ake, D. (2021). Optimizing Productivity in Oil Rims: Simulation Studies on Horizontal Well Placement under Simultaneous Oil and Gas Production. *J. Pet. Explor Prod. Technol.* 11, 385–397. doi:10.1007/s13202-020-01018-9

Piekutowska, M., Niedbała, G., Piskier, T., Lenartowicz, T., Pilarski, K., Wojciechowski, T., et al. (2021). The Application of Multiple Linear Regression and Artificial Neural Network Models for Yield Prediction of Very Early Potato Cultivars before Harvest. *Agronomy* 11, 885. doi:10.3390/agronomy11050885

Pokoradi, L., Kocak, S., and Toth-Laufer, E. (2021). "Fuzzy Hierarchical Failure Mode and Effect Analysis," in 2021 IEEE 19th International Symposium on Intelligent Systems and Informatics (SISY), Subotica, Serbia, September 16–18, 2021 (IEEE), 71–76. doi:10.1109/sisy52375.2021.9582523*2*

Pu, W., Gao, H., Zhao, S., and Gao, X. (2022). Microscopic Oil Displacement Mechanism of CO_2 in Low-Permeability Heterogeneous Glutenite Reservoirs in the Junggar Basin. *ACS Omega* 7, 4420. doi:10.1021/acsomega.1c06265

Sun, L. (2021). The Application of Fuzzy Comprehensive Evaluation Method in Evaluating Remaining Oil Potential of Oil Layer. *IOP Conf. Ser. Earth Environ. Sci.* 781, 022030. (IOP Publishing). doi:10.1088/1755-1315/781/2/022030

Xiaolong, C., Yiqiang, L., Xiang, T., Huan, Q., Xuebing, S., and Jianghao, L. (2021). Effect of Gravity Segregation on CO_2 Flooding under Various Pressure Conditions: Application to CO_2 Sequestration and Oil Production. *Energy* 226, 120294. doi:10.1016/j.energy.2021.120294

Xu, C., Yang, J., He, L., Wei, W., Yang, Y., Yin, X., et al. (2021). Carbon Capture and Storage as a Strategic Reserve against China's CO_2 Emissions. *Environ. Dev.* 37, 100608. doi:10.1016/j.envdev.2020.100608

Yáñez Angarita, E. E., Núñez-López, V., Ramírez, A., Castillo Monroy, E., and Faaij, A. (2022). Rapid Screening and Probabilistic Estimation of the Potential for CO_2-EOR and Associated Geological CO_2 Storage in Colombian Petroleum Basins. *Pet. Geosci.* 28, petgeo2020–110. doi:10.1144/petgeo2020-110

Yu, H., Fu, W., Zhang, Y., Lu, X., Cheng, S., Xie, Q., et al. (2021). Experimental Study on EOR Performance of CO_2-based Flooding Methods on Tight Oil. *Fuel* 290, 119988. doi:10.1016/j.fuel.2020.119988

Zandalinas, S. I., Fritschi, F. B., and Mittler, R. (2021). Global Warming, Climate Change, and Environmental Pollution: Recipe for a Multifactorial Stress Combination Disaster. *Trends Plant Sci.* 26, 588–599. doi:10.1016/j.tplants.2021.02.011

Zheng, Y., Gao, L., Li, S., and Wang, D. (2022). A Comprehensive Evaluation Model for Full-Chain Ccus Performance Based on the Analytic Hierarchy Process Method. *Energy* 239, 122033. doi:10.1016/j.energy.2021.122033

Zhou, W. (2021). Research and Practice of CO_2 Flooding Technology in Ultra-low Permeability Reservoir of XX Oilfield. *E3S Web Conf.* 329, 01037. (EDP Sciences). doi:10.1051/e3sconf/202132901037

Zhou, Y., Li, Z., Zhang, R., Wang, G., Yu, H., Sun, G., et al. (2019). CO_2 Injection in Coal: Advantages and Influences of Temperature and Pressure. *Fuel* 236, 493–500. doi:10.1016/j.fuel.2018.09.016

Conflict of Interest: The authors declare that the research was conducted in the absence of any commercial or financial relationships that could be construed as a potential conflict of interest.

Publisher's Note: All claims expressed in this article are solely those of the authors and do not necessarily represent those of their affiliated organizations or those of the publisher, the editors, and the reviewers. Any product that may be evaluated in this article or claim that may be made by its manufacturer is not guaranteed or endorsed by the publisher.

frontiers | Frontiers in Energy Research

ORIGINAL RESEARCH
published: 04 July 2022
doi: 10.3389/fenrg.2022.917740

Case Study of Successfully Staged Acid Fracturing on the Ultra-Deep Horizontal Well for the Qixia Fm HTHP Tight Carbonate Gas Reservoir in China

Fei Liu, Yu Fan, Li Li, Jinsui Li, Yan Chen, Zefei Lv and Tingting He*

Engineering Technology Research Institute, PetroChina Southwest Oil and Gas Field Company, Chengdu, China

The lower Permian Qixia formation gas reservoir is characterized by ultra-deep buried, high temperature and high pressure (HTHP), low porosity and permeability, ultra-high closure pressure, and thin thickness in the western Sichuan Basin, China. Acid fracturing has been adopted as the main well stimulation technology. The average test production of the acid-fractured vertical well was 46×10^4 m^3/d. The horizontal well with staged acid fracturing is considered a reliable measure to enhance gas production. However, the staged acid fracturing on the ultra-deep horizontal well has been challenged. The reaction rates of conventional, self-diverting, and gelled acid and the acid-etched fracture conductivity experiments under HTHP are measured to optimize the acid fracturing technique. The reaction rate of gelled acid with Qixia Fm limy dolomite at 150°C is 3.4–6.7 times faster than that with dolomite and similar to that with limestone. The gelled acid with better retardation and friction reduction performance is selected as the main acid to increase the effective acid-etched fracture length. The acid-etched fracture conductivity can be greatly enhanced by using gelled acid, increasing acid volume, and closed fracture acidizing (CFA) under a closure stress of 50 MPa. Moreover, the feasibility of staged acid fracturing for ultra-deep horizontal wells is discussed. The first stage is assembled by fracturing sleeve, spared ball drop sleeve, and circulating valve to ensure activation of the fracturing channel. The tested production is significantly enhanced with temporary plugging and open-hole packer and sliding sleeve staged acid fracturing.

Keywords: staged acid fracturing, ultra-deep horizontal well, tight carbonate, acid-etched fracture length, acid-etched fracture conductivity, open-hole staged acid fracturing

OPEN ACCESS

Edited by:
Yu Peng,
Southwest Petroleum University, China

Reviewed by:
Li Chengyong,
Chengdu University of Technology, China
Qianli Lu,
Southwest Petroleum University, China

****Correspondence:***
Fei Liu
liufei10628@aliyun.com

Specialty section:
This article was submitted to Advanced Clean Fuel Technologies, a section of the journal Frontiers in Energy Research

Received: *11 April 2022*
Accepted: *26 May 2022*
Published: *04 July 2022*

Citation:
Liu F, Fan Y, Li L, Li J, Chen Y, Lv Z and He T (2022) Case Study of Successfully Staged Acid Fracturing on the Ultra-Deep Horizontal Well for the Qixia Fm HTHP Tight Carbonate Gas Reservoir in China. Front. Energy Res. 10:917740. doi: 10.3389/fenrg.2022.917740

1 INTRODUCTION

Acid fracturing is widely used in carbonate (Jeon et al., 2016; Kalfayan, 2007; Asadollahpour et al., 2018), especially for low porosity and low permeability reservoirs. The effective acid-etched fracture length and conductivity are two key factors for the stimulation effect. Through several decades of development, a series of acid system, acid fracturing technique, and staged acid fracturing technique has been developed (Teklu et al., 2019; Zhu et al., 2019). The main acids are conventional acid (CA), gelled acid (GA), *in situ* gelled acid, self-diverting acid (SDA), surface and *in situ* cross-linked acid, solid acid, and organic acid (Taylor and Nasr-El-Din, 2002; Bybee 2006; Nasr-El-Din et al., 2007; Ding et al., 2010; Gomaa and Nasr-

El-Din, 2010; Liu et al., 2013). The acid frac techniques are acid frac with the aforementioned single and combined acid system, such as pad-acid-fracturing (PAF), multistage alternating injection acid frac, propped acid frac, and closed fracture acidizing (CFA) (Liu and Zhao, 1998; Nelson et al., 1998; Yi et al., 2010; Pournik et al., 2011). However, acid frac of ultra-deep high temperature and high pressure (HTHP) fractured-vuggy carbonate reservoirs is challenged by rapid acid rock reaction rate caused by limited acid-etched fracture length, high closure stress caused by limited acid-etched fracture conductivity, and natural developed fissure caused uncontrolled acid leak off and limited dynamic hydraulic fracture (Xue et al., 2019; Luo et al., 2020; Peng et al., 2019a; Li et al., 2019). The average test production of the acid fractured vertical well in the Qixia Fm gas reservoir was 46×10^4 m^3/d. The horizontal well with staged acid fracturing has been considered as a reliable measure to enhance gas production (Ugursal et al., 2019).

Horizontal wells have been widely used worldwide to provide a larger contact area with the reservoir to enhance well productivity. However, horizontal well cannot meet the anticipant productivity for low permeability or serious skin damage (Li et al., 2019; Yuan et al., 2019). Several artificial fractures along the horizontal segment created by staged acid fracturing are essential to enhance productivity and recovery. Through decades of development, a series of staged fracturing techniques for horizontal wells have been formed to adapt to different completion conditions. The main techniques are sealing ball staged fracturing, hydraulic jet fracturing, open-hole packer fracturing, and plug-perf fracturing (Wang et al., 2011; Li et al., 2012).

The geological conditions are complicated in the western Sichuan Basin. The well structure of an ultra-deep well is complicated for multi-pressure systems in the longitudinal direction. The lower Permian Qixia Fm gas reservoir is deep buried with true vertical depth (TVD) from 7,200 m to 7,500 m, and the measured depth (MD) of the horizontal well is deeper than 8,000 m. Moreover, the formation fluids contain sour gases such as H_2S and CO_2, which limited the application of plug-perf staged fracturing technology. The hydraulic jet staged acid fracturing technique is appropriate for well with a maximum depth of 6,400 m for high choke pressure (Li et al., 2012). Although the temporary plugging staged acid fracturing is widely used (Zhao et al., 2020), the validity of temporary plugging is uncertain, which may affect the stimulation effect. The packer and sliding sleeve staged acid fracturing would be a candidate but challenged on ultra-deep horizontal well.

The acid rock reaction rate and acid-etched fracture conductivity were investigated to optimize the main acid type and acid frac technique. Furthermore, two ultra-deep horizontal wells with temporary plugging, open hole packer, and sliding sleeve staged acid frac are discussed. It is referential for staged acid fracturing of ultra-deep horizontal wells.

2 RESERVOIR GEOLOGY

The Lower Permian Qixia limy dolomite formation is buried more than 7,200 m in the western Sichuan Basin. The reservoir spaces are mainly composed of intergranular pores, intergranular dissolved pores, and medium-to-small karst caves (**Figure 1**).

The gas reservoir is characterized of low porosity (ϕ_{avg} = 3.11%) and a low-to-medium-permeability (k_{avg} < 1mD). It shows a good correlation between porosity and permeability, while the natural fissure-developed cores show significantly higher permeability (**Figure 2**). The well-developed natural fissures improve permeability.

The Qixia Fm is a typical HTHP sour gas reservoir with a formation temperature of 154–165°C, formation pressure coefficient of 0.013 MPa/m, an average hydrogen sulfide content of 5.77 g/m^3, and average carbon dioxide content of 1.87 g/m^3.

Acid fracturing has been adopted as the main well stimulation technology. The average test production of the acid fractured vertical well is 46×10^4 m^3/d. The horizontal well with staged acid fracturing has been considered as a reliable measure to enhance gas production. However, the staged acid fracturing on ultra-deep horizontal well is challenged.

3 ACID ROCK REACTION EXPERIMENTS

The rotating disk instrument is widely used for gaining acid rock reaction kinetic parameters, such as acid consumption rate, reaction rate constants, reaction order, and activation energy (Anderson 1991; Fredd, 1998a; Alkattan et al., 1998; Fredd and Fogler, 1998b; Gdanski and Van Domelen, 1999; Frenier and Hill, 2002; Li et al., 2015). Downhole cores were cut into disks, and the acid solutions of 10wt% and 15wt% were allocated by 20 wt% fresh acid and $CaMg(CO_3)_2$ powder to consider the effect of Ca^{2+} and Mg^{2+}, for acid rock reaction kinetics experiments. A summary of all data obtained from the rotating-disk study is listed in **Table 1**.

The kinetic equations of the acid rock reaction are constructed as follows:

$$J_{CA} = 2.07 \times 10^{-4} \exp(-4643.78/RT) C^{0.1334}, \quad (1)$$

$$J_{GA} = 2.94 \times 10^{-1} \exp(-39215.48/RT) C^{1.3745}, \quad (2)$$

$$J_{SDA} = 3.51 \times 10^{-2} \exp(-26924.06/RT) C^{0.5102}, \quad (3)$$

where J is the acid rock reaction rate, mol/(cm^2·s); R is the universal gas constant, J/(mol·K); T is the temperature, K; C is the acid concentration, mol/L; the subscripts CA, GA, and SDA refer to conventional acid, gelled acid, and self-diverting acid, respectively.

The temperature has a significant influence on the reaction rate of Qixia Fm. The reaction rates were sharply increased with a temperature above 110°C. The GA and SDA showed similar retardation performance (**Figure 3**).

The reaction rates of 20wt% GA with Permian Qixia limy dolomite, Cambrian Longwangmiao Fm, Sinian Dengying Fm, Devonian Guanwushan Fm dolomite, and Permian Maokou Fm limestone in Sichuan Basin, were compared (**Figure 4**). It can be concluded that the reaction rate of Qixia limy dolomite at higher temperatures (150°C) is 3.4–6.7 times faster than that of typical dolomite, and similar to that of limestone, in Sichuan Basin. It is consistent with the previous study (Taylor et al., 2006; Rabie et al., 2014).

The friction reduction performance was compared as shown in **Figure 5**. The gelled acid is selected as the main acid for better retardation and friction reduction performance.

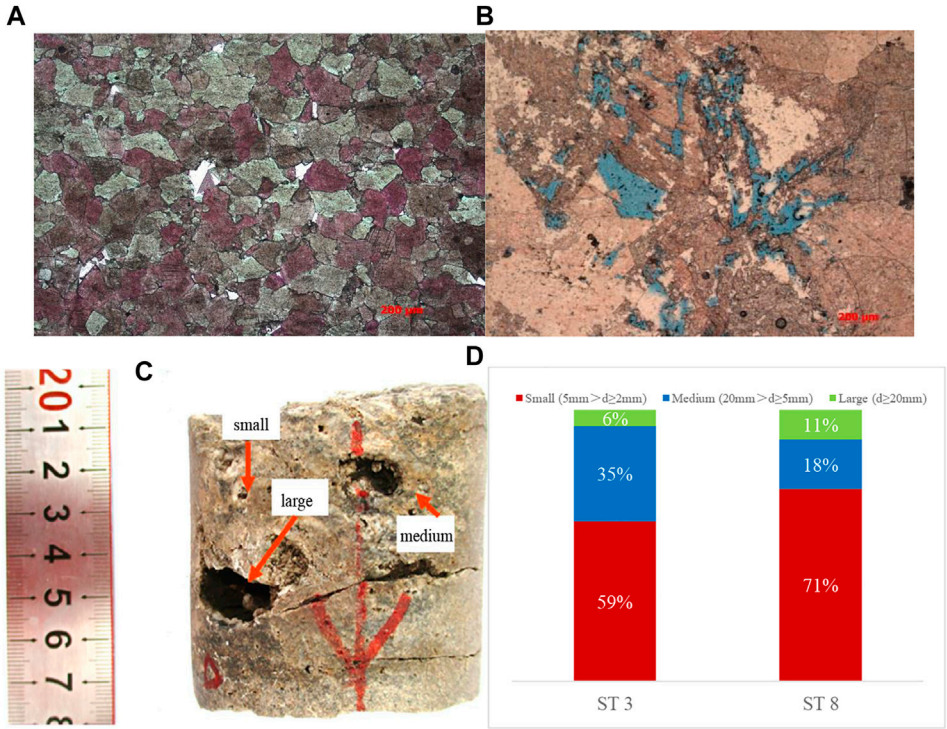

FIGURE 1 | Reservoir spaces of Qixia Fm limy dolomite. **(A)** ST8 downhole core, intergranular pores; **(B)** ST 3 downhole core, intergranular dissolved pores; **(C)** ST3 downhole core, medium-to-small karst caves; and **(D)** percentage of karst caves with different diameters.

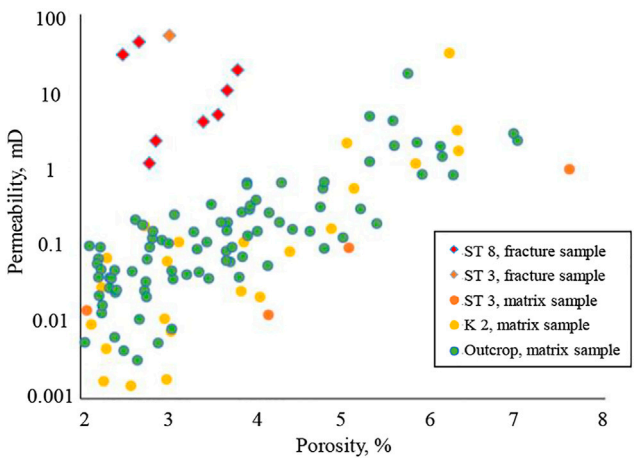

FIGURE 2 | Correlation diagram between porosity and permeability, Qixia Fm, Sichuan Basin, China.

4 ACID-ETCHED FRACTURE CONDUCTIVITY EXPERIMENTS

The standard and modified API fracture conductivity device is widely used for acid-etched fracture conductivity evaluation (Chen et al., 2005; Han et al., 2016; Jin et al., 2019; Li et al., 2003; Luo et al., 2008; Luo et al., 2018; Luo et al., 2019; Malagon et al., 2008; Peng et al., 2015; Xue et al., 2018; Yao et al., 2015; Zhao et al., 2017; Peng et al., 2019b; Peng et al., 2020). The influences of closure stress, temperature, injection rate, contact time, acid type, and stimulation technique on fracture conductivity were investigated.

The acid-etched fracture conductivity sharply decreased with increasing closure stress from 10 to 20 MPa and slowly decreased with increasing closure stress from 20 to 50 MPa as shown in **Figure 6A**. The grooving etched pattern and higher fracture conductivity would be created by acid fracturing for differential acid rock reaction rate between calcite and dolomite. Then, the supporting points collapsed, the supporting area increased, and the fracture conductivity decreased sharply to slowly with increasing closure stress. The conductivity increased by 62% (from 509 D·cm to 825 D·cm) with increasing temperature from 90 to 150°C for a significantly increased reaction rate (**Figure 6B**). Although the effective diffusion coefficient of H^+ and the reaction rate increased with increasing injection rate, the conductivity decreased by 18% (from 572 D·cm to 484 D·cm) because the increment of reaction rate is lesser than that of acid flow velocity and the acid flow too fast to react with rock (**Figure 6C**). The conductivity significantly increased by 25 times (from 18 D·cm to 572 D·cm) with increasing acid volume from 0.5 to 2.0 L (**Figure 6D**). The acid-etched fracture conductivity can be greatly enhanced by increasing acid volume.

The effect of the main acid type on conductivity was compared as shown in **Figure 7**. The conductivity of GA is obviously higher than that of SDA. The PAF technique will reduce the conductivity

TABLE 1 | Summary of the acid rock reaction rate.

Acid type	Initial acid concentration (wt%)	Temperature (°C)	Disk rotational speed (Rev/min)	Reaction rate (mol/cm^2·s)
CA	20	120	700	4.26×10^{-5}
	15	120	700	3.86×10^{-5}
	10	120	700	3.84×10^{-5}
	20	60	900	4.92×10^{-5}
	20	90	900	5.65×10^{-5}
	20	120	900	6.36×10^{-5}
GA	20	150	700	4.59×10^{-5}
	15	150	700	1.96×10^{-5}
	10	150	700	1.45×10^{-5}
	5	150	700	5.37×10^{-6}
	20	120	700	2.84×10^{-5}
	20	100	700	8.52×10^{-6}
	20	80	700	5.93×10^{-6}
SDA	20	120	700	1.39×10^{-5}
	15	120	700	1.17×10^{-5}
	10	120	700	9.52×10^{-6}
	20	60	900	6.40×10^{-6}
	20	90	900	7.66×10^{-6}
	20	120	900	2.92×10^{-5}

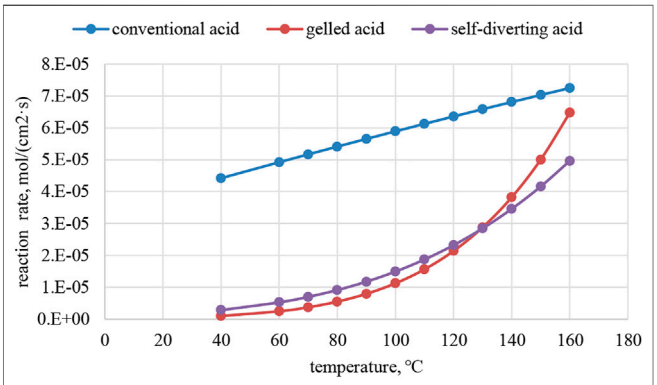

FIGURE 3 | Effect of temperature on the acid reaction rate.

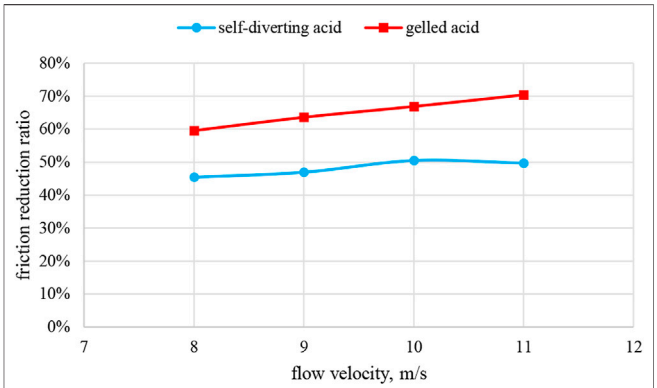

FIGURE 5 | Comparison of friction reduction for gelled and self-diverting acid.

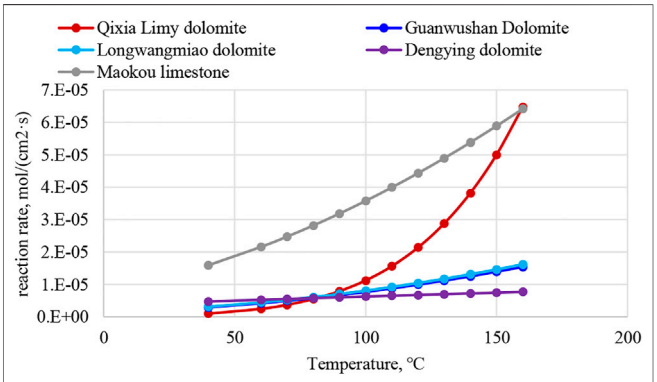

FIGURE 4 | Effect of temperature on the reaction rate of gelled acid with different carbonates.

by 23.5%, and the CFA technique will enhance the conductivity by 24.6%. CFA after main acid fracturing is essential to enhance the acid-etched fracture conductivity.

The long-term acid-etched fracture conductivity experiments were conducted to evaluate the stimulation valid period. These experiments were conducted at a temperature of 90°C, pad (0.4 L) and main acid (1.0 L) injection rate of 50 ml/min, closure stress of 50 MPa, and closed acid (0.1 L) injection rate of 10 ml/min.

The retention rate of long-term acid-etched fracture conductivity ranges from 70 to 82%, with an average of 75%. Under the same acid fracturing technique and injection parameters, the initial and long-term conductivity of GA is significantly higher than that of SDA. The initial and long-term conductivity of SDA is 44.5%–47.5% of that of GA (**Figure 8**).

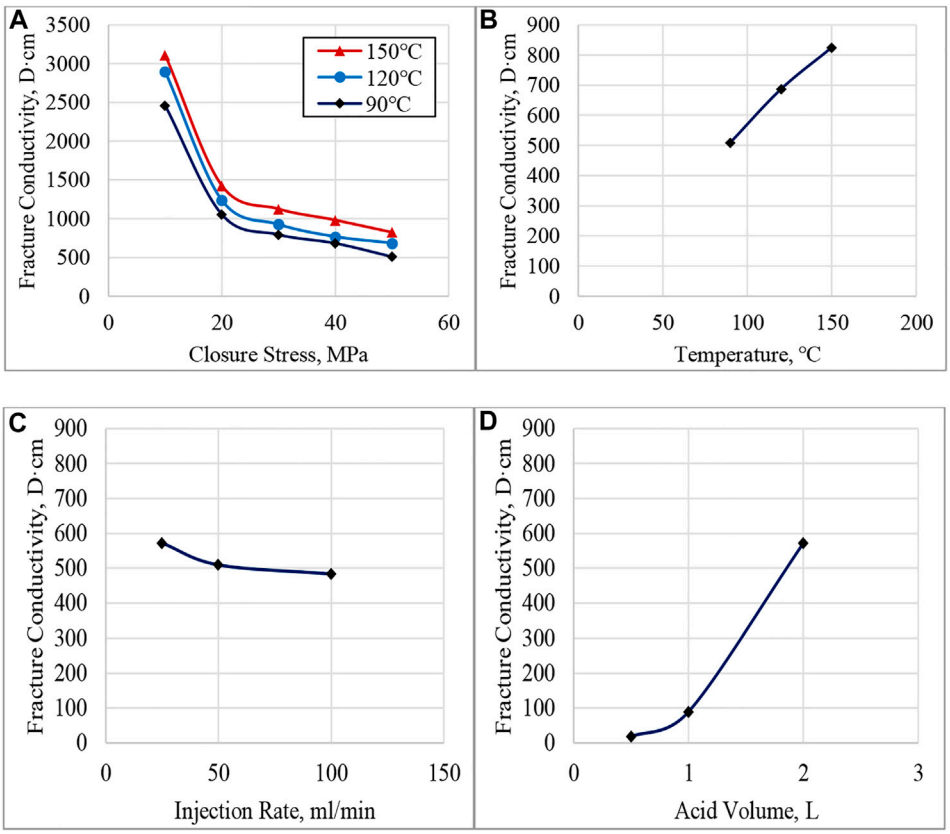

FIGURE 6 | Acid-etched fracture conductivity of Qixia Fm, Sichuan Basin. **(A)** Effect of closure stress; **(B)** effect of temperature; **(C)** effect of the acid injection rate; and **(D)** effect of acid volume.

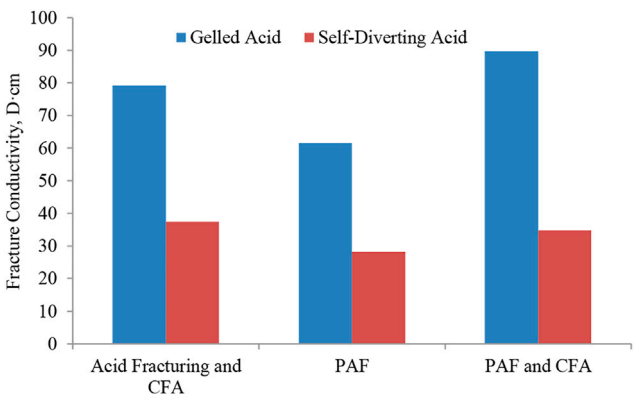

FIGURE 7 | Effect of main acid type on fracture conductivity.

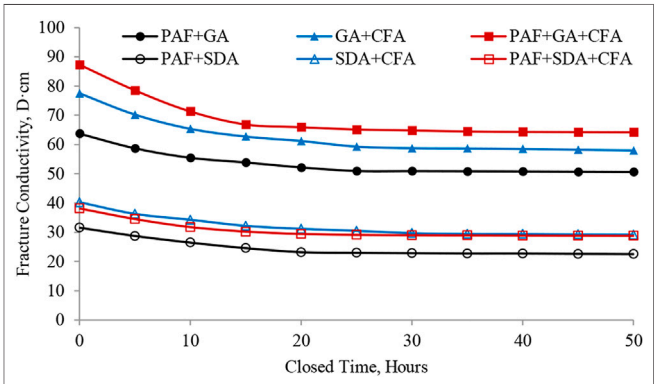

FIGURE 8 | Effect of the acid fracturing technique on long-term fracture conductivity.

5 STIMULATION DIFFICULTIES AND COUNTERMEASURES

The main difficulties and countermeasures of acid fracturing are listed in **Table 2**.

5.1 Feasibility of Staged Acid Fracturing

The hydraulic jet staged acid fracturing technique is unaccommodated for limited application depth, and the plug-perf staged fracturing is infeasible for casing tieback to the wellhead and unavailable coiled tube to handle the bridge

TABLE 2 | Difficulties and countermeasures of staged acid fracturing for well M.

No.	Difficulty	Cause	Countermeasure
1	Difficult to break the formation	High string friction and high *in situ* minimum horizontal principal stress (170–180 MPa)	Drain out the completion fluid in the wellbore and equip the wellhead with a high pressure level (140 MPa) to increase operation capability
2	Limited effective acid-etched fracture length	Rapid acid rock reaction rate and high Young's modulus (64.3–75 GPa) limited the dynamic artificial fracture width and exacerbated the acid rock reaction rate	Gelled acid with better retardation, friction reduction, and non-uniform etching performance is selected for massive acid fracturing The pumping rate should be increased
3	Limited acid-etched fracture conductivity	High effective closure stress (70 MPa)	Closed fracture acidizing
4	Difficult to uniformly stimulate	Long horizontal interval (383 m) and strong heterogeneous (the permeability ranges from 0.1 to 2.6 mD with a max–min ratio of 26)	Open-hole packer and sliding sleeve staged acid fracturing

TABLE 3 | Comparison of main advantages and disadvantages of different completions and related stimulation techniques.

Completion	Stimulation	Advantage	Disadvantage
Slotted liner	Matrix acidizing with self-diverting acid	1) Simple completion and stimulation. 2) The acid injection profile can be improved to some extent with self-diverting acid	1) Limited stimulation degree by matrix acidizing. 2) Limited diverting performance
	General acid fracturing	1) Simple completion and stimulation. 2) Form artificial acid fracture to improve productivity performance	1) Staged fracturing technique unavailable. 2) Limited stimulation degree for only one artificial fracture can be formed theoretically
Cased and perforated	Staged acid fracturing with tools (127 mm liner)	1) Form several artificial acid fractures to improve productivity performance. 2) Specified fracture initiation locations	1) New damage would be introduced with the running liner. 2) Difficult to run staged tools. 3) Limited stages
	Staged acid fracturing with temporary plugging (114.3 and 127 mm liner)	1) Simple stimulation. 2) Form several artificial acid fractures to improve productivity performance	1) New damage would be introduced with the running liner. 2) Uncertainty of temporary plugging
Open-hole	Open-hole staged acid fracturing	1) Form several artificial acid fractures to improve productivity performance. 2) Larger wellbore to increase stages	1) Difficult to run staged tools for ultra-deep horizontal wells. 2) Uncertainty of fracture initiation locations

plug. Therefore, the open-hole packer and sliding sleeve and temporary plugging would be the only viable staged fracturing technique. The advantages and disadvantages of different completions and related stimulation techniques are compared (**Table 3**). Although matrix acidizing with self-diverting acid and general acid fracturing would be the feasible technique for slotted liner completion, the stimulation effect would be limited to an inherent stimulation mechanism and unavailable staged fracturing technique. Although the staged acid fracturing with tools is feasible for liner cased and perforated completion with a liner diameter of 127 mm, the stimulation effect would be influenced by new damage introduced during liner cementing and limited stages. The temporary plugging technique would be a candidate for liner cased and perforated completion as well, but the fracturing effect would be influenced by the uncertainty of temporary plugging. The open hole staged acid fracturing would be the optimal selection to create enough artificial acid fractures along a horizontal interval of 383 m, and to enhance well productivity as much as possible.

5.2 Case 1: Temporary Plugging Staged Acid Frac

5.2.1 Well Information

Well X is a perforated ultra-deep horizontal well with MD of 7,859 m, TVD of 7,271.83 m, and a continuous perforated interval of 88 m. There are two gas formations with reservoir thickness (MD) of 80.6 m, average porosity of 5.7%, average permeability of 1.6 mD, and water saturation of 7.8% from logging interpretation.

5.2.2 Staged Acid Frac Technique

The challenge of proper acid placement is compounded in well X, for strong heterogeneous (permeability ranges from 0.1 to 19 mD and max-min ratio of 190), and small size of cemented and perforated tail pipe (inner diameter of 92.46 mm). The sealing ball temporary plugging staged fracturing is recommended to create several artificial acid-etched fractures along horizontal intervals. The productivity performance of the staged acid frac horizontal well was simulated to optimize the effects of acid-etched fracture numbers, length, and conductivity (**Figure 9**).

It is recommended that two stages with acid-etched fracture length above 50 m and conductivity above 20 D cm are preferably optimized.

5.2.3 Field Application

The completion fluid in the wellbore was drained out, and the tested gas production is 28.58×10^4 m^3/d with a wellhead pressure of 59.08 MPa before acid frac. The temporary plugging staged acid fracturing operation curve is shown in **Figure 10**. The treating pressure drops significantly from 94.46 to 76.58 MPa at the injection rate of 5.35 m^3/min, which indicates that the near wellbore damage is removed. The treating pressure increases from 76.55 to 77.53 MPa when

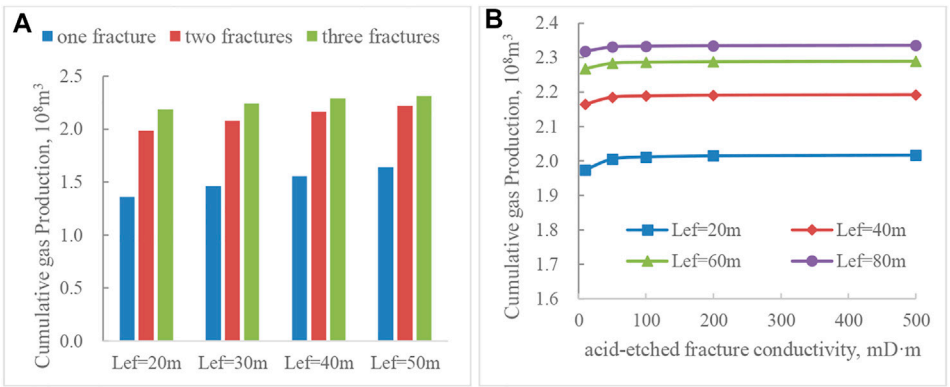

FIGURE 9 | Staged acid fracturing productivity performance simulation. **(A)** Cumulative gas production versus fractures; **(B)** cumulative gas production versus fracture length and conductivity.

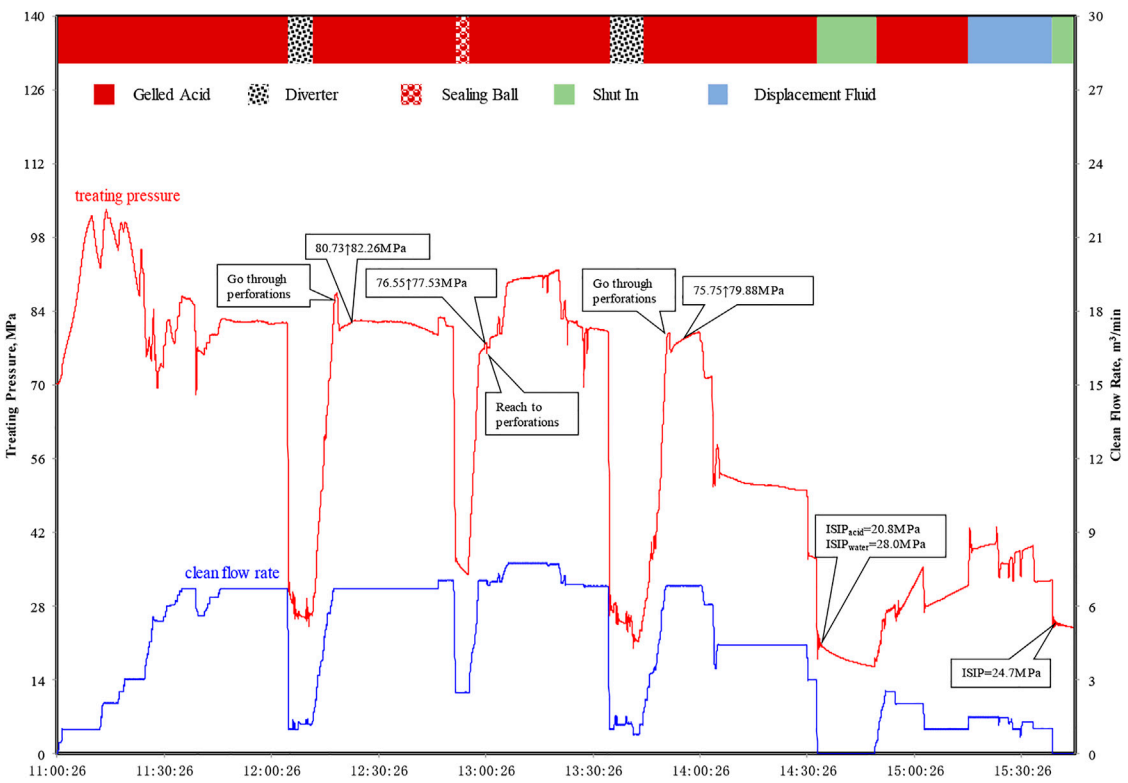

FIGURE 10 | Temporary plugging staged acid fracturing with the closed fracture acidizing operation curve of well X.

the sealing balls reach the perforations. It can be concluded that the temporary plugging staged acid frac is successfully implemented. The treating pressure increases from 80.73 to 82.26 MPa at an injection rate of 6.72 m^3/min, and 75.75–79.88 MPa at an injection rate of 6.83 m^3/min, after the diverters go through the perforations. It can be deduced that the degradable solid diverters decreased the acid leakage and increased the net fracture pressure to propagate the fracture. The instantaneous shut-in pressure (ISIP) difference before (converted to displacement fluid) and after acidizing is 3.3 MPa, which indicates that the acid-etched fracture conductivity is effectively enhanced by CFA.

The tested production is enhanced to 123.97 × 10^4 m^3/d (calculated open flow capacity of 381.86 × 10^4 m^3/d) under wellhead pressure of 50.5 MPa and converted bottom hole flow pressure of 84.3 MPa.

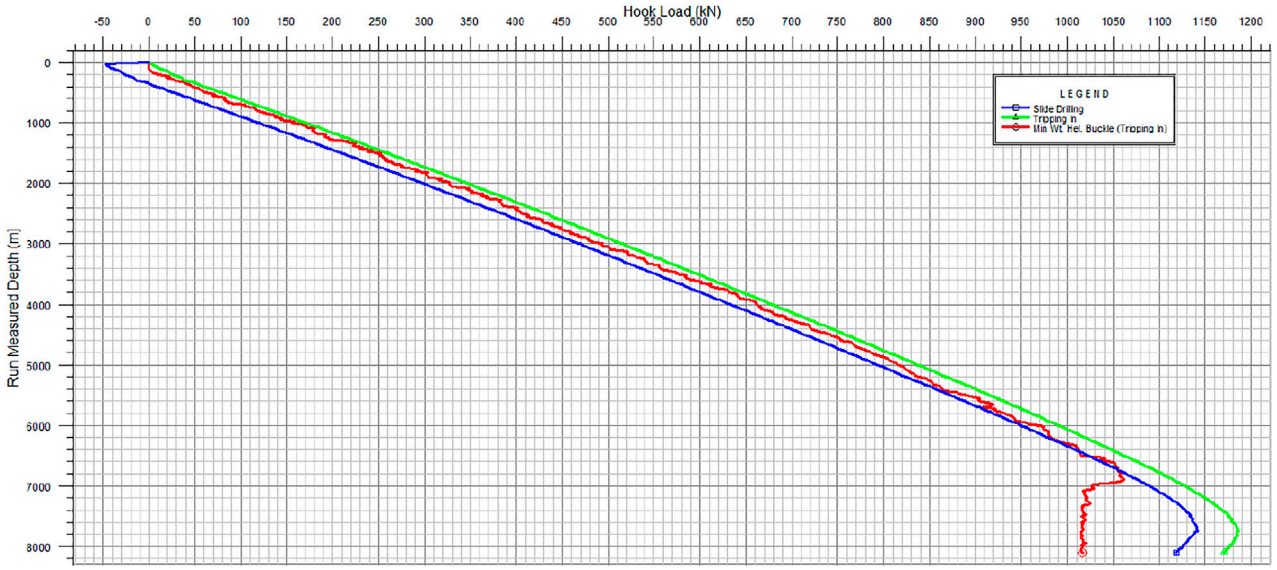

FIGURE 11 | Simulation of running in the open-hole staged fracturing tool for well M.

5.3 Case 2: Open-Hole Packer Staged Acid Frac

5.3.1 Well Information

Well M is an ultra-deep horizontal well of PetroChina, with MD of 8,102.0 m, TVD of 7,498.1 m, and horizontal interval length of 383 m. The Qixia Fm is characterized by low porosity and low permeability with reservoir thickness (MD), porosity, permeability, and water saturation of 333.6 m, 5.3%, 0.97 mD, and 21.8%, respectively.

The hook load of running in open hole packer and sliding sleeve staged fracturing tools with 88.9 mm base tube using 101.6 mm drill pipe to predetermined depth was simulated using WELLPLAN under the extreme condition with an open hole friction coefficient of 0.4, and front blocking of 0 KN and 50 KN (**Figure 11**). The open-hole packer and sliding sleeve staged fracturing tools can be run into predetermined depth smoothly without string buckling. Moreover, the suspension packer is rotatable to drive the whole staged fracturing string to a predetermined depth. The open hole staged acid fracturing is feasible for well M.

The opening of the toe fracturing sliding sleeve to form a fracturing passage is critical for successfully staged acid fracturing. The maximum length of existing coiled tubing in domestic is about 7,700 m, and the working depth of coiled tubing under high temperature, high pressure, and sour gas environment is about 7,000 m. There is no spare measure to handle the downhole complexity and the well would be abandoned to cause huge economic losses if the toe fracturing sliding sleeve cannot be activated. The first stage is assembled by fracturing sleeve, spared pitching sliding sleeve, and circulating valve. The soluble polymer ball should be pitched in to open the spared pitching sliding sleeve if the opening of the toe fracturing the sliding sleeve failed. Therefore, the activation of the first stage fracturing channel is guaranteed. The open-hole packer and sliding sleeve staged acid fracturing tool string is shown in **Figure 12**. The main risks and corresponding response plans are listed in **Table 4**.

5.3.2 Fracture Optimization

The productivity performance of the staged acid frac horizontal well was simulated with StimPlan, to optimize the effects of acid-etched fracture numbers, length, and conductivity. The wellbore azimuth is almost parallel to the maximum horizontal principal stress, and therefore the longitudinal fractures will be created. The productivity performance versus numbers of acid-etched fractures was simulated under fracture length of 50 m, fracture conductivity of 50 D·cm, and bottom hole flowing pressure of 75 MPa (**Figure 13**). The gas rate increased and its growth declined with increasing numbers of fractures, and four fractures are preferably optimized.

The productivity performance versus lengths and conductivities of acid-etched fracture was simulated under four fractures and bottom hole flowing pressure of 75 MPa (**Figure 14**). The gas rate increased and its growth declined with increasing fracture length and conductivity. The acid-etched fractures with a length above 50 m and conductivity above 20 D·cm are preferably optimized.

It is recommended that four stages of massive gelled acid fracturing with CFA for well M.

5.3.3 Field Application

The completion fluid in the wellbore was drained out before stimulation to reduce the formation breakdown pressure. The tested gas production is 36.31×10^4 m^3/d with a wellhead pressure of 59.99 MPa. The staged acid fracturing with the CFA operation curve is shown in **Figure 15**. The difference between ISIP and pumping pressure at the same injection rate

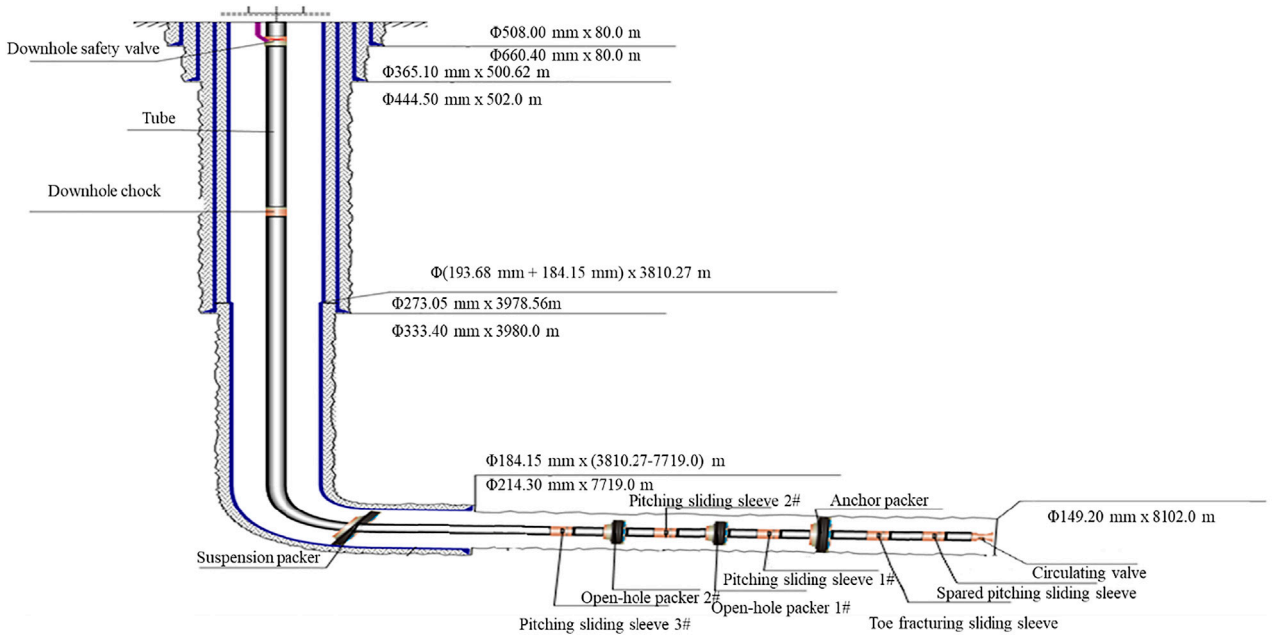

FIGURE 12 | Schematic diagram of the open-hole staged acid fracturing tool string for well M.

TABLE 4 | Main risks and corresponding response plans for running in staged fracturing tools.

No.	Risk	Response plan
1	Tools cannot run into a predetermined depth	The suspension packer is rotatable to drive the whole staged fracturing string to a predetermined depth
2	Blocking in the staged fracturing tool string	Pouring clear water to avoid blockage
3	Invalid check valve	The reverse gas seal check valve of 105 MPa
4	Unsuccessful hydraulic release	Mechanical rotation release
5	Unable to activate the toe fracturing sliding sleeve	The toe fracturing sliding sleeve, spared pitching sliding sleeve, and circulating valve are assembled. The polymer soluble ball is pitched to activate the pitching sliding sleeve and form a fracturing passage if the toe fracturing sliding sleeve cannot be activated

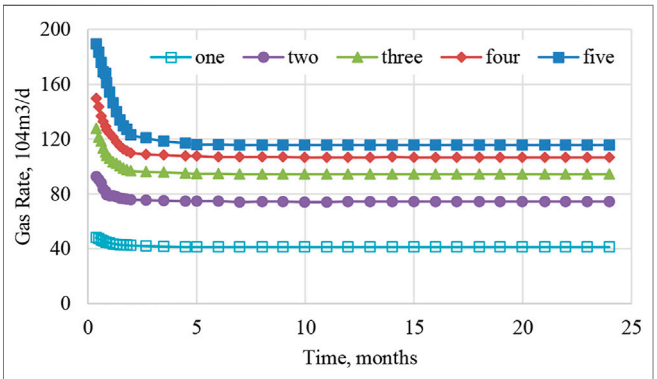

FIGURE 13 | Productivity performance versus numbers of fractures.

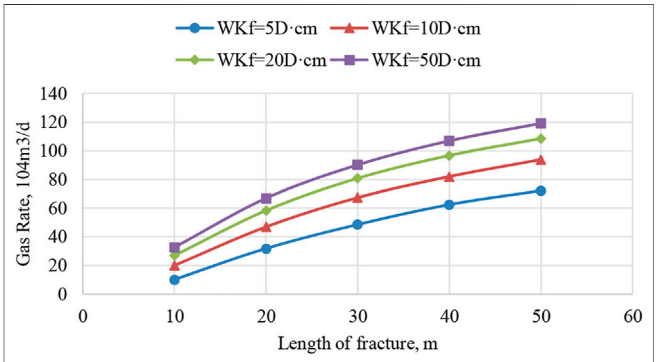

FIGURE 14 | Productivity performance versus fracture lengths and conductivities.

of each stage is obvious. It can be concluded that the open hole staged acid fracturing of the ultra-deep horizontal well is successfully operated. The ISIP difference between stage IV before (converted to displacement fluid) and after acidizing is 1.58 MPa, which indicates that CFA effectively enhances the acid-etched fracture conductivity.

The tested production is enhanced to 142.51 × 10^4 m^3/d, which is extremely closed to the predicted gas production

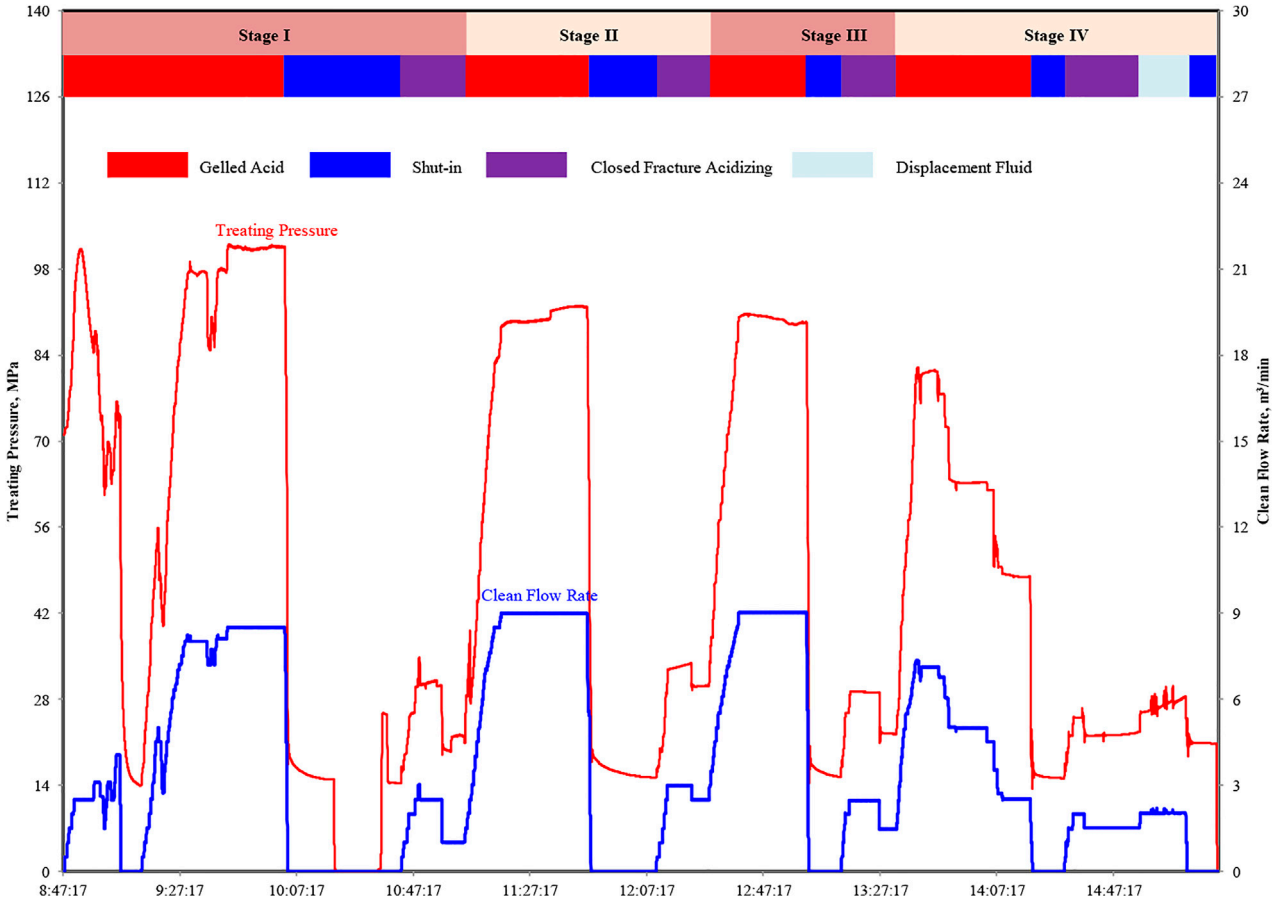

FIGURE 15 | Staged acid fracturing with the closed fracture acidizing operation curve of well M.

(149.58×10^4 m^3/d) at the initial stage, under wellhead pressure of 50.36 MPa and converted bottom hole flow pressure of 84.2 MPa. The productive performance of staged acid fractured horizontal well is significantly higher than that of acid fractured vertical wells.

6 CONCLUSION

The acid rock reaction and acid-etched fracture conductivity experiments of Qixia Fm tight carbonate are investigated to optimize the main acid type and acid frac technique. In addition, the feasibility of open-hole packer and sliding sleeve staged acid fracturing is discussed, and the staged acid frac tool string is optimized. Based on the research work, the following conclusions are drawn:

1) The gelled acid was selected as the main acid fracturing system for better retardation and friction reduction performance.
2) The acid-etched fracture conductivity sharply decreased with increasing closure stress, and it can be greatly enhanced by using gelled acid, increasing acid volume, and closed fracture acidizing technology.
3) The open-hole packer and sliding sleeve staged acid fracturing is feasible for the ultra-deep horizontal well. The first stage was assembled by fracturing sleeve, spared ball drop sleeve, and circulating valve to guarantee activation of fracturing channels.
4) The temporary plugging and open-hole staged massive gelled acid fracturing with closed fracture acidizing is successfully operated to significantly enhance gas production. It is referential for staged acid fracturing of ultra-deep horizontal wells.

DATA AVAILABILITY STATEMENT

The raw data supporting the conclusion of this article will be made available by the authors, without undue reservation.

AUTHOR CONTRIBUTIONS

FL: conceptualization, formal analysis, supervision, and writing—review and editing. YF: conceptualization, data curation, investigation, methodology, validation, visualization,

and writing—original draft. LL: project administration, resources, conceptualization, formal analysis, and supervision. JL: formal analysis and writing—review and editing. YC: formal analysis and supervision. ZL: conceptualization, formal analysis, and supervision. TH: methodology, validation, and visualization.

ACKNOWLEDGMENTS

The authors of this article gratefully acknowledge the support of the National Natural Science Foundation of China (NSFC, No. 51974264).

REFERENCES

Alkattan, M., Oelkers, E. H., Dandurand, J.-L., and Schott, J. (1998). An Experimental Study of Calcite and Limestone Dissolution Rates as a Function of pH from −1 to 3 and Temperature from 25 to 80°C. *Chem. Geol.* 151, 199–214. doi:10.1016/s0009-2541(98)00080-1

Anderson, M. S. (1991). Reactivity of San Andres Dolomite. *SPE Prod. Eng.* 6 (2), 227–232. doi:10.2118/20115-pa

Asadollahpour, E., Baghbanan, A., Hashemolhosseini, H., and Mohtarami, E. (2018). The Etching and Hydraulic Conductivity of Acidized Rough Fractures. *J. Petroleum Sci. Eng.* 166, 704–717. doi:10.1016/j.petrol.2018.03.074

Bybee, K. (2006). Continuous Improvements in Acid Fracturing at Lake Maracaibo. *J. Pet.. Tech.* 58 (7), 54–56. doi:10.2118/0706-0054-jpt

Chen, H., Guo, J., and Zhao, J. (2005). Problems and Countermeasures to Stimulate Sour Gas Reservoir with Low Permeability. *Nat. Gas. Ind.* 25 (7), 89–91. (In Chinese). doi:10.3321/j.issn:1000-0976.2005.07.030

Ding, Y., Li, Y., Xu, Y., Cheng, X., Wang, Y., Zhang, F., et al. (2010). "Propped Fracturing with a Novel Surface Cross-Linked Acid in High Temperature Deep Carbonate Formation," in Paper SPE 127312 presented at North Africa Technical Conference and Exhibition, Cairo, Egypt, 14-17 Feb. doi:10.2118/127312-ms

Fredd, C. N., and Scott Fogler, H. (1998b). The Kinetics of Calcite Dissolution in Acetic Acid Solutions. *Chem. Eng. Sci.* 53 (22), 3863–3874. doi:10.1016/s0009-2509(98)00192-4

Fredd, C. N. (1998a). The Influence of Transport and Reaction on Wormhole Formation in Carbonate Porous Media: A Study of Alternative Stimulation Fluids. PhD dissertation. Michigan: U. of Michigan.

Frenier, W. W., and Hill, D. G. (2002). "Effect of Acidizing Additives on Formation Permeability during Matrix Treatments," in Paper SPE 73705 presented at the SPE International Symposium and Exhibition on Formation Damage Control, Lafayette, Louisiana, 20-21 Feb. doi:10.2118/73705-ms

Gdanski, R., and Van Domelen, M. S. (1999). "Slaying the Myth of Infinite Reactivity of Carbonates," in Paper SPE 50730 presented at the SPE International Symposium of Oilfield Chemistry, Houston, 16-19 Feb. doi:10.2118/50730-ms

Gomma, A. M., and Nasr-El-Din, H. A. (2010). "New Insights into Wormhole Propagation in Carbonate Rocks Using Regular, Gelled and *In-Situ* Gelled Acids," in Paper SPE 133303 presented at SPE Production and Operations Conference and Exhibition, Tunis, Tunisia, 8-10 Jun.

Han, H., Sang, Y., and Yang, J. (2016). Experimental Study and Application of Stimulation Technologies for Sinian Dengying Formation Reservoirs in the Sichuan Basin. *Nat. Gas. Ind.* 36 (1), 81–88. (In Chinese). doi:10.3787/j.issn.1000-0976.2016.01.010

Jeon, J., Bashir, M. O., Liu, J., and Wu, X. (2016). "Fracturing Carbonate Reservoirs: Acidizing Fracturing or Fracturing with Proppants?," in Paper SPE 181821 presented at SPE Asia Pacific Hydraulic Fracturing Conference, Beijing, China, 24-26 Aug.

Jin, X., Zhu, D., Hill, A. D., and Mcduff, D. (2019). "Effects of Heterogeneity in Mineralogy Distribution on Acid Fracture Efficiency," in Paper SPE 194377 presented at SPE Hydraulic Fracturing Technology Conference and Exhibition, Woodlands, Texas, 5-7 Feb.

Kalfayan, L. J. (2007). "Fracture Acidizing: History, Present State, and Future," in Paper SPE 106371 presented at SPE Hydraulic Fracturing Technology Conference, College Station, Texas, 29-31 Jan.

Li, G., Sheng, M., Tian, S., Huang, Z., Li, Y., and Yuan, X. (2012). Multistage Hydraulic Jet Acid Fracturing Technique for Horizontal Wells. *Pet.. explor. Dev.* 39 (1), 100–104. doi:10.1016/s1876-3804(12)60021-4

Li, N., Feng, Y., Liu, P., Luo, Z., and Zhao, L. (2015). Study of Acid-Rock Reaction Kinetics under High Temperature and Pressure Conditions Based on the Rotating Disk Instrument. *Arab. J. Sci. Eng.* 40 (1), 135–142. doi:10.1007/s13369-014-1504-x

Li, N., Zhao, L., Zhang, Q., Ren, X., and Liu, P. (2003). Acid Etched Fracture Conductivity Study in Acid Fracturing. *Drill. Prod. Technol.* 26 (3), 22–25. (In Chinese). doi:10.3969/j.issn.1006-768X.2008.06.019

Li, Q., Chen, W., Lu, Y., and Xiao, Q. (2019). Etched Surface Morphology Analysis Experiments under Different Reaction Rates. *J. Petroleum Sci. Eng.* 172, 517–526. doi:10.1016/j.petrol.2018.09.063

Liu, H., and Zhao, Z. (1998). "Successful Application of Multistage Acid Fracturing Technology in Changqing Gas Field," in Paper SPE 50911 presented at SPE International Oil and Gas Conference and Exhibition, Beijing, China, 2-6 Nov. doi:10.2118/50911-ms

Liu, M., Zhang, S., Mou, J., Zhou, F., and Shi, Y. (2013). Diverting Mechanism of Viscoelastic Surfactant-Based Self-Diverting Acid and its Simulation. *J. Petroleum Sci. Eng.* 105, 91–99. doi:10.1016/j.petrol.2013.03.001

Luo, Y., Liu, A. H., Wang, J. M., Yang, C. Y., and Qi, W. S. (2008). Application of Crosslinked Acid Sand-Adding Acid-Fracturing Technique in Complex Lithologic Reservoir. *Acta Pet.. Sin.* 29 (2), 266–269. (In Chinese). doi:10.3321/j.issn:0253-2697.2008.02.020

Luo, Z., Zhang, N., Zhao, L., Liu, H., Luo, P., and Liu, J. (2019). Innovative Encapsulating Acid with Release Dually Controlled by the Concentration of Hydrogen Ions and Temperature. *Energy fuels..* 33 (6), 4976–4985. doi:10.1021/acs.energyfuels.9b00673

Luo, Z., Zhang, N., Zhao, L., Yao, L., and Liu, F. (2018). Seepage-stress Coupling Mechanism for Intersections between Hydraulic Fractures and Natural Fractures. *J. Petroleum Sci. Eng.* 171, 37–47. doi:10.1016/j.petrol.2018.07.019

Luo, Z., Zhang, N., Zhao, L., Zeng, J., Liu, P., and Li, N. (2020). Interaction of a Hydraulic Fracture with a Hole in Poroelasticity Medium Based on Extended Finite Element Method. *Eng. Analysis Bound. Elem.* 115, 108–119. doi:10.1016/j.enganabound.2020.03.011

Malagon, C., Pournik, M., and Hill, A. D. (2008). The Texture of Acidized Fracture Surfaces: Implications for Acid Fracture Conductivity. *SPE Prod. Oper.* 23 (3), 343–352. doi:10.2118/102167-pa

Nasr-El-Din, H. A., Solares, J. R., Al-Zahrani, J. A., and Garzon, F. O. (2007). "Acid Fracturing of Gas Wells Using Solid Acid: Lessons Learned from First Field Application," in Paper SPE 110895 presented at SPE Annual Technical Conference and Exhibition, Anaheim, California, 11-14 Nov. doi:10.2118/110895-ms

Nelson, R. L., Jamieson, F. M., and Jenkins, R. A. (1998). "Multiple Pad-Acid Fracs in a Deep Horizontal Well," in Paper SPE 39943 presented at SPE Rocky Mountain Regional/Low-Permeability Reservoirs Symposium, Denver, Colorado, 5-8 Apr.

Peng, Y., Li, Y., Zhao, J., Wang, L., Zhang, Y., and Luo, P. (2015). Simulation and Analysis of Acid-Etched Fracture Conductivity of Fracture-Cavity Carbonate Reservoir. *Acta Pet.. Sin.* 36 (5), 606–611. (In Chinese). doi:10.7623/syxb201505010

Peng, Y., Zhao, J., Sepehrnoori, K., Li, Y., and Li, Z. (2019b). The Influences of Stress Level, Temperature, and Water Content on the Fitted Fractional Orders of Geomaterials. *Mech. Time-Depend Mater* 24, 221–232. doi:10.1007/s11043-019-09417-0

Peng, Y., Zhao, J., Sepehrnoori, K., Li, Y., Yu, W., and Zeng, J. (2019a). Study of the Heat Transfer in Wellbore during Acid/Hydraulic Fracturing Based on Semi-analytical Transient Model. *SPE J.* 24 (2), 877–890. doi:10.2118/194206-pa

Peng, Y., Zhao, J., Sepehrnoori, K., and Li, Z. (2020). Fractional Model for Simulating the Viscoelastic Behavior of Artificial Fracture in Shale Gas. *Eng. Fract. Mech.* 228, 106892. doi:10.1016/j.engfracmech.2020.106892

Pournik, M., Nasr-El-Din, H. A., and Mahmoud, M. A. (2011). A Novel Application of Closed-Fracture Acidizing. *SPE Prod. Oper.* 26 (1), 18–29. doi:10.2118/124874-pa

Rabie, A. I., Shedd, D. C., and Nasr-El-Din, H. A. (2014). Measuring the Reaction Rate of Lactic Acid with Calcite and Dolomite by Use of the Rotating-Disk Apparatus. *SPE J.* 19 (6), 1192–1202. doi:10.2118/140167-pa

Taylor, K. C., and Nasr-El-Din, H. A. (2002). "Coreflood Evaluation of *In-Situ* Gelled Acids," in Paper SPE 73707 presented at International Symposium and Exhibition on Formation Damage Control, Lafayette, Louisiana, 20-21 Feb.

Taylor, K. C., Nasr-El-Din, H. A., and Mehta, S. (2006). Anomalous Acid Reaction Rates in Carbonate Reservoir Rocks. *SPE J.* 11 (4), 488–496. doi:10.2118/89417-pa

Teklu, T. W., Park, D., Jung, H., Amini, K., and Abass, H. (2019). Effect of Dilute Acid on Hydraulic Fracturing of Carbonate-Rich Shales: Experimental Study. *SPE Prod. Oper.* 34 (1), 170–184. doi:10.2118/187475-pa

Ugursal, A., Zhu, D., and Hill, A. D. (2019). Development of Acid Fracturing Model for Naturally Fractured Reservoirs. *SPE Prod. Oper.* 34 (4), 735–748. doi:10.2118/189834-pa

Wang, X., Liu, G., Wang, D., and Economides, M. J. (2011). "The Use of Sealing Ball Staged Fracturing," in Paper SPE 140529 presented at SPE Hydraulic Fracturing Technology Conference, Woodlands, Texas, 24-26 Jan.

Xue, H., Huang, Z., Liu, F., Liu, P., Wang, H., Zhang, B., et al. (2019). "3D Acid Fracturing Simulation and Application in the Upper Sinian Dengying Fm Gas Reservoirs in China," in Paper IPTC 19137 presented at International Petroleum Technology Conference, Beijing, China, 26-28 Mar.

Xue, H., Huang, Z. X., Zhao, L. Q., Jiang, W. D., Liu, P. L., and Liang, C. (2018). A Simulation Study on the Preflush Acid Fracturing Considering Rock Heterogeneity. *Nat. Gas. Ind.* 38 (2), 59–66. (In Chinese). doi:10.3787/j.issn.1000-0976.2018.02.008

Yao, M. T., Mou, J. Y., Li, D., Xue, Y. P., Jiang, F., and Zhang, L. F. (2015). An Experimental Study of Long-Term Conductivity in High Temperature and Pressure Carbonate Formation. *Sci. Tech. Eng.* 15 (2), 193–195. (In Chinese). doi:10.3969/j.issn.1671-1815.2015.02.035

Yi, X., Lu, Y., Li, Q., Li, Y., and J, W. (2010). On New Acid Fracturing Technique with Proppant-Carrying Crosslinked Acid on Carbonate Reservoirs. *China Sci. Pap.* 5 (11), 837–839. doi:10.3969/j.issn.2095-2783.2010.11.001

Yuan, L., Wang, Y., Li, Q., Chen, K., and Li, Y. (2019). Evaluation of a Control-Released *In-Situ* Generated Acid Tablet for Acid Fracturing. *J. Petroleum Sci. Eng.* 174, 384–393. doi:10.1016/j.petrol.2018.09.081

Zhao, L., Chen, X., Zou, H., Liu, P., Liang, C., Zhang, N., et al. (2020). A Review of Diverting Agents for Reservoir Stimulation. *J. Petroleum Sci. Eng.* 187, 106734. doi:10.1016/j.petrol.2019.106734

Zhao, L. Q., Gao, Y. J., Yuan, X. F., Luo, Z. F., and Yuan, Z. B. (2017). Research on Flow Conductivity of Acid Etched Fracture of Carbonate Reservoir under High Temperature. *Rsvr. Eval. Dvlopmt.* 7 (1), 20–26. (In Chinese). doi:10.3969/j.issn.2095-1426.2017.01.004

Zhu, D., Hu, Y., Cui, M., Chen, Y., Liang, C., He, Y., et al. (2019). Feasibility Analysis on the Pilot Test of Acid Fracturing for Carbonate Reservoirs in Halfaya Oilfield, Iraq. *Energy Sci. Eng.* 7 (3), 721–729. doi:10.1002/ese3.290

Conflict of Interest: Authors FL, YF, LL, JL, YC, ZL, and TH were employed by PetroChina Southwest Oil and Gas Field Company.

frontiers | Frontiers in Energy Research

METHODS
published: 14 July 2022
doi: 10.3389/fenrg.2022.958040

Casing Deformation Response and Controlling Technology Based on Diagnostics of Shale Gas Fracturing Curve

Cheng Shen, Bo Zeng, Jianfa Wu, Yi Song, Xingwu Guo, Xiaojin Zhou and Junfeng Li*

Shale Gas Research Institute, CNPC Southwest Oil and Gas Field Company, Chengdu, China

Casing deformation (CD) will seriously affect the fracturing progress and stimulation effect of shale gas. Taking 105 gas wells in the Luzhou shale gas area in southern Sichuan as an example, the CD prediction model was established by introducing the fracture operation curve diagnosis method to analyze the changes in net pressure and propagation mode during fracturing. The fracturing stage induced by CD is called the excited (ET) stage, and the fracturing stage that occurs during CD is called the CD stage. It is concluded that the change of net pressure and the propagation mode are coupled with each other. By natural fracture development, formation curvature and horizontal well trajectory, natural fractures and bedding have been active by high fracturing strength, or because of the frequent crossing-layer in single stage, local stress reverse, makes the net pressure decrease and makes the formation in strike-slip stress state to reverse fault stress state, liquid leak-off and blocked fracture propagation time are increased, thus inducing CD. According to the response law induced by CD, the CD pre-control mode is formed, and the CD pre-control technology is established to quantitatively evaluate the wellbore risk and optimize the fracturing operation order and time arrangement. The CD rate is reduced from 56% in the early stage to 20%, and the integrity of the wellbore is guaranteed to be 100%. The method has strong applicability in the field and can be further popularized.

Keywords: diagnostics of fracturing curve, deep shale gas, casing deformation, net pressure, induced stress, pre-control technology

OPEN ACCESS

Edited by:
Shuai Zhao,
Southwest Petroleum University, China

Reviewed by:
Zhezhi Liu,
Chongqing University of Science and Technology, China
Qiong Wang,
China University of Petroleum

****Correspondence:***
Cheng Shen
shenc_victor@163.com

Specialty section:
This article was submitted to Advanced Clean Fuel Technologies, a section of the journal Frontiers in Energy Research

Received: *31 May 2022*
Accepted: *21 June 2022*
Published: *14 July 2022*

Citation:
Shen C, Zeng B, Wu J, Song Y, Guo X, Zhou X and Li J (2022) Casing Deformation Response and Controlling Technology Based on Diagnostics of Shale Gas Fracturing Curve. Front. Energy Res. 10:958040. doi: 10.3389/fenrg.2022.958040

1 INTRODUCTION

According to the results of many scholars at home and abroad, casing deformation (CD) is mainly affected by geological and engineering factors. In terms of geology, the main media of CD in shale gas wells is a large number of natural fractures and faults in the reservoir (Daneshy, 2005; Yu et al., 2014; Bao and Eaton, 2016; Chen et al., 2016; Chen et al., 2017; Chen et al., 2019; Yan et al., 2019; Chen et al., 2021; Meyer et al., 2018; Schultz et al., 2018; Liu et al., 2019; Liu et al., 2020; Fan et al., 2020; Hu et al., 2020; Peng et al., 2020a; Peng et al., 2020b; Qiao and Ye, 2021; Tong et al., 2021a; Cheng et al., 2022; Meng et al. 2020). In terms of engineering, CD occurs mostly after fracturing, so it is proposed that natural fractures and faults slip when large volume fracturing fluid enters the reservoir. Natural fracture and fault slip and stratum slip and dislocation are the main engineering causes of casing shear deformation (Gao et al. 2017; Gao et al. 2021; Lu et al., 2021). For the casing itself, Zhang et al. (2015) suggest that sudden

pressure release within the casing at the end of large-rate fracturing places the casing in the most vulnerable conditions of collapse failure. Yin et al. (2018a), Yin et al. 2018b, Yin et al. 2018c) proposed that variation of annular pressure caused by cold fracturing fluid increases the risks of casing deformation. Sugden et al. (2012), Xi et al. (2019), Lian et al. (2020), Guo et al. (2018), Guo et al. (2019), Zhang X. et al (2021) and others proposed that the cementing quality problems such as casing eccentricity and lack of cement sheath cause asymmetric load on the casing, and the effects of fracturing fluid on the difference of temperature from the heel to the toe end of the lateral increases the risks of casing failure at the heel end stages.

In the south of the Sichuan shale block, engineers of drilling and fracturing have taken different measures to solve the CD: ①The drilling operator prevented casing deformation by increasing the cement sheath and casing wall thickness to enhance casing strength. Nevertheless, the maximum casing curvature is merely reduced by 8% (Gao et al. 2017; Yin et al., 2018c; Lu et al., 2021), and casing deformation still occurs in seven out of eight test wells. ②According to the geological model, the fracturing engineer simulated the effects of fault activation and bedding plane hydration expansion on fracturing treatment (McClure and Horne, 2011; Rutqvist et al., 2015; Zhang et al., 2020a, Zhang et al., 2020b; Zhang Xin et al., 2021; Li J. et al., 2021; Li X. et al., 2021), high-density completion, reduction in the fracturing fluid volume and treatment rate, compound temporary plugging technique have been used to reducing the activity of the fracture system. Nevertheless, these approaches are still ineffective in the study area (Zhang X. et al., 2021; Tong et al., 2021b; Zhang P. et al., 2021). Analysis shows that the existing CD prevention and control methods have a large probability of failure in the study area, which is mainly caused by the insufficient accuracy of fracture prediction and the untimely adjustment of fracturing parameters.

Mainguy (2016) proposed that deformation of the weak surface is caused by slippage and dislocation along a discontinuous surface, which results from energy accumulation triggering the weak surface to reach the slippage state, and there is an energy accumulation process. The fracturing curve reflects and indicates energy variation and accumulation during the fracturing treatment, and it has been widely used in evaluation of stimulation effects and proppant plugging risks in carbonate rock, coalbed methane, tight gas, volcanic rock, and shale gas reservoirs (Nolte and Smith., 1981; Pirayesh et al., 2015; Bian et al., 2016; Zhang et al., 2018; Zhuang et al., 2019; Chen et al., 2020; Hu et al., 2020; Zhao et al., 2022; Shen et al. 2022). It provides the visual data for controlling the fracturing process. In this paper, the geological-engineering parameters of 56 CD gas wells in the study area were acquired to fully excavate the information from the fracturing curve, and the "process control" was emphasized. A model and technology for prevention and pre-control of casing deformation based on diagnostics of shale gas fracturing curves were formed and applied in the field, which provides guidance for fracturing treatment in the current and later stages and reduces the rate of casing deformation.

1.1 Prediction Model of Casing Deformation Based on Fracturing Curve

To prevent and control casing deformation in shale gas fracturing, it is necessary to establish a bottom-hole net pressure model, an induced stress model, and a casing deformation prediction model.

1.2 Real-Time Bottom Hole Net Pressure

When not considering the induced stress generated by the prior fracturing stage, the bottom hole net pressure of fracturing stages is obtained by calculating casing pressure at wellhead, hydrostatic column pressure, perforation friction, borehole friction, and minimum horizontal principal stress as follows:

$$P_{\mathrm{net}\,n} = P_{\mathrm{head}\,n} + P_{\mathrm{String}\,n} - P_{\mathrm{nf}\,n} - P_{\mathrm{wf}\,n} - \sigma_{\mathrm{min}\,n}. \tag{1}$$

Here $P_{\mathrm{net\ n}}$-real-time net pressure when considering the induced stress during the fracturing process of the nth stage, MPa; $P_{\mathrm{Head\ n}}$-real-time treatment casing pressure at the wellhead during the fracturing process of the n th stage, Mpa; $P_{String\ \mathrm{n}}$-real-time proppant-carrying slurry static column pressure in the nth stage, Mpa; $P_{nf\ n}$-real-time perforation hole friction on the fracture entry in the nth stage, Mpa; Pwf n-real-time borehole friction in the nth stage, Mpa; $\sigma_{min\ n}$-minimum horizontal principal stress of the nth stage, Mpa.

In addition, $P_{String\ n}$, $P_{nf\ n}$, $P_{nf\ n,}$ and $P_{\mathrm{wf\ n}}$ are calculated as follows.

1.2 1 Real-Time Proppant-Carrying Slurry Column Static Pressure

The real-time proppant-carrying slurry column static pressure is calculated by referring to the hydrostatic column pressure at the burial depth of each stage:

$$P_{\mathrm{String}\,n} = \frac{\rho_{\mathrm{frac}\,n} g h_n}{1000000}. \tag{2}$$

Here $\rho_{frac\ n}$ is the real-time fracturing fluid density of the nth stage, kg/m^3; g is the acceleration of gravity, m/s^2, which is 9.8; h_n is the average vertical depth from the logging interpretation of the fracturing stage, m.

During the fracturing process, the slurry is carrying the proppant; the real-time proppant-carrying slurry column static pressure cannot be calculated only by the hydrostatic column pressure, and the fracturing fluid density should be modified.

$$\rho_{\mathrm{frac}\,n} = \left[\frac{w_n}{\rho_{\mathrm{PropV}}}\rho_{\mathrm{Prop}} + \left(1 - \frac{w_n}{\rho_{\mathrm{PropV}}}\right)\rho_{\mathrm{Fluid}}\right]. \tag{3}$$

Here w_n is the actual proppant concentration of slurry in fracturing stage, kg/m^3; ρ_{PropV} is the proppant density applied in fracturing stage, kg/m^3; ρ_{Prop} is the apparent density of the proppant applied in fracturing stage, kg/m^3; ρ_{Fluid} is the fracturing fluid density applied in fracturing stage, kg/m^3.

1.2.2 Real-Time Borehole Friction

When the fracturing fluid flows through the borehole to the reservoir, friction is generated within the borehole. The

friction is currently related to the treatment rate and fluid properties. A real-time borehole friction model is established as follows:

$$P_{\mathrm{wf}\,n} = \lambda \frac{L v_s^2 \rho_{\mathrm{Fluid}}}{2000000D}. \tag{4}$$

Here λ is the hydraulic friction coefficient, dimensionless; L is the bottom measured depth of fracturing stage, m; v_s is the real-time flow rate of proppant-carrying slurry, m/s; D is the borehole diameter, m.

The real-time flow rate of proppant-carrying slurry is calculated as follows:

$$v_s = \frac{q}{15\pi D^2}. \tag{5}$$

Here q is the real-time fracturing rate, m^3/min.

In addition, the hydraulic friction coefficient is determined by defining the Reynolds number:

$$\mathrm{Re} = \frac{1000\rho_{\mathrm{Fluid}} v_s D}{\mu}. \tag{6}$$

Here R_e is the Reynolds number, dimensionless; μ is the fracturing fluid viscosity, mPa·s.

Based on the Reynolds number, the criterion for the hydraulic friction coefficient is established: when R_e2000, the hydraulic friction coefficient is determined by **Eq. 8**; when 2000 < Re < 59.7/(2R/D)8/7, it is determined by **Eq. 9**; when 59.7/(2R/D)8/7 < Re< [665-765z (2R/D)]/(2R/D), it is determined by **Eq. 10**; when Re> [665-765lg (2R/D)]/(2R/D), it is determined by **Eq. 11**.

$$\lambda = 64/\mathrm{Re}, \tag{7}$$

$$\lambda = 0.3164/\mathrm{Re}^{0.25}, \tag{8}$$

$$\frac{1}{\sqrt{\lambda}} = -1.8\lg\left[\frac{6.8}{\mathrm{Re}} + \left(\frac{R}{3.7D}\right)^{3.11}\right], \tag{9}$$

$$\lambda = \frac{1}{4\lg(3.7D)^2}. \tag{10}$$

1.2.3 Real-Time Perforation Hole Friction on the Fracture Entrance

When the fracturing fluid flows through the borehole to the formation, it passes through the perforation holes, resulting in frictional resistance. The friction is currently related to the perforation hole numbers, hole diameter, and fracturing rate. A real-time perforation hole friction model is established as follows:

$$P_{\mathrm{nf}} = \frac{9q^2\rho_{\mathrm{Fluid}}}{4\times 10^9 n_{\mathrm{nf}}^2 d_{\mathrm{nf}}^4 \alpha_{\mathrm{nf}}^2}. \tag{11}$$

Here R is the absolute roughness of the borehole wall, m; P_{nf} is the real-time perforation hole friction on the fracture entry during fracturing, MPa; n_{nf} is the perforation hole number of the fracturing stage, number; d_{nf} is the perforation hole diameter of the fracturing stage, m; α_{nf} is the flow coefficient at the perforation hole, dimensionless.

1.3 Model of Real-Time Induced Stress Superposition

The previous stage will produce superimposed induced stress on the current stage, which will cause the original formation stress state to change and affect the real-time net pressure of this section. Stress influence, establishes a real-time induced stress superposition model:

$$P_{\mathrm{net}}(n) = P_{\mathrm{net}\,n} - \sum_{i=1}^{n-1}\sigma_{xin}. \tag{12}$$

Here $P_{net}(n)$ is the real-time effective net pressure when considering the induced stress generated in the fracturing process of the nth stage, MPa; σ_{xin} is the real-time induced stress generated at the fracture entry of the nth stage by the fracture entry of the ith stage at the minimum horizontal principal stress direction, MPa.

The induced stress generated by the fracturing stage itself and the prior stage is acted upon along the minimum horizontal principal stress and the maximum horizontal principal stress. The induced stress generated at the fracture entry of the nth stage by the fracture entry of the ith stage at the minimum horizontal principal stress direction is calculated as follows:

$$\sigma_{xin} = P_{\mathrm{net}}(n)\left(1 - \frac{\frac{L(i,n)}{2c}}{\sqrt{\left(\frac{L(i,n)}{2c}\right)^2 + \frac{1}{4}}} + \frac{\frac{L(i,n)}{2c}}{4\left(\sqrt{\left(\frac{L(i,n)}{2c}\right)^2 + \frac{1}{4}}\right)^3}\right). \tag{13}$$

Here c is the reservoir half thickness, m; L (i, n) is the difference in measured depth between the middle of the ith stage and the middle of the nth stage, m.

Similarly, the induced stress generated at the fracture entry of the nth stage by the fracture entry of the ith stage at the maximum horizontal principal stress direction is calculated as follows:

$$\sigma_{yin} = 2P_{\mathrm{net}}(n)\nu\left(1 - \frac{\frac{L(i,n)}{2c}}{\sqrt{\left(\frac{L(i,n)}{2c}\right)^2 + \frac{1}{4}}}\right). \tag{14}$$

Here σ_{yin} is the real-time induced stress generated at the fracture entry of the nth stage by the fracture entry of the ith stage at the maximum horizontal principal stress direction, MPa; ν is the average Poisson's ratio obtained from logging interpretation of the fractured stage, dimensionless.

In addition, to carry out research on the *in situ* stress in the study area, the current *in situ* stress field is calculated as follows:

$$\begin{cases} \sigma_x' = \sigma_x + \sum_{i=1}^{n}\sigma_{xin}, \\ \sigma_y' = \sigma_y + \sum_{i=1}^{n}\sigma_{yin}. \end{cases} \tag{15}$$

Here σ_x' is the real-time minimum horizontal principal stress during fracturing, MPa; σ_y' is the real-time maximum horizontal principal stress during fracturing, MPa; σ_y is the average maximum horizontal principal stress obtained from logging interpretation point in the fractured stage, MPa.

1.4 Models for Predicting Casing Deformation

A total of six response trends, including fluid leak-off and fracture propagation blockage (Zhao et al., 2022) when the hydraulic fracture encounters the natural fracture, are identified. First, the curve is divided into several sections. The net pressure curve obtained from fracture diagnostics is divided into multiple sections according to the trend of monotonic increase and decrease by using Fisher's optimal segmentation method, and the slope of the monotonic change of net pressure in each section is read as follows:

$$\bar{n}_j = \frac{P_{\text{net}}(n)_{\text{end}j} - P_{\text{net}}(n)_{\text{start}j}}{t(n)_{\text{end}j} - t(n)_{\text{start}j}}. \tag{16}$$

Here $P_{\text{net}}(n)_{\text{start } j}$ is the initial real-time effective net pressure when considering the induced stress during the jth section in the nth stage, MPa; $P_{\text{net}}(n)_{\text{end } j}$ is the final real-time effective net pressure when considering the induced stress during the jth section in the nth stage, MPa; $t(n)_{\text{start } j}$ is the time when the jth section in the nth stage starts, min; $t(n)_{\text{end } j}$ is the time when the jth section in the nth stage ends, min.

A model for determining fluid leak-off is established as follows:

$$\begin{cases} \bar{n}_j < 0.2, \\ P_{\text{net}}(n) < \Delta S. \end{cases} \tag{17}$$

Here ΔS is the stress contrast in the reservoir and upper and lower interlayers, MPa.

A model for determining fracture propagation blockage has been established as follows:

$$\begin{cases} \bar{n}_j > 0.3, \\ P_{\text{net}}(n) > \min\left[\left(\sigma_{\text{nf}} + S_{\text{tnf}}\right), \left(\sigma_{\text{nf}} - \dfrac{\tau_{\text{nf}} - \tau_0}{k_{\text{nf}}}\right)\right]. \end{cases} \tag{18}$$

Here

$$\begin{cases} \sigma_{\text{nf}} = \sigma'_y \sin^2\theta_{\text{nf}} \sin^2\varphi_{\text{nf}} + \sigma'_x \cos^2\theta_{\text{nf}} \sin^2\varphi_{\text{nf}} + \sigma'_z \cos^2\varphi_{\text{nf}}, \\ \tau_{\text{nf}} = \left[\left(\sigma'_y \sin\theta_{\text{nf}} \sin\varphi_{nf}\right)^2 + \left(\sigma'_x \cos\theta_{\text{nf}} \sin\varphi_{\text{nf}}\right)^2 + \left(\sigma'_z \cos\varphi_{\text{nf}}\right)^2 \right. \\ \qquad \left. - \left(\sigma'_y \sin^2\theta_{\text{nf}} \sin^2\varphi_{\text{nf}} + \sigma'_x \cos^2\theta_{\text{nf}} \sin^2\varphi_{\text{nf}} + \sigma'_z \cos^2\varphi_{\text{nf}}\right)^2\right]^{0.5}. \end{cases} \tag{19}$$

Here $\sigma_z{}'$ is the real-time vertical stress in the fracturing process, MPa; θ_{nf} is the approach angle, °; φ_{nf} is the dip angle, °; S_{tnf} is the tensile strength, MPa; τ_o is the cohesion, MPa; k_{nf} is the friction coefficient, dimensionless; σ_{nf} is the normal stress on the fracture wall, MPa; σ_τ is the tangential stress on the fracture wall, MPa.

It is assumed that fluid leak-off and fracture propagation blockage occur during the jth section in the nth stage, and the duration is recorded as t_{lnj} and $t_{rnj,}$ respectively. When fluid leak-off or fracture propagation blockage occurs, the risk of casing deformation in the fracturing process is determined. If necessary, the sum of the duration of increasing the risk of casing deformation in the nth stage is recorded as:

$$t_{tn} = \sum_{j=1}^{\bar{n}_j < 0.2} t_{1nj} + \sum_{j=1}^{\bar{n}_j > 0.3} t_{rnj}. \tag{20}$$

Here t_{tn} is the total duration of fluid leak-off and fracture propagation blockage in the nth stage, min; t_{lnj} is the duration of fluid leak-off during the jth section of the nth stage; t_{rnj} is the duration of fracture propagation blockage during the jth section of the jth stage, min.

2 DIAGNOSIS OF THE FRACTURING CURVE

The study area covers the well blocks L and Y in the Luzhou Area. Natural fractures and faults have developed in the area, which also shows strong segmentation characteristics with formation in blocks. Because the horizontal stage frequently passes through natural fractures, faults, or different horizons, it is difficult to drill gas wells in the area. The horizontal stage of the gas well in the area is about 1800 m long in total and about 60–80 m long in each segmented stage. The number of clusters in one individual stage is about 6–8. Drilling of each stage requires drilling fluids of 1800–2000 m^3 and sand of 100–150 t approximately. The pump rate during stimulation is about 14–18 m^3/min. Currently, there are 105 horizontal wells with fracturing treatment completed or in progress. Among them, 56 wells have CD to various degrees. To facilitate analysis, diagnosis has been performed for 2,488 stages in all of the 105 wells within the study area. Diagnosis results show there are 1,100 stages in 56 wells with CD and 1,388 stages in 49 wells with no CD. In other words, CD has a significant impact on operations in gas wells.

2.1 Characteristics of Net Pressures

Calculation results of net pressures in 2,488 stages show that the average real-time net pressure in the area is about 16.2 MPa with an overall distribution characterized by non-standard normal distribution (**Figure 1**). Analysis results show that the net operation pressure of 14.04 MPa in the 1,100 stages with casing deformation (CD) is significantly lower than the average net pressure of 17.94 MPa in the 1,388 stages with casing intact (CI). It can be seen that under the same operating conditions, it is more difficult to establish sufficient net pressure in the CD wells through a large pump rate.

There are 198 casing deformation points in the CD wells, corresponding to 198 casing deformation stages in fracturing. Correspondingly, the fracturing section that induces the casing deformation, or the section that involves resistance after fracturing, is called the excited (ET) stage. In total, there are 198 ET stages. All stages fractured before this are collectively referred to as the preceding fracturing stages, with a total number of 198. According to the calculation results of **Eq. 13** and **Eq. (14)**, when the action range is greater than the increase of the two-dimensional stress caused by induced stress beyond 300 m, is only

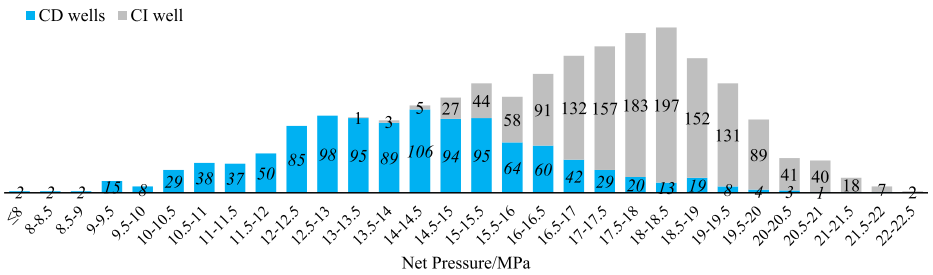

FIGURE 1 | Distribution of the number of stages at different real-time net pressures in the whole area.

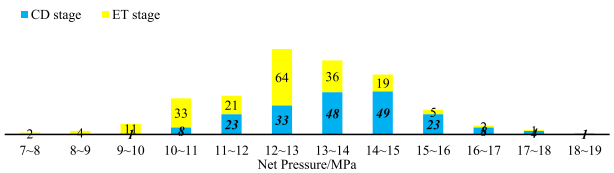

FIGURE 2 | Average real-time net pressure distribution of casing deformation (CD) and excited stages (ET).

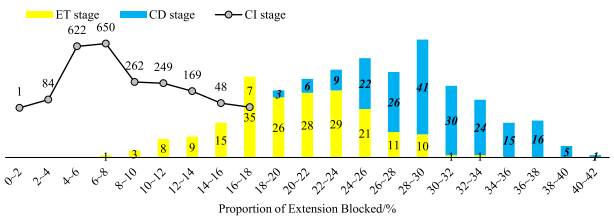

FIGURE 3 | Distribution of fracture stages with different proportions of extension blocked time.

0.001 MPa. Therefore, the fracturing stages (about 4 to 6 stages) within 300 m of the preceding fracturing stages are focused on the concerned research. Statistics show that the CD stages have an average net pressure of 13.68 MPa, the ET stages have an average net pressure of 12.28 MPa, and the preceding stages have a net pressure of 15.2 MPa (**Figure 2**).

2.2 Characteristics of Extension

In this study, the time proportion of two modes in fracturing was reviewed: liquid leak-off and fracture extension blockage,. The statistics of the time proportion of two modes in 2,488 stages show that the average fracturing liquid leak-off time accounts for 24.19% and the average extension blocking time accounts for 10.42%. To be more specific, the average liquid leak-off time accounts for 30.1%, and average extension blocked time accounts for 29.86% in CD stages; the average liquid leak-off time accounts for 40.49%, and average extension blocked time accounts for 20.15% in excited stages; the average liquid leak-off time accounts for 24.21%, and average extension blocked time accounts for 11.44% in preceding fracturing stages (**Figure 3**, **Figure 4**).

3 Responses, to Prevention and Control of Casing Deformation

Comprehensive theoretical research results show there are two internal reasons for the occurrence of casing deformation: one is the communication and activation of weak surfaces such as natural fractures and bedding, and the other is the accumulation of energy to a certain extent. In cases with large volumes of fracturing fluids injected to a certain limit during

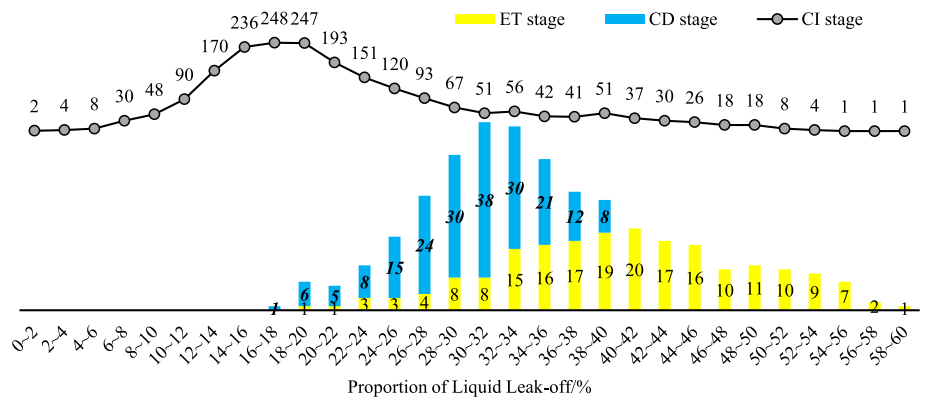

FIGURE 4 | Distribution of fracture stages with different proportion of liquid leak-off time.

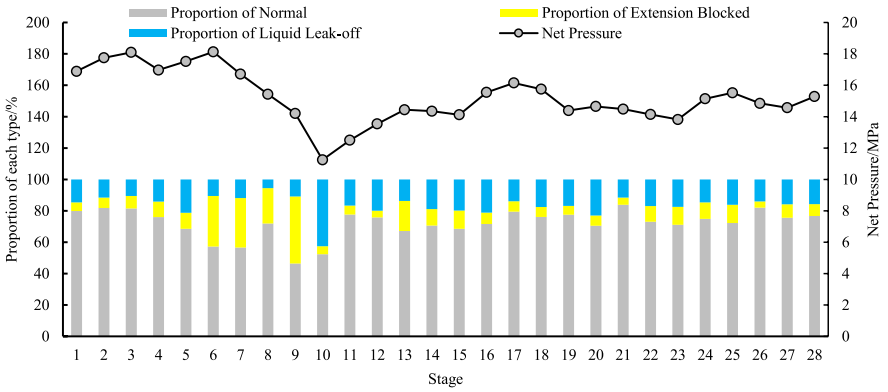

FIGURE 5 | Statistics of the ratio of net pressure, leak-off, and extension time in each stage of well H7–4.

fracturing, the instability of natural fractures or bedding may eventually induce casing deformation. For consideration of these two internal reasons, the net pressure and extension mode are used to carry out historical backtracking. In addition, the casing deformation inducing opportunity and energy limit in the fracturing process are found in view of the geological characteristics of each fracturing stage.

3.1 Overall Geological-Engineering Responses Determined Through Diagnosis of Fracturing Curves

3.1.1 Overall CD Pattern

According to the statistical results of extension modes, the proportion of liquid leak-off and extension blocking time in the excited stage is higher than the overall average value, whereas the liquid leak-off and extension blocking time in the preceding fracturing stage is lower than that in the excited stage but higher than the overall average (**Figure 5**). Under such circumstances, the first fractured intervals in the preceding fracturing stages have a proportion of the diagnosed liquid leak-off and extension blocking time slightly lower or consistent with the overall average. By analyzing the two extension modes, it can be concluded that the excited stages have the highest proportions of liquid leak-off times, followed by the preceding fracturing stages. In addition, intervals closer to the preceding fracturing stages have lower liquid leak-off time proportions. At the same time, proportions of liquid leak-off time in casing deformation stages are slightly higher than the overall average. On the other hand, proportions of extension blocking time in both excited stages and casing deformation stages are higher than the overall average. It is also worth noticing that the proportions of extension blocking time in casing deformation stages are significantly higher than those in the excited stages. The average extension blocking time in preceding fracturing stages is lower than that in the excited stages but slightly higher than the overall average. Intervals in the preceding fracturing stages closer to the excited stages have longer extension blocking times.

Taking well H7-4 as an example, fracturing occurred in the 10th stage and casing deformation occurred in the 13th stage. It can be clearly seen that in the process of fracturing from stage 6–10, the proportion of time blocked and leak-off is particularly prominent, and the net pressure shows a trend of obvious gradual decrease, which has become the typical data change characteristic of casing deformation in the current study area.

3.1.2 Geological Responses of CD Stages Determined Through Diagnosis of Fracturing Curves

The features of excited stages and casing deformation stages are closely related to different geologic and drilling conditions. Because casing deformation is related to weak surface slippage and formation dislocation, data related to the natural fracture development, formation curvatures, and penetration of horizontal well trajectories in different excited stages and casing deformation stages are collected in this study.

Firstly, the influence of natural fracture on casing deformation is analyzed. According to the relationship between CD stage and natural fracture, the majority of natural fractures are distributed at 50–100 m from ET stages and 0–50 m from CD stages. In contrast, the probability of CD caused by natural fracture slippage in the CD stage is higher. On the other hand, it can be seen from the conditions of the pre-preceding fracturing stages of different wells that starting from the first intervals of the preceding fracturing stages, the distances between the preceding fracturing stages and the natural fractures are reducing, which is also one of the reasons why the proportions of liquid leak-off time in the fracturing process gradually increase with the progress of fracturing treatments (**Figure 6**, **Figure 7**).

In addition to reductions in distances between the preceding fracturing stages and natural fractures, there are also reductions in included angles between natural fractures and the borehole. This is the key reason for the higher extension blockages of fractures. Set 7th to 10th stages in H7-4 well as an example, natural fractures do not develop in stage 7, and the net pressure curve is characterized by gradual uplift of fracture network propagation. There were low-angle natural fractures near the

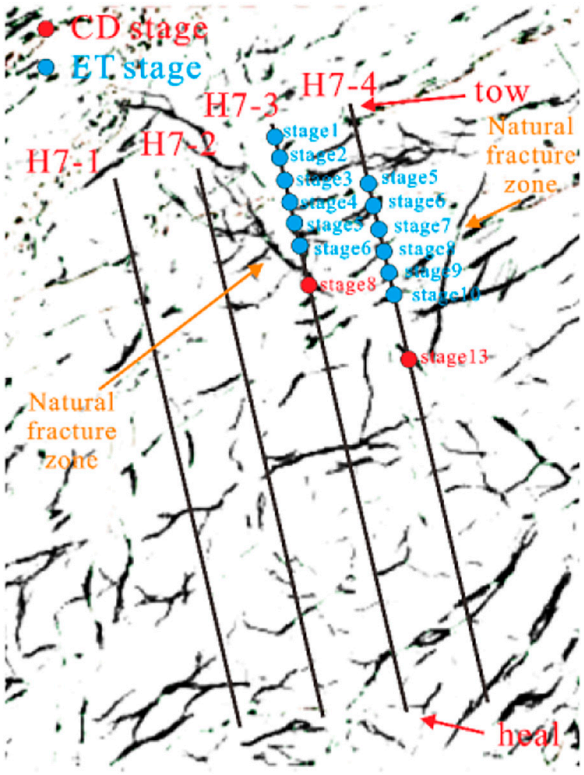

FIGURE 6 | Location distribution and natural fracture development characteristics of fore-sequence excited stage groups and casing deformation stages in H7 platform.

wellbore in stage 8, and the net pressure curve showed a sudden and steep increase in the initial stage of fracturing, followed by a gradual uplift pattern of fracture network propagation. In the late fracturing operation of stage 9, the net pressure curve shows an obvious continuous downward trend, indicating that the natural fractures far from the wellbore are gradually approaching, and the hydraulic fractures have been able to extend to the intersection to cause liquid leak-off. At stage 10, the net pressure curve shows frequent steep increases due to both a natural fracture at a small angle near the wellbore and another natural fracture approaching the wellbore.

Secondly, the influence of formation curvature is analyzed. Formation curvatures are identified as the curvature volumes of geophysical interpretation. From the curvature prediction results, it can be seen that most positions with casing deformation are in abnormally distorted states. In other words, formations around these positions are characterized by local unevenness. On the other hand, only half of the formations in the excited and preceding fracturing stages are characterized by abnormal curvatures. This is also the main reason why the casing deformation occurs not in the excited stage but at some distance away from the excited stages during fracturing of the excited stages (**Figure 8**). At the same time, the unevenness of the formation is the external reflection of the change in the magnitude and direction of the formation stress, which becomes the main reason for the differential formation dislocation after the arrival of energy. In general, when the stage with abnormal curvature was not fractured, the fracturing operation curve tends to be stable or uplifted. Once the fracture stage with abnormal curvature is fractured,

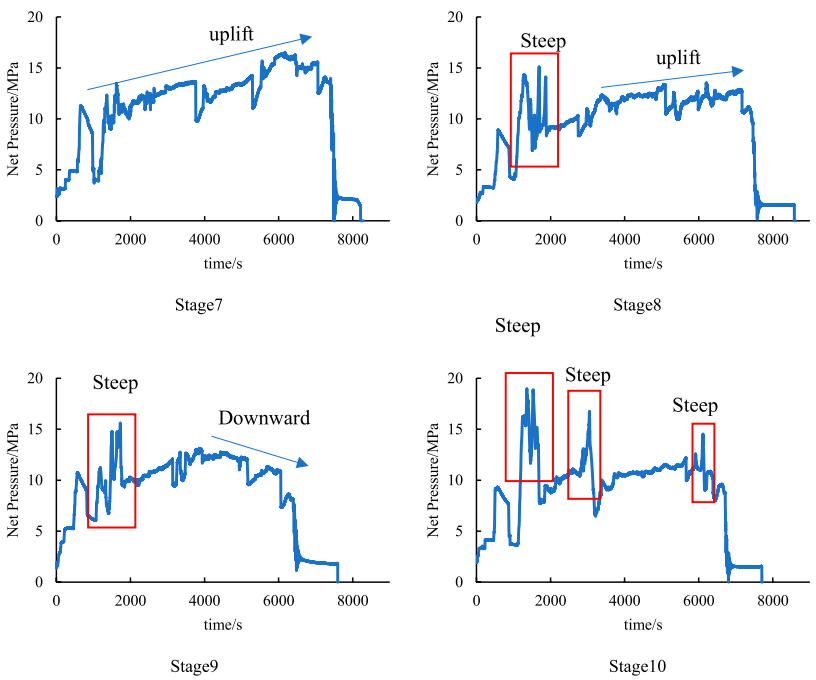

FIGURE 7 | Net pressure curves for stages 7 through 10 of well H7–4.

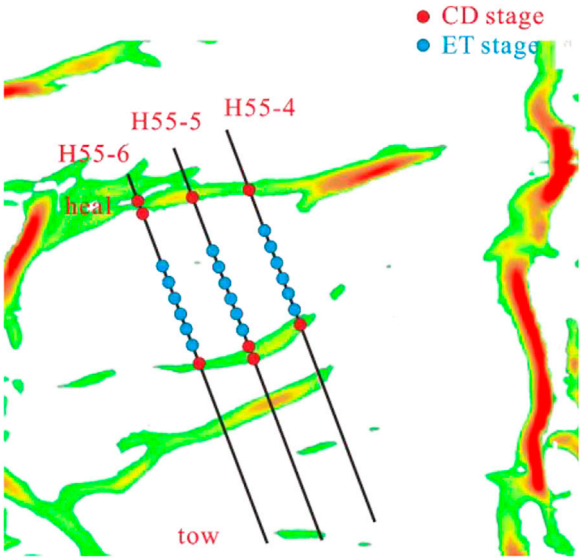

FIGURE 8 | Relationship between the position of casing variation and the distribution of the curvature anomaly zone in the H55 platform.

large through-through connectivity zones will be formed between platforms and wells. In other words, energy generated in fracturing at certain intervals may be transmitted over long distances through curvature belts with CD. As a result, corresponding fractured intervals in different wells along the entire curvature belt may have CD of various degrees.

In the case of Platform H55, the platform is fractured with a pull chain. Well four was the first to undergo casing fracture, followed by well 5 and 6. Due to the penetration of the curvature anomaly zone, the time of filtration and blocked extension on the fracturing curve gradually increases and the curve shape becomes more complex (**Figure 9**), indicating that the penetration of curvature will seriously lead to an increased risk of CD in multiple wells.

The combined action of formation penetration and distortion is more likely to lead to CD. Most CD stages have frequent formation penetration. By counting the number of formation penetrations (the number of differential formations penetrated by the horizontal intervals of the deviated wells) before, during, and after the casing deformation stage (within a 100 m range) during fracturing treatments, it was found the average number is 3.8 (**Figure 10**). In other words, because of the difference in rock mechanics and geomechanics in different horizons, the stresses in the whole casing deformation stage vary greatly. With the study area under strike-slip stresses, the induced stress produced by fracturing may change the original maximum horizontal principal stress > vertical stress >the minimum horizontal principal stress state to a reverse fault state with the maximum horizontal principal stress >the minimum horizontal principal stress > vertical stress. As a result, the interlayer sliding at the location of the casing deformation may promote sliding of natural fractures and, eventually, enhance the risk of CD.

3.1.3 Engineering Responses of CD Stages Determined Through Diagnosis of Fracturing Curves

Through comprehensive analysis, it is concluded that the changes in net pressures and extension modes are coupled

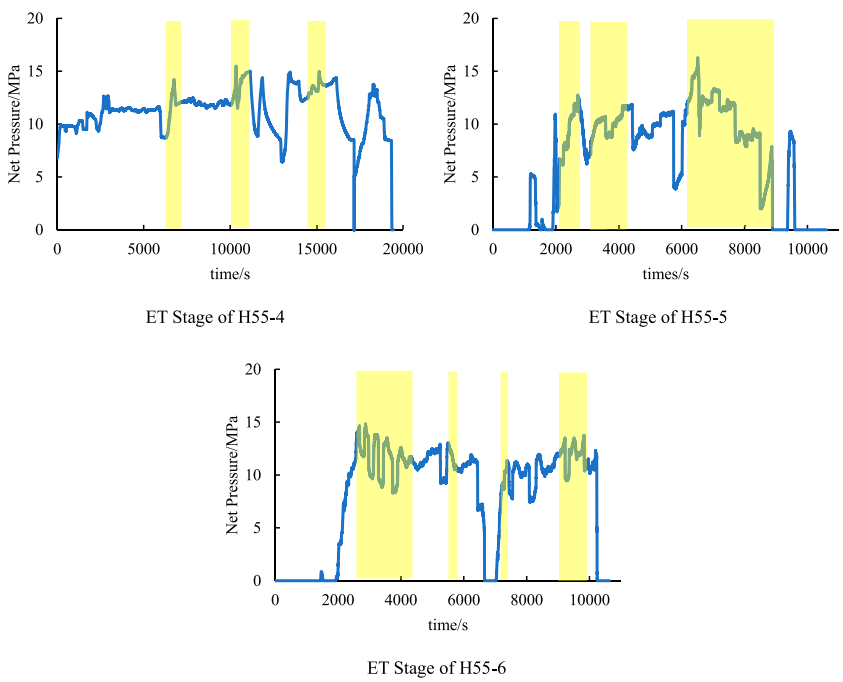

FIGURE 9 | Net pressure curve of ET stage in H55 platform.

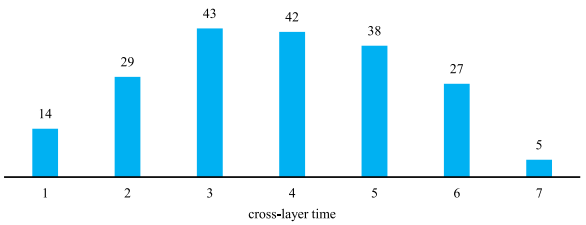

FIGURE 10 | Total times of cross-layers in a range of 200 m of 198 CD stages.

with each other. Before the CD induced by fracturing in the excited stages, most of the preceding fracturing stages had fracturing treatments with scales larger than necessary. With fluid intensities of over 30 m^3/m and a pump rate of over 16 m^3/min, external forces are applied to these formations continuously and intensively in subsequent fracturing treatments. At this time, the proceeding fracturing stages have relatively high average real-time net pressures (**Figure 9**). With down-hole faults and fractures potentially re-activated, these high pressures may involve liquid leak-off or extension blockage, with the net pressures lower than those in conventional fracturing treatments. The proportions of time related to liquid leak-off and extension blockage usually increase with the progress of the fracturing process, indicating that the fracture system near the well-bore may be closer to the well-bore, and it also indicates the increase of casing deformation risk. During the fracturing in the excited stages, due to insufficient attention to the impact of fracturing intensity, the continuous high-intensity operations often fail to achieve the desirable average real-time net pressures while the time of liquid leak-off and extension blockage reaches their peak. Since it is difficult to maintain the formation stability, casing deformation may be induced. In order to minimize the operation risk and avoid the occurrence of secondary CD, fracturing treatments are usually implemented by reducing the operation scales when the treatment measures are carried out after the CD through fracturing. At this time, the real-time net pressures of fracturing treatments are basically normal. However, due to the negative impacts of complicated geologic conditions and poor extension of fractures due to compromised strengths in positions with CD, proportions of time related to extension blockage increased significantly.

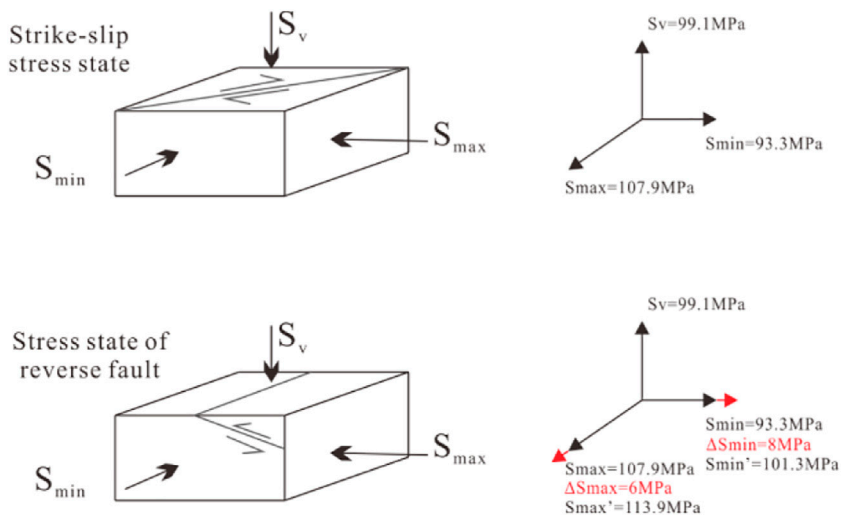

FIGURE 11 | Model diagram of the formation stress state change caused by fracturing.

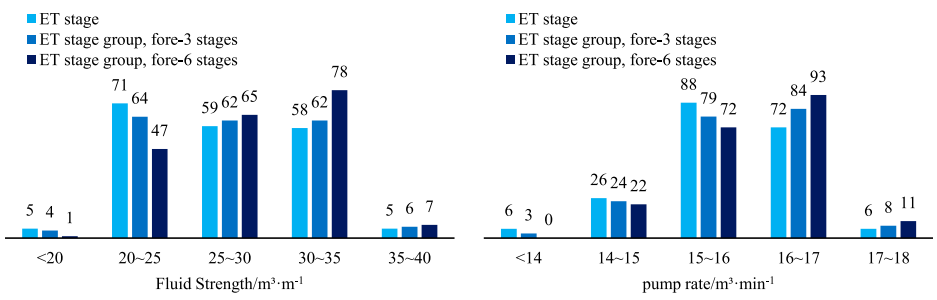

FIGURE 12 | Comparison of liquid strength and displacement in ET stages and ET stage groups.

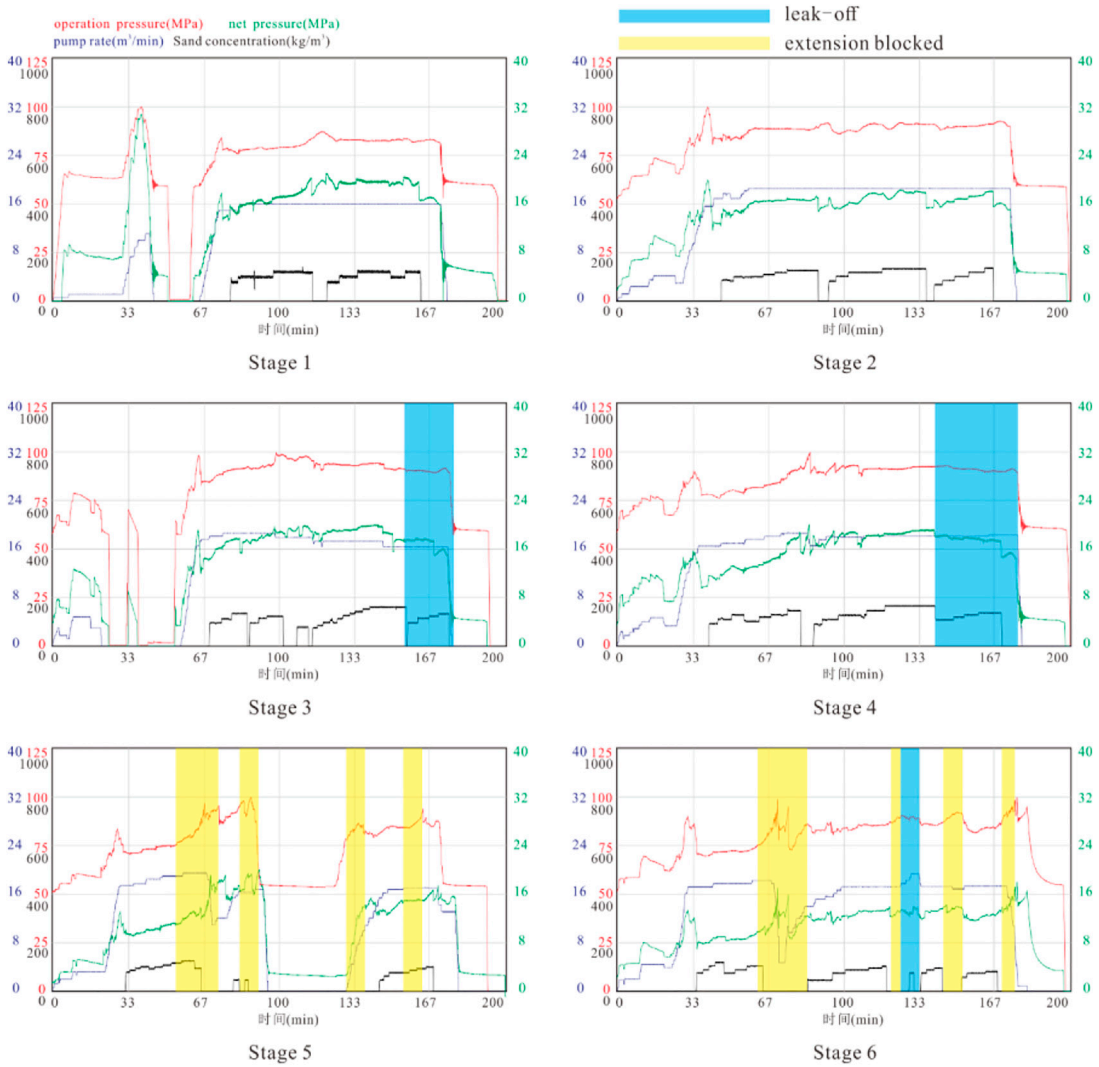

FIGURE 13 | Net pressure results of stage 1 through six frac operation curve diagnosis in H7–3 well.

3.1.4 Case Studies

We may take the Well H7-3 in Block L as an example: casing deformation was observed in Stage 8 (CD stage) after fracturing of Stage 6 (ET stage) in the Well. From **Figure 6**, we can see that there is a natural fracture approaching the wellbore from stage 1 to stage 8. From Stage 1 to Stage 6, fracturing treatments were implemented with a stage length of 70 m, 6 clusters in one stage, fluid intensity of 35 m^3/min, pump rate of 16–18 m^3/min, and sand intensities of 2.5–3.0 t/m (**Figure 13**). By reviewing the diagnosis for fracturing treatments in Stage 1 to Stage 6, it was found that real-time pressures in Stage 1 and Stage 2 were generally over 17 MPa and up to 20 MPa. At the same time, fracture extension modes are predominantly network extension or extension along bedding, which are favorable for achieving desirable fracturing performances in individual stages. By the end of fracturing in Stage 3, net pressure curves show obvious signs of liquid leak-off with the time proportions increasing gradually in Stage 4. At the same time, the time with significant liquid leakage moved up. Starting from the end of fracturing treatments in Stage 3, natural fractures or faults approached the well-bore rapidly at high angles. Consequently, the time for the intersecting of hydraulic fractures in fracturing of Stage 4 and natural fractures moved up. In Stage 5 and Stage 6, extensions of fractures were blocked at a time earlier than those in the preceding two fracturing stages. At this time, fractures are developed at low angles or parallel to the well-bore. Consequently, it was difficult for hydraulic fractures to crack natural fractures. During fracturing of Stage 5, hydraulic fractures extended along bedding after blockage of a certain time. Multiple extension blockages in fracturing of Stage 6 indicated cluster development of natural fractures in near-well zones, which are not suitable for high-intensity fracturing treatments. Casing deformation was observed after fracturing of Stage 6 due to the following two reasons: high-intensity fracturing treatments and energy transmission in belts with

natural fractures due to extremely well-developed natural fractures in the vicinity of the well-bore.

3.2 Prevention and Control of CD in Gas Wells Based on Diagnosis of Fracturing Curves

There are multiple geologic factors that may induce casing deformation. During the fracturing, the energy injection may break the formation stress balance and further increase the risk of casing deformation. However, it may not necessarily lead to casing deformation. Statistics related to 198 points with casing deformation show approximately 68% casing deformation points (stages) distributed in zones with extremely well developed natural fractures or with horizontal wells penetrated minor structures frequently. From the analysis of geological mechanisms, the casing deformation points are mostly located in the weak geological zones, that is, the area with natural fracture development, or the area with micro-amplitude structures, pointing to the positions with natural fractures and bedding (bedding fractures) extremely well developed. For boreholes with these geological conditions, the risk of casing deformation can be predicted and evaluated before fracturing. Due to the limited interpretation accuracy of geophysical exploration data, 32% of the casing deformation points may be difficult to predict and describe, so it is necessary to derive real-time data based on the diagnosis of fracturing curves. The advantage of real-time characterization is that it can quickly limit the fracturing scale and intensity through risk identification, so as to reduce the energy injection intensity, slow down the formation activation, and eventually eliminate the possibility of casing deformation.

In this way, the techniques for prevention and control of casing deformation in gas wells are developed based on diagnosis of fracturing curves. Differential fracturing treatments can be implemented when the natural fractures that can be detected or interpreted by geophysical exploration technology or the identifiable frequent penetrations by drilling trajectory tracking can be detected. With approaching of fracturing treatments to zones with complicated geologic conditions, intensities of such fracturing treatments can be reduced. Once the fracturing stages with complex geological conditions are passed, the intensity of fracturing treatments can be restored gradually. During this period, the net pressures and its curve shape diagnosed by fracturing curves shall be monitored in real-time to determine the proportions of leak-off and extension blockage times, so as to highlight the unidentified risks; In areas with no geophysical exploration data interpretation available and where the drilling trajectory is smooth and does not frequently penetrate the formation, if it is recognized that the net pressure diagnosed by the fracturing curve is significantly reduced, accompanied by liquid leak-off and blocked extension, real-time prediction of natural fractures between wells should be carried out. If the leak-off time accounts for a large proportion or is gradually moved up, the development of high-angle fractures with the well-bore is predicted. At the same time, real-time monitoring and prediction will be carried out for adjacent wells on the same drilling pad to avoid inferences among wells on the same pad. In the same way, the large proportion of the extension blocking time indicates that the fracture development angle is gradually lowered or parallel, and the temporary plugging can be used to turn to divert the flow and to minimize the risk. At the same time, the same fracturing process should be carried out for the fracturing stages parallel to the gas well on the same drilling pad to avoid further interference due to their contact with the same natural fractures. As soon as it is found through the fracturing curve diagnosis that the net pressures of two consecutive stages decrease, and the time when the fracture extension is blocked and the liquid leak-off occurs is significantly moved up, it will be regarded as the stage with natural fractures and the fracturing treatment scale will be reduced regardless of whether the geophysical exploration technology has identified the natural fractures.

3.3 Prevention and Control of CD Based on Diagnosis of Shale Gas Fracturing Curves

With the prevention and control modes as a guide, it is possible to develop casing deformation prevention and control technologies for the responses of the construction curves.

Step 1. Quantitatively evaluate whether the well-bore has the risks of casing deformation such as fracture development, frequent formation penetration, and excessive dogleg of well trajectory. To evaluate local points, natural fractures identified by multiple fracture prediction technologies may serve as the marks for development of fractures, whereas frequent penetration of well trajectory over 3 times or doglegs over 0.3°/m may serve as marks for frequent formation penetration or excessive doglegs. Low-intensity fracturing treatments can be implemented in fracturing stages with the development of natural fractures and frequent formation penetration. Medium-intensity fracturing treatments are implemented in fracturing stages with one condition satisfied. High-intensity fracturing treatments can be implemented in fracturing stages with high formation stability. With regard to angles of natural fracture development, if such fractures are tended to communicate with neighboring wells, or intersect perpendicularly with the well-bore, it is also necessary to control the volume of liquid to eliminate the possibility of casing deformation in multiple wells induced by inferences among offset wells. As for natural fractures parallel to the well-bore or intersected with the well-bore at lower angles, care should be taken to eliminate possible casing deformation in that particular well.

Step 2. Optimization of operation sequence and time efficiency of fracturing treatments under induced stresses. With regard to zipper fracturing on the drilling pad, with the present well spacing of 300 m, zipper fracturing treatments shall be converted to zipper fracturing treatments in every two wells to eliminate the possibility of casing deformation induced by excessive concentration of stresses locally; As for the timing of operations in neighboring wells, fracturing can be implemented alternatively in two neighboring wells with differences of 200–300 m (4–5 stages) to minimize the interference; Within

the same drilling pad with singular or multiple rigs, multiple fracturing units can be divided in accordance with the distribution of faults within the pad. In addition, fracturing treatments can be implemented in units with lower risks to minimize negative impacts of casing deformation; intensities of fracturing treatments can be enhanced gradually. When approaching the stages with higher risks, intensities of fracturing treatments can be reduced gradually. When moving away from such stages, fracturing intensities can be restored step by step to minimize risks related to slippage of the fault. At the same time, parameters for such fracturing treatments can be adjusted in real-time in accordance with the distribution of microscopic seismic and pressure responses. With the application of high-viscosity pre-flush fluid, multiple temporary plugging and sand plugging in fracture, pumping sequences can be optimized in real-time.

Upon application of these prediction and optimization operations, fracturing treatments have been implemented in 20 wells on 5 drilling pads, among which 1 pad experienced no casing deformation, whereas 16 wells on the other four pads have four wells with minor casing deformation. Since the 98 mm bridge plugs can be installed to maintain continuous operations, the well-bore integrity can be maintained effectively. The rate of casing deformation was reduced to 20%, which is significantly lower than the preceding 56%. In addition, degrees of casing deformation were greatly reduced greatly (as for degrees of casing deformation, 32% of wells can have 85–98 mm bridge plugs installed; 41% of wells can have 54–85 mm bridge plugs installed; and 27% of wells can have >54 mm bridge plugs installed). On-site performances can verify the reliability and applicability of these technologies.

4 CONCLUSION

In the concerned research, we have developed a set of models based on the fracturing curves for casing deformation prediction, so that we can predict the real-time net pressures in the fracturing process and the time proportion of the expansion mode of risks that may induce CD. It is found that it is difficult to establish sufficient net pressure through a high pump rate in CD wells. The stage induced CD is called the ET stage, and the stage-occurring CD is called the CD stage. Statistics show that the average net pressure of CD stages is 13.68MPa, the average time of leak-off is 30.1%, and the average blocked extension time accounts for 29.86%. The average net pressure in the ET stage was 12.28MPa, the average time of leak-off accounted for 40.49%, and the average blocked time accounted for 20.15%. The CD stage is characterized by low net pressure, strong liquid loss, and obvious blockage.

The geological and engineering factors that induce the CD are analyzed. The geological factors mainly include natural fractures, formation curvature, and horizontal well trajectory. Small angle natural fractures, abnormal curvature bodies that run through multiple wells and platforms, and well trajectories that frequently cross different layers are the most likely to cause CD. The engineering factor is mainly the continuous high-strength liquid pumping in the fracturing process, which changes the *in situ* stress state, induces the change of strike-slip stress state to a reverse fault stress state, and increases the risk of CD induced by interlayer dislocation.

According to responses from CD, prevention and control technologies have been developed. In real-time record the total time of fracturing curve response to liquid leak-off and extension block, and carry out prevention and control measures for gas wells with these two situations gradually accumulating and gradually advancing. By adopting the prevention and control technologies with quantitative evaluation of well-bore risks, optimized fracturing sequences and proper time efficiency, rates of casing deformation were reduced from previous 56% to the present 20% with 100% guarantee of well-bore integrity. This method has strong applicability in the field and can be deployed more extensively.

DATA AVAILABILITY STATEMENT

The original contributions presented in the study are included in the article/Supplementary Material; further inquiries can be directed to the corresponding author.

AUTHOR CONTRIBUTIONS

SC:Paper writing, data statistics and analysis ZB:Technical guidance WJ:Theoretical research, technical guidance SY:Data collection and analysis GX:Site construction and data acquisition LJ:The data analysis, data statistics and analysis.

REFERENCES

Bao, X., and Eaton, D. W. (2016). Fault Activation by Hydraulic Fracturing in Western Canada. *Science* 354 (6318), 1406–1409. doi:10.1126/science.aag2583

Bian, X., Jiang, T., Jia, C., Wang, H., Li, S., Su, Y., et al. (2016). A New Post-frac Evaluation Method for Shale Gas Wells Based on Fracturing Curves. *Nat. Gas. Ind. B* 3 (2), 146–151. doi:10.1016/j.ngib.2016.03.010

Chen, C., Huang, R., Zeng, B., Song, Y., and Zhou, X. (2021). Analysis and Optimization of Construction Parameters for Preventing Casing Deformation in the Changning Shale Gas Block, Sichuan Basin [J]. *Pet. Drill. Tech.* 49 (1), 93–100.

Chen, C., Lin, S., and Xiang, D. (2016). Casing Deformation Mechanism and Countermeasures in Changning-Weiyuan Shale Gas Demonstration Area[J]. *Nat. Gas. Ind.* 36 (11), 70–75.

Chen, C., Wang, P., and Xiang, D. (2017). Analysis of Casing Deformation in Changning-Weiyuan Block Based on Focal Mechanism Relationship[J]. *Pet. Drill. Technol.* 45 (4), 110–114.

Chen, C., Xiang, D., Zhang, F., An, M., Yin, Z., Jiang, Z., et al. (2019). Mechanism and Prevention and Control Strategy of Fault Slip and Casing Deformation Caused by Hydraulic Fracturing in Changning-Weiyuan Block, Sichuan[J]. *Petroleum Sci. Bull.* 4 (4), 364–377.

Chen, Y., Liu, D., Cai, Y., Yao, J., et al. (2020). Fracturing Curve and its Corresponding Gas Productivity of Coalbed Methane Wells in the

Zhengzhuang Block, Southern Qinshui Basin, North China[J]. *Energy Explor. Exploitation* 38 (5), 1387–1408.

Cheng, S., Wu, J., Fu, Y., and Zeng, B. (2022). Integrated Dynamic Evaluation of Long Lateral Fracturing in Shale Gas Wells: A Case Study on the Changning National Shale Gas Demonstration Area[J]. *Nat. Gas. Ind.* 42 (2), 123–132.

Daneshy, A. A. "Impact of Off-Balance Fracturing on Borehole Stability and Casing Failure[C]," in SPE Western Regional Meeting.

Fan, Yu, Huang, R., Zeng, B., Chen, C., Zhou, X., Xiang, D., et al. (2020). Fault Slip Induced by Hydraulic Fracturing and Risk Assessment of Casing Deformation in the Sichuan Basin[J]. *Petroleum Sci. Bull.* 03, 366–375. doi:10.3969/j.issn.2096-1693.2020.03.031

Gao, Li, Li, Z., Li, H., Jiang, Z., and He, L. (2021). Study on the Mechanism of Shale Expansion on Casing Deformation in Weirong Field[J]. *Chin. J. Undergr. Space Eng.* 17 (6), 2007–2014.

Gao, L., Liu, Z., Qiao, L., Zhuang, Z., and Yang, H. (2017). Mechanism Analysis and Numerical Simulation of Casing Failure in Hydraulic Fracturing of Shale Gas Formation[J]. *Pet. Mach.* 45 (1), 75–80.

Guo, X., Li, J., Liu, G., Xi, Y., Zeng, Y., He, M., et al. (2019). Numerical Simulation of Casing Deformation during Volume Fracturing of Horizontal Shale Gas Wells. *J. Petroleum Sci. Eng.* 172, 731–742. doi:10.1016/j.petrol.2018.08.0610.1016/j.petrol.2018.08.067

Guo, X., Li, J., Liu, G., Chen, C., Ren, K., and Lai, D. (2018). Research on Casing Deformation for Shale Gas Wells Based on Focal Mechanism[J]. *Fault-Block Oil Gas Field* 25 (5), 665–669.

Hu, J., Zhang, S., Zeng, R., and Liu, Z. (2020). Early Warning Method for Sand Plugging Accidents in Shale Gas Fracturing Based on Deep Leaning[J]. *China Saf. Sci. J.* 30 (9), 108–114.

Hu, Meng, Ge, Hongkui, Fu, Dengwei, and Wang, Xiaoqiong (2020). Numerical Investigation of Casing Shear Deformation Due to Fracture/fault Slip during Hydraulic Fracturing[J]. *Energy Sci. Eng.* 8 (10), 3588–3601.

Li, J., Zhao, C., Liu, G., Zhang, H., Zhang, X., and Ren, K. (2021). Assessment of Fault Slip in Shale Formation during Hydraulic Fracturing and its Influence Factors[J]. *J. China Univ. Petroleum(Edition Nat. Sci.* 45 (2), 63–70. doi:10.3969/j.issn.1673-5005.2021.02.007

Li, X., Gu, C., Feng, Y., and Ding, Z. (2021). Numerical Study of Shear Deformation of Casings during Hydraulic Fracturing Considering Wellbore Loading History. *Petroleum Sci. Bull.* 6 (2), 245–261. doi:10.3969/j.issn.2096-1693.2021.02.019

Lian, W., Li, J., Liu, G., Yan, X., Wu, L., and Chen, L. (2020). Analysis of Casing Stress Difference at Different Positions in Horizontal Segment of Shale Gas Well during Fracturing Process[J]. *Drill. Prod. Technol.* 43 (2), 11–14+1.

Liu, K., Dahi Taleghani, A., and Gao, D. (2020). Semianalytical Model for Fault Slippage Resulting from Partial Pressurization. *SPE J.* 25 (03), 1489–1502. doi:10.2118/199348-pa

Liu, K., Dahi Taleghani, A., and Gao, D. (2019). Calculation of Hydraulic Fracture Induced Stress and Corresponding Fault Slippage in Shale Formation[J]. *Fuel* 254, 115525.1–115525.12. doi:10.1016/j.fuel.2019.05.108

Lu, Q., Liu, Z., Guo, J., He, L., Li, Y., Zeng, Ji, et al. (2021). Hydraulic Fracturing Induced Casing Deformation and a Prediction Model of Casing Deformation [J]. *Petroleum Explor. Dev.* 48 (2), 394–401. doi:10.1016/s1876-3804(21)60037-x

Mainguy, M. (2016). Monitoring Shear Deformations above Compacting High-Pressure High-Temperature Reservoirs with Calliper Surveys. *Int. J. Rock Mech. Min. Sci.* 86, 292–302. doi:10.1016/j.ijrmms.2016.05.007

McClure, M. W., and Horne, R. N. (2011). Investigation of Injection-Induced Seismicity Using a Coupled FLuid FLow and Rate/state Friction Model[J]. *Geophysics* 76 (6), 181–198. doi:10.1190/geo2011-0064.1

Meyer, J. J., Gallop, J., Chen, A., Reynolds, S., Mildren, S., et al. (2018). "Can Seismic Inversion Be Used for Geomechanics? A Casing Deformation Example[C]," in The Unconventional Resources Technology Conference.

Meng, H., Ge, H., Fu, D., and Wang, X. (2020). Numerical Investigation of Casing Shear Deformation Due to Fracture/Fault Slip During Hydraulic Fracturing. *Energy Sci. and Engg.* 8 (10), 3588–3601.

Nolte, K. G., and Smith, M. B. (1981). Interpretation of Fracturing Pressures. *J. Pet. Technol33* 33 (9), 1767–1775. doi:10.2118/8297-PA

Peng, Y., Zhao, J., Sepehrnoori, K., Li, Y., and Li, Z. (2020b). The Influences of Stress Level, Temperature, and Water Content on the Fitted Fractional Orders of Geomaterials. *Mech. Time-Depend Mater* 24 (2), 221–232. doi:10.1007/s11043-019-09417-0

Peng, Y., Zhao, J., Sepehrnoori, K., and Li, Z. (2020a). Fractional Model for Simulating the Viscoelastic Behavior of Artificial Fracture in Shale Gas. *Eng. Fract. Mech.* 228, 106892. doi:10.1016/j.engfracmech.2020.106892

Pirayesh, E., Soliman, M. Y., Rafiee, M., and Jamali, A. (2015). A New Method to Interpret Fracturing Pressure-Application to Frac Pack. *SPE J.* 20 (03), 508–517. doi:10.2118/166132-pa

Qiao, Z., and Ye, C. (2021). Cause Analysis of Casing Deformation in Fracturing of Horizontal Wells in Weirong Deep Shale Gas Field[J]. *Reserv. Eval. Dev.* 11 (2), 89–95. doi:10.13809/j.cnki.cn32-1825/te.2021.02.012

Rutqvist, J., Rinaldi, A. P., Cappa, F., and Moridis, G. J. (2015). Modeling of Fault Activation and Seismicity by Injection Directly into a Fault Zone Associated with Hydraulic Fracturing of Shale-Gas Reservoirs. *J. Petroleum Sci. Eng.* 127, 377–386. doi:10.1016/j.petrol.2015.01.019

Schultz, R., Atkinson, G., Eaton, D. W., Gu, Y. J., and Kao, H. (2018). Hydraulic Fracturing Volume Is Associated with Induced Earthquake Productivity in the Duvernay Play. *Science* 359 (6373), 304–308. doi:10.1126/science.aao0159

Shen, C., Wu, J., Fu, Y., and Zeng, B. (2022). Integrated Dynamic Evaluation of Long Lateral Fracturing in Shale Gas Wells: A Case Study on the Changning National Shale Gas Demonstration Area. *Natural Gas Industry* 42 (2), 123–132.

Sugden, C., Johnson, J., Chambers, M., Gary, R., Suryanarayana, P. V., et al. (2012). Specialconsiderations in the Design Optimization of the Production Casing in High-Rate, Multistage-Fractured Shale Wells[J]. *SPE Drill. Complet.* 27 (4), 459–472. doi:10.2118/151470-pa

Tong, H., Liu, Z., Zhang, H., Zhang, P., Deng, C., Ren, X., et al. (2021a). Theory and Method of Temporary Macrofracture Plugging to Prevent Casing Deformation in Shale Gas Horizontal Wells[J]. *Nat. Gas. Ind.* 41 (5), 92–100. doi:10.3787/j.issn.1000-0976.2021.05.010

Tong, H., Zhang, P., Zhang, H., Liu, Z., Ren, X., Xiao, K., et al. (2021b). Geomechanical Mechanisms and Prevention Countermeasures of Casing Deformation in Shale Gas Horizontal Wells[J]. *Nat. Gas. Ind.* 41 (1), 189–197. doi:10.3787/j.issn.1000-0976.2021.01.017

Xi, Y., Li, G., Zeng, Y., and Li, J. (2019). Overview of Casing Deformation in Multistage Fracturing of Shale Gas Horizontal Wells. *Special Oil and Gas Reservoirs* 26 (1), 1–6.

Yan, X., Li, J., Liu, G., Zeng, Y., and Li, J. (2019). Overview of Casing Deformation in Multistage Fracturing of Shale Gas Horizontal Wells[J]. *Special Oil Gas Reservoirs* 26 (1), 1–6.

Yin, F., Deng, Y., He, Y., Gao, D., and Hou, B. (2018a). Mechanical Behavior of Casing Crossing Slip Formation in Waterflooding Oilfields. *J. Petroleum Sci. Eng.* 167, 796–802. doi:10.1016/j.petrol.2017.12.069

Yin, F., Han, L., Yang, S., Deng, Y., He, Y., and Wu, X. (2018c). Casing Deformation from Fracture Slip in Hydraulic Fracturing. *J. Petroleum Sci. Eng.* 166, 235–241. doi:10.1016/j.petrol.2018.03.010

Yin, F., Xiao, Y., Han, L., and Wu, X. (2018b). Quantifying the Induced Fracture Slip and Casing Deformation in Hydraulically Fracturing Shale Gas Wells. *J. Nat. Gas Sci. Eng.* 60, 103–111. doi:10.1016/j.jngse.2018.10.005

Yu, H., Lian, Z., and Lin, T. (2014). Finite Element Analysis of Failure Mechanism of Casing during Shale Gas Fracturing[J]. *China Pet. Mach.* 42 (8), 84–88+93.

Zhang, F., Jiang, Z., Chen, Z., Yin, Z., and Tang, J. (2020a). Hydraulic Fracturing Induced Fault Slip and Casing Shear in Sichuan Basin: A Multi-Scale Numerical Investigation. *J. Petroleum Sci. Eng.* 195, 107797. doi:10.1016/j.petrol.2020.107797

Zhang, F., Yin, Z., Chen, Z., Maxwell, S., Zhang, L., and Wu, Y. (2020b). Fault Reactivation and Induced Seismicity during Multistage Hydraulic Fracturing: Microseismic Analysis and Geomechanical Modeling. *SPE J.* 25 (02), 692–711. doi:10.2118/199883-pa

Zhang, P., He, Y., Liu, Z., Tong, H., Deng, C., Ren, X., et al. (2021). Shear Compression Deformation Test and Deformation Prevention Practice of Casing in Shale Gas Horizontal Wells[J]. *Nat. Gas. Ind.* 41 (5), 84–91. doi:10.3787/j.issn.1000-0976.2021.05.009

Zhang, W., Fan, H., Zha, Y., Chen, Z., and Lubin, Z. (2015). A Recommended Calculating Method for Casing Bending Force after Large Scale Volume Fracturing[J]. *China Pet. Mach.* 43 (12), 29–32.

Zhang, X., Li, J., He, L., Qiao, Z., and Zhang, D. (2021b). Optimization of Fracturing Cluster Spacing in Shale Gas Wells Based on Casing Protection [J]. *China Pet. Mach.* 49 (12), 105–112.

Zhang, X., Li, J., Zhang, H., Sun, X., Deng, T., Yao, Y., et al. (2021a). Analysis on Casing Deformation Failure in Deep Shale Gas Wells in Weirong Shale Gas Play [J]. *Drill. Prod. Technol.* 44 (1), 23–27.

Zhang, X., Zhang, L., and Hu, J. (2018). Real-time Diagnosis and Alarm of Down-Hole Incidents in the Shale-Gas Well Fracturing Process. *Process Saf. Environ. Prot.* 116, 243–253. doi:10.1016/j.psep.2018.02.011

Zhao, J., Fu, Y., Wang, Z., Song, Y., Ren, L., Lin, R., et al. (2022). Study on Diagnosis Model of Shale Gas Fracture Network Fracturing Operation Pressure Curves[J]. *Nat. Gas. Ind.* 42 (2), 11–19.

Zhuang, D., Wang, Y., Tao, C., and Yan, C. (2019). Response Relation between Fracturing Curve and Reservoir Pollution Degree of Coalbed Methane Wells[J]. *Coal Geol. Explor.* 47 (1), 96–100.

Conflict of Interest: SC, ZB, WJ, SY, GX, ZX, and LJ were employed by CNPC Southwest Oil and Gas Field Company.

frontiers | Frontiers in Energy Research

TYPE Original Research
PUBLISHED 10 August 2022
DOI 10.3389/fenrg.2022.974655

OPEN ACCESS

EDITED BY
Yu Peng,
Southwest Petroleum University, China

REVIEWED BY
Haiyan Zhu,
Chengdu University of Technology, China
Zhenglan Li,
Southwest Petroleum University, China

*CORRESPONDENCE
Dongyu Fu,
swpufudongyu@hotmail.com

SPECIALTY SECTION
This article was submitted to Advanced Clean Fuel Technologies, a section of the journal Frontiers in Energy Research

RECEIVED 21 June 2022
ACCEPTED 18 July 2022
PUBLISHED 10 August 2022

CITATION
Guo T, Fu D, Xiong L and Wang Y (2022), The investigation of microporous structure and fluid distribution mechanism in tight sandstone gas reservoirs: A case study on the second member of Xujiahe gas reservoirs in Yuanba area.
Front. Energy Res. 10:974655.
doi: 10.3389/fenrg.2022.974655

The investigation of microporous structure and fluid distribution mechanism in tight sandstone gas reservoirs: A case study on the second member of Xujiahe gas reservoirs in Yuanba area

Tonglou Guo[1], Dongyu Fu[2]*, Liang Xiong[2] and Yongfei Wang[2]

[1]Southwest Oil and Gas Company, SINOPEC, Chengdu, China, [2]Exploration and Development Research Institute, Southwest Oil and Gas Company, SINOPEC, Chengdu, China

Tight sandstone reservoir is characterized by ultra-low porosity, complex microporous structure and water residues, which shows different gas storage and transport mechanism from conventional reservoirs. Therefore, effective development of tight sandstone gas reservoirs is faced with technical challenges. Microporous structures, distribution mechanism of fluid is a basic issue in gas reservoir evaluation. In this work, we take gas reservoir in the 2nd member of Xujiahe Formation in Yuanba area as an example to analyze the microscopic feature of pore structure and fluid distribution. The three-dimensional digital core has been applied to represent the real microporous structure. Specifically, a digital core reconstruction method based on SEM and casting slice images has been proposed. Ultimately, the mechanism of distribution, mode of occurrence of water residues in tight sandstone reservoirs has been simulated and quantitatively analyzed. The results show that the water residues could been visualized and categorized into three modes, water mass in corner, water film on surface, and water column in throat. The water residues could cause dramatic influence on pore structures, active pore size could be decreased with rising residual water saturation, the magnitude falls by over 50%. In addition, grain size would affect the distribution of water residues, which shows different percentage in medium and fine sand. Pore connectivity is another characteristic factor to describe the microporous structures. In this study, cluster marking algorithm has been applied to obtain the pore connectivity in tight sandstone with different grain size. In medium sand, the pore connectivity is dramatically decreased with rising water saturation, the downward trend become slower when water saturation reaches to 60%. Compared to fine sand, the tendency variation appears when water saturation reaches to 40%. This paper provides an applicable method to reveal the micro-scale reservoir properties and fluid distribution mechanisms in tight sandstone gas reservoirs.

KEYWORDS

tight sandstone gas reservoirs, digital core reconstruction, sandstone grain size, microporous structure, water residues

Introduction

China has large amount of unconventional oil and gas resources represented by tight gas, shale oil and gas reservoirs. In recent years, with the continuously in-depth oil & gas exploration and development, the unconventional resources have become increasingly important in China's petroleum industry system (Tong et al., 2018; Zou et al., 2018; Li et al., 2019a; Ji et al., 2019; Jiao, 2019; Li et al., 2020). After the successful development of marine reef and shoal facies reservoirs in Yuanba area of northeastern Sichuan, the tight sandstone gas reservoirs of the upper triassic Xujiahe formation also showed a great potential of resource (Zhang et al., 2016; Long et al., 2020). Different from the conventional gas reservoirs, the tight sandstone gas reservoirs in Yuanba area are characterized by ultra-low porosity and permeability, complex porous structures and high initial water saturation resulting from complicated sedimentation and diagenesis (Guo, 2013), which brings challenges to the efficient development of the gas reservoirs. Matrix pores are the main fluid storage and transport space, the microstructures and physical properties directly affect the gas productivity (Li et al., 2019b). Therefore, it is necessary to study the micro pore structures and fluid distribution mechanisms of tight sandstone gas reservoir to clarify the influence on gas storage and flow.

The microporous structure is an umbrella term for pore throat distribution, size, morphology, connectivity and configuration (Qiao et al., 2019; Song et al., 2019; Zhu et al., 2019). These parameters are usually obtained by scanning electron microscopy (SEM), Nano/Micro-CT imaging, mercury injection, nitrogen adsorption and other experimental methods (Guo et al., 2018; Sui et al., 2018; Gou et al., 2019; Viktorovich et al., 2021). Micro/nano pores and fractures have been well developed and serious heterogeneity has been noticed in the tight sandstone reservoirs of the 2nd member of Xujiahe formation in Yuanba area. Consequently, the detailed investigation of the tight gas reservoirs was limited by the quality of coring and the experiment cost in present technical condition. The accurate characterization of microscopic pore structure and research of fluid distribution mechanism has been faced with technical challenges. As an emerging numerical simulation technique, digital core technology was featured by low requirements for core samples, adjustable parameters and repeatable experiment, leading to the large-scale application in research of unconventional reservoirs. H.K. Hasnan et al. (2020) applied X-ray Mico-CT scanner to obtain the microstructure of the sandstone layers at millimeter-to-centimeter scale, and digital core has been constructed to estimate the reservoir propertied and characterize the connectivity of sandstone layers in cooperation with core plug data. Lv et al. (2019) established the nanoscale 3-D pore network model considering the stress sensitivity by Scanning Electron Microscopy and nano-CT scanning. Sui et al. (2020) simplified the real pore structure to prolate ellipsoids, oblate ellipsoids and spheroids, and an elliptical-pore model of digital core has been proposed. To sum up, the method of pore structure characterization using digital core technology can be divided into two categories, experimental test method and numerical reconstruction method. The experimental testing method is to scan and observe the real core through physical experiment and get the digital core directly. Although this kind of method can get the real structure of core, the modeling quality is limited by the core quality and resolution of experimental equipment. The numerical reconstruction method can be achieved based on a small amount of real core information. Besides, this method showed strong repeatability, the reconstruction process can be modified whenever necessary.

In this paper, a modified numerical reconstruction method of digital core has been proposed. On the basis of SEM images in the second member of Yuanba Xujiahe gas reservoir, a digital tight sandstone core with micro pore structure and natural microfractures has been reconstructed. Furthermore, the digital core model has been verified by using some experimental data. In second part, the reconstructed digital core would be applied to quantitatively investigate the pore structure and physical properties of the reservoir fluid. In this study, a new insight for the microporous structure and reservoir fluid distribution mechanism of tight sandstone reservoir has been proposed which might provide theoretical support for the effective development of Xujiahe formation gas reservoir in Yuanba area.

Methods

In this study, a low-cost digital reconstruction method has been proposed. According to the method, we only used the SEM and casting slice images to obtain the structural properties. Firstly, the core samples acquired during drilling was evaluated by means of scanning electron microscopy. And the rock debris has been collected to make casting slice. Secondly, the SEM and casting slice images has been numerically analyzed to obtain the statistical characterization of the multi-scale porous structure. Thirdly, a modified model has been deduced to reconstruct the digital core based on the data from the second step.

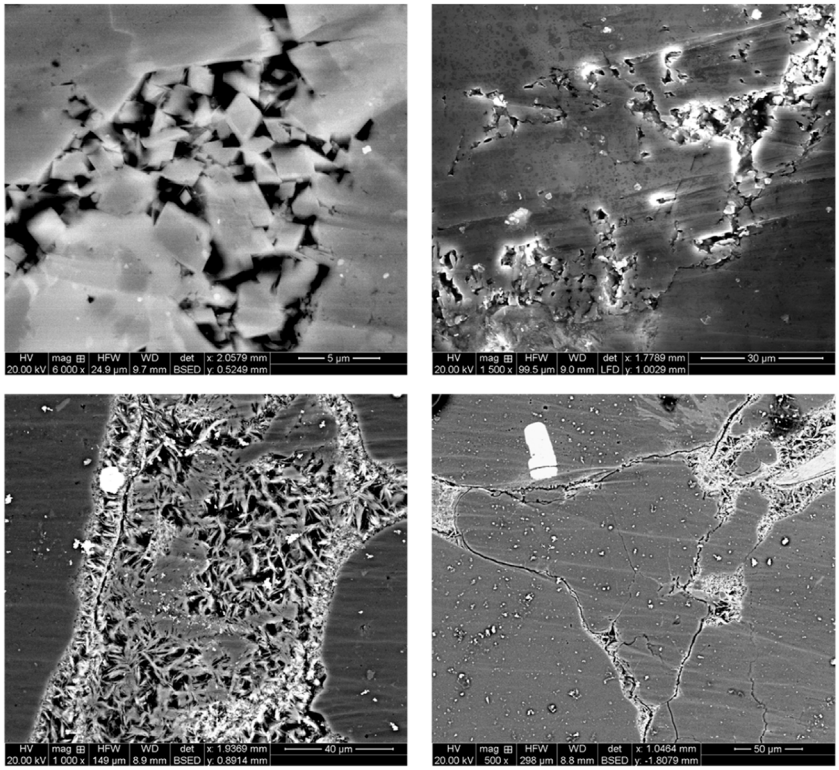

FIGURE 1
The SEM images of the second member of Yuanba Xujiahe gas reservoir.

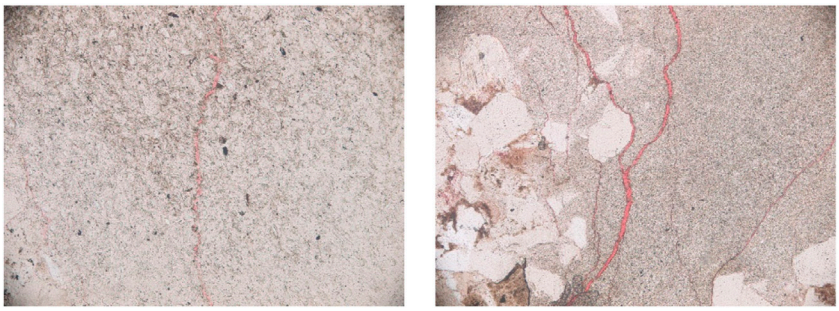

FIGURE 2
The casting slice images of rock debris from the second member of Yuanba Xujiahe gas reservoir.

Digital core reconstruction

To obtain the applicable information in the SEM and casting slice images, the images should be pretreated. The SEM images and casting slice images was displayed in Figure 1, Figure 2, respectively. Due to the different resolution, we use SEM images to obtain microporous structure of nano/microscale pores. And the casting slice images could be used to obtain the microfractures. Then, the numeralization process has been proposed to make connections between real pore structures and digital core models. As shown in Figure 3, it can be divided into three main steps. In step 1, the greyscale images

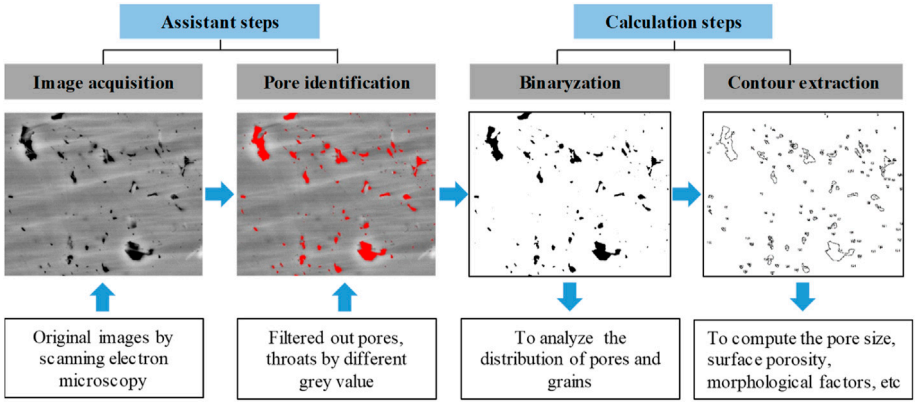

FIGURE 3
The workflow for numeralization process of core images (take SEM images as an example).

have been manipulated by OTSU method to identify the pores and matrix (Ostu, 1979). In step 2, choose the optimized threshold value to binarize those images. In step 3, to extract the pore contours and count. Finally, we could obtain these parameters, the distribution of pores and throats, pore size, surface porosity and morphological factors, etc.

In this study, the Pearson coefficient was applied to quantitatively characterize the statistical distribution of congeners in porous media (Zhao et al., 2018). Pearson coefficient can be calculated by Eq. 1.

$$P_{Rz(x)z(x+h)} = \frac{\mathrm{cov}[z(x), z(x+h)]}{\sqrt{\mathrm{D}[z(x)]} \cdot \sqrt{\mathrm{D}[z(x+h)]}} \quad (1)$$

Among them:

$z(x)$-the definition of the particles in binarized images, dimensionless.

cov $[z(x), z(x+h)]$- the spatial covariance of $z(x)$ and $z(x+h)$, dimensionless.

D $[z(x)]$, D $[z(x+h)]$-the spatial variance of $z(x)$ and $z(x+h)$, respectively, dimensionless.

In this work, the definition of Pearson coefficient can be simplified. According to Shen et al. (2015), the Pearson coefficient in 0–1 matrix could be obtained by Eq. 2.

$$P_{Rz(x)z(x+h)} = \frac{\mathrm{E}[z(x)z(x+h)] - \phi^2}{\phi - \phi^2} \quad (2)$$

Amang them:

E $[z(x)\, z(x+h)]$- mathematical expectation of $z(x)$, $z(x+h)$, dimensionless.

ϕ-porosity, dimensionless.

The Pearson coefficient of core samples has been obtained by using the procedures displayed in Figure 3. Firstly, pores could be identified by analyzing grey values of SEM images in assistant steps, then pore area has been remarked for the next steps. The following step is calculation step, including binaryzation and contour extraction. In the step of binaryzation, OSTU method has been applied to get pores and throats, so that the distribution of pores and grains could be analyzed. In step of contour extraction, the contour of pores and throats has been extracted for calculating the pore size, morphology factor, etc. After finishing all the procedures in Figure 3, the Pearson coefficient can be calculated. In this study, all the calculation steps has beem programmed, and results are displayed in Figure 4. As shown in Figure 4, all the Pearson coefficient shared a same distribution pattern. The magnitude of Pearson coefficient decreased with the rising h, and the reduction rate changed in descending order from 1 to maximum mesh grids. At

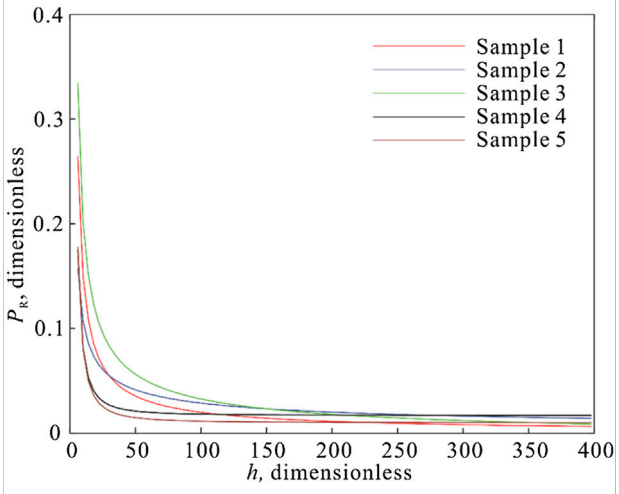

FIGURE 4
The magnitude of Pearson coefficient of core samples.

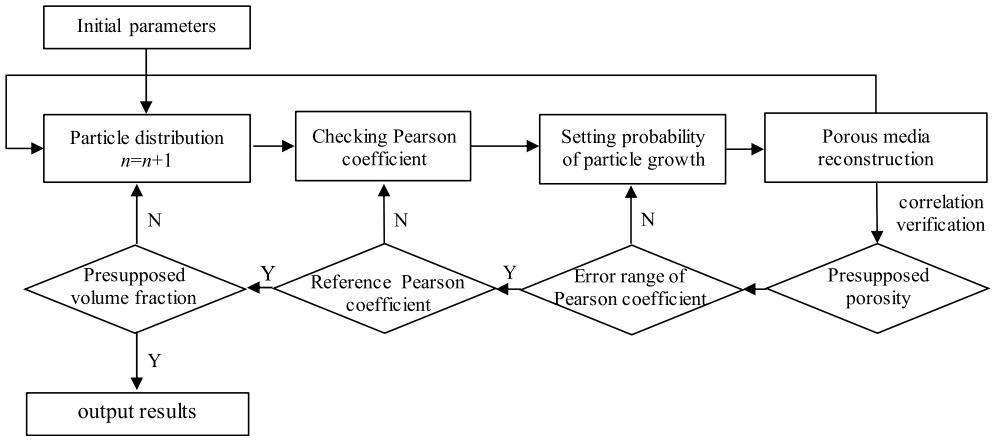

FIGURE 5
The flowcharts of digital core reconstruction.

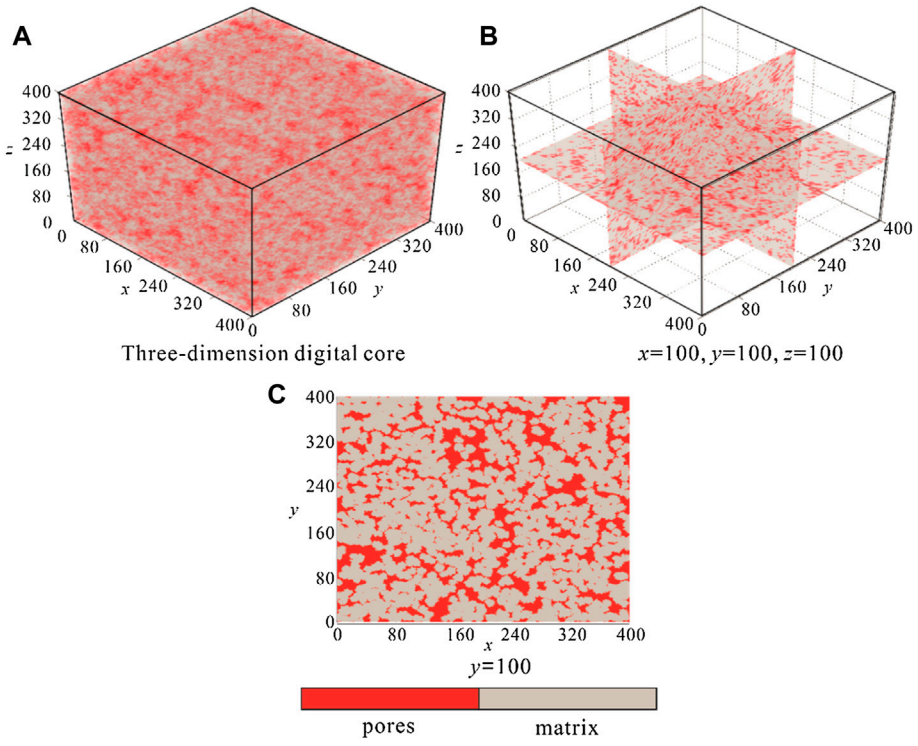

FIGURE 6
The three-dimensional reconstructed digital core by modified model **(A)**; The slices (x, y, z = 100, respectively) of the three-dimensional reconstructed digital core **(B)**; an exemplary profile map (y = 100) of the three-dimensional reconstructed digital core **(C)**.

this point, the relationship between real pore structures and digital core has been established, which was the important preparatory step for digital core reconstruction.

A specific numerical model has been applied to perform the digital core reconstruction after the preparatory step. In this study, we choose quartet structure generation set (QSGS) model

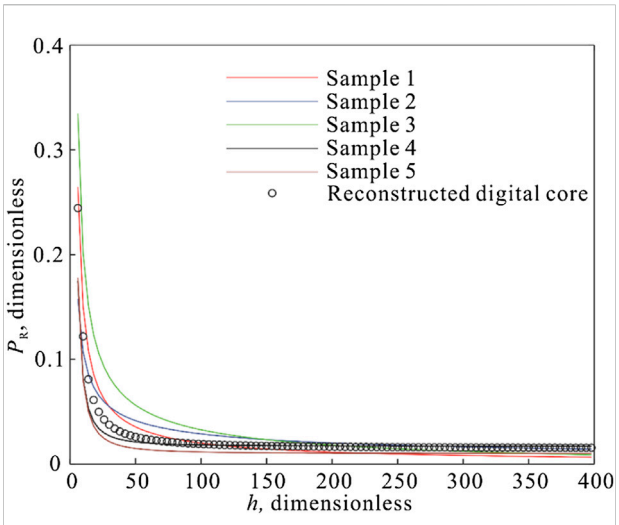

FIGURE 7
Comparison of Pearson coefficient of two grid points between reconstructed digital cores and core samples.

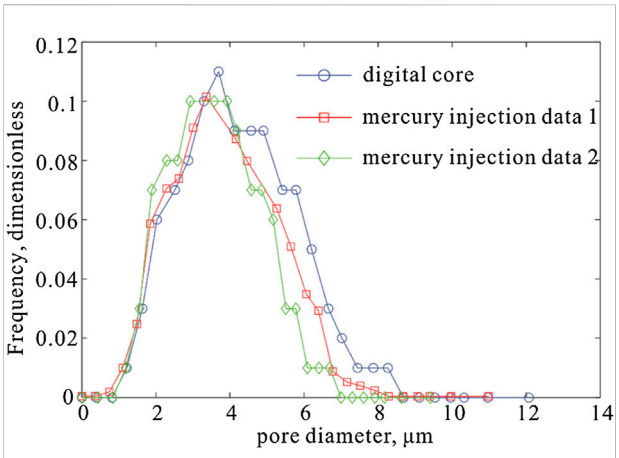

FIGURE 8
Comparison of pore diameter between reconstructed digital core and mercury injection data.

to reconstruct digital cores (Wang et al., 2007). In this model, the porous media reconstruction can be performed by four parameters, probability of growth phase distribution P_{cd}, probability of particle growth P_{di}, probability density $I_i^{m,n}$ and porosity φ. However, the traditional QSGS model cannot control the randomness during modeling, which may cause large deviation from the real reservoir characteristics. Therefore, this model should be modified to control the randomness in order to ensuring the representativeness of reconstructed digital cores.

In this work, referring to Shen et al. (2015), a modified numerical model has been deduced by designing constraints for the modeling process. There has been two differentia compared to Shen's model. Firstly, two parameters are set to control the modeling process, including Pearson coefficient and morphology factor. Secondly, the Constraint procedures has been upgraded from two steps to several necessary steps. In this modified model, Pearson coefficient is used to control the particle distribution, morphology factor is used to control the pore-throats shape. Pearson coefficient and morphology factor could be obtained by Eqs 2, 3, respectively.

$$F = \frac{4\pi S}{c^2} \tag{3}$$

Among them:

S-pore area, m^2.

c-pore perimeter, m.

Specifically, the procedures of digital core reconstruction in this model are displayed in Figure 5. In the process, we set Pearson coefficient and morphology factor at two particles as objective function in each calculation step, the reference values are obtained by the analysis of core images. Moreover, the cut-and-try procedure has been used to guarantee against unacceptable deviation. Finally, the spacing h should be constantly increased until arriving the presupposed volume fraction. In summary, a modified digital core reconstruction model with multi-stage constrains. As shown in Figure 6, the digital core has been reconstructed with the $400 \times 400 \times 400$ grid.

Validation

After reconstruction process, it is necessary to validate the accuracy of reconstructed digital core to ensure that it can effectively characterize the real microscopic pore-throat structure of the second member of Xujiahe reservoir in Yuanba area. In this work, we used two factors to validate the reconstructed digital core, including the spatial distribution of pores and the pore size. Firstly, the comparison of Pearson coefficient of two grid points between reconstructed digital cores and core samples has been displayed in Figure 7. In Figure 7, the Pearson coefficient in digital core is in good agreement with it in core samples, the maximum deviation is less than 5%.

In this study, the pore size of core samples has been obtained by mercury injection experiment. And the magnitude of pore size in reconstructed digital core can be calculated by mathematical method called thirteen-directional average distance algorithm. As shown in Eq. 4, the pore size can be obtained by counting the distance among homogeneous grids in digital core.

$$d(x_0, y_0, z_0) = \frac{1}{13}\left(\sum_{i=1}^{6} N_i + \sqrt{2}\sum_{i=7}^{18} N_i + \sqrt{3}\sum_{i=19}^{26} N_i\right) \tag{4}$$

Among them,

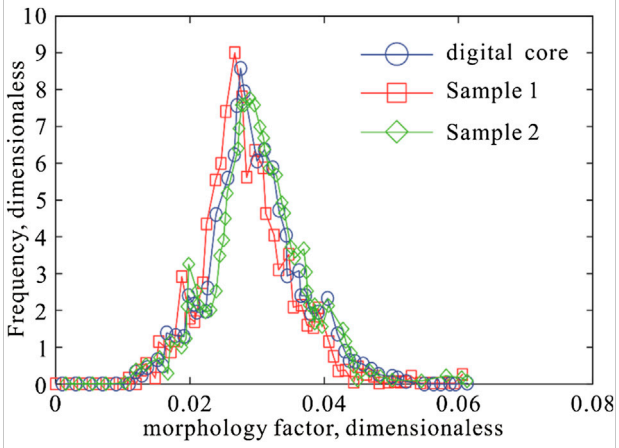

FIGURE 9
Comparison of pore diameter between reconstructed digital core and core samples.

d (x_0, y_0, z_0)-The average diameter of pores in digital core, μm;

N_i-The distance of a grid in pore space from the nearest matrix, μm.

The calculated magnitude of pore size of digital core and mercury injection data has been shown in Figure 8. It is found that the pore size of digital core shares the similar distribution pattern with mercury injection data. Specifically, the pore size of reconstructed digital core distributes mainly in 2–8.5 μm. Besides, the morphology features of reconstructed digital core has been testified. As shown in Figure 9, the morphology fators between digital core and core samples has been compared. Noteworthily, the only 3D CT results has been used to obtain the morphology factor of the core samples. The different morohology factor curves shows the similar distribution tendency, and the relative error value is less than 4.7%. Therefore, the reconstructed digital core is able to represent morphology features of the real cores.

In summary, according to the three-factor validation, the validity of our digital core model has been confirmed. That is to say, the reconstructed digital cores are applicable to characterize the real microporous structures in our target sandstone gas reservoirs.

Results and discussion

Pores and throats are the main space for formation fluid to store and transport. Consequently, pore structures and physical properties have a direct effect on gas productivity. In this section, the reconstructed digital cores would be applied to investigate the microporous structure and fluid distribution mechanism in tight sandstone reservoirs.

The mode of water storage in tight sandstone gas reservoirs

The water phase in gas reservoirs can be categorized to two types, mobile water and residual water (Zhong et al., 2020). The mobile water is a kind of liquid phase which could be driven to flow under certain conditions. The driving force can be the pressure difference, capillary force, etc. Correspondingly, residual water is not able to transport in any reservoir conditions, leading to the strong impacts on active porosity and pore-throat connectivity. According to the well logging data, the residual water saturation in 2nd member of Xujiahe reservoir in Yuanba area reaches up to 60%–80%, which poses great challenges to the further exploration and exploitation. Therefore, to quantitatively investigate the existing state of

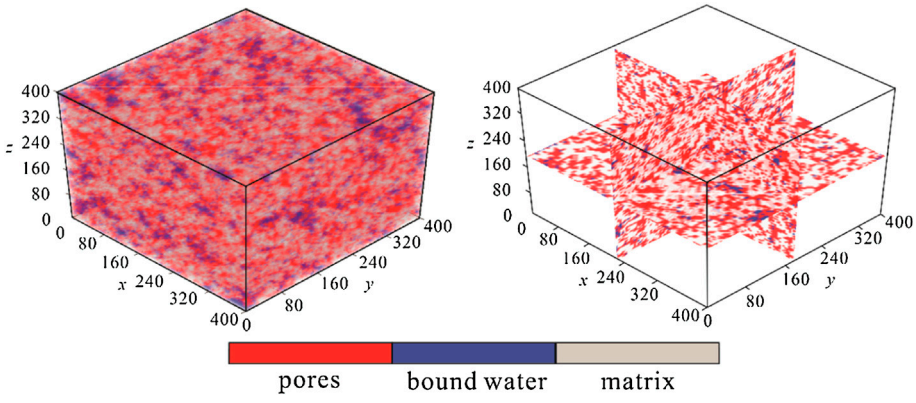

FIGURE 10
Reconstructed digital core considering residual water (residual water saturation is 45%).

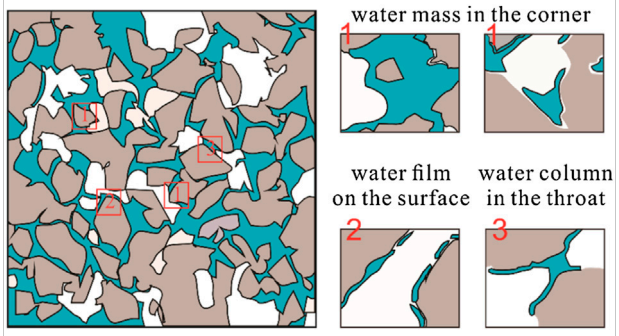

FIGURE 11
The schematic diagram of different category of residual water(revived according to He et al., 2020).

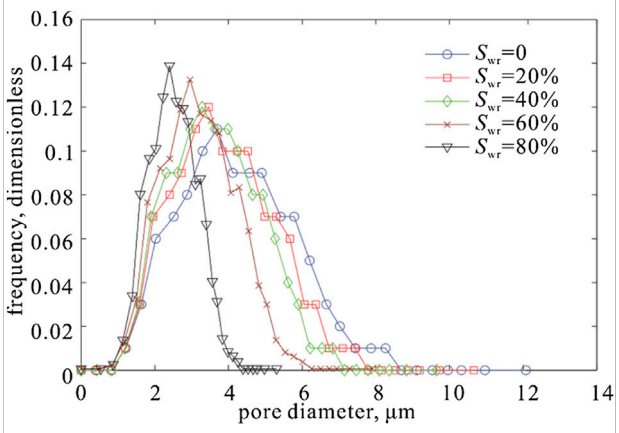

FIGURE 12
The distribution of pore size with different residual water saturation.

residual water and analyze the influences on pore-throat structure plays a key role in reservoir evaluation.

In this work, residual water would be located in digital cores referring to the core concepts of QSGS model. Initially, all grids in digital core would be traversed and checked, the void area could be found out. Secondly, the growing particles of water phase would be set in void area. Significantly, the solid boundary should be set as the stop point of growing step in the procedure code. Once arriving the presupposed saturation, the reconstructed digital core considering residual water could be carried out. As shown in Figure 10, the presupposed residual water saturation is 45%, and water phase randomly distributes in the pores and throats.

To be more specific, the residual water can be classified to three categories by different mode of occurrence: water mass in corner, water film on surface, and water column in throat. As shown in Figure 11, the schematic diagram of different category of residual water has been displayed. Water mass in corner is a kind of water phase has stuck in blind holes or the corner of pores; Water phase distributes along the surface of pores and fractures, this kind of water has been named water film on surface; In addition, the water transports from large channels to smaller channels, it may stuck in the joint and gradually accumulated. The typical example in gas reservoir is that water phase flows through the pore-throat, so it can be called water column in throat.

Different categories of residual water shows different mechanism. The amount of water mass in corner is mainly controlled by the surface tension, and pore morphology could be another important controlling factor. According to Hou et al. (He et al., 2020), the empirical equation of capillary force considering pore morphology can be obtained by Eq. 5. It indicated that pore morphology could pose impacts on capillary force, leading to the increasing water saturation. In our target reservoir, the morphology factor is 0.43, which means water phase could easily stuck in the intergranular-intercrystalline pores.

$$R = \frac{2\gamma \cos\theta}{rF} \tag{5}$$

Among them,

r-The pore-throat radius, m;

F-The morphology factor, which can be calculated by Eq. 3, dimensionless;

γ-The fluid surface tension, N/m;

θ-The fluid contact angle, °.

As for water film on surface, the key mechanism is surface tension and adsorption. The capillary force is the dominant factor controlling the amount of water column in pore throat. In accumulation process, capillary force is regard as resistance to limit the gas alternating water (GAW). As shown in Eq. 5, the blocking effect could be increasingly serious with declining pore-throat radius. In fact, this phenomenon is known as Jamin effect.

Sensitive analysis

By the study above, it is cleared that residual water plays an important role on the pore-throats structure. In this part, the sensitive analysis has been performed to quantitatively investigate the influence of residual water on the pore structure.

Firstly, in order to reveal the pore size changes under different water saturation, the distribution of pore size with rising residual water saturation has been displayed in Figure 12. According to the tendency of pore size distribution shown in Figure 11, the active pore size decreases with rising residual water saturation, and the declining rate is growing. Statistically speaking, the

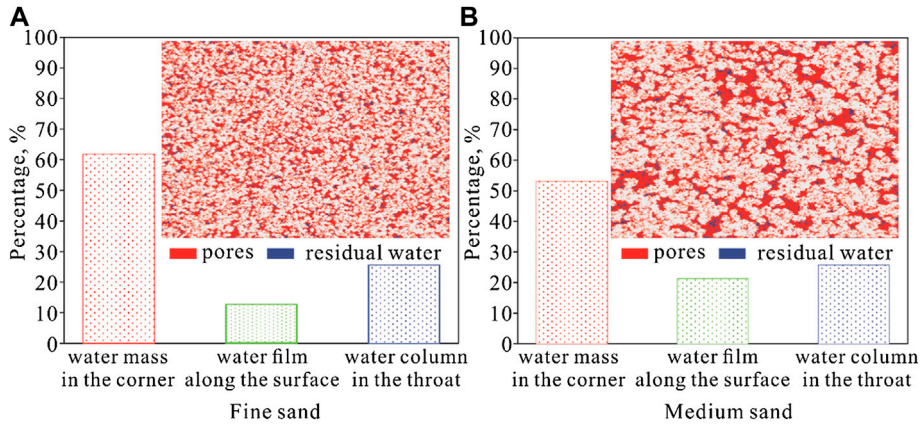

FIGURE 13
The percentage of various residual water in sandstones of different grain sizes **(A)** shows the percentage of various residual water in fine sand; **(B)** shows the percentage of various residual water in medium sand.

magnitude of pore diameter ranges from 2 to 8.5 μm, the peak value is around 4.5 μm without considering residual water. In case that residual water saturation rises up to 80%, the magnitude of pore size reduces to 1.5–3.5 μm, which falls by over 50%. Secondly, we analyzed the percentage of different categories of residual water under given water saturation. Noteworthy, as for tight sand stone, varying grain size would have different pore-throat structures (Qi et al., 2021). In 2nd member of Xujiahe reservoir, the main lithology is defined as fine sand and medium sand. The percentage of different categories of residual water in fine and medium sands has been shown in Figure 13. According to this figure, in both of fine and medium sand, water mass in corner takes up the largest proportion, then water column in throat, water film on surface in descending order. It is noticeable that the percentage of all water residues has been changed with different grain size. The proportion of water mass in corner shows a decline trend compared between fine sand and medium sand. This phenomenon is resulting from the abundant blind holes and irregular pores in sand with smaller grain size. With rising grain size, the surface area of pore-throats is gradually increased. As a result, the water phase is more likely to adsorbed along the pore-throat surface. Compare to another water residue, the percentage of water column in throat changes little with the increasing grain size. The reason is that the variation of grain size cannot cause significant changes of pore-throat diameter. That is to say, the proportion of water column in throat remains almost the same.

Pore connectivity is another important parameter affecting reservoir development. In fact, only the interconnected pores have a contribute to the gas transport. To count the magnitude of interconnected pores and obtain

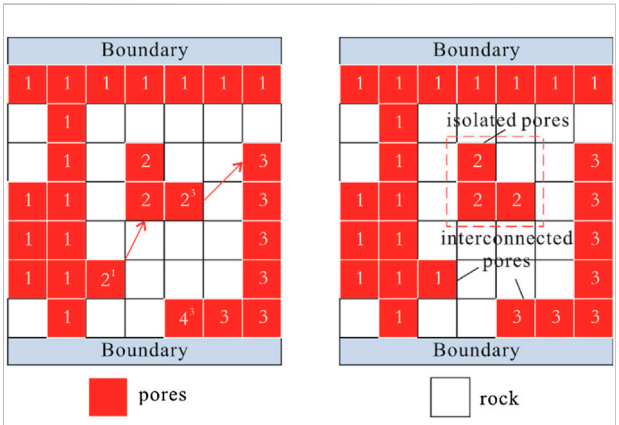

FIGURE 14
The schematic diagram of pore connectivity evaluation.

effective porosity is essential for the reservoir evaluation. In this study, we put emphasis on the variation trend of pore connectivity caused by residual water. The throat-to-pore coordination number has been applied to represent the degree of pore connectivity. In our digital core, cluster marking algorithm has been adopted to count the interconnected pores. The specific implementary procedures are shown in Figure 14. Firstly, all the grids in pore space would be coded sequentially. Once the adjacent grid changed in three-dimensional space, the coding procedure would be terminated, and then the new round of coding would start. Secondly, the isolated pores would be marked particularly. According to this method, the throat-to-pore coordination number of 2nd member of Xujiahe reservoir in Yuanba area ranges from 0 to 17, average value is 4.14.

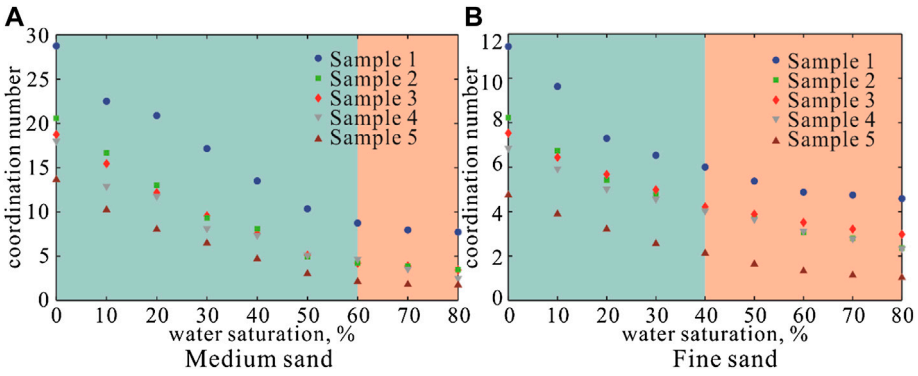

FIGURE 15
The variation of pore connectivity with increasing water saturation in sandstones of different grain sizes **(A)** shows the variation of pore connectivity with increasing water saturation in medium sand; **(B)** shows the variation of pore connectivity with increasing water saturation in fine sand.

Furthermore, some interconnected pores would become clogging and even completely blocked by the residual water. As a result, the pore connectivity would be decreased to some degree. In this study, the variation of pore connectivity with changing water saturation in fine and medium sand has been analyzed. Figure 15 shows the variation of throat-to-pore coordination number with different residual water saturation. Specifically, the influence of grain size has been analyzed. In medium sand, the pore connectivity is dramatically decreased with rising water saturation. However, the downward trend become slower when water saturation reached to 60%. In fine sand, the curve shares almost the same trend with it in medium sand. But the tendency variation appears when water saturation reached to 45%. The results show that the influence of pore connectivity caused by residual water is more significant in fine sand.

Conclusions

In this study, a novel method to investigate microporous structure and fluid distribution has been proposed. Based on SEM and casting slice images of real cores, the traditional digital core reconstruction method has been modified by combining image processing techniques and geostatistics. Compared to the traditional algorithm, the proposed method can effectively avoid the randomness and increase the accuracy of simulation. Besides, aiming at the exploration and development of gas reservoir in 2nd member of Xujiahe reservoir in Yuanba area, the distribution of residual water has been visualized and categorized by simulating in the reconstructed digital core. Moreover, the influence on microporous structure caused by residual water has been quantificationally analyzed. Digital cores reconstructed by our method shared the similar statistical law with real reservoir characteristics, and the microporous structure could be precisely obtained. Based on the mode of residual water occurrence, residual water in 2nd member of Xujiahe reservoir could be divided into three categories, water mass in corner, water film on surface, and water column in throat. In both of fine and medium sand, water mass in corner takes up the largest proportion, then water column in throat, water film on surface in descending order. According to sensitive analysis, the active pore size decreased with rising residual water saturation, and the declining rate is growing. In case that residual water saturation raised up to 80%, the magnitude of pore size fell by over 50%. Varying grain size would have great influence on water residues, the percentage of water residues showed different features in medium and fine sand. Pore connectivity is another important parameter affecting reservoir development. In medium sand, the pore connectivity is dramatically decreased with rising water saturation, the downward trend become slower when water saturation reached to 60%. In comparison of fine sand, the variation curve shared almost the same trend with medium sand, but the tendency variation appeared when water saturation reached to 40%. This study provided an applicable method to reveal the micro-scale reservoir properties and fluid distribution mechanisms in tight sandstone gas reservoirs.

Data availability statement

The original contributions presented in the study are included in the article/supplementary material, further inquiries can be directed to the corresponding author.

Author contributions

TG: Conception and design of our study, Project administration, Supervision. DF: Methodoloty, Writting original Draft, Data curation, Validation. LX: Formal analysis, Coding, Software. YW: Data Curation, Review and Editing.

Funding

This study is supported by Sinopec. Specifically, the Sinopec Pilot Program Potential Evaluation of Xujiahe Formation Gas Reservoir in Northeast Sichuan (YTBXD-QTKF-2022-001-001).

Conflict of interest

TG, DF, LX, and YW were employed by the company Southwest Oil and Gas Company, SINOPEC.

Publisher's note

All claims expressed in this article are solely those of the authors and do not necessarily represent those of their affiliated organizations, or those of the publisher, the editors and the reviewers. Any product that may be evaluated in this article, or claim that may be made by its manufacturer, is not guaranteed or endorsed by the publisher.

References

Gou, Q., Shang, X., Fang, H., Feng, Y., Zhang, B., Shu, Z., et al. (2019). Full-scale pores and micro-fractures characterization using FE-SEM, gas adsorption, nano-CT and micro-CT: A case study of the silurian longmaxi formation shale in the fuling area, sichuan basin, China. *Fuel* 253 (1), 167–179. doi:10.1016/j.fuel.2019.04.116

Guo, J., Li, Y., and Wang, S. (2018). Adsorption damage and control measures of slick-water fracturing fluid in shale reservoirs. *Petroleum Explor. Dev.* 45 (2), 320–325. doi:10.11698/PED.2018.02.15

Guo, T. (2013). Key controls on accumulation and high production of large non-marine gas fields in northern Sichuan Basin. *Petroleum Explor. Dev.* 40 (2), 150–160. doi:10.1016/s1876-3804(13)60018-x

Hasnan, H. K., Hassan, M., Wan, H. A., and Abdullah, W. H. (2020). Digital core analysis: Characterizing reservoir quality through thin sandstone layers in heterolithic rocks. *J. Appl. Geophys.* 182 (1), 104178. doi:10.1016/j.jappgeo.2020.104178

He, B., He, J., Zou, H., Lao, T., and Bi, E. (2020). Pore-scale identification of residual morphology and genetic mechanisms of nano emulsified vegetable oil in porous media using 3D X-ray microtomography. *Sci. Total Environ.* 763 (1), 143015. doi:10.1016/j.scitotenv.2020.143015

Ji, G., Jia, A., Meng, D., Guo, Z., Wang, G., Cheng, L., et al. (2019). Technical strategies for effective development and gas recovery enhancement of a large tight gas field: A case study of sulige gas field, ordos basin, NW China. *Petroleum Explor. Dev.* 46 (3), 602–612. doi:10.11698/PED.2019.03.19

Jiao, F. (2019). Re-recognition of "unconventional" in unconventional oil and gas. *Petroleum Explor. Dev.* 46 (5), 803–810. doi:10.1016/S1876-3804(19)60244-2

Li, T., Li, M., Jing, X., Xiao, W., and Cui, Q. (2019). Influence mechanism of pore-scale anisotropy and pore distribution heterogeneity on permeability of porous media. *Petroleum Explor. Dev.* 46 (3), 569–579. doi:10.1016/S1876-3804(19)60039-X

Li, Z., Duan, Y., Peng, Y., Wei, M., and Wang, R. (2020). A laboratory study of microcracks variations in shale induced by temperature change. *Fuel* 280, 118636. doi:10.1016/j.fuel.2020.118636

Li, Z., Duan, Y., Wei, M., Peng, Y., and Chen, Q. (2019). Pressure performance of interlaced fracture networks in shale gas reservoirs with consideration of induced fractures. *J. Petroleum Sci. Eng.* 178, 294–310. doi:10.1016/j.petrol.2019.03.048

Long, S., You, Y., Jiang, S., Liu, G., Feng, Q., Gao, Y., et al. (2020). Integrated characterization of ultradeep reef-shoal reservoir architecture: A case study of the upper permian changxing formation in the giant Yuanba gas field, sichuan basin, China. *J. Petroleum Sci. Eng.* 195 (6), 107842. doi:10.1016/j.petrol.2020.107842

Lv, W., Chen, S., Kong, C., Jia, N., He, L., Wang, R., et al. (2019). Evaluating seepage radius of tight oil reservoir using digital core modeling approach. *J. Petroleum Sci. Eng.* 178 (1), 609–615. doi:10.1016/j.petrol.2019.03.072

Ostu, N. (1979). A threshold selection method from gray-histogram. *IEEE Trans. Syst. Man, Cybern.* 9 (1), 62–66. doi:10.1109/TSMC.1979.4310076

Qi, Y., Ju, Y., Yu, K., Meng, S., and Qiao, P. (2021). The effect of grain size, porosity and mineralogy on the compressive strength of tight sandstones: A case study from the eastern ordos basin, China. *J. Petroleum Sci. Eng.* 208 (1), 109461. doi:10.1016/j.petrol.2021.109461

Qiao, J., Zeng, J., Jiang, S., Feng, S., Feng, X., Guo, Z., et al. (2019). Heterogeneity of reservoir quality and gas accumulation in tight sandstone reservoirs revealed by pore structure characterization and physical simulation. *Fuel* 253 (1), 1300–1316. doi:10.1016/j.fuel.2019.05.112

Shen, L., Wang, Z., and Li, S. (2015). Numerical simulation for seepage field of soil based on mesoscopic structure reconfiguration technology. *J. Rock Soil Mech.* 36 (11), 3307–3314. doi:10.16285/j.rsm.2015.11.036

Song, S., Liu, J., Yang, D., Hong, Y., Huang, B., Zhang, K., et al. (2019). Pore structure characterization and permeability prediction of coal samples based on SEM images. *J. Nat. Gas Sci. Eng.* 67 (1), 160–171. doi:10.1016/j.jngse.2019.05.003

Sui, W., Quan, Z., Hou, Y., and Cheng, H. (2020). Estimating pore volume compressibility by spheroidal pore modeling of digital rocks. *Petroleum Explor. Dev.* 47 (3), 564–572. doi:10.11698/PED.2020.03.12

Sui, W., Tian, Y., and Yao, C. (2018). Investigation of microscopic pore structure variations of shale due to hydration effects through SEM fixed-point observation experiments. *Petroleum Explor. Dev.* 45 (5), 894–901. doi:10.1016/S1876-3804(18)30099-5

Tong, X., Zhang, G., Wang, Z., Wen, Z., Tian, Z., Wang, H., et al. (2018). Distribution and potential of global oil and gas resources. *Petroleum Explor. Dev.* 45 (4), 727–736. doi:10.1016/S1876-3804(18)30081-8

Viktorovich, M. A., Viktorovich, G. D., Ivanovich, P. M., Anatol'yevich, F. S., and Olegovna, V. Y. (2021). 3D pore-scale modeling of nanofluids-enhanced oil recovery. *Petroleum Explor. Dev.* 48 (4), 825–834. doi:10.1016/S1876-3804(21)60080-0

Wang, M., Wang, J., Pan, N., and Chen, S. (2007). Mesoscopic predictions of the effective thermal conductivity for microscale random porous media. *Phys. Rev. E* 75 (3), 036702. doi:10.1103/physreve.75.036702

Zhang, L., Guo, X., Hao, F., Zou, H., and Li, P. (2016). Lithologic characteristics and diagenesis of the upper triassic Xujiahe formation, Yuanba area, northeastern sichuan basin. *J. Nat. Gas. Sci. Eng.* 35, 1320–1335. doi:10.1016/j.jngse.2016.09.067

Zhao, J., Fu, D., Li, Y., Jiang, Y., Xu, W., and Chen, X. (2018). REV-scale simulation of gas transport in shale matrix with lattice Boltzmann method. *J. Nat. Gas Sci. Eng.* 57 (1), 224–237. doi:10.1016/j.jngse.2018.07.008

Zhong, J., Yan, R., Zhang, H., Feng, Y., Li, N., and Liu, X. (2020). A decomposition method of nuclear magnetic resonance T2 spectrum for identifying fluid properties. *Petroleum Explor. Dev.* 47 (4), 691–702. doi:10.1016/S1876-3804(20)60089-1

Zhu, H., Zhang, T., Zhong, D., Li, Y., Zhang, J., and Chen, X. (2019). Binary pore structure characteristics of tight sandstone reservoirs. *Petroleum Explor. Dev.* 46 (6), 1220–1228. doi:10.1016/S1876-3804(19)60283-1

Zou, C., Yang, Z., He, D., Wei, Y., Li, J., Jia, A., et al. (2018). Theory, technology and prospects of conventional and unconventional natural gas. *Petroleum Explor. Dev.* 45 (4), 575–587. doi:10.1016/S1876-3804(18)30066-1

frontiers | Frontiers in Energy Research

TYPE Original Research
PUBLISHED 24 August 2022
DOI 10.3389/fenrg.2022.984144

OPEN ACCESS

EDITED BY
Yibo Li,
Southwest Petroleum University, China

REVIEWED BY
Jiaqi Wang,
Harbin Engineering University, China
Xiaorong Yu,
Yangtze University, China
Zhezhi Liu,
Chongqing University of Science and Technology, China

*CORRESPONDENCE
Huan Peng,
282600120@qq.com

SPECIALTY SECTION
This article was submitted to Advanced Clean Fuel Technologies, a section of the journal Frontiers in Energy Research

RECEIVED 01 July 2022
ACCEPTED 25 July 2022
PUBLISHED 24 August 2022

CITATION
Peng H, Yang J, Peng J, Pu J, Liu Q, Su J and Liu J (2022), Experimental investigation of the mechanism of supercritical CO_2 interaction with tight sandstone.
Front. Energy Res. 10:984144.
doi: 10.3389/fenrg.2022.984144

Experimental investigation of the mechanism of supercritical CO_2 interaction with tight sandstone

Huan Peng[1,2]*, Jian Yang[1,2], Junliang Peng[1,2], Junhong Pu[3], Qiang Liu[3], Jun Su[1,2] and Jin Liu[4]

[1]Engineering Technology Research Institute of Southwest Oil & Gas Field Company, PetroChina, Chengdu, China, [2]Key Laboratory of Oil & Gas Well Stimulation Technology of Southwest Oil & Gas Field Company, Chengdu, China, [3]Southwest Oil & Gas Field Company, PetroChina, Chengdu, China, [4]No. 8 Oil Extraction Plant of Changqing Oilfield Company, PetroChina, Xi'an, China

One of the important technologies for combating global climate change is CCUS (Carbon Capture, Utilization, and Storage), which aims to address the issue of "greenhouse effect" generated by a significant amount of greenhouse gas emissions. Supercritical CO_2, a new type of anhydrous fracturing fluid with broad application prospects in low-pressure tight sandstone gas reservoirs, has several advantages over traditional water-based fracturing fluids, including quick flowback, minimal damage to the reservoir, and the ability to realize *in-situ* storage of greenhouse gases. The tight sandstone cores from the Jinqiu Gas field in the Sichuan Basin were used in an experimental investigation on the interaction mechanism between supercritical CO_2 and tight sandstone to examine the viability of supercritical CO_2 fracturing with tight sandstone, and analysis of the samples' post-reaction samples' mineral composition, microstructure, mass change, and total salinity change. The interaction of tight sandstone with supercritical CO_2 results in an increase in quartz content, a decrease in clay mineral content, the formation of new minerals, and partial mineral dissolution on the surface of the sample. Since the degree of mineral dissolution of sandstone samples increases with time, CO_2 can be stored in tight sandstone as carbonate minerals. This study evaluates how supercritical CO_2 interacts with tight sandstone and can offer a solid theoretical foundation and experimental evidence in favor of CO_2 *in-situ* storage in tight sandstone gas reservoir.

KEYWORDS

supercritical CO_2, tight sandstone, interaction mechanism, CCUS, fracturing technology, experimental evaluation

1 Introduction

The "greenhouse effect," which is brought on by a significant quantity of greenhouse gas emissions, has sparked widespread worry as social economy continues to advance and global industrialisation picks up speed. The average CO_2 concentration in the atmosphere has risen to its greatest level in almost a million years since the globe started the industrialization era, and temperatures are increasing (Grainger and Smith, 2021). Both

the ecosystem of the world and the advancement of human society are in grave danger. Future climate change will cause a number of chain reactions that will get worse as time goes on, including an increase in extreme weather occurrences, a rise in sea level, and the extinction of marine and terrestrial ecosystems (Zou et al., 2021). If CO_2 emissions continue to climb, the world's temperature will rise by 2°C by the end of the century, the sea level will rise by almost 1 m, most coral reefs will vanish, 13% of terrestrial ecosystems will be lost, and many plants and animals may be in danger (Umar et al., 2022). Although the industrial age has brought about great advancement and ease, it has also led to major environmental issues and unsustainable expansion.

The Paris Climate Agreement, which proposed achieving the goal of "net zero emissions" of CO_2 around 2050, or carbon neutrality, was adopted at the 21st United Nations Climate Change Conference in order to address global climate change (Zhao et al., 2022), realize the advancement of human civilization, and ensure the sustainable development of the earth's ecosystem (Tapia et al., 2018). As a result, countries have adopted policies that reflect the significance of lowering greenhouse gases, particularly CO_2 emissions.

The geological storage method of CO_2 is currently the best efficient way to deal with CO_2, a greenhouse gas. It involves gathering the CO_2 gas produced by fixed point sources (industrial point sources or power plants) and storing it in a reasonably closed geological structure (Hasan et al., 2015). All deep salt water bearing strata, oil and gas reservoirs, barren coal seams, and deep ocean have the perfect storage location. Their individual CO_2 storage mechanisms, however, differ as a result of the various storage sites.

Researchers proposed three pathways for CO_2 disposal in deep saline water layer in the CO_2 storage in deep saline water layer study (Wang et al., 2021). First, in a process known as dissolution landfill technology, CO_2 is directly dissolved in formation water. This approach is expected to raise the acidity of the formation water, which will increase the solubility of minerals in the parent rock because the formation water with CO_2 dissolved is already mildly acidic (Zhou et al., 2019); Second, after CO_2 injection, it directly or indirectly reacts with minerals in the formation to produce secondary carbonate minerals, which are precipitated in the form of new minerals (Zhou et al., 2018). Third, CO_2 is stored under the cover of low permeability rock in the form of gas or supercritical fluid, that is, CO_2 is loaded into "sealed tank," which is typically referred to as liquid landfill technology (Yue et al., 2022). Mineral landfill technique is the name given to this process. This process has a good chance of success since it can solidify CO_2 into a component of solid minerals over an extended period of time.

Theoretical study and practical experience demonstrate that oil and gas reservoirs can store CO_2 for a long period because of their effective capping. The chance of CO_2 stored there leaking out is the smallest compared to other geological entities such deep salt water layers, basalt, and non-minable coal seams. Additionally, it is easier to store CO_2 and has higher economic benefits now that production wells and injection wells have been constructed in the oil and gas reservoirs. A long-term technique of storing CO_2 is in oil and gas reservoirs. One of the primary methods for storing CO_2 is to inject supercritical CO_2 into oil and gas reservoirs using oil field injection wells or production wells (Bachu, 2016). Therefore, increased oil recovery is paired with CO_2 reservoir storage as the primary method. Oil and gas reservoir storage uses CO_2 to force crude oil to flow to production wells, similar to how water drive enhance oil recovery. The main mechanism of CO_2 oil displacement involves interphase mass transfer, crude oil volume expansion, viscosity reduction, lowering of oil-gas interfacial tension, and oil-gas mixing, all of which occur during the contact between CO_2 and crude oil (Mouahid et al., 2022).

Supercritical CO_2 has been employed as a working fluid in various theoretical and experimental studies in petroleum engineering (Nikolai et al., 2019; Peng et al., 2019), and it can be used to displace oil. Supercritical CO_2 hydraulic fracturing is regarded as one of the most environmentally benign fracturing technologies since it has several benefits in reservoirs (Zhao et al., 2017; Hazarika and Boruah, 2022), particularly for water-sensitive formations (Liu et al., 2014), low pressure reservoirs, and water-stressed regions (Cao et al., 2017). Although it is well known that supercritical CO_2 has many advantages over water-based fracturing fluid, the majority of the work is still done on shale (Jiang et al., 2016; Jia et al., 2018; Memon et al., 2022). For example, the matrix minerals dissolve (Ao et al., 2017), the dissolved minerals precipitate (Chen et al., 2022), the rock breakdown pressure is lowered (Gathitu et al., 2009; Wang et al., 2018; Peng et al., 2020), the rock matrix swells (Day et al., 2008), and so on. Uncertainty exists regarding the exact mechanism of action between supercritical CO_2 and tight sandstone. Tight sandstone and supercritical CO_2 will interact physicochemically during supercritical CO_2 fracturing (Peng et al., 2016). The flow condition of subsurface oil and gas will be impacted by changes in tight sandstone's pore characteristics, porosity, permeability, and other physical qualities (Lin et al., 2008; Lin et al., 2022). The evaluation of the mineral composition, microstructure, mass change, and total salinity change of supercritical CO_2 fracturing in low pressure tight sandstone reservoirs is therefore critical; nevertheless, there have only been a few publications in the literature up to this point.

This study examines the feasibility of fracturing supercritical CO_2 with tight, low-pressure sandstone. We investigate how tight sandstone and supercritical CO_2 interact. Different tight sandstone samples were treated with supercritical CO_2 using the tight sandstone cores from the Jinqiu Gas field in the Sichuan Basin, and the results were evaluated for changes in mineral composition, microstructure, mass change, and total salinity under various time, pressure, and temperature conditions. To

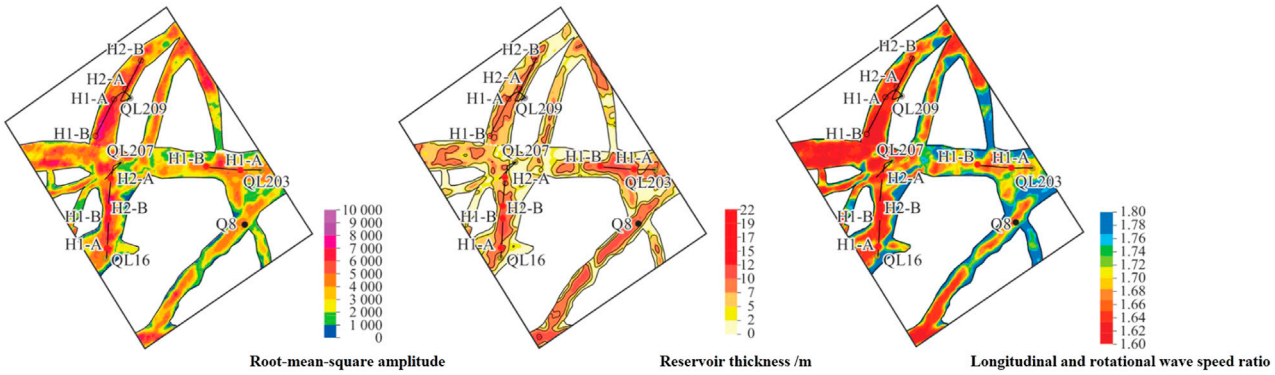

FIGURE 1
Three dimensional carving stereogram of channel sand body of Shaximiao Formation in Central Sichuan.

FIGURE 2
Sampled from tight sandstone cores.

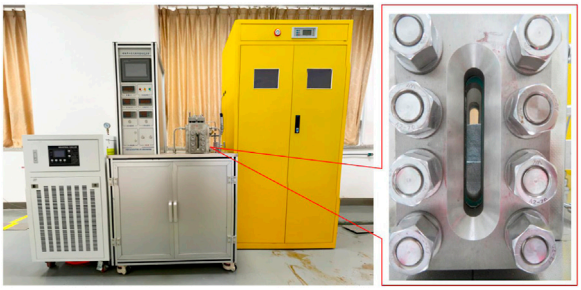

FIGURE 3
Visualization device for rock and supercritical CO_2 interactions.

further enhance the interaction mechanism between supercritical CO_2 and low pressure tight sandstone, quantify the impact of supercritical CO_2 on the mineral composition, microstructure, mass change, and total salinity of tight sandstone. This discovery evaluates the mechanism of supercritical CO_2's interaction with tight sandstone, and it can offer a theoretical foundation and experimental support for CO_2 *in-situ* storage in tight sandstone gas reservoirs.

2 Materials and methods

2.1 Core sample

The channel sand bodies in the Shaximiao Formation in the Sichuan Basin are found to be very developed longitudinally, widely dispersed on the plane, with good reservoir physical properties, and to have great exploration potential, according to recent comprehensive geological research on the Shaximiao Formation System. The three-dimensional carving stereogram of river sand body is shown in Figure 1 (Zhang and Yang, 2022).

The Shaximiao formation's natural gas has the advantages of shallow burial, low cost, short cycle, and quick effect. At the moment, it is one of the important practical fields of benefit development under low oil prices, and has drawn a lot of attention. Major natural gas exploration breakthroughs have been made in Qiulin, Jinhua, Yanting, and other locations in the central and western Sichuan region. As a result, Shaximiao formation has emerged as the Sichuan Basin's newest focus for oil and gas exploration (Zhang et al., 2022).

The reservoir temperature is 1.9–2.5°C/100 m, the reservoir depth is 1,500–2800 m, the cumulative thickness of the reservoir is 20–70 m, the reservoir porosity is mainly 8%–15%, the permeability is mainly 0.01–1.00 mD, and the pressure coefficient of the seven# sand body is only 0.47, belonging to the normal temperature and low pressure tight sandstone gas reservoir (Zheng et al., 2021).

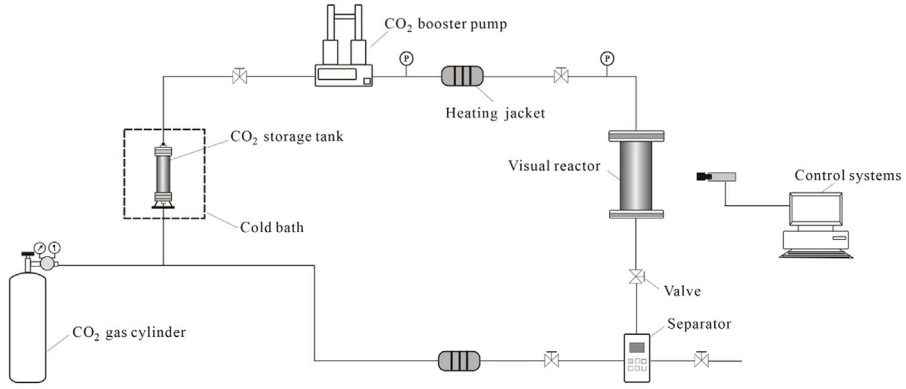

FIGURE 4
Visualization device for rock and supercritical CO_2 interactions flow chart.

Select a sandstone core that is underground that has a complete exterior and no visible fractures. Drill, cut, and polish the two ends with an end grinder to make sure they are parallel and smooth. The core measures 15 mm in length and 25 mm in diameter, As shown in Figure 2. The end face of the core sample must be vertical to the circumference and the maximum deviation must not be greater than 0.05 mm. The height and diameter errors of the core sample must not be greater than 0.3 mm. The core must be processed in accordance with the standards of the International Society of Rock Mechanics (ISRM) to make the sample error within the following range. The sandstone sample must be wrapped and covered with fresh-keeping film after preparation in order to shield it from air reaction during following studies.

2.2 Apparatus

As shown in Figure 3, the visualization apparatus for the interaction of supercritical CO_2 with rock consists of a CO_2 gas cylinder, a CO_2 storage tank, a cold bath, a CO_2 booster pump, a visual reactor, a heating jacket, and control systems. Visual reactor is a crucial part of the experimental system. As seen in Figure 3, the sapphire glass window in the visual reactor allows for real-time observation of the interaction process between supercritical CO_2 and rock. The visual reactor has a volume of 500 ml, the CO_2 storage tank has a volume of 5 L, the temperature range is −5°C–150°C, and the pressure bearing capability of the entire unit is 50 MPa. The flow chart of the experimental device is shown in Figure 4. By using the control system and changing the settings of the heating jacket and CO_2 booster pump, the liquid CO_2 is converted to supercritical CO_2, as shown in Figure 5, which can be used for the interaction process between supercritical CO_2 and rock at different temperatures, pressures and times.

The scanning electron microscopy apparatus is represented in Figure 6, and it is primarily made up of an electron

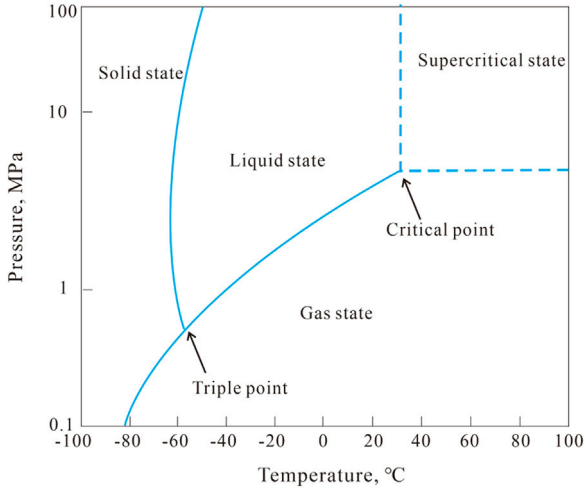

FIGURE 5
CO_2 phase diagram.

microscope, an electron gun filament, a vacuum system, and an automated system for acquiring and processing samples and images. With a maximum magnification of ×150000 and a resolution higher than 10 nm, it can swiftly produce images with rich surface features that can be used to measure samples that are smaller than a micron or even smaller than a nanometer in size. It is used to research how supercritical CO_2 interacts with rock and to track trends in reservoir physical qualities like permeability and porosity.

Figure 7 shows an X-ray diffractometer. A high stability X-ray source, a sample and sample position orientation adjustment mechanism system, a ray detector, and a system for processing and analyzing diffraction patterns make up its core parts. Equipment specifications: A common size light tube is used

FIGURE 6
Scanning electron microscopes equipment.

FIGURE 7
X-ray diffractometer.

FIGURE 8
Ion chromatograph.

as the Cu target, and a theta/theta vertical goniometer is used. The theta angle range is 2–160, and the angle accuracy is 0.0001. The X-ray needed for measurement is produced by the high stability X-ray source. The X-ray tube's anode target material can alter the wavelength of the radiation. The intensity of the X-ray source can be changed by adjusting the anode voltage. This allows for routine phase analysis and semi-quantitative analysis of polycrystalline powder, block, and liquid samples, as well as the determination and correction of unit cell parameters, the X-ray diffraction indexation of unidentified polycrystalline samples, and the determination of grain size and crystallinity.

The flow compatibilizer, high-pressure infusion pump, sampler, chromatographic column, detector, and data processing system are the key components of the ion chromatograph, as shown in Figure 8. The chromatographic pump has a maximum operating pressure of 50 MPa, a flow rate of 0.001–20 ml/min, a minimum graduation value of 0.001 ml/min, a concentration range of 0–100% for the ion chromatograph's eluent, an effective injection volume of 0.5–11 ml, and a measurement range of 0–15000 us/cm without section switching. The plasma concentrations of K^+, Na^+, Ca^{2+}, Mg^{2+}, Cl^-, F^-, and SO_4^{2-} in aqueous solution are used in a liquid chromatography method for separation and detection that uses the ionic properties of the tested substances. This method is a powerful reference for the variation characteristics and laws of ion concentration in liquid.

2.3 Methods

It is required to examine and identify changes in the microscopic properties, mineral composition, and ion concentration of the solution of sandstone samples before and after the experiment in order to research the mechanism of interaction between supercritical CO_2 and sandstone. The steps of the experiment are as follows:

1) In order to accurately obtain the change of core weight, sandstone samples should be cleaned with distilled water to remove surface impurities, and then dried and weighed.
2) Assemble the visualization tool for the interaction between supercritical CO_2 and rock and wait until it is ready for usage. It is used to carry out the interaction process between supercritical CO_2 and tight sandstone.
3) Place the formation water-prepared container into the visualization device for the interaction between supercritical CO_2 and rock, then insert it into the sandstone core. Next, start the booster pump to inject CO_2 for pressurization. Then, set the pressurization temperature and time according to different experiments. Finally, determine the sampling times according to the time. Take a core and 20 ml of liquid each time, and inspect and analyze the core with scanning electron microscopy.
4) After the reaction, allow the reactor to cool to ambient temperature before opening it to remove the sample. The sandstone sample should then be cleaned with distilled water, dried, and weighed in an oven.

TABLE 1 Tight sandstone weight variation after supercritical CO_2 at various times.

Project	Test time, h		
	48	168	360
Tight sandstone weight before being treated to supercritical CO_2, g	17.6625	17.6319	17.6132
Tight sandstone weight after being treated to supercritical CO_2, g	17.3251	17.1239	16.7597
Weight change of tight sandstone, g	0.3374	0.5080	0.8535
Tight sandstone's rate of weight change, %	1.91	2.88	4.85

5) Following the aforementioned treatment, the core was examined and evaluated using a scanning electron microscope and an X-ray diffractometer; an ion chromatograph was used to ascertain the composition of the reaction solution. The interaction mechanism between supercritical CO_2 and tight sandstone is analyzed.

3 Process of supercritical CO_2 reacting with tight sandstone

When supercritical CO_2 comes into contact with sandstone at the proper temperature and pressure, it first diffuses into the rock aquifer's pores, interacts with formation water to form a weak acidic fluid, and then reacts with the rocks to produce a series of complicated chemical reactions that lead to the decomposition of brittle minerals like carbonate and feldspar in the sandstone and the precipitation of new minerals, altering the microstructure, weight, porosity, and permeability of sandstone.

The fluid changes into a weak acidic fluid as a result of CO_2 first coming into touch with the water in the pores, followed by it dissolving in the water at the water-air interface and reacting with it to generate carbonic acid (Bierg and Banwart, 2000).The reaction formula is:

$$CO_2 + H_2O = H_2CO_3$$

Carbonic acid quickly breaks down into bicarbonate ions:

$$H_2CO_3 = H^+ + HCO_3^-$$

The released hydrogen ions will result in the complexation of dissolved cations with bicarbonate ions and the disintegration of carbonate minerals and silicates in tight sandstone rocks, including:

$$H^+ + CaCO_3 = Ca^{2+} + HCO_3^-$$

$$Ca^{2+} + HCO_3^- = CaHCO_3^+$$

$$4H^+ + 4H_2O + KA1Si_3O_8 = K^+ + A1^3 + 3H_4SiO_4$$

$$4H^+ + 4H_2O + NaA1Si_3O_8 = Na^+ + A1^{3+} + 3H_4SiO_4$$

$$4H^+ + Mg_2SiO_4 = 2Mg^{2+} + H_4SiO_4$$

$$4H^+ + Fe_2SiO_4 = 2Fe^{2+} + H_4SiO_4$$

Finally, the dissolved bicarbonate combines with cations to produce additional carbonate minerals such as calcite, magnesite, siderite, and dawsonite:

$$HCO_3^- + Ca^{2+} = CaCO_3 \downarrow + H^+$$

$$HCO_3^- + Mg^{2+} = MgCO_3 \downarrow + H^+$$

$$HCO_3^- + Fe^{2+} = FeCO_3 \downarrow + H^+$$

$$HCO_3^- + Na^+ + A1^{3+} + 2H_2O = NaA1CO_3(OH)_2 \downarrow + 3H^+$$

Therefore, soluble minerals in the rock are dissolved after CO_2 and tight sandstone come into contact, and new minerals are also generated, modifying the sandstone.

4 Results and discussion

4.1 Effect of supercritical CO_2 on the weight of tight sandstone

According to the formation conditions and the characteristic time stage after simulated fracturing treatment. Tight sandstone and supercritical CO_2 reaction for 48, 168, and 360 h, respectively, at 60°C under a test pressure of 10 MPa, the temperature is the formation temperature, the pressure is the difference between the minimum principal stress of the formation and the formation pore pressure, and the action time is selected as several characteristic time points after fracturing treatment. The samples of sandstone are weighed after the reaction. Table 1 shows the test results. The weight of the rocks decreases after the test. After supercritical CO_2 dissolves in water, the hydrogen ions decomposed by weak acidic fluid dissolve potassium feldspar, plagioclase and some clay minerals, resulting in rock weight changes. The weight of the tight sandstone samples reduces by 1.91% after 48 h, 2.88% after 168 h, and 4.85% after 360 h. More weight loss over time suggests that the supercritical CO_2 and rock primarily have a certain

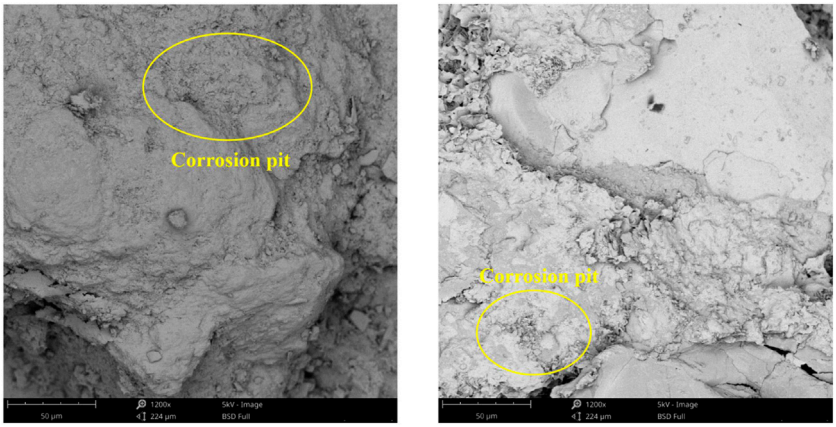

FIGURE 9
Effect of supercritical CO_2 on microstructure of tight sandstone (After 48 h).

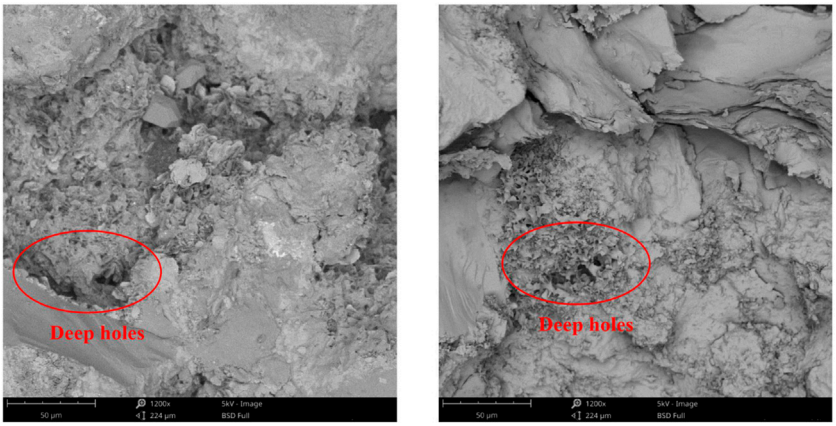

FIGURE 10
Effect of supercritical CO_2 on microstructure of tight sandstone (After 168 h).

dissolving response during the experiment, and that the degree of dissolution gradually increases as time goes on.

4.2 Effect of supercritical CO_2 on microstructure of tight sandstone

Tight sandstone and supercritical CO_2 reacted at 60°C for 48 h, 168 h, and 360 h, respectively, under an experimental pressure of 10 MPa. After the reaction, sandstone samples were examined under a scanning electron microscope to reveal that after 48 h, the feldspar was only mildly corroded while the quartz and clay minerals remained comparatively stable, generating a few corrosion pits, as seen in Figure 9. As depicted in Figure 10, after 168 h of reaction, the degree of feldspar dissolution increased, quartz and clay minerals also started to undergo weak dissolution, and some deep holes developed on the visible surface; After 360 h of reaction, the feldspar's degree of dissolution increased further, and quartz and clay minerals started to dissolve somewhat as well, resulting in a broken dissolution phenomena, as illustrated in Figure 11.

4.3 Effect of supercritical CO_2 on mineral composition of tight sandstone

When CO_2 is in a supercritical state, it reacts with tight sandstone. It initially diffuses into the tight sandstone aquifer pores at formation temperature and pressure, reacts with formation water to form weak acidic fluid, and then interacts with rocks to produce a series of intricate chemical processes.

TABLE 2 Initial sample samples' mineral composition.

Component type	Quartz	Potassium feldspar	Plagioclase	Clay
Content, %	54.2	2.8	34.5	8.5

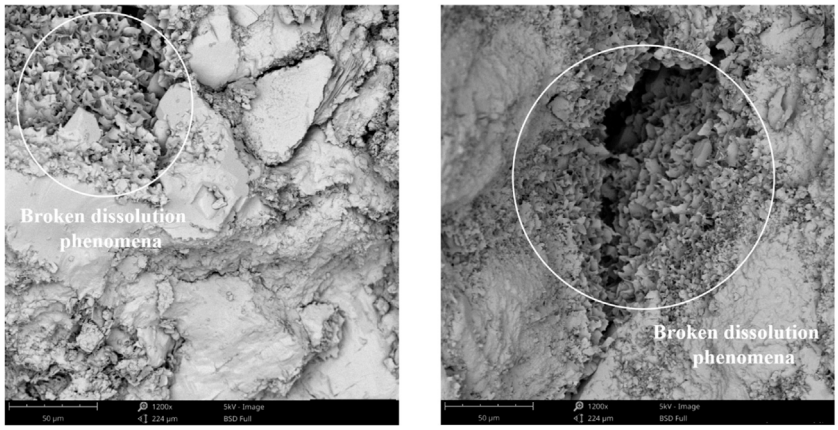

FIGURE 11
Effect of supercritical CO_2 on microstructure of tight sandstone (After 360 h).

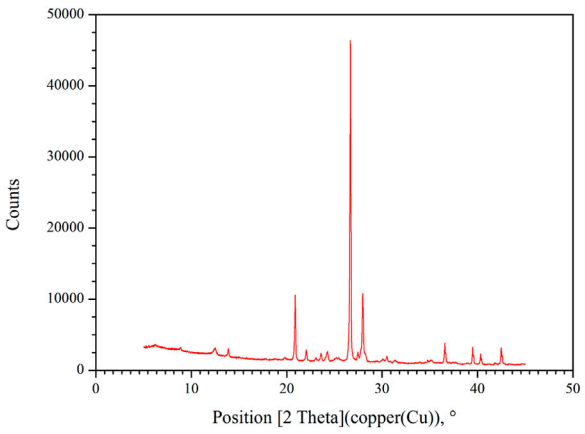

FIGURE 12
Results of the sample's initial X-ray diffraction test.

The mineral compositions of sandstone before and after supercritical CO_2 and tight sandstone were qualitatively and quantitatively examined by XRD in order to further characterize the CO_2 water rock interaction mechanism.

In Figure 12 and Table 2, the results of the analysis and interpretation of the relative content test of mineral components of tight sandstone samples prior to the action of supercritical CO_2 are displayed. The examination of sandstone composition shows that Jinqiu tight sandstone has the highest concentrations of quartz and plagioclase, at 54.2% and 34.5%, respectively.

The tight sandstone reacts with supercritical CO_2 after 48 h, 168 h, and 360 h at 60°C under an experimental pressure of 10 MPa. The sandstone samples are analyzed by X-ray diffraction after the reaction. In Figure 13, the experimental results are displayed.

Following the experiment, the sandstone's material composition was compared and examined. It can be seen that after 48 h of reaction with supercritical CO_2, the quartz content of Jinqiu tight sandstone increased by 1.5%, the potassium feldspar content decreased by 0.2%, the plagioclase content decreased by 1.2%, and the clay minerals content decreased by 0.4%. 0.3% of newly formed calcite was discovered at the same time. After 168 h of reaction, quartz's content increased by 3.4%, potassium feldspar's content dropped by 0.7%, plagioclase's content dropped by 2.8%, the content of clay minerals dropped by 0.6%, and the content of newly formed calcite increased to 0.7%. After 360 h of reaction, there was a 5.3% increase in quartz content, a 1.1% decrease in potassium feldspar content, a 4.3% drop in plagioclase content, a 1.0% decrease in clay mineral content, and a 1.0% increase in newly created calcite content.

Generally speaking, when supercritical CO_2 interacts with Jinqiu tight sandstone, quartz content rises, potassium feldspar

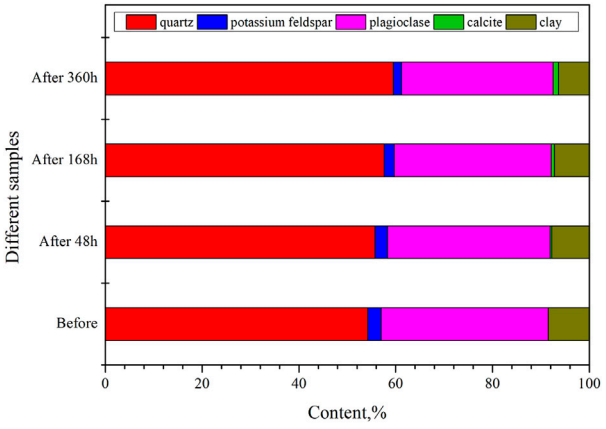

FIGURE 13
Mineral composition of tight sandstone changes after various supercritical CO_2 reaction times.

and plagioclase content fall, and new calcite minerals form. Thus, it is clear how the ionic reaction $Ca^{2+} + CO_3^{2-} \leftrightharpoons CaCO_3$ (calcite) in the solution and the deposition of the resulting calcite on the sample surface occur during the experiment as a result of the interaction between CO_2 and the sandstone samples. It is possible to implement the underground storage of CO_2 using material traps, as evidenced by the development of calcite, which shows that CO_2 can be stored in the solution as insoluble carbonate and precipitated as calcite and other CO_2 capture minerals.

4.4 Effect of supercritical CO_2 on solution composition

Feldspar, quartz, and other soluble minerals in the reservoir sandstone can dissolve in the acidic fluid created when CO_2 dissolves in water, creating new carbonate minerals. The formation temperature and pressure of the reservoir are simulated in accordance with the detection results of the formation water quality of the reservoir in order to further study the dissolution of feldspar, quartz, clay minerals, and other soluble minerals, combined with the change of ion concentration in the reaction solution. The production of CO_2 fluid and the interaction of water and sandstone are further discussed.

After completely soaking the dense sandstone samples, Table 3 displays the formation water data of the sha1-2 sub member of the Shaximiao Formation in the Jinqiu gas field. $CaCl_2$ type formation water is used. According to the salt formed by the final combination of Na^+, Cl^- and other ions, the name of this kind of salt is water type. It mainly includes $NaHCO_3$ type, Na_2SO_4 type, $MgCl_2$ type and $CaCl_2$ type. $CaCl_2$ type formation water represents the water formed under the deep closed structural environment, with good sealing property, which is conducive to the accumulation and preservation of oil and gas, and is a sign of good oil and gas.

The tight sandstone reacts with supercritical CO_2 over 48 h, 168 h, and 360 h at 60°C under a test pressure of 10 MPa. Following the reaction, the water quality of the solution containing the samples of sandstone is examined and evaluated. Figure 14 displays the examination results.

In cations, the mass concentrations of K^+, Na^+, Ca^{2+} increased with reaction time. K^+ mainly came from the dissolution of potassium feldspar, and the K^+ concentration increased from 5,133 mg/L to 5,339 mg/L, an increase of 206 mg/L. Na^+ and Ca^{2+} are mainly from the dissolution of plagioclase, indicating that the dissolution degree of potassium feldspar and plagioclase is gradually increasing. The concentration of Na^+ increases from 6,227 mg/L to 6,401 mg/L, an increase of 174 mg/L, and the concentration of Ca^{2+} increases from 18,000 mg/L to 18,200 mg/L, an increase of 200 mg/L. The mass concentration of Mg^{2+} and Ba^{2+} changed slightly with time. The concentration of Mg^{2+} increased from 233 mg/L to 272 mg/L, increased by 39 mg/L, the concentration of Ba^{2+} increased from 1815 mg/L to 1821 mg/L, increased by 6 mg/L, and Al^{3+} also increased from nothing, but the content was low. Al^{3+} concentration increased from 0 mg/L to 12 mg/L, an increase of 12 mg/L.

In anions, a small amount of clay minerals dissolved, resulting in a slow increase in anionic Cl^- concentration, which increased from 51,323 mg/L to 51,569 mg/L, an increase of 246 mg/L. The mass concentration of SO_4^{2-} changed little, and the concentration of SO_4^{2-} increased from 5 mg/L to 12 mg/L, an increase of 7 mg/L. The concentrations of HCO_3^- and CO_3^{2-} in the solution first increased rapidly, and then the growth rate gradually decreased. HCO_3^-

TABLE 3 Initial ion content of formation water.

Water type	Ion content of formation water, mg/L							
	Cation					Anion		
	K^+	Na+	Ca^{2+}	Mg^{2+}	Ba^{2+}	Cl^-	$SO4^{2-}$	$HCO3^-$
$CaCl_2$	5,133	6,227	18,000	233	1815	51,323	5	123

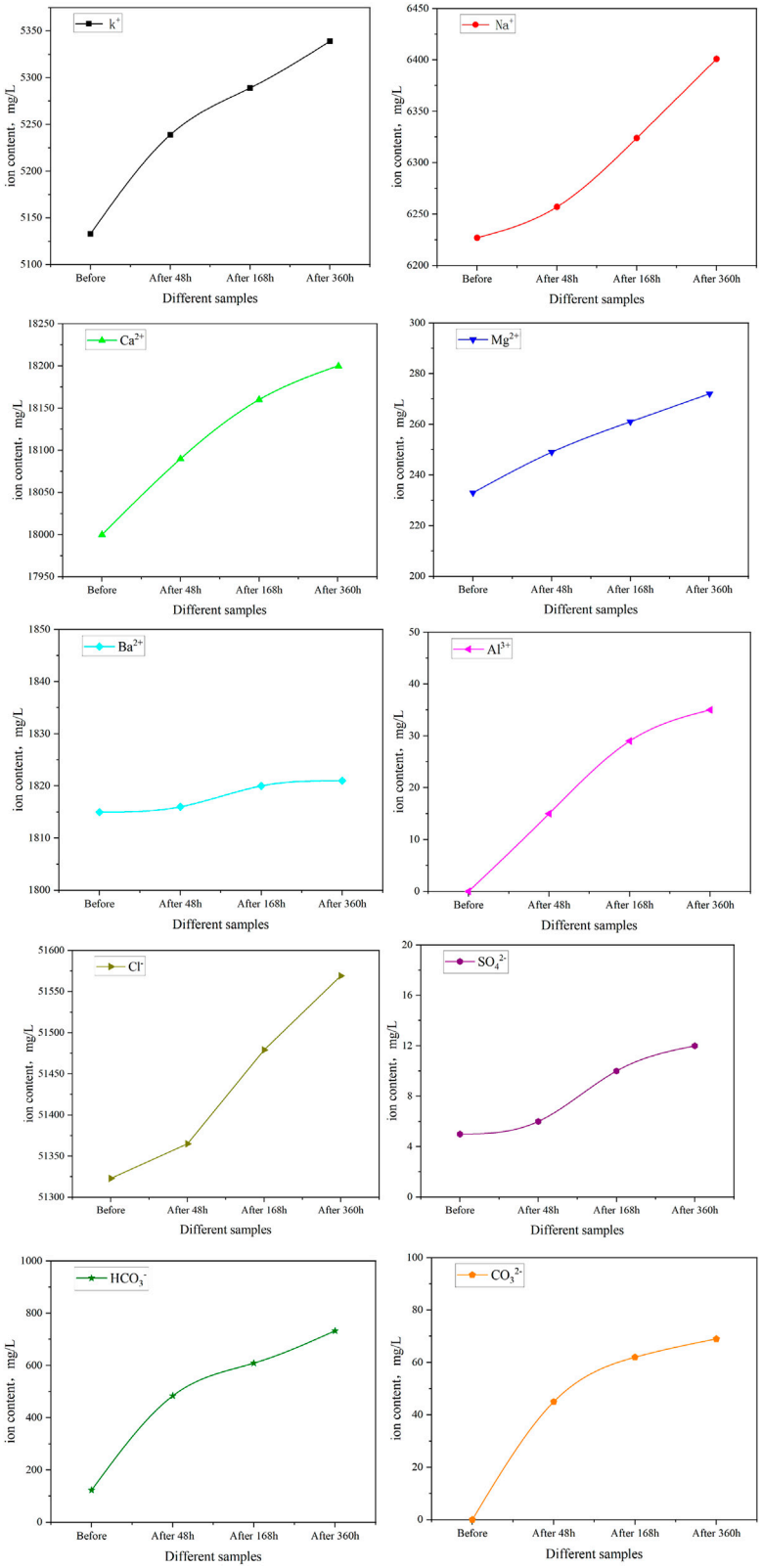

FIGURE 14
Change of mineral composition of after different action time of sandstone and supercritical CO_2.

concentration increased from 123 mg/L to 733 mg/L, an increase of 610 mg/L. The concentration of CO_3^{2-} increased from 0 mg/L to 69 mg/L, an increase of 69 mg/L. The two reactions $H_2CO_3 = H^+ + HCO_3^-$ and $HCO_3^- = H^+ + CO_3^{2-}$ can be used to illustrate the changing process. The CO_3^{2-} is consumed by the reaction equation ($HCO_3^- = H^+ + CO_3^{2-}$), which causes the divalent cations dispersed in the solution and CO_3^{2-} to form insoluble carbonate. As the minerals dissolve, the divalent cations dissolve and produce carbonate precipitation, which slows the pace at which HCO_3^- and CO_3^{2-} concentrations develop in the solution.

5 Summary and conclusions

1) Supercritical CO_2 is a new type of anhydrous fracturing fluid that can achieve *in-situ* storage of greenhouse gases and has a wide range of potential applications in low-pressure tight sandstone gas reservoirs. It differs from conventional water-based fracturing fluid in that it can achieve *in-situ* storage of greenhouse gases.
2) In this study, tight sandstone reacts with supercritical CO_2 after 360 h at 60°C under pressure of 10 MPa, there was a 5.3% increase in quartz content, a 1.1% decrease in potassium feldspar content, a 4.3% drop in plagioclase content, a 1.0% decrease in clay mineral content, and a 1.0% increase in newly created calcite content. Time increases the degree to which sandstone samples dissolve, and CO_2 can be tightly trapped in sandstone as carbonate minerals.
3) After the tight sandstone reacts with supercritical CO_2. In cations, the mass concentrations of K^+, Na^+, Ca^{2+} increased with reaction time, indicating that the dissolution degree of potassium feldspar and plagioclase is gradually increasing. The mass concentration of Mg^{2+} and Ba^{2+} changed slightly with time. In anions, a small amount of clay minerals dissolved, resulting in a slow increase in anionic Cl^- concentration. The mass concentration of SO_4^{2-} changed little. The concentrations of HCO_3^- and CO_3^{2-} in the solution first increased rapidly, and then the growth rate gradually decreased.The interaction mechanism between supercritical CO_2 and sandstone is very important for understanding the feasibility, long-term and safety of CO_2 underground storage and supercritical CO_2 fracturing.

Data availability statement

The original contributions presented in the study are included in the article/Supplementary Material, further inquiries can be directed to the corresponding author.

Author contributions

HP is responsible for the overall structure and revision. JY, JLP, JHP, and QL help evaluate and improve the paper. JS and JL help in setting up the device test, writing, and the experiment.

Funding

The authors declare that this study received funding from Southwest Oil and Gas Field Company, PetroChina. The funder was not involved in the study design, collection, analysis, interpretation of data, the writing of this article or the decision to submit it for publication.

Conflict of interest

Authors HP, JY, JLP and JS were employed by Engineering Technology Research Institute of Southwest Oil & Gas Field Company, PetroChina and Key Laboratory of Oil & Gas Well Stimulation Technology of Southwest Oil & Gas Field Company JHP and QL were employed by Southwest Oil & Gas Field Company, PetroChina. JL was employed by No. 8 Oil Extraction Plant of Changqing Oilfield Company, PetroChina.

Publisher's note

References

Ao, X., Lu, Y., Tang, J., Chen, Y., and Li, H. (2017). Investigation on the physics structure and chemical properties of the shale treated by supercritical CO_2. *J. CO_2 Util.* 20, 274–281. doi:10.1016/j.jcou.2017.05.028

Bachu, S. (2016). Identification of oil reservoirs suitable for CO_2-EOR and CO_2 storage (CCUS) using reserves databases, with application to Alberta, Canada. *Int. J. Greenh. Gas Control* 44, 152–165. doi:10.1016/j.ijggc.2015.11.013

Berg, A., and Banwart, S. A. (2000). Carbon dioxide mediated dissolution of Ca-feldspar: Implications for silicate weathering. *Chem. Geol.* 163 (1-4), 25–42. doi:10.1016/s0009-2541(99)00132-1

Cao, Y., Zhang, J., Zhai, H., Fu, G., Tian, L., and Liu, S. (2017). CO_2 gas fracturing: A novel reservoir stimulation technology in low permeability gassy coal seams. *Fuel* 203, 197–207. doi:10.1016/j.fuel.2017.04.053

Chen, K., Liu, X., Nie, B., Zhang, C., Song, D., Wang, L., et al. (2022). Mineral dissolution and pore alteration of coal induced by interactions with supercritical CO_2. *Energy* 248, 123627. doi:10.1016/j.energy.2022.123627

Day, S., Fry, R., and Sakurovs, R. (2008). Swelling of Australian coals in supercritical CO_2. *Int. J. Coal Geol.* 74 (1), 41–52. doi:10.1016/j.coal.2007.09.006

Gathitu, B. B., Chen, W. Y., and McClure, M. (2009). Effects of coal interaction with supercritical CO_2: Physical structure. *Ind. Eng. Chem. Res.* 48 (10), 5024–5034. doi:10.1021/ie9000162

Grainger, A., and Smith, G. (2021). The role of low carbon and high carbon materials in carbon neutrality science and carbon economics. *Curr. Opin. Environ. Sustain.* 49, 164–189. doi:10.1016/j.cosust.2021.06.006

Hasan, M. F., First, E. L., Boukouvala, F., and Floudas, C. A. (2015). A multi-scale framework for CO_2 capture, utilization, and sequestration: CCUS and CCU. *Comput. Chem. Eng.* 81, 2–21. doi:10.1016/j.compchemeng.2015.04.034

Hazarika, S., and Boruah, A. (2022). Supercritical CO_2 (SCO_2) as alternative to water for shale reservoir fracturing. *Mater. Today Proc.* 50, 1754–1757. doi:10.1016/j.matpr.2021.09.187

Jia, Y., Lu, Y., Elsworth, D., Fang, Y., and Tang, J. (2018). Surface characteristics and permeability enhancement of shale fractures due to water and supercritical carbon dioxide fracturing. *J. Petroleum Sci. Eng.* 165, 284–297. doi:10.1016/j.petrol.2018.02.018

Jiang, Y., Luo, Y., Lu, Y., Qin, C., and Liu, H. (2016). Effects of supercritical CO_2 treatment time, pressure, and temperature on microstructure of shale. *Energy* 97, 173–181. doi:10.1016/j.energy.2015.12.124

Lin, H., Fujii, T., Takisawa, R., Takahashi, T., and Hashida, T. (2008). Experimental evaluation of interactions in supercritical CO_2/water/rock minerals system under geologic CO_2 sequestration conditions. *J. Mat. Sci.* 43 (7), 2307–2315. doi:10.1007/s10853-007-2029-4

Lin, R., Yu, Z., Zhao, J., Dai, C., Sun, Y., Ren, L., et al. (2022). Experimental evaluation of tight sandstones reservoir flow characteristics under CO_2–brine–rock multiphase interactions: A case study in the chang 6 layer, ordos basin, China. *Fuel* 309, 122167. doi:10.1016/j.fuel.2021.122167

Liu, H., Wang, F., Zhang, J., Meng, S., and Duan, Y. (2014). Fracturing with carbon dioxide: Application status and development trend. *Petroleum Explor. Dev.* 41 (4), 513–519. doi:10.1016/s1876-3804(14)60060-4

Memon, S., Feng, R., Ali, M., Bhatti, M. A., Giwelli, A., Keshavarz, A., et al. (2022). Supercritical CO_2-Shale interaction induced natural fracture closure: Implications for scCO2 hydraulic fracturing in shales. *Fuel* 313, 122682. doi:10.1016/j.fuel.2021.122682

Mouahid, A., Claeys-Bruno, M., Bombarda, I., Amat, S., Ciavarella, A., Myotte, E., et al. (2022). Supercritical CO_2 extraction of oil from Moroccan unroasted Argan Kernels: Effects of process parameters to produce cosmetic oil. *J. CO_2 Util.* 59, 101952. doi:10.1016/j.jcou.2022.101952

Nikolai, P., Rabiyat, B., Aslan, A., and Ilmutdin, A. (2019). Supercritical CO_2: Properties and technological applications-A review. *J. Therm. Sci.* 28 (3), 394–430. doi:10.1007/s11630-019-1118-4

Peng, Y., Li, Y., and Zhao, J. (2016). A novel approach to simulate the stress and displacement fields induced by hydraulic fractures under arbitrarily distributed inner pressure. *J. Nat. Gas Sci. Eng.* 35, 1079–1087. doi:10.1016/j.jngse.2016.09.054

Peng, Y., Zhao, J., Sepehrnoori, K., Li, Y., and Li, Z. (2020). The influences of stress level, temperature, and water content on the fitted fractional orders of geomaterials. *Mech. Time. Depend. Mat.* 24 (2), 221–232. doi:10.1007/s11043-019-09417-0

Peng, Y., Zhao, J., Sepehrnoori, K., Li, Z., and Xu, F. (2019). Study of delayed creep fracture initiation and propagation based on semi-analytical fractional model. *Appl. Math. Model.* 72, 700–715. doi:10.1016/j.apm.2019.03.034

Tapia, J. F. D., Lee, J. Y., Ooi, R. E., Foo, D. C., and Tan, R. R. (2018). A review of optimization and decision-making models for the planning of CO_2 capture, utilization and storage (CCUS) systems. *Sustain. Prod. Consum.* 13, 1–15. doi:10.1016/j.spc.2017.10.001

Umar, M., Farid, S., and Naeem, M. A. (2022). Time-frequency connectedness among clean-energy stocks and fossil fuel markets: Comparison between financial, oil and pandemic crisis. *Energy* 240, 122702. doi:10.1016/j.energy.2021.122702

Wang, J., Elsworth, D., Wu, Y., Liu, J., Zhu, W., and Liu, Y. (2018). The influence of fracturing fluids on fracturing processes: A comparison between water, oil and SC-CO_2. *Rock Mech. Rock Eng.* 51 (1), 299–313. doi:10.1007/s00603-017-1326-8

Wang, N., Akimoto, K., and Nemet, G. F. (2021). What went wrong? Learning from three decades of carbon capture, utilization and sequestration (CCUS) pilot and demonstration projects. *Energy Policy* 158, 112546. doi:10.1016/j.enpol.2021.112546

Yue, P., Zhang, R., Sheng, J. J., Yu, G., and Liu, F. (2022). Study on the influential factors of CO_2 storage in low permeability reservoir. *Energies* 15 (1), 344. doi:10.3390/en15010344

Zhang, B. J., Pan, K., and Wu, C. J. (2022). Compound gas accumulation mechanism and model of jurassic Shaximiao formation multistage sandstone formations in Jinqiu gas field of the Sichuan Basin. *Nat. Gas. Ind.* 42 (1), 51–61. doi:10.3787/j.issn.1000-0976.2022.01.005

Zhang, D. W., and Yang, Y. (2022). Exploration potential and development direction of continental tight sandstone gas in the Sichuan Basin[J]. *Nat. Gas. Ind.* 42 (1), 1–11. doi:10.3787/j.issn.1000-0976.2022.01.001

Zhao, J., Peng, Y., Li, Y., and Tian, Z. (2017). Applicable conditions and analytical corrections of plane strain assumption in the simulation of hydraulic fracturing. *Petroleum Explor. Dev.* 44 (3), 454–461. doi:10.1016/s1876-3804(17)30052-6

Zhao, X., Ma, X., Chen, B., Shang, Y., and Song, M. (2022). Challenges toward carbon neutrality in China: Strategies and countermeasures. *Resour. Conservation Recycl.* 176, 105959. doi:10.1016/j.resconrec.2021.105959

Zheng, Y., Han, X., Zeng, J., Zhou, C., Zhou, L., and Chen, W. (2021). Practice of high-intensity volume fracturing in the Shaximiao Formation tight sandstone gas reservoirs of the Qiulin Block, central Sichuan Basin. *Nat. Gas. Ind. B* 8 (4), 367–375. doi:10.1016/j.ngib.2021.07.007

Zhou, D., Zhang, G., Prasad, M., and Wang, P. (2019). The effects of temperature on supercritical CO_2 induced fracture: An experimental study. *Fuel* 247, 126–134. doi:10.1016/j.fuel.2019.02.099

Zhou, J., Xie, S., Jiang, Y., Xian, X., Liu, Q., Lu, Z., et al. (2018). Influence of supercritical CO_2 exposure on CH_4 and CO_2 adsorption behaviors of shale: Implications for CO_2 sequestration. *Energy fuels.* 32 (5), 6073–6089. doi:10.1021/acs.energyfuels.8b00551

Zou, C., Xue, H., Xiong, B., Zhang, G., Pan, S., Jia, C., et al. (2021). Connotation, innovation and vision of "carbon neutrality". *Nat. Gas. Ind. B* 8 (5), 523–537. doi:10.1016/j.ngib.2021.08.009

frontiers | Frontiers in Energy Research

TYPE Original Research
PUBLISHED 07 September 2022
DOI 10.3389/fenrg.2022.1007224

OPEN ACCESS

EDITED BY
Daoyi Zhu,
China University of Petroleum, China

REVIEWED BY
Liwu Jiang,
University of Regina, Canada
Changan Shan,
Xi'an Shiyou University, China
Tao Huang,
Zhejiang Ocean University, China

*CORRESPONDENCE
Yitao Huang,
huangyitao518@163.com

SPECIALTY SECTION
This article was submitted to Advanced Clean Fuel Technologies, a section of the journal Frontiers in Energy Research

RECEIVED 30 July 2022
ACCEPTED 15 August 2022
PUBLISHED 07 September 2022

CITATION
Li Y, Huang Y, Ma H, Chang C and Xie W (2022), Study on the development options of tight sandstone oil reservoirs and their influencing factors. *Front. Energy Res.* 10:1007224. doi: 10.3389/fenrg.2022.1007224

Study on the development options of tight sandstone oil reservoirs and their influencing factors

Yongming Li[1], Yitao Huang[1]*, Hanwei Ma[2], Cheng Chang[3] and Weiyang Xie[3]

[1]State Key Laboratory of Oil and Gas Reservoir Geology and Development Engineering, Southwest Petroleum University, Chengdu, China, [2]No.1 Cementing Company, CNPC Bohai Drilling Engineering Company Limited, Renqiu, China, [3]Shale Gas Research Institute, PetroChina Southwest Oil & Gasfield Company, Chengdu, China

The research area of tight sandstone oil reservoirs was selected, a numerical model of the oil reservoir was developed, and a study of the development options and influencing factors was carried out to analyze the influence of different development methods, physical and engineering parameters on the development dynamics. Study shows that the two main factors limiting the efficient development of tight sandstone reservoirs are reservoir properties and formation energy. Fractured horizontal well injection huff and puff development can effectively improve reservoir physical properties and timely replenish formation energy, which is suitable for the development of such oil reservoirs. In dense sandstone reservoirs, its impact on production capacity is also relatively small when the permeability ratio is small. Due to both gravity and reservoir physical properties, the permeability ratio increases, the cumulative oil production of positive rhythm reservoirs decreases and that of reverse rhythm reservoirs increases, and the location of high-quality reservoirs in the upper part of producing wells is conducive to increasing the final recovery rate. A lower oil to water viscosity ratio can significantly increase the swept volume and improve development effect. Hydrophilic reservoirs can reduce the injection pressure and increase the spread range, effectively improving the problem of inability to inject, and improving reservoir hydrophilicity through surface activators can increase reservoir recovery. The water injection rate determines the recovery rate of formation energy. Generally, the faster the rate, the higher the cumulative oil production. Therefore, the rate of water injection should be increased as much as possible, taking into account construction conditions and economic evaluation. Additionally, the effect of water injection on the development effect is different at different stages, so the appropriate timing of water injection is very important to the water injection huff and puff development effect, and the use of early water injection in this research area is not conducive. Soaking can promote pressure and fluid redistribution and improve water injection huff and puff development effect, but soaking for a long time can lead to reservoir contamination and reduce crude oil production, so the preferred time for a soaking is about 20 days.

KEYWORDS

tight sandstone oil reservoir, numerical simulation, development mode, geological factor, engineering factor

Introduction

In recent years, the rapid development of the global economy has led to an increasing demand for oil and gas resources. Since tight oil and gas is widely distributed around the world (Liu; Shi et al.,; Zhang et al., 2022a; Zou, 2014), it has attracted widespread attention worldwide due to its resource potential and exploration value, and the exploration and development of oil and gas is striding from conventional to unconventional oil and gas fields (Hu et al., 2018; Zou et al., 2018; Sun et al., 2019). As a typical tight sandstone oil reservoir with low porosity, low permeability and complex pore roar structure, the H oil reservoir of Liaohe oilfield is a low-porosity and low-permeability reservoir (Wang et al., 2014; Ji, 2016; Wu et al., 2018), and has remarkable characteristics of tight reservoir development. Its production is high in the early stage of development, but it decreases rapidly, with the rate of decrease reaching more than 50% (Liu, 2022). Therefore, the efficient and sustainable development of tight oil reservoirs has become the focus and difficulty of current study.

At present, horizontal well technology combined with segmented multi-stage fracturing technology is commonly used worldwide to achieve efficient development of tight oil reservoirs (Jiang et al., 2017; Zhang, 2020; Guo et al., 2021; Zheng et al., 2021), and the recovery rate can be improved by increasing the stimulated reservoir volume. However, the fracture expansion of tight oil reservoirs is influenced by their own geological conditions with diverse situations (Zhao et al., 2015; Peng et al., 2016; Zhao et al., 2017; Li et al., 2020; Peng et al., 2020), some reservoirs are strongly heterogeneity with positive and reverse rhythm in the vertical direction (Li et al., 2019a; Zhang et al., 2022b), and the two-phase or even three-phase seepage is superimposed on the influence of engineering factors on the development process (Ma et al., 2021; Shen et al., 2022), which makes the seepage mechanism and development law of tight reservoirs very complex (Zafar et al., 2020; Zhao et al., 2021), and the dominant seepage channel is not clear (Li et al., 2019b). At present, the relevant research is still at the core scale (Jing et al., 2021) (Figure 1), and the lack of understanding of the development rules and factors influencing production capacity cannot effectively guide the preparation of development plans for such reservoirs. Based on the numerical model of H reservoir in Liaohe oilfield and comprehensively considered the effects of gravity, capillary force and imbibition, this paper extracts the characteristic wells in typical blocks and conducts a study on the selection of development methods and factors affecting production capacity through the control variables approach to analyze the production performance and remaining oil distribution of characteristic wells in tight oil reservoirs under different development methods, different geological conditions and different engineering conditions, optimize a reasonable development method, analyze the influence laws of different factors, put forward reasonable development strategy suggestions, and provide certain technical support for the preparation of tight oil reservoir development plans.

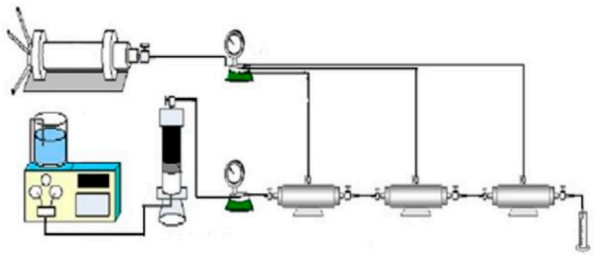

FIGURE 1
Core-scale experimental device for tight oil reservoirs.

Typical reservoir characteristics

The top depth of the H reservoir in the Liaohe field is 2,759.4 m and the bottom depth is 5,507.35 m, with a total thickness of 2,747.95 m. Generally, the reservoir thickness is large and the effective thickness is 100–500 m. The lithology of the block is mainly fine sandstone, siltstone, oil shale and dark red mudstone, with a small amount of sand conglomerate (Figure 2), and the reservoir space is mainly primary pore space, with a very small amount of secondary pore space formed by dissolution (intergranular pores and intra-grain pores, Figure 3). It was found through the porosity and permeability statistics of 203 rock samples from the H reservoir that the reservoir rock gas test permeability was mainly distributed in the range of $1\ \mu m^2 \times 10^{-7}\ \mu m^2$~$16.5\ \mu m^2 \times 10^{-3}\ \mu m^2$, with an average permeability of $0.1\ \mu m^2 \times 10^{-3}\ \mu m^2$, which belonged to the ultra-low permeability type, and the porosity was generally distributed between 2 and 18%, with an average porosity of 7.13%, and the reservoir porosity evaluation was poor. Influenced by sedimentation, diagenesis, dissolution and the degree of filling, the reservoir not only has extremely low porosity and permeability, but also exhibits strong reservoir inhomogeneity, with the local reservoir showing obvious positive and reverse rhythmic features in the longitudinal direction.

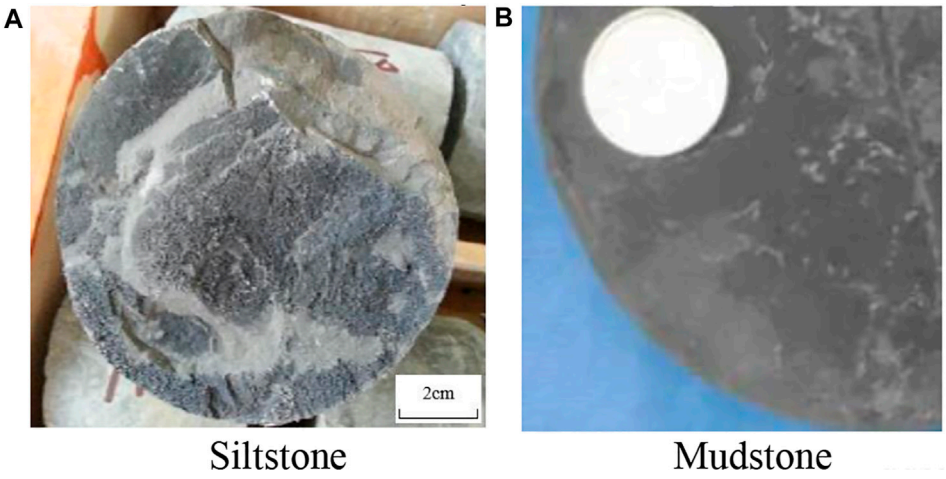

FIGURE 2
Photographs of representative rock samples from the H oil reservoir in the Liaohe Oilfield.

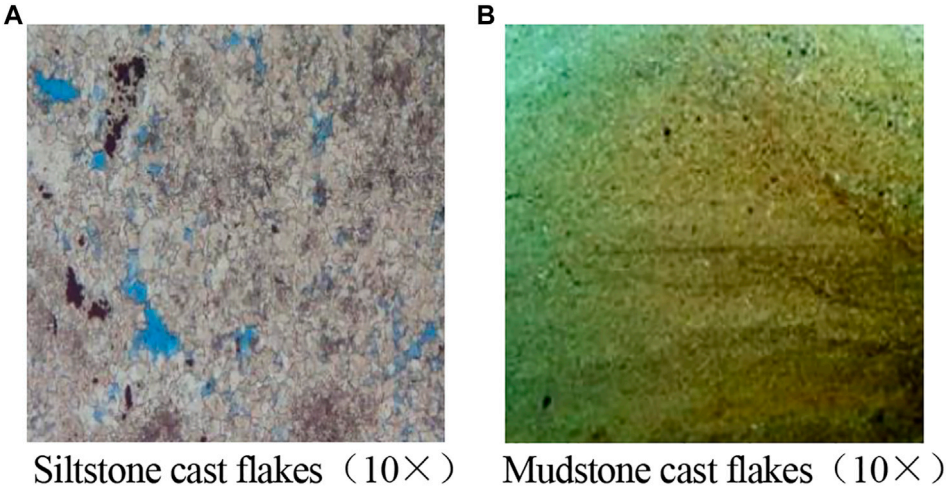

FIGURE 3
Rock cast flake of tight oil reservoir in H reservoir of Liaohe oilfield.

Model building and development solution optimization

A numerical oil reservoir model of the H oil reservoir in the Liaohe oilfield was established, and the characteristic well of the target block-W well was selected for a single well numerical simulation after historical fitting to ensure the accuracy of the model, and a rectangular reservoir with I × J × K of 600 m × 300 m × 100 m was intercepted as the research area (Figure 4), with a grid step of 10 m and a total grid number of 18,000 (60 × 30×10), and the detailed geological parameters are shown in Table 1. In the middle of the research area, there is a horizontal well with a length of 380m, which is both a production well and an injection well.

The research area is being developed with horizontal wells without fracturing for depletion development, horizontal wells after fracturing for depletion development and horizontal wells after fracturing for water injection huff and puff, their development scheme and fracture parameters are listed in Table 2 and Table 3, respectively. As shown in Figure 5, the daily production and cumulative oil production of W wells under three different development methods, from which it can be seen

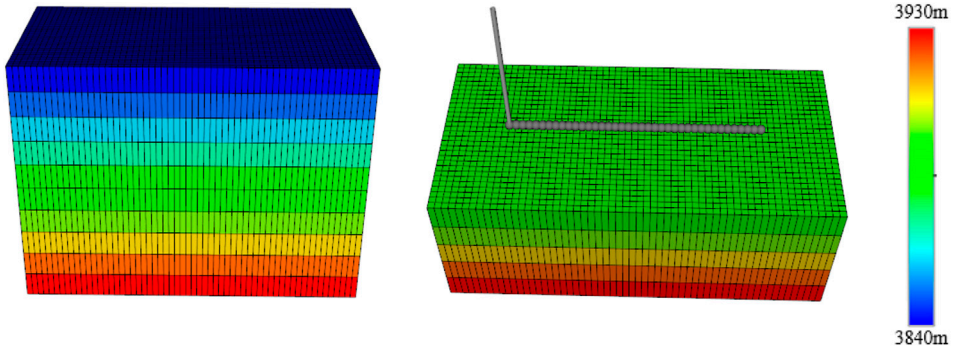

FIGURE 4
Schematic diagram of the burial depth and well location in the research area of well W in the H oil reservoir of the Liaohe oilfield.

TABLE 1 Values of reservoir properties and fluid properties parameters in the research area.

Model parameter	Value	Unit
Reservoir thickness	100	m
Depth at top of reservoir	3,840	m
Porosity	0.145	—
Permeability	0.1	mD
Initial oil saturation	0.7	—
References pressure	30	MPa
Rock Compressibility	0.00025	MPa^{-1}
Water Density	1,000	kg/m^3
Crude oil Density	800	kg/m^3
Viscosity of water	1	mPa·s
Viscosity of crude oil	12	mPa·s

that the effect of reservoir physical properties on production capacity is significant in the early stages of development, with the daily production rate of a single well in a fractured horizontal well being more than five times the capacity of the well in a horizontal well without fracturing measures, but as development progresses this difference decreases rapidly with the decay of formation energy, with better reservoir physical properties and faster decay of daily production in fractured horizontal wells.

Significantly, the formation pressure drops rapidly in the horizontal well fracturing followed by depletion development (Figure 6) in the middle and late stages. Because the depletion development cannot replenish the bottom energy timely and the formation is not supplied with enough fluid, the daily production rate of horizontal wells after fracturing for depletion development decreases rapidly and the daily production rate is extremely low, just like horizontal wells without fracturing for depletion development, and even appears to be lower in the middle and late stages. In contrast, the adoption of horizontal well fracturing followed by water injection huff and puff development can effectively and timely replenish the formation energy, and the high pressure fluid around the fracture timely replenishes the formation pressure deficit and delays the formation pressure drop, which can relatively steadily keep a certain daily production continuous production and thus obtain the highest cumulative oil recovery. In the early stage of development, reservoir energy is sufficient and reservoir physical properties are the main factor controlling single well production. But

TABLE 2 Specific parameters for different development methods.

Development method	Horizontal wells without fracturing for depletion development	Horizontal wells after fracturing for depletion development	Horizontal wells after fracturing for water injection huff and puff	Unit
hydraulic fracture	×	√	√	—
BHP	25	25	25	MPa
water injection rate	—	—	6	m^3/day
water injection time	—	—	30	day
soaking time	—	—	30	day
development time	10	10	10	year

TABLE 3 Fracture parameters of fractured horizontal Wells.

Fracture parameter	Value	Unit
Length of horizontal section	380	m
fracture interval	20	m
number of fractures	20	—
fracture half-length	100	m
fracture width	0.002	m
fracture height	10	m
Permeability of fracture	10,000	mD

in the middle and late stages of development, the formation energy becomes the main factor limiting the production. Therefore, water injection huff and puff development after horizontal well fracturing can effectively improve the reservoir properties of tight reservoirs and timely replenish the underlying energy to achieve stable production in the block.

Impact of physical parameters on water injection huff and puff development

The main physical parameters that affect the effectiveness of water injection huff and puff in tight sandstone reservoirs include reservoir permeability distribution, oil to water viscosity ratio and reservoir wettability (Sun et al., 2021; Zhu et al., 2021).

Impact of permeability on development effectiveness

Usually speaking, tight sandstone oil reservoirs exhibit strong reservoir inhomogeneity, and the local reservoirs show positive rhythm and reverse rhythm characteristics in the longitudinal direction. According to the reservoir physical conditions of H reservoir in Liaohe oilfield, the influence of different permeability ratios (Table 4) on the development effect under positive and reverse rhythm conditions was designed in conjunction with the permeability statistics of reservoir rock samples.

As shown in Figure 7, the two curves are the cumulative oil production for different permeability ratios under positive and reverse rhythm conditions respectively. It can be seen, from the figure, that the positive rhythm reservoirs, with increasing permeability ratios, show a decreasing trend in cumulative oil recovery and overall show a negative phase relationship. Conversely, cumulative oil recovery from reverse rhythm reservoirs increases with increasing permeability ratio in a positive correlation. Bounded by a permeability ratio of 4, when the permeability ratio is less than 4, production is less affected by permeability, and when the permeability ratio is greater than 4, production capacity varies significantly with permeability. The main reason for this is that the permeability of tight reservoirs is extremely small, and changes in permeability ratio in the range 0–4 have a small effect on permeability; when the permeability ratio is greater than 4, the permeability of the upper part of the reservoir is reduced by an order of magnitude and the permeability of the lower part of the reservoir is significantly

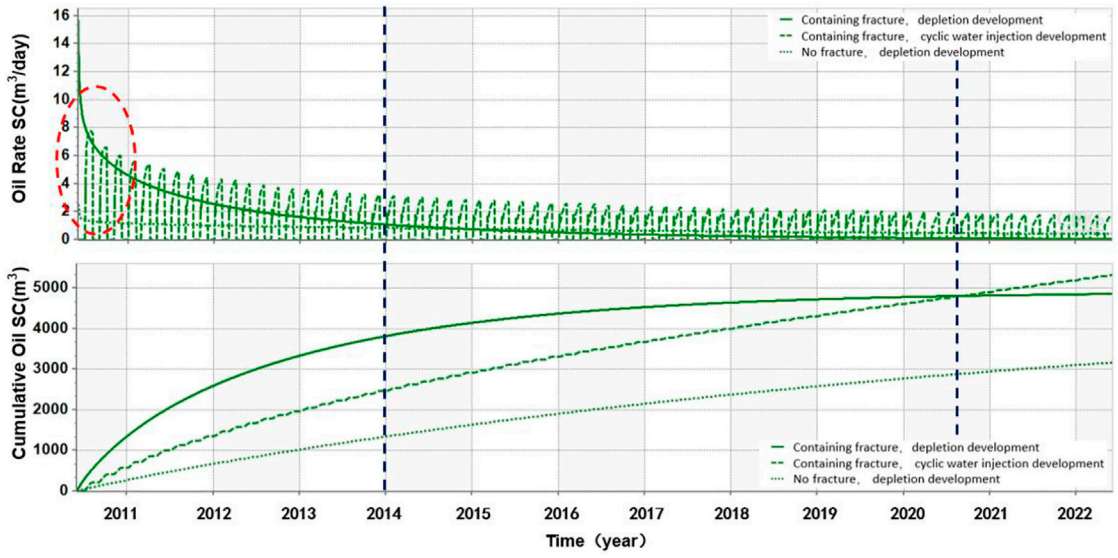

FIGURE 5
Daily and cumulative oil production curves for well W under different development methods.

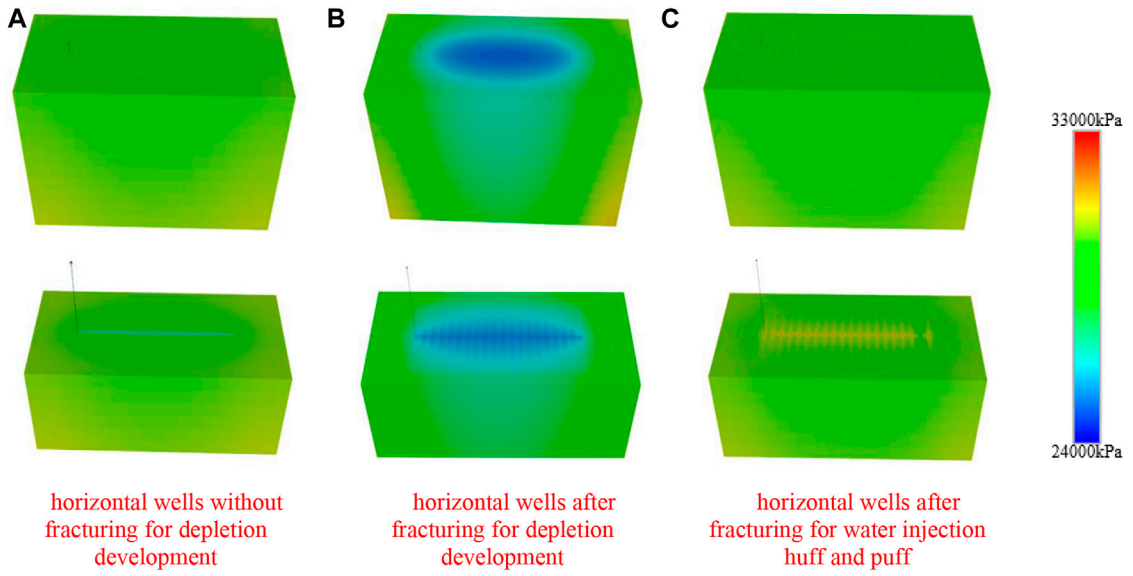

FIGURE 6
Pressure distribution under different development methods in metaphase development.

improved, resulting in significant changes in cumulative production.

Statistics on the ratio of the production in the upper and lower parts of the reservoir to the geological reserves under different permeability ratios (Figure 8) show that the production share of both the upper and lower part of the positive rhythm reservoir decreases to different degrees as the permeability ratio increases. As the producing wells are in the middle of the reservoir, the decrease in the production share in the lower part of the reservoir is more pronounced due to the influence of gravity. Although the physical properties of the lower part of the reservoir become better, no effective seepage channel is established between the reservoir and the wellbore, so it cannot make an effective contribution to production; with the increase in permeability ratio, the physical properties of the upper part of the reverse rhythm reservoir are significantly improved, and the production share of the lower part of the reservoir decreases, but the decrease is smaller, making the overall trend of reservoir production increase.

Impact of oil to water viscosity ratio on development effectiveness

The oil to water viscosity ratio is the ratio of the viscosity of the crude oil in the reservoir to the viscosity of the replacement fluid (water is used in this research), which not only affects the area swept efficiency but also the volume swept coefficient. In order to investigate the effect of different viscosity ratios on the development effect of tight oil reservoirs, the influence law of oil-water viscosity ratio from 1 to 60 on the cumulative oil production of H oil reservoir was designed. Figure 9 shows the cumulative oil production for different oil-water viscosity ratios, which is clear that the cumulative oil production is

TABLE 4 Distribution of oil reservoir permeability at different permeability ratios.

Permeability grade difference	Level 1 (μm²)	Level 2 (μm²)	Level 3 (μm²)	Level 4 (μm²)	Level 5 (μm²)	Level 6 (μm²)	Level 7 (μm²)	Level 8 (μm²)	Level 9 (μm²)	Level 10 (μm²)
1.21	0.0909	0.0927	0.0945	0.0964	0.0982	0.1	0.1025	0.105	0.1075	0.11
2.25	0.0667	0.0733	0.0800	0.0867	0.0933	0.1	0.1125	0.125	0.1375	0.15
4	0.0500	0.0600	0.0700	0.0800	0.0900	0.1	0.125	0.15	0.175	0.2
16	0.0025	0.0220	0.0415	0.0610	0.0805	0.1	0.175	0.25	0.325	0.4
25	0.0200	0.0360	0.0520	0.0680	0.0840	0.1	0.2	0.3	0.4	0.5
100	0.0100	0.0280	0.0460	0.0640	0.0820	0.1	0.325	0.55	0.775	1

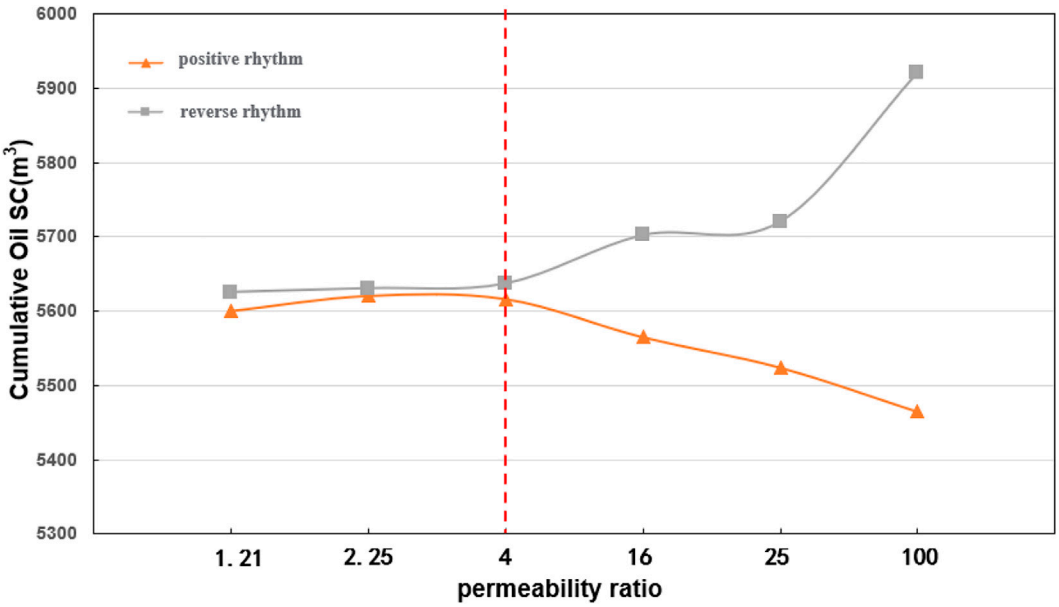

FIGURE 7
Cumulative oil production from W wells under different permeability ratios in positive and reverse rhythm.

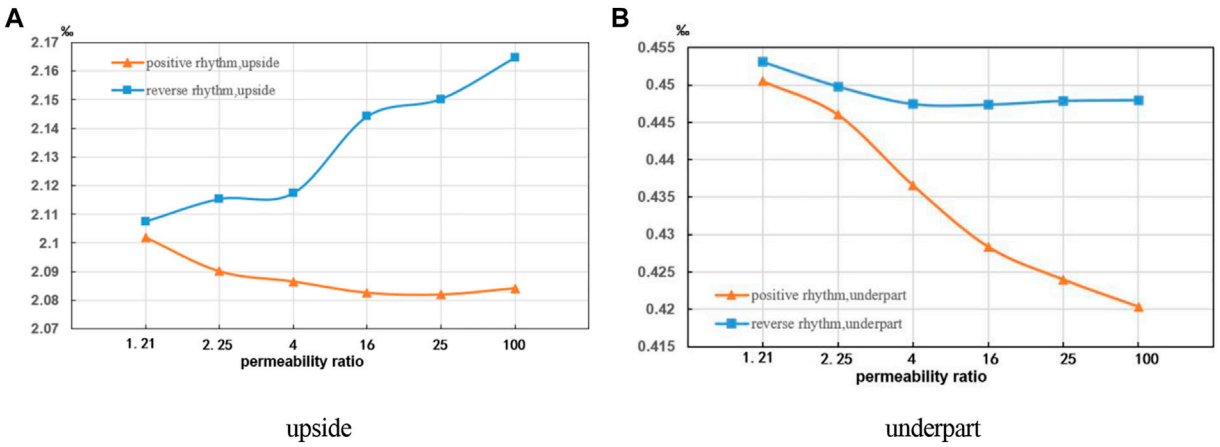

FIGURE 8
Production ratio of upper and lower reservoirs under different permeability ratios of positive and reverse rhythms.

negatively related to the oil-water viscosity ratio, and the cumulative oil production corresponding to different oil-water viscosity ratios varies greatly. When the crude oil viscosity changes from 1 mPa s to 60 mPa s, the cumulative oil production corresponding to an oil-water viscosity ratio of 60 is less than 1/4 of the oil production corresponding to an oil-water viscosity ratio of 1. From the start of production, the low oil-water viscosity ratio shows an obvious production advantage, laying the foundation for the highest recovery rate in the end.

Comparing the pressure distribution in the layer with wellbore at the completion of the oil recovery phase of the first water injection huff and puff cycle under different oil-water viscosity ratios (Figure 10), it can be found that the pressure spreading range gradually decreases with the increase of oil-water viscosity ratio, only the four corners of the

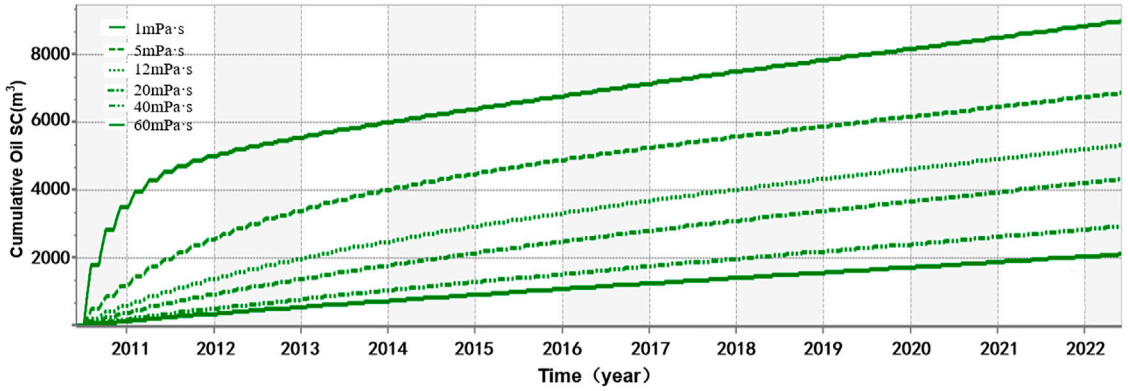

FIGURE 9
Cumulative oil production versus oil to water viscosity ratio curve.

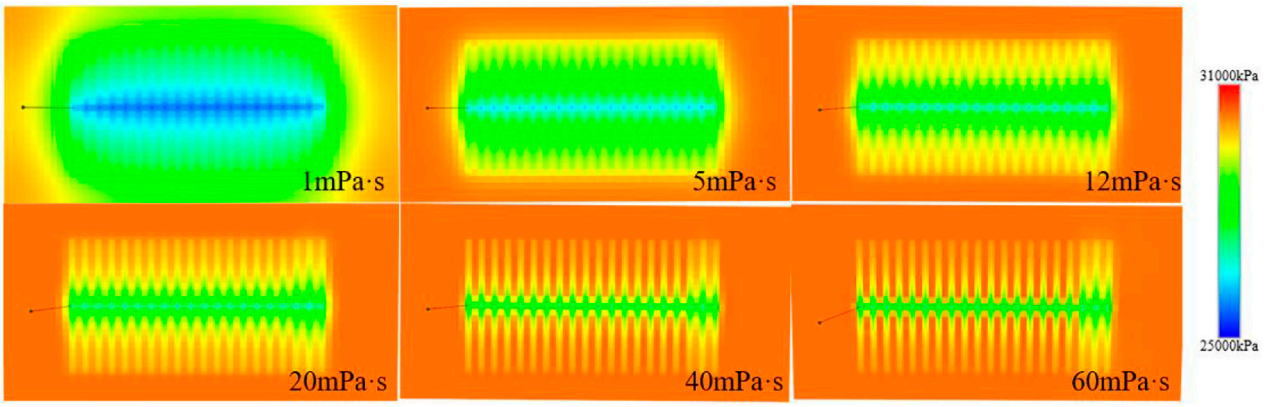

FIGURE 10
Pressure sweep range for different oil to water viscosity ratios at the end of the first production phase.

reservoir are difficult to spread under 1 mPa s condition, while under 40 mPa s, and 60 mPa s conditions, the pressure can only spread to a very small part of the area near the wellbore and the fracture. During the injection stage (Figure 11), reservoirs with low oil-water viscosity ratios are able to spread the energy replenished to the formation relatively evenly throughout the reservoir, while the larger the oil-water viscosity ratio, the smaller the spread of replenished energy, holding pressure near the wellbore and fractures, making the injection water repeatedly flush near the well and near the fractures, which cannot effectively improve the final recovery. In practice, the oil to water viscosity ratio can be reduced by reducing the viscosity of the crude oil or increasing the viscosity of the replacement fluid, thereby increasing the recovery of the reservoir.

Impact of wettability on development effectiveness

Reservoir wettability will affect the distribution of reservoir fluids within the pores of the rock and the ability of the oil and water phases to percolate through the reservoir porous media. When the oil and water saturation in the reservoir are the same, the wettability of the reservoir rock will have a decisive influence on the final effect of water injection huff and puff development. The relative permeability curves (Figure 12) of different wettability obtained experimentally were substituted into the numerical model, and the cumulative oil recovery results obtained for the research area under different wettability conditions are shown in Figure 13, with the final oil recovery from hydrophilic reservoirs being significantly higher than that

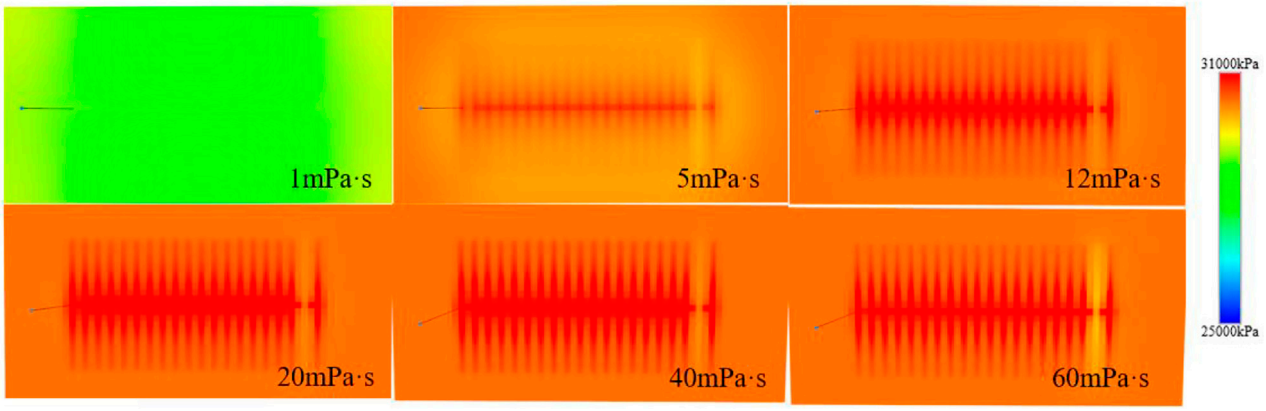

FIGURE 11
Pressure sweep range for different oil to water viscosity ratios at the end of the second injection phase.

from oleophilic reservoirs. It is easy to see, combined with the bottom well flow pressure (Figure 14) and the pressure distribution of the different wetting reservoirs at the end of the second injection phase (Figure 15), that the bottom well flow pressure of the oil-wet reservoir is always higher than the bottom well flow pressure of the water-wet reservoir during water injection, and the high-pressure zone near the wellbore and fracture of the reservoir is more widely distributed; while the pressure ripple range is smaller than that of the water-wet reservoir during production. When water is injected, water in the oil-wet reservoir as a non-wetting phase has a greater resistance to percolation, which is not conducive to pressure diffusion to replenish the energy deficit of the formation. In the actual production process, surface activators can be used to change the reservoir wettability to achieve the purpose of improving the water injection huff and puff effect.

Impact of engineering parameters on water injection huff and puff development

The main engineering parameters that affect the effect of water injection huff and puff in tight sandstone reservoirs

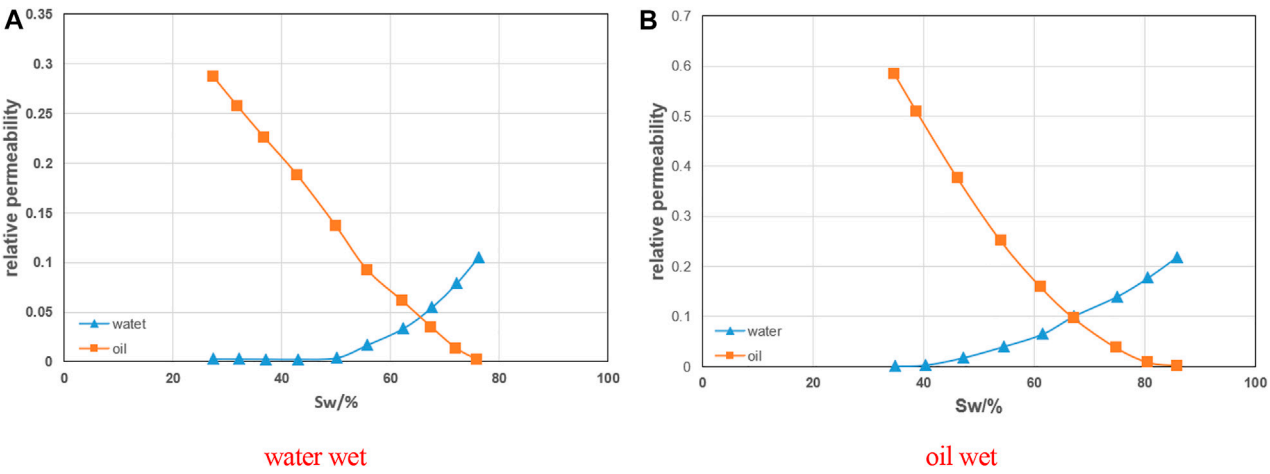

FIGURE 12
The relative permeability curves of different wettability.

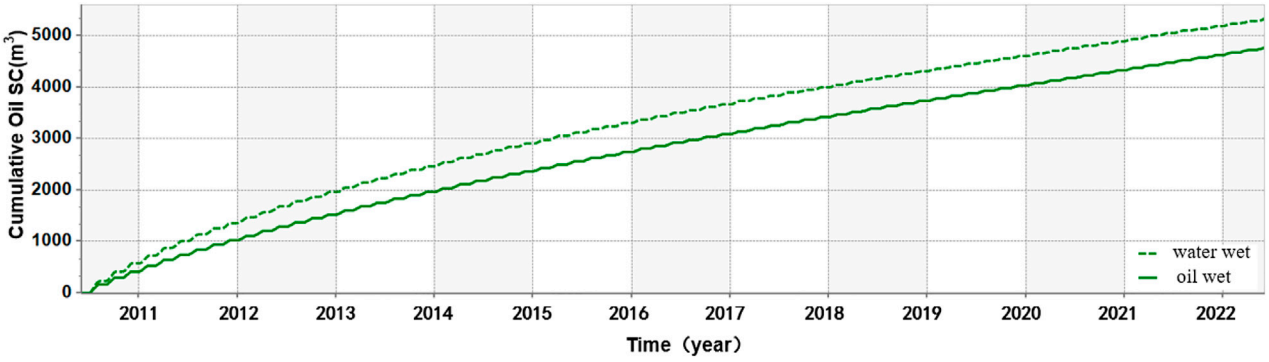

FIGURE 13
Cumulative oil recovery of reservoirs with different wettability.

include injection rate, injection volume and soaking time (Wang et al., 2021), and the effect of these engineering parameters on the development effect was studied for the sixth round of water injection huff and puff.

Impact of water injection rate on development effectiveness

Keeping the water injection volume and production pressure differential constant, the production of a single well in round six was simulated at water injection rates of 3 m3/d, 6 m3/d, 9 m3/d, 12 m3/d, 15 m3/d, 18 m3/d and 30 m3/d respectively. It is easy to see from Figure 16 that if the water injection rate is kept constant, the higher the water injection rate is, the greater the cumulative oil production from the reservoir, and the rate of increase in cumulative oil production gradually slows down as the water injection rate increases; while when the water injection rate is 30 m3/d, the rate of increase in cumulative oil production is already very small, and increasing the water injection rate has less impact on the increase in production. The flow pressure at the bottom of the producing well increases gradually with the rate of water injection, which effectively replenishes the formation energy and is an important reason for increasing the rate of water injection to increase production, and the injection rate can be increased as much as possible to increase crude oil production while meeting the construction pressure conditions.

Impact of water injection volume on development effectiveness

Holding the injection rate and production pressure differential constant, the reservoir production was

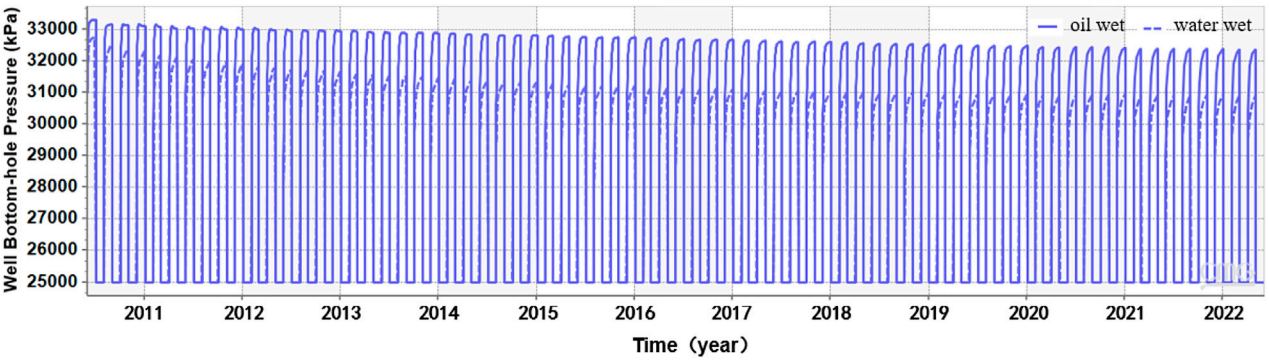

FIGURE 14
Bottom flow pressure in well W under different wettability conditions.

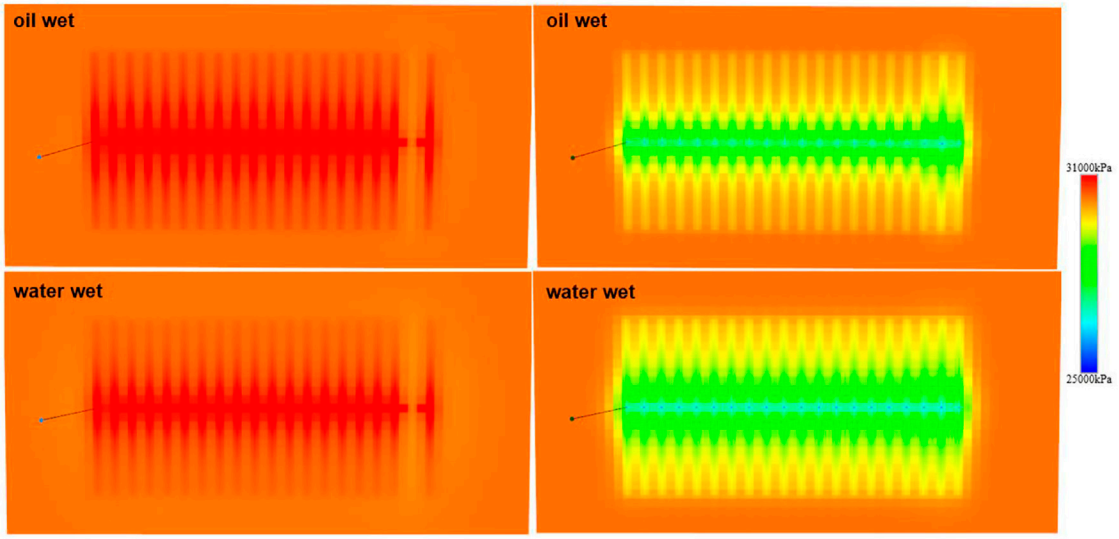

FIGURE 15
Pressure distribution in reservoirs with different wettability at the end of the second phase of water injection.

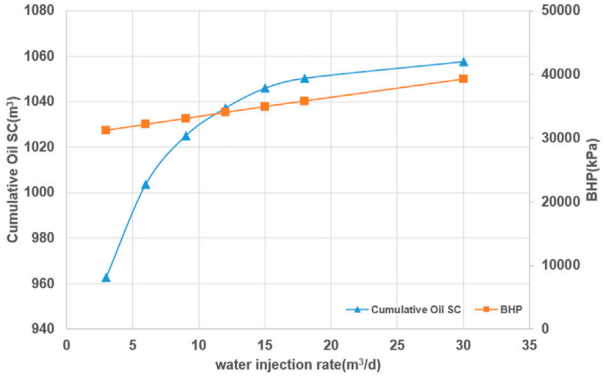

FIGURE 16
Cumulative oil recovery for the first six rounds and bottomhole flow pressure for the sixth round at different injection rates.

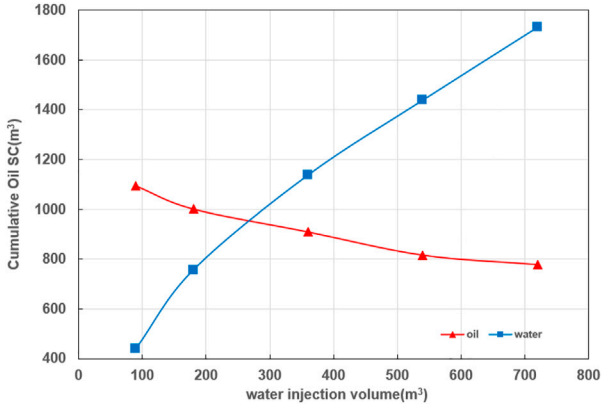

FIGURE 17
Sub-cumulative oil and water production from the first six rounds (pre-development) under different water injection conditions.

simulated for injection volumes of 90 m^3, 180 m^3, 360 m^3, 540 and 720 m^3 respectively. As shown in Figure 17, the relationship between cumulative oil production, cumulative water production and water injection, i.e., cumulative oil production from the reservoir gradually decreases with increasing water injection, and the two are negatively correlated, but cumulative water production rises rapidly with increasing water injection, and the two are positively correlated. This phenomenon is due to the turns of water injection selected for this research was at the pre-development stage, with high remaining recoverable reserves and sufficient formation energy. Excessive injection water formed a high pressure zone near the wellbore and fractures (Figure 18), which impeded the percolation of crude oil into the wellbore and fractures, while the extremely poor physical properties of the dense reservoir made it difficult for both injection water and energy to spread to the far well zone. When the well is opened up again, the injection water is rapidly produced to the surface

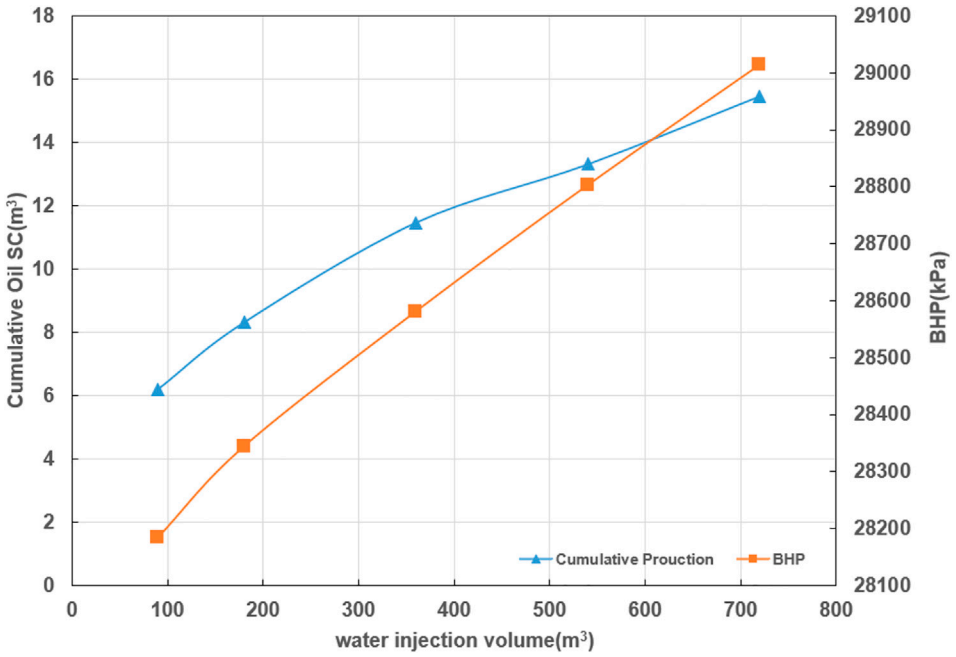

FIGURE 18
Reservoir pressure distribution after the sixth round of water injection under different water injection conditions.

along the fracture and wellbore, resulting in ineffective circulation of the injection water. In the later stages of development, after a long period of production, the reservoir energy deficit, when water injection can effectively replenish the formation energy, the cumulative oil production within a round rises gradually with the increase of water injection (Figure 19). Although water injection can effectively replenish the energy of the formation, the right timing and volume of water injection should be selected in the actual production process.

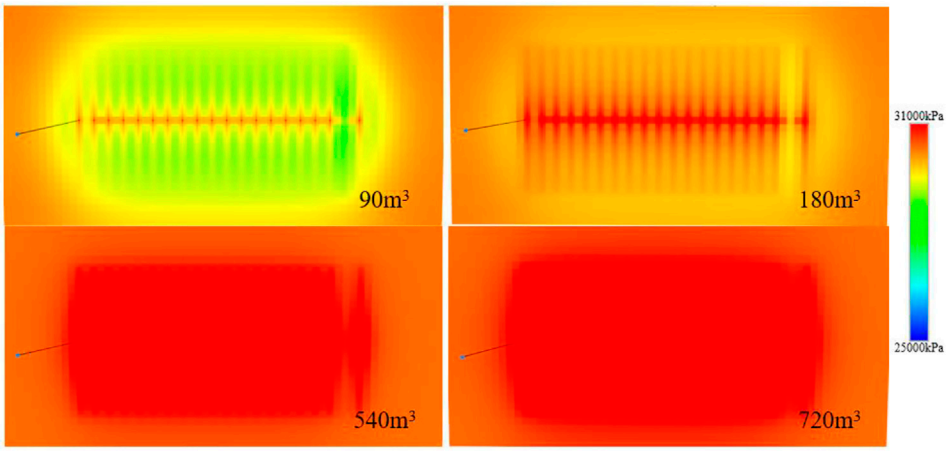

FIGURE 19
Cumulative oil production and bottomhole pressure in late development rounds under different water injection conditions.

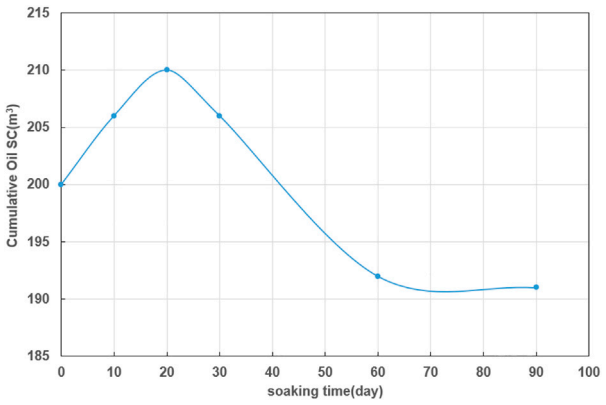

FIGURE 20
The sixth round of oil recovery with different soaking time.

Impact of soaking time on development effectiveness

The water injection rate, water volume and production pressure differential were kept constant, and soaking times of 0, 10, 20, 30, 60, and 90 days were designed to investigate the effect of it on the development effect.

The relationship between oil recovery and soaking time for the sixth round is shown in Figure 20, which shows that as the soaking time increases, the cumulative oil recovery first increases, then decreases and finally plateaus. When the soaking time is less than 20 days, the time for pressure and fluid redistribution in the reservoir is more adequate as the soaking time increases, avoiding the accumulation of injection water and supplementary formation energy in the near-well zone (Figure 21), which is conducive to improving the water injection huff and puff effect. However, with the further increase of the soaking time, influenced by the capillary force, the injection water enters the deep part of the formation and contaminates the reservoir, which is not conducive to improving the recovery rate. The optimal soaking time for this research area is 20 days.

Conclusion

1) Reservoir physical properties and formation energy are the two key factors limiting the efficient development of tight sandstone reservoirs; water injection huff and puff development of fractured horizontal wells can effectively improve reservoir physical properties and timely replenish the formation energy deficit, which is the optimal development method for H oil reservoirs in Liaohe oilfield.
2) The cumulative oil production in positive rhythm reservoirs is negatively correlated with the permeability ratio, while it in reverse rhythm reservoirs is positively correlated with the permeability ratio. In tight reservoirs, when the permeability ratio is lower than 4, the effect of permeability ratio on production capacity can be ignored. In the actual development process, formation classification should be based on reverse rhythm as far as possible. The oil-water viscosity ratio is negatively correlated with cumulative oil production, the larger the oil-water viscosity ratio, the smaller the spread area, in the actual development process, the oil-water viscosity ratio can be reduced by reducing the viscosity of the crude oil or increasing the viscosity of the replacement fluid to improve recovery. Hydrophilic reservoirs can effectively reduce water injection pressure and expand the swept area, which is conducive to water injection huff and puff development.
3) The injection rate determines how quickly the formation energy is replenished and is also an important factor affecting the construction cycle, the best injection rate for this research area is 15 m^3/d~18 m^3/d. Water injection can effectively replenish the formation energy, but in the actual production process should choose the right timing of water injection, this research area can try to replenish the formation energy by water injection in the middle and late stages. Soaking can promote the redistribution of pressure and fluid in the reservoir and improve the development effect of water injection huff and puff, but shutting in the well for too long can lead to reservoir contamination and reduced

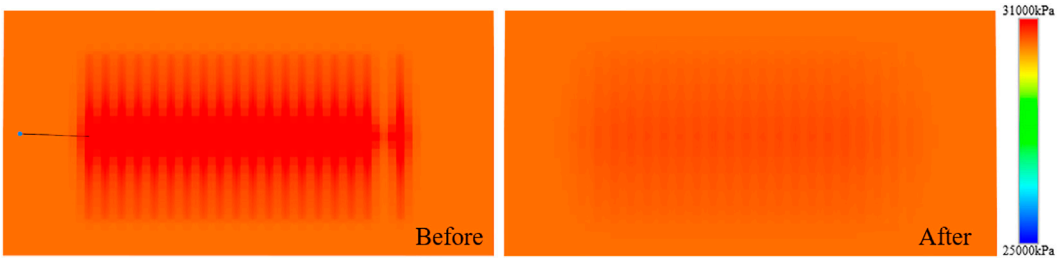

FIGURE 21
Reservoir pressure distribution before and after soaking.

crude oil production. The optimum soaking time for the research area is 20 days.

Data availability statement

The raw data supporting the conclusions of this article will be made available by the authors, without undue reservation.

Author contributions

YH, YL, and CC contributed to conception and design of the study. WX organized the database. HM performed the statistical analysis. YH wrote the first draft of the manuscript. YH and YL wrote sections of the manuscript. All authors contributed to manuscript revision, read, and approved the submitted version.

Funding

This study was supported by the Science and Technology Cooperation Project of the CNPC-SWPU Innovation Alliance, the National Natural Science Foundation of China (Grant no. U19A2043, U21B2071, and 52174033), and Natural Science Foundation of Sichuan Province (NSFSC) (No. 2022NSFSC0971).

Conflict of interest

Author HM was employed by the company CNPC Bohai Drilling Engineering Company Limited. Authors CC and WX were employed by PetroChina Southwest Oil & Gasfield Company.

The remaining authors declare that the research was conducted in the absence of any commercial or financial relationships that could be construed as a potential conflict of interest.

Publisher's note

References

Guo, J., Zhou, F., Hu, X., Liu, X., and Wang, B. (2021). Mechanical mechanism of enhanced fracturing of tight oil horizontal Wells in Santanghu Basin. *Fault-block oil gas fields* 28 (01), 57–62. doi:10.6056/dkyqt202101010

Hu, S., Zhu, R., Wu, S., Bai, B., Yang, Z., and Cui, J. (2018). Profitable exploration and development of continental tight oil in China. *Petroleum Explor. Dev.* 45 (4), 737–748. doi:10.11698/PED.2018.04.20

Ji, T. (2016). *Characteristics of tight oil accumulation in Leijia area, Liaohe Depression*. East China: China University of Petroleum.

Jiang, T., Teng, X., and Yang, X. (2017). Integrated techniques for rapid and highly-efficient development and production of ultra-deep tight sand gas reservoirs of Keshen 8 Block in the Tarim Basin. *Nat. Gas. Ind. B* 4 (1), 30–38. doi:10.1016/j.ngib.2017.07.005

Jing, L., Li, X., Song, M., Liu, H. M., Feng, Y. C., and Liu, C. (2021). Investigating microscopic seepage characteristics and fracture effectiveness of tight sandstones: a digital core approach. *Pet. Sci.* 18, 173–182. doi:10.1007/s12182-020-00464-8

Li, Z., Duan, Y., Mingqiang, W., Peng, Y., and Chen, Q. (2019). Pressure performance of interlaced fracture networks in shale gas reservoirs with consideration of induced fractures. *J. Petroleum Sci. Eng.* 178, 294–310. doi:10.1016/j.petrol.2019.03.048

Li, X. Z., Lu, D. T., Luo, R. L., Sun, Y., Shen, W., Hu, Y., et al. (2019). Quantitative criteria for identifying main flow channels in complex porous media. *Petroleum Explor. Dev.* 46 (5), 998–1005. doi:10.1016/s1876-3804(19)60256-9

Li, Z., Duan, Y., Peng, Y., Wei, M., and Wang, R. (2020). A laboratory study of microcracks variations in shale induced by temperature change. *Fuel* 280, 118636. doi:10.1016/j.fuel.2020.118636

Liu, M. Logging evaluation technology and development direction of tight reservoir. *Special oil gas reservoirs*, 1–12.

Liu, Y. (2022). *Study on seepage law and production prediction of multi-stage fracturing of horizontal well in tight reservoir*. Beijing: University of Science and Technology Beijing.

Ma, T. R., Zhang, K. N., Shen, W. J., Guo, C., and Xu, H. (2021). Discontinuous and continuous Galerkin methods for compressible single-phase and two-phase flow in fractured porous media. *Adv. Water Resour.* 156, 104039. doi:10.1016/j.advwatres.2021.104039

Peng, Y., Li, Y., and Zhao, J. (2016). A novel approach to simulate the stress and displacement fields induced by hydraulic fractures under arbitrarily distributed inner pressure. *J. Nat. Gas Sci. Eng.* 35, 1079–1087. doi:10.1016/j.jngse.2016.09.054

Peng, Y., Zhao, J., Sepehrnoori, K., and Li, Z. (2020). Fractional model for simulating the viscoelastic behavior of artificial fracture in shale gas. *Eng. Fract. Mech.* 228, 106892. doi:10.1016/j.engfracmech.2020.106892

Shen, W. J., Ma, T. R., Li, X. Z., Sun, B., Hu, Y., and Xu, J. (2022). Fully coupled modeling of two-phase fluid flow and geomechanics in ultra-deep natural gas reservoirs. *Phys. Fluids* 34 (4), 043101. doi:10.1063/5.0084975

Shi, X., Sun, L., Zhan, J., Li, B., Han, X., Lu, H., et al. . Carbon dioxide hubbub technology and its application in tight oil horizontal Wells in northern Songliao Basin. *Acta Pet. Sin.*, 1–9. doi:10.7623/syxb202207010

Sun, L., Zou, C., Jia, A., Wei, Y., Zhu, R., Wu, S., et al. (2019). Development characteristics and orientation of tight oil and gas in China. *Petroleum Explor. Dev.* 46 (6), 1015–1026. doi:10.1016/S1876-3804(19)60264-8

Sun, Y., Xin, Y., Lyu, F., and Dai, C. L. (2021). Experimental study on the mechanism of adsorption-improved imbibition in oil-wet tight sandstone by a nonionic surfactant for enhanced oil recovery. *Petroleum Sci.* 18 (4), 1115–1126. doi:10.1016/j.petsci.2021.07.005

Wang, Y., Dong, Y., Chen, N., Wang, Q., and Zheng, X. (2014). Formation conditions and resource potential of tight oil in Ludong Sag. *Special oil gas reservoirs* 21 (04), 53–57+153. doi:10.3969/j.issn.1006-6535.2014.04.012

Wang, J., Liu, H., Qian, G., and Peng, Y. C. (2021). Mechanisms and capacity of high-pressure soaking after hydraulic fracturing in tight/shale oil reservoirs. *Pet. Sci.* 18, 546–564. doi:10.1007/s12182-020-00524-z

Wu, L., Guo, X., Luo, W., Zhang, Z., and Zhang, W. (2018). Study on influencing factors of productivity of fractured horizontal wells in tight oil reservoirs: A case study of damintun tight oil horizontal wells in Liaohe oilfield. *Unconv. oil gas* 5 (03), 56–62. doi:10.3969/j.issn.2095-8471.2018.03.009

Zafar, A., Su, Y., Li, L., Fu, J. G., Mehmood, A., Ouyang, W. P., et al. (2020). Tight gas production model considering TPG as a function of pore pressure, permeability and water saturation. *Pet. Sci.* 17, 1356–1369. doi:10.1007/s12182-020-00430-4

Zhang, D., Zhang, L., Tang, H., and Zhao, Y. (2022). Fully coupled fluid-solid productivity numerical simulation of multistage fractured horizontal well in tight

oil reservoirs. *Petroleum Explor. Dev.* 49 (2), 338–347. doi:10.1016/S1876-3804(22)60032-6

Zhang, L., Wang, T., Albouzedy, I., Wang, W., and Ren, X. (2022). Factors influencing the horizontal inter-well interference in tight gas reservoirs. *Nat. Gas. Ind. B* 9 (3), 308–317. doi:10.1016/j.ngib.2022.06.003

Zhang, K. (2020). Research on influencing factors of productivity after multistage fracturing of tight oil horizontal Wells. *China Petroleum Chem. Stand. Qual.* 40 (17), 39–40. doi:10.3969/j.issn.1673-4076.2020.17.020

Zhao, J., Peng, Y., Li, Y., and Xiao, W. (2015). Analytical model for simulating and analyzing the influence of interfacial slip on fracture height propagation in shale gas layers. *Environ. Earth Sci.* 73 (10), 5867–5875. doi:10.1007/s12665-015-4360-4

Zhao, J., Peng, Y., Li, Y., and Tian, Z. (2017). Applicable conditions and analytical corrections of plane strain assumption in the simulation of hydraulic fracturing. *Petroleum Explor. Dev.* 44 (3), 454–461. doi:10.1016/s1876-3804(17)30052-6

Zhao, Y., Liu, X., Zhang, L., Tang, H., Xiong, Y., Guo, J., et al. (2021). Laws of gas and water flow and mechanism of reservoir drying in tight sandstone gas reservoirs. *Nat. Gas. Ind. B* 8 (2), 195–204. doi:10.1016/j.ngib.2020.09.018

Zheng, Y., Han, X., Zeng, J., Zhou, C., Zhou, L., and Chen, W. (2021). Practice of high-intensity volume fracturing in the Shaximiao Formation tight sandstone gas reservoirs of the Qiulin Block, central Sichuan Basin. *Nat. Gas. Ind. B* 8 (4), 367–375. doi:10.1016/j.ngib.2021.07.007

Zhu, C., Guo, W., Wang, Y., Li, Y., Gong, Y., Xu, L., et al. (2021). Experimental study of enhanced oil recovery by CO2 huff-n-puff in shales and tight sandstones with fractures. *Pet. Sci.* 18, 852–869. doi:10.1007/s12182-020-00538-7

Zou, C. (2014). *Unconventional petroleum geology*. Beijing: Geological Publishing House.

Zou, C., Yang, Z., He, D., Wei, Y., Li, J., Jia, A., et al. (2018). Theory, technology and prospects of conventional and unconventional natural gas. *Petroleum Explor. Dev.* 45 (4), 575–587. doi:10.11698/PED.2018.04.04

frontiers | Frontiers in Energy Research

TYPE Original Research
PUBLISHED 07 September 2022
DOI 10.3389/fenrg.2022.958830

OPEN ACCESS

EDITED BY
Yibo Li,
Southwest Petroleum University, China

REVIEWED BY
Kang Zhou,
Shandong University of Science and Technology, China
Hanmin Tu,
Southwest Petroleum University, China

*CORRESPONDENCE
Chuanbao Zhang,
zhangchuanbao333@126.com

SPECIALTY SECTION
This article was submitted to Advanced Clean Fuel Technologies, a section of the journal Frontiers in Energy Research

RECEIVED 01 June 2022
ACCEPTED 25 July 2022
PUBLISHED 07 September 2022

CITATION
Zhang C, Wu G, Huang H and Zhan H (2022), Improvement of oil recovery factor in tight reservoirs: A laboratory approach based on carbon dioxide enhanced oil recovery methods. *Front. Energy Res.* 10:958830. doi: 10.3389/fenrg.2022.958830

Improvement of oil recovery factor in tight reservoirs: A laboratory approach based on carbon dioxide enhanced oil recovery methods

Chuanbao Zhang[1]*, Gang Wu[2], Hao Huang[3] and Hongyang Zhan[4]

[1]Exploration and Development Research Institute, Shengli Oilfield Company, SINOPEC, Dongying, China, [2]The Tianjin Gas Storage Branch, PetroChina Dagang Oilfield Company, Tianjin, China, [3]11th Oil Production Plant of Changqing Oilfield Company, PetroChina, Xi'an, China, [4]Research Institute of Petroleum Exploration & Development, PetroChina Xinjiang Oilfield Company, Karamay, China

Production from unconventional oil reservoirs has always been a critical issue for the oil industry. In this regard, we implemented a set of experimental scenarios containing CO_2/N_2 cyclic injection, the foams generated by nitrogen and carbon dioxide, cyclic carbon dioxide injection, and a combined effect of carbon dioxide and surfactant enhanced oil recovery methods. As water injection has reached a plateau around two pore volume injection, we continued the tests from two pore volume injection for different scenarios. It was observed that CO_2/N_2-foam has the highest oil recovery factor of 34.9%; however, CO_2-foam, regarding more feasibility than N_2, witnessed the highest oil recovery factor after CO_2/N_2-foam. On the other hand, the incremental oil recovery factor for surfactant flooding, carbonated water flooding, and carbonated water with surfactant flooding is measured at 4.9, 8.5, and 10.6%, respectively.

KEYWORDS

enhanced oil recovery, carbon dioxide, cyclic injection, generated foam, carbonated water with surfactant, tight oil reservoirs

Introduction

Due to the importance of unconventional oil reservoirs to produce more oil volume and supply the various industrial demands, these reservoirs have become the most priority for oil production (Jia et al., 2012; Wang et al., 2015; Sheng, 2017). Another reason is reducing the oil production rate in conventional reservoirs, and they could not satisfy the

Abbreviations: CO_2, Carbon dioxide; N_2, Nitrogen; EOR, Enhanced oil recovery; PV, Pore Volume; SLPM, the foaming agent provided by Shengli Oilfield Company SINOPEC; SLBHJ, the surfactant provided by Shengli Oilfield Company SINOPEC.

TABLE 1 The component of dead oil, solution gas, and live oil.

Component	Dead oil mole fraction	Solution gas mole fraction	Live oil mole fraction
CO_2	/	0.51	0.13
N2	/	0.92	0.45
C1	/	65.87	31.06
C2	0.01	19.80	9.57
C3	0.04	12.00	5.78
IC4	0.14	0.38	0.29
NC4	0.49	0.31	0.58
IC5	0.98	0.13	0.89
NC5	0.36	0.06	0.36
C6	0.69	0.02	0.61
C7	1.78	/	1.56
C8	0.93	/	0.75
C9	3.42	/	2.65
C10	5.08	/	3.85
C11	86.08	/	41.47

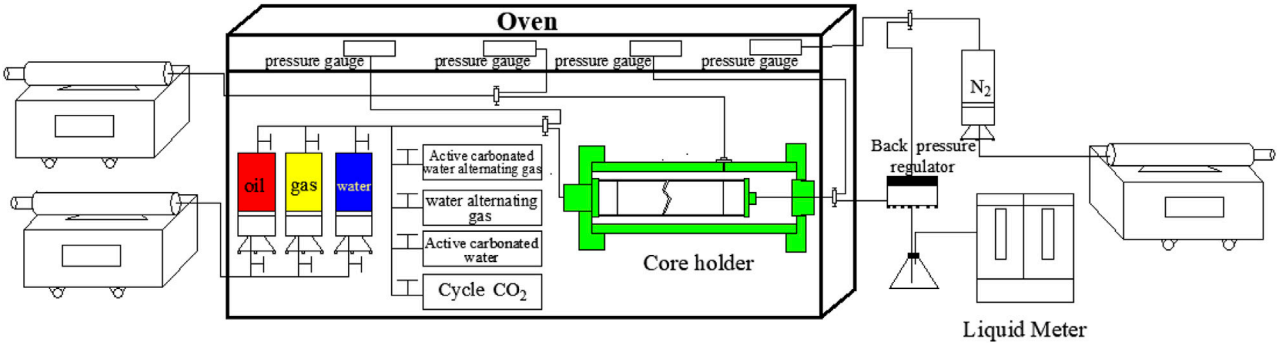

FIGURE 1
Experimental apparatus for coreflooding.

petroleum industries' subsections. Implementation of carbon dioxide would be of significance in unconventional reservoirs as it can reduce the crude oil viscosity during the injection of CO_2 (Carbon dioxide) and increase the sweep efficiency in porous media (Holm et al., 1974; Chung et al., 1988; Manrique et al., 2010; Luo et al., 2017). Furthermore, it can provide better mobilization for oil, especially in trapped zones and low permeable layers during the CO_2 injection (Tovar et al., 2014; Yu et al., 2015; Zhou et al., 2020). Another application of CO_2 injection would be related to the geological storage of carbon dioxide, which enables proper climate change mitigation (Busch et al., 2008; Torres et al., 2018; Mahzari et al., 2020; Guo et al., 2021). Some researchers developed comprehensive models based on the geological and petrophysical data to determine the appropriateness of EOR (Enhance oil recovery) methods based on carbon dioxide injection. The following characteristics have been considered in the model to provide more valid results. These are minimum miscible pressure, hydraulic fracture processes, and observed data from swelling tests. It is concluded that injection of CO_2 could increase the oil production rate from 43 to 58% in a single permeability-porosity model. However, this method is adequately efficient in unconventional reservoirs; it is utterly dependent on the relative permeability, which can change the simulation results significantly. Therefore, it was recommended to provide sensitivity analysis before any operational performances and field test applications to ensure

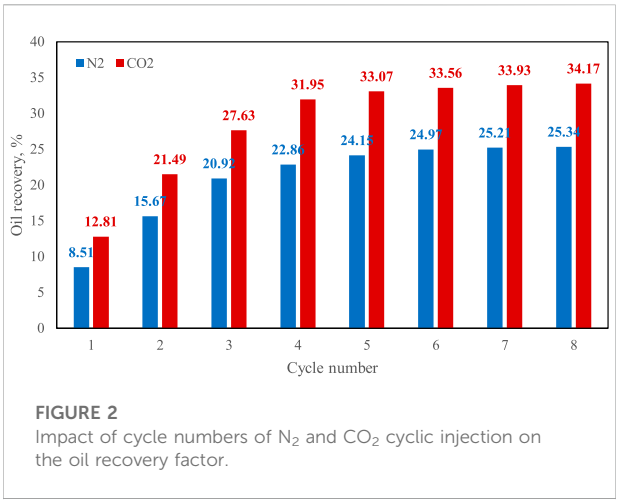

FIGURE 2
Impact of cycle numbers of N_2 and CO_2 cyclic injection on the oil recovery factor.

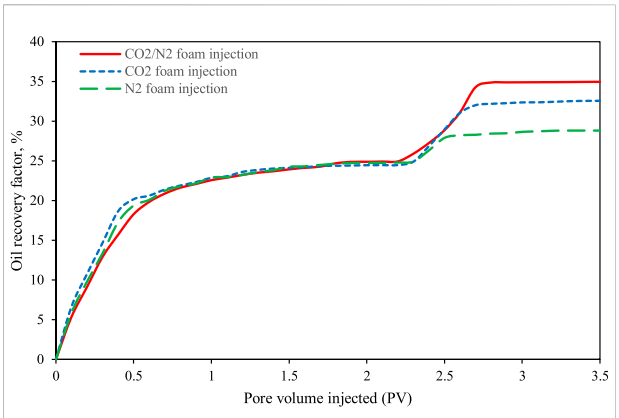

FIGURE 4
Comparison of foams injection with CO_2 and N_2.

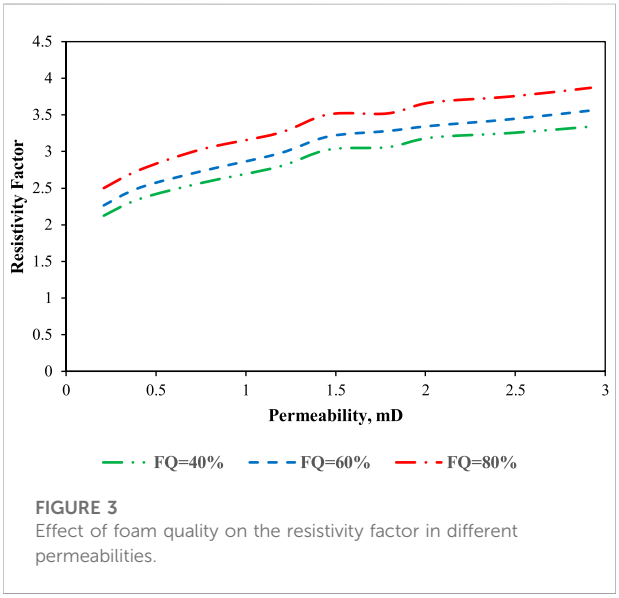

FIGURE 3
Effect of foam quality on the resistivity factor in different permeabilities.

the effectiveness of CO_2 injection (Liu et al., 2014; Kanfaret al., 2017). Pu performed a set of experimental tests to evaluate the efficiency of CO_2-huff-n-puff to improve oil recovery. It was observed that the solubility of carbon dioxide and oil swelling had been increased by the pressure increase, which corresponds to the appropriateness of this method for the oil recovery enhancement from tight oil reservoirs. Moreover, it was concluded that by increasing the number of injectivity cycles from one to four, the oil recovery factor had increased about 10%; however, the increase of oil recovery is not stable with the increase of cycle numbers, and pressure would be a significant parameter (Pu et al., 2016). When CO_2 is injected into the formation, the gas-oil interfacial tension decreases, and the oil in the smaller pores begins to flow (Wei et al., 2021). Ding has performed other research activities to investigate the effect of miscibility and the bypassed oil size on the recovery and mobilization of bypassed oil (Ding et al., 2019). The EOR mechanism of foam flooding mainly includes stabilizing the displacement front, reducing the capillary forces, modifying the rock wettability, and enhancing the interfacial mass transfer (Talebian et al., 2014). When foam-enhanced CO_2-EOR is implemented, foam formation is a kind of gas-liquid coexistence material; the water phase or oil phase is continuously distributed in the rock, while the gas phase is discontinuous. (Gauglitz et al., 2002; Li, et al., 2020). In tight reservoirs, CO_2 and foam can improve displacement efficiency in small and large pores by implementing CO_2-based surfactant-alternating-gas injection (Wei et al., 2021). The surfactant stabilizes foam and reduces the rate of foam and liquid discharge (Ahmed et al., 2017).

In this study, we aimed to provide a set of experimental investigations based on foams injection and CO_2-EOR-based methods such as cyclic carbon dioxide injection and surfactant-CO_2-based methods to determine the optimum oil recovery methods. The structure of the paper is as follows: in section 2, the materials and methods we used in this study are illustrated and discussed with previous literature. Next, the main experimental results were categorized and discussed explicitly. In the final section, the main findings are described in conclusion section.

Materials and methods

Materials

Reservoir core samples were taken from the tight oil formation of Block F in the Shengli oilfield, and the exact core sample sizes with the approximate length of 5 cm and outer diameter of 2.54 cm were provided. In order to measure the permeability and porosity of tight core samples, purified

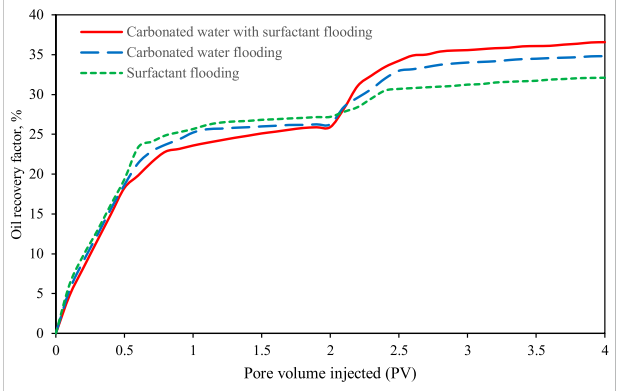

FIGURE 5
Comparison of different surfactant-CO_2 based EOR methods.

nitrogen (99.9% purity) was used. Thereby, permeability has ranged from 0.1–3 mD, indicating the core samples have low permeabilities. Average porosity is recorded between 10 and 12%. The dead oil and produced hydrocarbon gas samples were collected in the field and were mixed based on the gas oil ratio of 79.3 m^3/m^3 in the lab to form a live oil sample. The compositional analysis results of dead oil produced hydrocarbon gas and live oil is shown in Table 1.

The viscosity and density of the crude oil were 2.14 mPa s and 0.77 g/cm3, measured at the temperature of 100°C. The analysis of formation water depicted that formation water salinity is about 6000 mg/L. Synthesized brine has been formed to present a proper match with reservoir features. Its salinity is recorded at 6,000 mg/L. Shengli Oilfield Company SINOPEC provides SLPM and SLBHJ foam agents and surfactants in this experiment.

Methods

To start the coreflooding procedure, we divided each vessel containing chemical and non-chemical agents separately, and they were connected to the system by the various control valve. It helped us to control the process *via* a computer and define the limitations and stopping points for each setup. Due to the reservoir temperature of 100°C, an oven is implemented to control the temperature of the core-holder system. The confining pressure in the system is controlled by using a syringe pump. Another syringe pump was used to control the injection rate of the fluids introduced into the system. The back pressure was set to 25 MPa and controlled by a back-pressure valve. To record the oil and water saturation, synthesized brine with 0.02 cm^3/min was injected into the system, and then two PVs (Pore Volumes) of this prepared brine were injected to measure the oil production rate. The purpose of this scenario is to simulate the water injection performances through the system, especially in primary and secondary enhanced oil recovery methods. Then, each method was performed individually, and the recovery performances were recorded in a spreadsheet to normalize and compare them (see Figure 1).

Results and discussion

Cyclic CO_2 injection with different cycles

As tight reservoirs have contained low permeable layers, the gaseous phase can mobilize more conveniently through the pores and throats regarding their lower viscosity. It can help to increase the sweep efficiency of trapped oil in those layers. Both CO_2 and N_2 (Nitrogen) were used for cyclic injection to reduce the oil viscosity and the interfacial tension respectively to study the oil recovery factor by increasing cycles. The primary purpose of cyclic carbon dioxide injection is to improve oil recovery by giving the core samples a soaking time called the huff cycle. Oil production on the core holder is followed by pressure depletion as a puff cycle. Previous studies review this method as huff-n-puff (Abedini and Torabi, 2014).

It can be observed in Figure 2 that the CO_2 cyclic injection has achieved higher oil recoveries in each cycle. That is because compared with N_2, CO_2 could be more dissolved into the crude oil phase and has a more significant ability to cause oil expansion, a decrease in oil viscosity, and interfacial tension. However, by increasing the number of injection cycles, the oil recovery has been the same for CO_2 and N_2. It was observed that the oil recovery rose significantly in the first three cycles and increased very slightly after four cycles.

TABLE 2 The experimental results of the surfactant-CO_2 based EOR methods.

Injection scenarios	Water flooding RF	Total RF	Incremental RF by EOR
Surfactant flooding	27.19	32.1	4.91
Carbonated water flooding	26.26	34.81	8.55
Carbonated water with surfactant flooding	25.91	36.57	10.66

Foam-CO_2-based EOR methods

Foams are one of the practical agents in EOR processes as they can block the high permeable layers and provide higher sweep and displacement efficiency for fluid flow in the layers with lower permeability. Thereby, we considered foam qualities of 40–80% to measure the oil production in the system. First, we determined the best foam quality as a factor of permeability increase in the system, and then the oil recovery factor was calculated as seen in Figure 3, the increase of permeability in the presence of foam quality increases. It was observed that the increase of foam quality has increased the resistivity factor. Thereby, 80% of foam quality was selected for foams injection.

After defining the optimum foam quality, the generated foam was injected through the system to calculate the oil recovery factor. The pure CO_2, N_2, and the mixture of CO_2 and N_2 (the ratio of CO_2/N_2 is 80:20) were used to generate foams during the core flooding experiments in order to investigate how the foams generated by different gases (CO_2, N_2, and CO_2/N_2) would affect the oil recovery factor in tight oil reservoirs. All the experiments were performed after the primary water injection into the system, where there was no significant change in the oil recovery factor. The maximum oil recovery factors at the two-pore volumes of water injection are 24.45, 24.7, and 24.9% for pure CO_2, N_2, and mixed CO_2/N_2 foam injection, respectively. As shown in Figure 4, generated foams have been performed after water injection. At the beginning of foams injection (before 0.3 PVs foam was injected), the oil recovery factor increased slightly for all three cases. Then, the oil in the low permeable layers has been mobilized more quickly, during 0.3–0.7 pore volumes foams injection. This point is the starting point for the oil recovery increase by foam.

It was observed that CO_2/N_2-foam has the highest oil recovery factor of 34.9% and CO_2-foam would be feasibility than N_2-foam. CO_2–foam increased the oil recovery factor of 32.56 and 28.87% for N_2-foam. However, when N2 replaced 20% of CO_2, the foam generated by mixed CO_2/N_2 achieved the largest oil recovery factor of 34.95%. The experimental results represent that adding N_2 into the pure CO_2 system can increase the strength of the generated foam, which is consistent with the previous results by Hassan et al. and Abdelaal et al. (Hassan and Gajbhiye, 2018; Abdelaal et al., 2020).

Surfactant-CO_2-based EOR methods

One of the purposes of adding surfactants to carbonated water is the wettability alteration and reduction of interfacial tension to increase the mobility of the oil phase through pores and throats. Wettability alteration is one of the most essential issues in unconventional reservoirs such as tight oil and shale oil reservoirs. This part includes surfactant-based EOR methods such as surfactant (SLBHJ) injection, carbonate water injection, and carbonated water-surfactant injection (the surfactant added into the carbonated water injection). Then, the experiments should be performed for three core samples that have similar permeability (0.3–0.4 mD) to determine the best injectivity scenario. As shown in Figure 5, the carbonated water-surfactant injection has the maximum total oil recovery of 36.57%. The incremental oil recovery was measured at 10.66%. Carbonated water flooding and surfactant flooding are the next steps of the oil recovery factor, respectively. There were 34.81 and 32.1%, respectively (more details can be seen in Table 2).

Conclusion

Regarding the importance of the gaseous phase to increase the mobility ratio in tight oil reservoirs, we compare a set of experiments based on carbon dioxide-EOR methods to determine the efficiency of each injectivity scenario on the oil recovery factor. The most notable features in this study are;

- It was observed that CO_2/N_2-foam has the maximum oil recovery factor of 34.9%; however, CO_2-foam, regarding more feasibility than N_2, has witnessed as the highest oil recovery factor after CO_2/N_2-foam.
- Introducing N_2 into pure CO_2 strengthens the generated foams' stability and achieves higher oil recovery.
- Carbonated water with surfactant flooding has the highest oil recovery factor of 36.5%. Carbonated water flooding can be combined with surfactant flooding to enhance oil recovery further.
- The incremental oil recovery factor for surfactant flooding, carbonated water flooding, and carbonated water with surfactant flooding is measured at 4.9, 8.5, and 10.6%, respectively.

Data availability statement

The raw data supporting the conclusions of this article will be made available by the authors, without undue reservation.

Author contributions

CZ: performed the experiment and wrote the draft; GW: assisst with performing the experiment and results analysis; HH: analyze the experimental results; HZ: review the draft.

Conflict of interest

Author CZ was employed by the company Exploration and Development Research Institute SINOPEC Shengli Oilfield Company. Author GW was employed by the company PetroChina Dagang Oilfield Company. Author HH was employed by the company 11th Oil Production Plant of Changqing Oilfield Company. Author HZ was employed by the company PetroChina Xinjiang Oilfield Company.

Publisher's note

All claims expressed in this article are solely those of the authors and do not necessarily represent those of their affiliated organizations, or those of the publisher, the editors and the reviewers. Any product that may be evaluated in this article, or claim that may be made by its manufacturer, is not guaranteed or endorsed by the publisher.

References

Abdelaal, A., Gajbhiye, R., and Al-shehri, D. (2020). Mixed CO_2/N_2 foam for EOR as a novel solution for supercritical CO_2 foam challenges in sandstone reservoirs. *ACS Omega* 5 (51), 33140–33150. doi:10.1021/acsomega.0c04801

Abedini, A., and Torabi, F. (2014). Oil recovery performance of immiscible and miscible CO_2 huff-and-puff processes. *Energy fuels.* 28 (2), 774–784. doi:10.1021/ef401363b

Ahmed, S., Elraies, K. A., Tan, I. M., and Hashmet, M. R. (2017). Experimental investigation of associative polymer performance for CO_2 foam enhanced oil recovery. *J. Petroleum Sci. Eng.* 157, 971–979. doi:10.1016/j.petrol.2017.08.018

Busch, A., Alles, S., Gensterblum, Y., Prinz, D., Dewhurst, D. N., Raven, M. D., et al. (2008). Carbon dioxide storage potential of shales. *Int. J. Greenh. Gas Control* 2 (3), 297–308. doi:10.1016/j.ijggc.2008.03.003

Chung, F. T. H., Johnes, R. A., and Nguyen, H. T. (1988). Measurement and physical properties of CO_2/heavy-crude-oil mixtures. *SPE Reserv. Eval. Eng.* 3 (3), 822–828.

Ding, M., Wang, Y., Wang, Y., Gao, M., Liu, D., and Chen, W. (2019). Experimental investigation of bypassed-oil recovery via CO_2 soaking plateau around two pore volume injection, we continued the tests from two pore volume injection for differenand huff and puff injection: Effects of miscibility and bypassed-oil size. *Fuel* 248, 152–160. doi:10.1016/j.fuel.2019.03.088

Gauglitz, P. A., Friedmann, F., Kam, S. I., and R. Rossen, W. (2002). Foam generation in homogeneous porous media. *Chem. Eng. Sci.* 57 (19), 4037–4052. doi:10.1016/s0009-2509(02)00340-8

Guo, Q., Ahmadi, M. H., Lahafdoozian, M., Palyanitsina, A., Kuzichkin, O. R., Alizadeh, S. M., et al. (2021). A laboratory approach on the improvement of oil recovery and carbon dioxide storage capacity improvement by cyclic carbon dioxide injection. *Energy Rep.* 7, 1571–1580. doi:10.1016/j.egyr.2021.03.012

Hassan, M., and Gajbhiye, R. (2018). "Performance of CO_2/N_2 foam in enhanced oil recovery," in Paper presented at the SPE Trinidad and Tobago Section Energy Resources Conference, Port of Spain, Trinidad and Tobago, June 2018.

Holm, L. W., and Josendal, V. A. (1974). Mechanisms of oil displacement by carbon dioxide. *J. Pet. Technol.* 26 (12), 1427–1438. doi:10.2118/4736-PA

Jia, C., Zheng, M., and Zhang, Y. (2012). Unconventional hydrocarbon resources in China and the prospect of exploration and development. *Petroleum Explor. Dev.* 39 (2), 139–146. doi:10.1016/s1876-3804(12)60026-3

Kanfar, M. S., Ghaderi, S. M., Clarkson, C. R., Reynolds, M. M., and Hetherington, C. (2017). "A modeling study of EOR potential for CO_2 huff-n-puff in tight oil reservoirs - example from the bakken formation," in Paper presented at the SPE Unconventional Resources Conference, Calgary, Alberta, Canada, February 2017.

Li, S., Wang, Q., and Li, Z. (2020). Stability and flow properties of oil-based foam generated by CO_2. *SPE J.* 25, 416–431. doi:10.2118/199339-pa

Liu, G., Sorensen, J. A., Braunberger, J. R., Klenner, R., Ge, J., Gorecki, C. D., et al. (2014). "CO_2-base enhanced oil recovery from unconventional reservoirs: A case study of the bakken formation," in Paper presented at the SPE Unconventional Resources Conference, The Woodlands, Texas, USA, April 2014.

Luo, P., Luo, W., and Li, S. (2017). Effectiveness of miscible and immiscible gas flooding in recovering tight oil from Bakken reservoirs in Saskatchewan, Canada. *Fuel (Lond).* 208, 626–636. doi:10.1016/j.fuel.2017.07.044

Mahzari, P., Jones, A. P., and Oelkers, E. H. (2020). Impact of *in-situ* gas liberation for enhanced oil recovery and CO_2 storage in liquid-rich shale reservoirs. *Energy Sources, Part A Recovery, Util. Environ. Eff.* 1, 1–21. doi:10.1080/15567036.2020.1815907

Manrique, E. J., Thomas, C. P., Ravikiran, R., Kamouei, M. I., Lantz, M., Romero, J. L., et al. (2010). "Eor: Current status and opportunities," in Paper presented at the SPE Improved Oil Recovery Symposium, Tulsa, Oklahoma, USA, April 2010.

Pu, W., Wei, B., Jin, F., Li, Y., Jia, H., Liu, P., et al. (2016). Experimental investigation of CO_2 huff-n-puff process for enhancing oil recovery in tight reservoirs. *Chem. Eng. Res. Des.* 111, 269–276. doi:10.1016/j.cherd.2016.05.012

Sheng, J. J. (2017). Critical review of field EOR projects in shale and tight reservoirs. *J. Pet. Sci. Eng.* 159, 654–665. doi:10.1016/j.petrol.2017.09.022

Talebian, S. H., Masoudi, R., Tan, I. M., and Zitha, P. L. J. (2014). Foam assisted CO_2-EOR: A review of concept, challenges, and future prospects. *J. Petroleum Sci. Eng.* 120, 202–215. doi:10.1016/j.petrol.2014.05.013

Torres, J. A., Lu, J., Bosshart, N. W., Pekot, L. J., Sorensen, J. A., Peterson, K., et al. (2018). "Multiscale modeling to evaluate the mechanisms controlling CO_2-based enhanced oil recovery and CO_2 storage in the bakken formation," in Paper presented at the SPE/AAPG/SEG Unconventional Resources Technology Conference, Houston, Texas, USA, July 2018.

Tovar, F. D., Eide, O., Graue, A., and Schechter, D. S. (2014). "Experimental investigation of enhanced recovery in unconventional liquid reservoirs using CO_2: A look ahead to the future of unconventional EOR," in Paper presented at the SPE Unconventional Resources Conference, The Woodlands, Texas, USA, April 2014.

Wang, J., Feng, L., Steve, M., Tang, X., Gail, T. E., and Mikael, H. (2015). China's unconventional oil: A review of its resources and outlook for long-term production. *Energy* 82, 31–42. doi:10.1016/j.energy.2014.12.042

Wei, J., Zhou, X., Zhou, J., Li, J., and Wang, A. (2021). Experimental and simulation investigations of carbon storage associated with CO_2 EOR in low-permeability reservoir. *Int. J. Greenh. Gas Control* 104, 103203. doi:10.1016/j.ijggc.2020.103203

Yu, W., Lashgari, H., Wu, K., and Sepehrnoori, K. (2015). CO_2 injection for enhanced oil recovery in Bakken tight oil reservoirs. *Fuel* 159, 354–363. doi:10.1016/j.fuel.2015.06.092

Zhou, X., Wang, Y., Zhang, L., Zhang, K., Jiang, Q., Pu, H., et al. (2020). Evaluation of enhanced oil recovery potential using gas/water flooding in a tight oil reservoir. *Fuel* 272, 117706. doi:10.1016/j.fuel.2020.117706

frontiers | Frontiers in Energy Research

TYPE Original Research
PUBLISHED 19 September 2022
DOI 10.3389/fenrg.2022.979526

OPEN ACCESS

EDITED BY
Shuang Zheng,
Aramco Services Company,
United States

REVIEWED BY
Hao Yan,
China University of Mining and Technology, China
Fei Wang,
China University of Petroleum, China
Zhoujie Wang,
China University of Petroleum, China

*CORRESPONDENCE
Ang Luo,
1054158736@qq.com

SPECIALTY SECTION
This article was submitted to Advanced Clean Fuel Technologies, a section of the journal Frontiers in Energy Research

RECEIVED 27 June 2022
ACCEPTED 24 August 2022
PUBLISHED 19 September 2022

CITATION
Li Y, Luo A, Chen X, Cheng L, Chang C and Xie W (2022), A Novel model for simulating the integration process of hydraulic fracturing, shut-in period, and well production.
Front. Energy Res. 10:979526.
doi: 10.3389/fenrg.2022.979526

A Novel model for simulating the integration process of hydraulic fracturing, shut-in period, and well production

Yongming Li[1], Ang Luo[1]*, Xi Chen[2], Leiming Cheng[2], Cheng Chang[3] and Weiyang Xie[3]

[1]State Key Laboratory of Oil and Gas Reservoir Geology and Exploitation, Southwest Petroleum University, Chengdu, China, [2]Research Institute of Engineering Technology, PetroChina Xinjiang Oilfield Company, Karamay, Xinjiang, China, [3]Shale Gas Research Institute, PetroChina Southwest Oil & Gas Field Company, Chengdu, Sichuan, China

Distributions of pore pressure and water saturation in matrix around fractures after hydraulic fracturing and shut-in period will impact the shale gas well production significantly. However, the influences of hydraulic fracturing and shut-in period on pore pressure and water saturation are not considered in the classical reservoir simulations. In this work, the embedded discrete fracture model (EDFM), which is convenient to be coupled with an existing reservoir simulator with high computational efficiency, was employed to simulate the hydraulic fracture propagation coupled with matrix flow. Then, we developed a model for simulating the integration process of hydraulic fracturing, shut-in period, and well production based on the dual media theory. Distributions of pore pressure and water saturation varying in different periods and the production decline of shale gas well were obtained through the integrated simulation model. The calculation result was validated by the field bottom hole pressure data of a shale gas well in Sichuan Province, China. Simulation results show that the variation of bottom hole pressure is not smooth during the fracture propagation process because the initiations of different fractures are not simultaneous. The fracturing fluid flow-back rate of shale gas well is much lower than that of conventional reservoirs. There is still a large amount of fracturing fluid retained in micro-fracture systems and matrix of shale after production. It is also found that the permeability of the micro-fracture system determines the drop rate of bottom hole pressure and the size of stimulated reservoir volume (SRV) determines the decrease amplitude of bottom hole pressure.

KEYWORDS

shale gas, hydraulic fracturing, reservoir simulation, EDFM, integration process

Introduction

At present, shale gas has become an important part of unconventional oil and gas resources (Yue et al., 2020; Zhou et al., 2021; Zhao et al., 2022). Hydraulic fracturing is a key technology in shale gas development (Zhang et al., 2022a; Zhang et al., 2022b). And the fracturing fluid leak-off during hydraulic fracturing impacts the distributions of pore pressure and water saturation of matrix around hydraulic fractures significantly. However, the three stages in the life of shale gas well development are not fully considered in current reservoir simulations. Taking into consideration the effects of invaded fracturing fluid, it is important for simulation and prediction of shale gas well production to obtain the distributions of pore pressure and water saturation in the reservoir after fracturing and shut-in period. To achieve that, a model which can simulate the integration process of hydraulic fracturing, shut-in period, and well production is essential.

In the hydraulic fracturing studies, Carter leak-off equation (Zhao et al., 2020) and Darcy's law (Salimzadeh et al., 2017; Wang et al., 2017; Wang et al., 2020a) are often employed to describe the fracturing fluid invasion during hydraulic fracturing. Usually only the leak-off volume of fracturing fluid can be recorded in current fracture propagation models; the fluid flow in reservoir is not considered. And the distributions of pore pressure and water saturation varying in hydraulic fracturing periods also cannot be described. Therefore, coupling the fracture propagation with the fluid flow in the reservoir becomes an important issue. The embedded discrete fracture model (EDFM) (Li and Lee, 2008), which is widely used to describe hydraulic fractures in reservoir simulation, becomes a possible solution.

In recent years, the EDFM is very popular due to its high compatibility with existing reservoir simulators (Yu et al., 2018; Dong et al., 2019; Zhang et al., 2020; Zhu et al., 2020). This method can smoothly embed fractures in the reservoir without impacting the existing grid. And the EDFM is both suitable for Cartesian grids (Cavalcante-Filho et al., 2015; Cavalcante-Filho and Sepehrnoori, 2017; Du et al., 2017) and unstructured grids (Xu et al., 2019). In addition, the EDFM overcomes shortcomings of complex grid division and low computational efficiency brought by discrete-fracture models (DFMs) (Xu et al., 2017). And the EDFM has been applied in various situations of reservoir simulation, such as the simulation of CO_2 Huff-n-Puff process (Sun et al., 2019) and the history matching (Dachanuwattana et al., 2018). In this study, the EDFM coupled fluid flow in reservoir with fracture propagation. And this method is also used to simulate shut-in period and production of shale gas well.

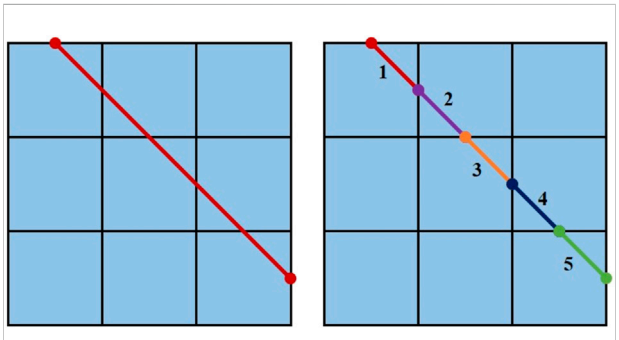

FIGURE 1
Explanation of fracture segments division in the EDFM.

Current researches show that capillary pressure guides fracturing fluid invade into the matrix during shut-in period, which changes the distributions of pore pressure and water saturation in the matrix (Ghanbari and Dehghanpour, 2016; Shen et al., 2016; Liu et al., 2017; Liang et al., 2021; Liu et al., 2021) and may enhance the viscosity of shale (Peng et al., 2020a). The pressure gradient caused by hydraulic fracturing also guides the fluid flow between fractures and matrix during shut-in period (Zhao et al., 2019; Wang et al., 2020b). The influences of capillary pressure and pressure gradient caused by hydraulic fracturing on pore pressure and water saturation in the matrix become more and more significant when the shut-in continues. And this process can impact the initial productivity of shale gas well and the flow-back rate of fracturing fluid (Fakcharoenphol et al., 2016). In order to analysis the influence of shut-in time on the production and fracturing fluid flow-back rate of shale gas well, it is essential to compare the simulation results of different shut-in times.

In this paper, we developed a model for simulating the integration process of hydraulic fracturing, shut-in period, and well production based on the EDFM and the dual media model. The EDFM was employed to develop the hydraulic fracture propagation model coupled with matrix flow. And the distributions of pore pressure and water saturation varying in different periods and the production decline of shale gas well were obtained through the above integrated simulation model. Then, how the shut-in time impacts the production of shale gas well was discussed. Finally, the influences of the size of SRV and the permeability of micro-fracture system on bottom hole pressure during shut-in period were analyzed.

Fracture propagation model coupled with reservoir seepage

Distributions of pore pressure and water saturation and the parameters of fractures after hydraulic fracturing directly impact the shut-in and production process of shale gas well. The fracture morphology and propagation patterns of hydraulic fracture are the main focus in current fracture propagation models (Zhao et al., 2015; Peng et al., 2019; Peng et al., 2020b). Therefore, distribution changes of pore pressure and water saturation in

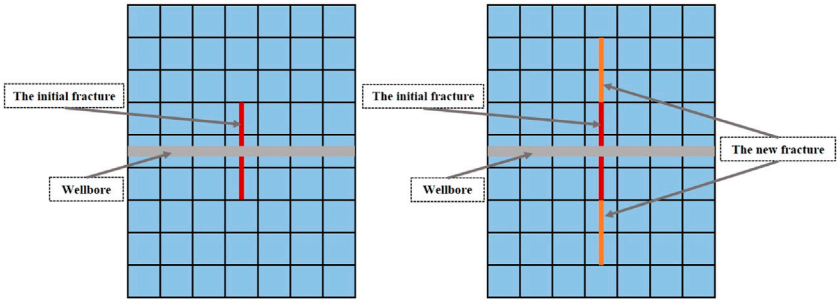

FIGURE 2
Schematic diagram of fracture propagation in the EDFM.

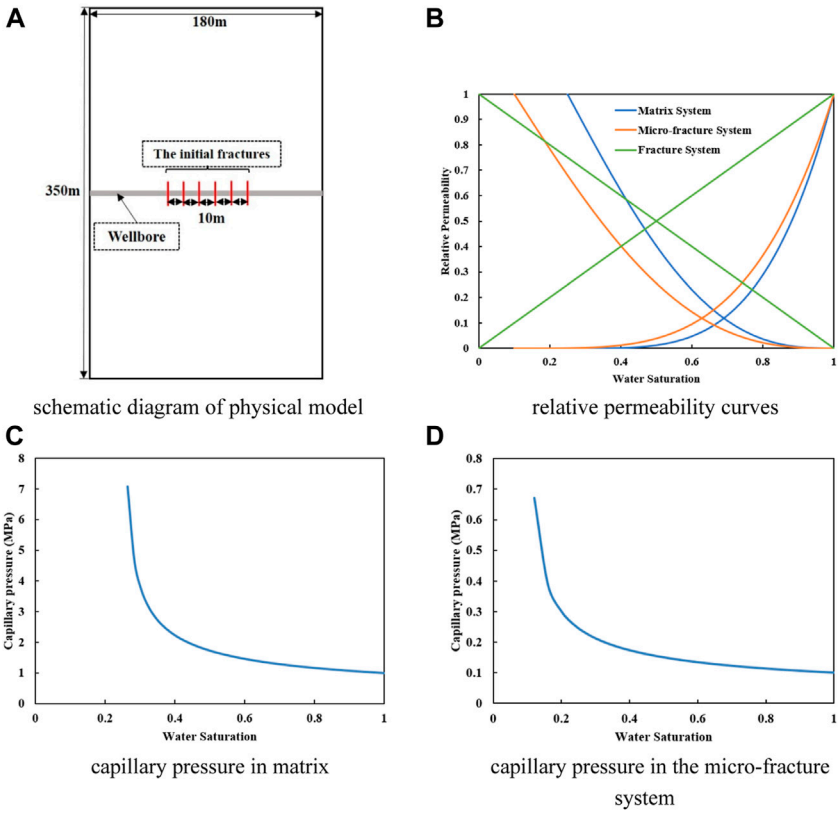

FIGURE 3
Parameters of the simulations. **(A)** Schematic diagram of physical model. **(B)** Relative permeability curves. **(C)** Capillary pressure in matrix. **(D)** Capillary pressure in the micro-fracture system.

reservoir during hydraulic fracturing were not fully considered in current fracture propagation models. Unfortunately, it is difficult to smoothly couple fluid flow in the reservoir with the existing fracture propagation models. In this paper, the embedded discrete fracture model (EDFM), which has good compatibility with reservoir simulators and outstanding computational efficiency (Wang et al., 2021), is the method to solve this problem. The EDFM is a fracture description method widely used in reservoir simulator. In the two-dimensional (2D) reservoir model, a fracture described by the EDFM will be divided into multiple fracture segments by reservoir grid, as shown in Figure 1.

TABLE 1 Basic parameters used for the simulations.

Parameter	Value	Unit	Parameter	Value	Unit
Initial reservoir pressure	40	MPa	Pumping rate	12	m^3/min
Reservoir thickness	30	m	Fracture height	30	m
Reservoir temperature	352	K	Number of fractures	6	—
Rock density	2,500	kg/m^3	Cluster spacing	10	m
Young's modulus	20,000	MPa	Initial matrix permeability	0.005	mD
Poisson ratio	0.22	—	Micro-fracture permeability	0.7	mD
Fracture toughness	2	MPa$\sqrt{m}$	Matrix porosity	0.10	—
Rock compressibility	0.000145	1/MPa	Micro-fracture porosity	0.01	—
Gas density (1 atm, 293.15 K)	0.58	kg/m^3	Initial micro-fracture water saturation	0.30	—
Gas molar mass	16	kg/kmol	Initial matrix water saturation	0.30	—
Langmuir pressure	4.48	MPa	Stress sensitivity coefficient	0.07	1/MPa
Langmuir volume	0.00272	m^3/kg	Maximum horizontal principal stress	50	MPa
Fracturing fluid viscosity	1	mPa·s	Minimum horizontal principal stress	70	MPa
Wellbore radius	0.06	m	Initial fracture length	3	m
Rarefaction parameter	0.9807	—	Knudsen number	0.2102	—
The slip coefficient	-1	—			

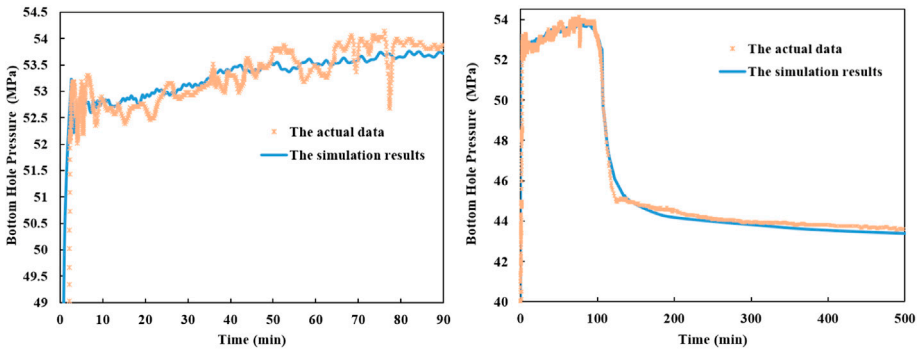

FIGURE 4
Comparison between the actual data and the simulation results in bottom hole pressure.

Fluid flow model in fracture

In the 2D reservoir model, the fluid flow between fracture segments is one-dimensional. There is flow exchange between each fracture segment and the micro-fracture cell which is intersected by a fracture segment. Therefore, the fluid flow in the fracture can be described by

$$\frac{\partial}{\partial \xi}\left(\frac{\beta K_{\mathrm{Fri}} K_{\mathrm{F}}}{\mu_{\mathrm{i}} B_{\mathrm{i}}} \frac{\partial P_{\mathrm{Fi}}}{\partial \xi}\right)+\delta_{\mathrm{well}} \frac{q_{\mathrm{Fi}}}{V_{\mathrm{F}}}+\frac{Q_{\mathrm{F-f\ i}}}{V_{\mathrm{F}}}=\frac{\partial}{\partial t}\left(\frac{\phi_{\mathrm{F}} S_{\mathrm{Fi}}}{B_{\mathrm{i}}}\right) \quad (1)$$

where $Q_{\mathrm{F-f\ i}}$ is the volume flow rate of phase i between a fracture segment and the micro-fracture grid, m^3/s; q_{Fi} is the volume flow rate of phase i between a fracture segment and wellbore, m^3/s; P_{Fi} is the pressure of phase i in a fracture segment, MPa; K_{Fri} is the fracture relative permeability of phase i; V_{F} is the volume of a fracture segment, m^3; ϕ_{F} is the porosity of fracture; S_{Fi} is the saturation of phase i in a fracture segment; B_{i} is the volume coefficient of water phase i; δ_{well} is the coefficient for judging the intersection of a fracture segment and wellbore, if a fracture segment intersects wellbore, $\delta_{\mathrm{well}} = 1$; if not, $\delta_{\mathrm{well}} = 0$.

When a fracture segment intersects the micro-fracture grid, the flow exchange between the fracture segment and the micro-fracture cell occurs under the pressure gradient. $Q_{\mathrm{F-f\ i}}$ can be described as (Xu et al., 2017)

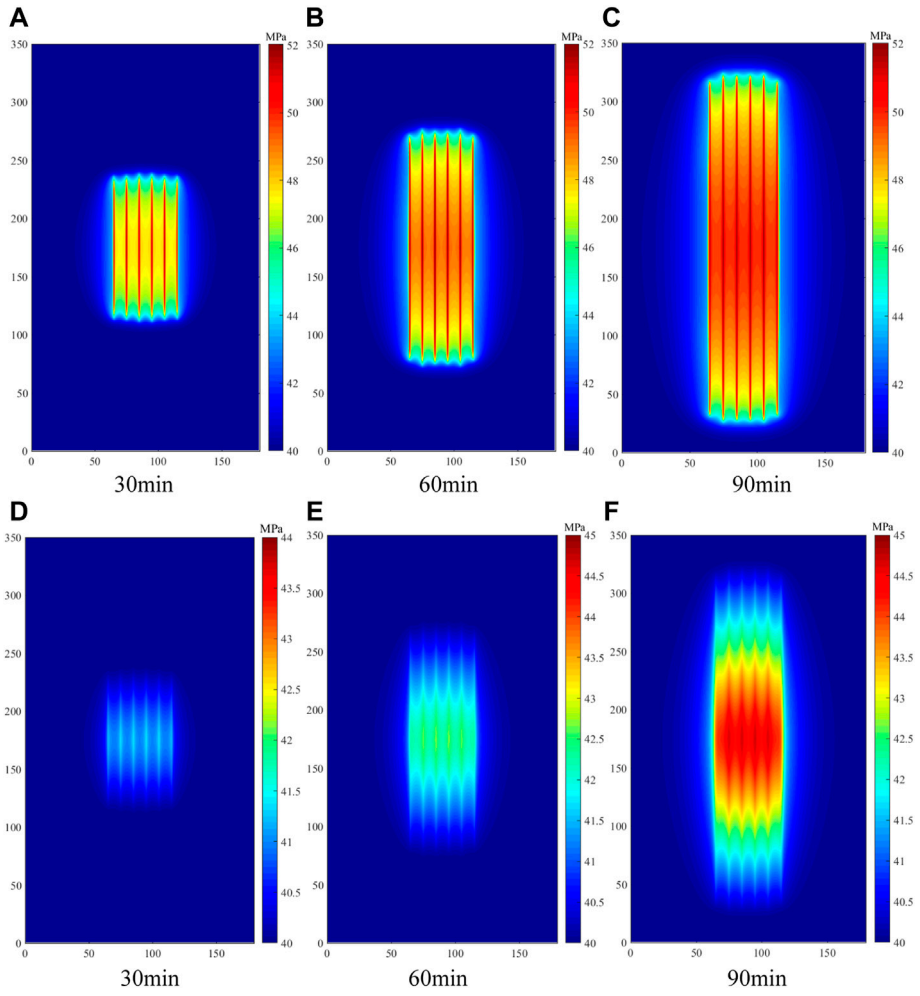

FIGURE 5
Distribution of pressure in the micro-fracture system and matrix during fracture propagation. (In **(A–C)**, the range of pressure in the micro-fracture system is from 40 to 52 MPa. In **(D)**, the range of pressure in matrix is from 40 to 44 MPa. In **(E,F)**, the range of pressure in the matrix is from 40 to 45 MPa).

$$Q_{\mathrm{F-f\ i}} = \frac{2K_{\mathrm{f}} l_{\mathrm{F}} H_{\mathrm{F}} \left(P_{\mathrm{Fi}} - P_{\mathrm{fi}}\right)}{\mu_{\mathrm{i}} d_{\mathrm{F-f\ i}}} \tag{2}$$

where K_{f} is the permeability of micro-fracture cell which is intersected by a fracture segment, mD; l_{F} is the length of fracture segment, m; H_{F} is height of fracture segment, m; μ_{i} is the viscosity of phase i, mPas; $\bar{d}_{\mathrm{F-f}}$ is the average normal distance from micro-fracture cell to fracture segment; P_{fi} is the pressure of phase i in a micro-fracture cell, MPa.

Subsequently, the well-fracture flow was described by the EDFM and the Peaceman method (Moinfar et al., 2013). This method ignores the effect of wellbore friction:

$$q_{\mathrm{Fi}} = \frac{2\pi\beta K_{\mathrm{F}} K_{\mathrm{Fri}} w_{\mathrm{F}} \left(P_{\mathrm{Fi}} - P_{\mathrm{wf}}\right)}{\mu_{\mathrm{i}} B_{\mathrm{i}} \left[\ln\left(\frac{r_{\mathrm{eq}}}{r_{\mathrm{well}}}\right) + s\right]} \tag{3}$$

$$r_{\mathrm{eq}} = 0.14\left[\left(l_{\mathrm{F}}\right)^2 + \left(H_{\mathrm{F}}\right)^2\right]^{1/2} \tag{4}$$

where β is unit conversion factor; w_{F} is the width of a fracture segment, m; P_{wf} is the bottom hole pressure, MPa; r_{eq} is the effective radius, m; r_{well} is the wellbore radius, m; s is the skin factor. For multi-cluster fracturing, the sum of flow rates into all fracture segments that intersect the well trajectory must be equal to the fluid injection rate in the wellbore. Therefore, the internal boundary condition is

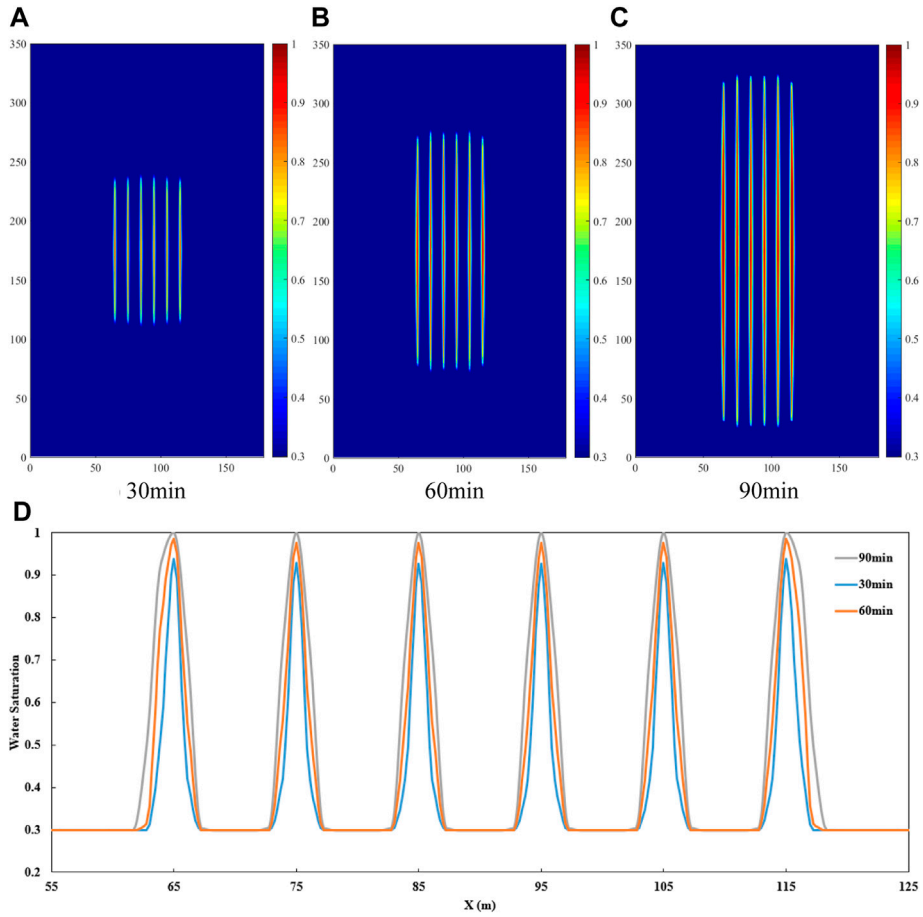

FIGURE 6
Distribution of water saturation in micro-fracture during fracture propagation. (In **(A–C)**, the range of water saturation is from 0.3 to 1.0. **(D)** is profile of water saturation which is drawn from the data in the figure of water saturation distributon in micro-fracture during fracture propagation (such as (A–C) and so on)).

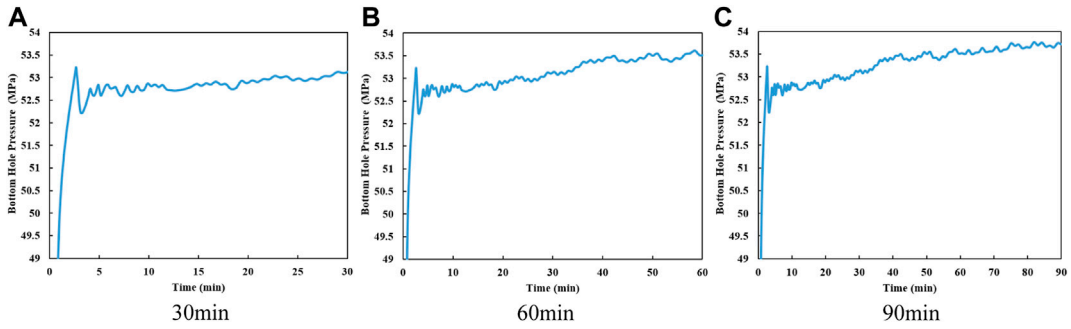

FIGURE 7
Curves of bottom hole pressure after 30 min, 60 min, and 90 min of hydraulic fracturing. (wellbore resistance is neglected, and the bottom hole pressure is the same in the fracturing section).

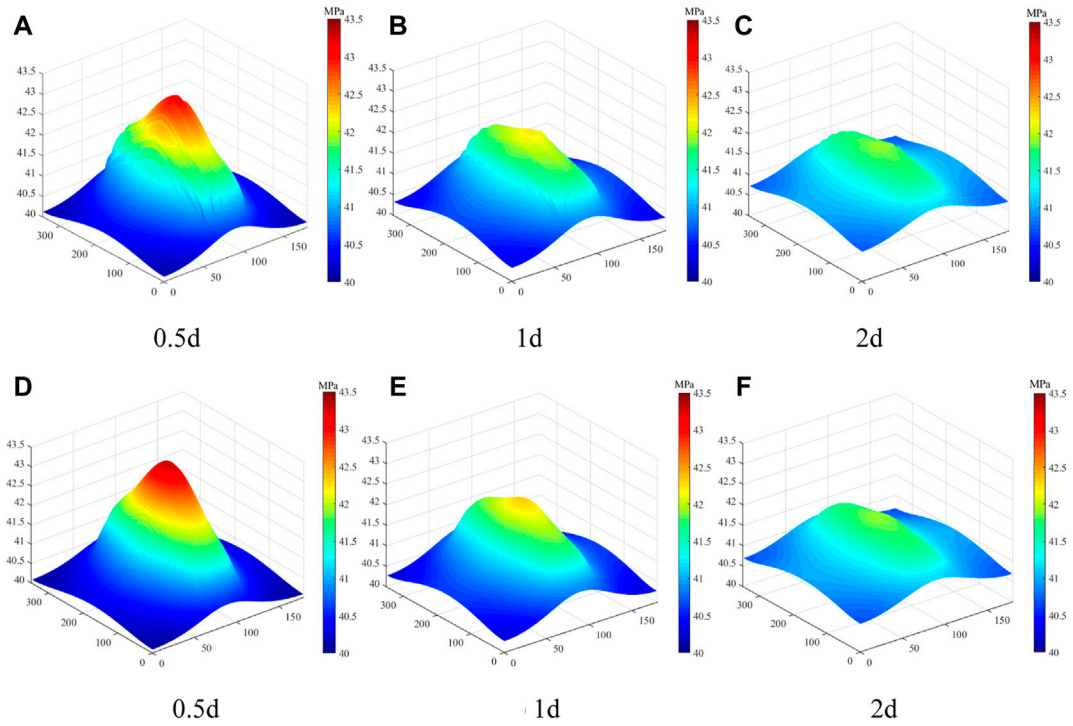

FIGURE 8
Distribution of pressure in micro-fracture system and matrix during shut-in period. (The range of pressure is from 40 to 43.5 MPa. The distribution of pressure in micro-fracture system is shown in **(A–C)**. The distribution of pressure in matrix is shown in **(D–F)**.

$$\sum_{j=1}^{N} (q_{\mathrm{Fi}})_j = Q_t \tag{5}$$

where Q_t is pump rate, m^3/s; N is the number of fractures.

Fracture propagation simulation

The fracture propagation is judged by comparing the stress intensity factor K_I and fracture toughness K_{IC}. If $K_I > K_{IC}$, the hydraulic fracture will expand, the length of the fracture will increase, and new fracture segments will generate, as shown in Figure 2. If $K_I \leq K_{IC}$, the length of the fracture will remain, and the fracture segment will be unchanged.

The stress intensity factor of the hydraulic fracture K_I can be calculated by Eq. 6 (Zhao et al., 2019).

$$K_I = \frac{(P_{\mathrm{Fi}} - \sigma_{\mathrm{h}})H}{2E}\sqrt{\frac{2\pi}{L_{\mathrm{F}}}} \tag{6}$$

where E is the Young's modulus, MPa; σ_{h} is the minimum horizontal principal stress, MPa; L_{F} is the length of the hydraulic fracture.

Fracture toughness K_{IC} is a commonly used parameter to judge the propagation of cracks. When $K_I > K_{IC}$, the length of the fracture increases by 1 m. If a new fracture segment is generated, the fracture parameters of the adjacent fracture segment are selected for assignment.

Reservoir seepage model

Fluid flow in reservoir occurs in hydraulic fracturing, shut-in period and production of shale gas well. In order to take the fluid flow in the reservoir during fracturing and shut-in period into consideration, we developed a gas-water two-phase seepage model for shale reservoirs which considers shale gas desorption, Knudsen diffusion, slippage effect, stress sensitivity, and capillary pressure effect in dual media.

The description of the flow in hydraulic fractures is the same as Eq. 1 in the fracture propagation model. However, during the processes of shut-in period and well production have different boundary conditions in comparison to the hydraulic fracturing stage. However, the boundary conditions of shut-in period and well

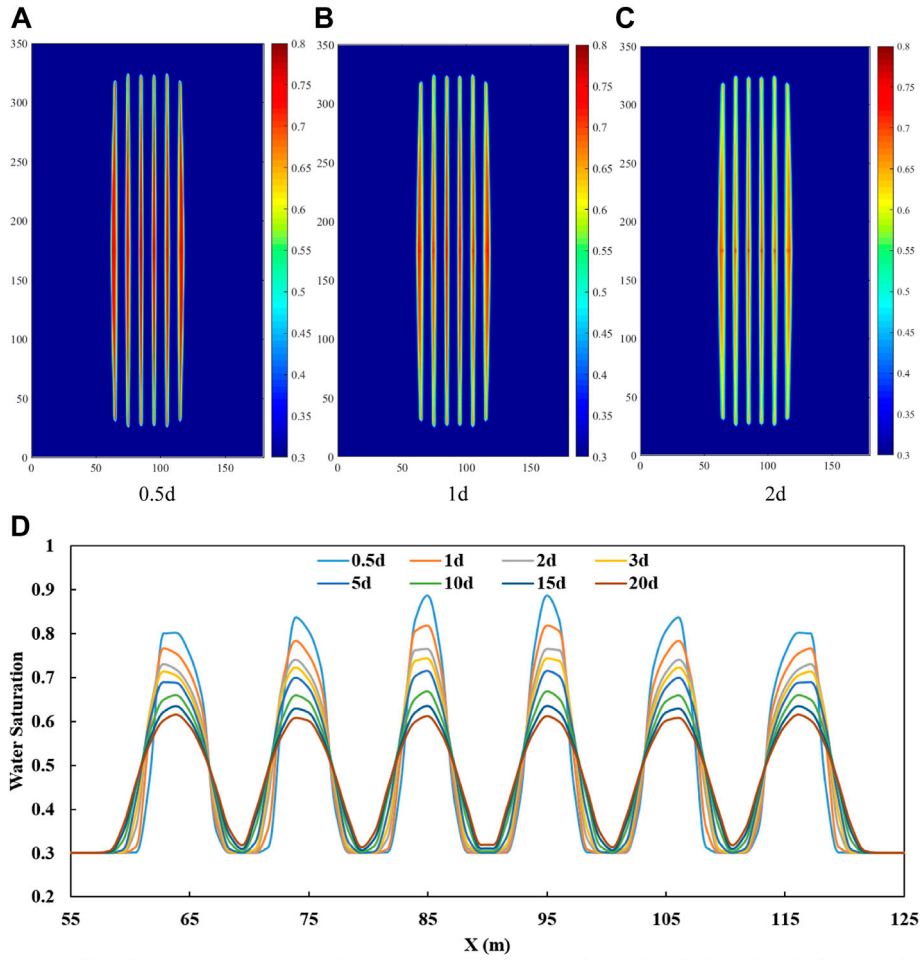

Profile of water saturation in micro-fracture system at horizontal well direction during shut-in period. (Y=125m)

FIGURE 9
Distribution of water saturation in micro-fracture system during shut-in period. (In **(A–C)**, the range of water saturation is from 0.3 to 0.8. **(D)** is profile of water saturation which is drawn from the data in the figure of water saturation distribution in micro-fracture system during shut-in period (such as **(A–C)** and so on).

production are different form that of hydraulic fracturing stage.

During the shut-in period, the sum of the flow rate of each fracture is zero, which could be expressed as

$$\sum_{j=1}^{N} (q_{\mathrm{Fi}})_j = 0 \tag{7}$$

The boundary condition in the production process is expressed as

$$P_{\mathrm{wf}} = const. \tag{8}$$

The gas-water two-phase flow equation in micro-fracture system is

$$\nabla\left(\beta \frac{K_{\mathrm{f}} K_{\mathrm{fri}}}{\mu_{\mathrm{i}} B_{\mathrm{i}}} \nabla P_{\mathrm{fi}}\right) - \delta_{\mathrm{f}} \frac{Q_{\mathrm{F-f\,i}}}{V_{\mathrm{f}}} + \alpha \frac{\beta K_{\mathrm{m}} K_{\mathrm{mri}}}{\mu_{\mathrm{i}} B_{\mathrm{i}}} (P_{\mathrm{mi}} - P_{\mathrm{fi}}) = \frac{\partial}{\partial t}\left(\frac{\phi_{\mathrm{f}} S_{\mathrm{fi}}}{B_{\mathrm{i}}}\right) \tag{9}$$

where K_{f} is the permeability of micro-fracture system, mD; K_{fri} is the relative permeability of phase i in micro-fracture system; P_{fi} is the pressure of phase i in micro-fracture system, MPa; α is shape factor; β is unit conversion factor; K_{m} is the permeability of matrix, mD; K_{mri} is the relative permeability of phase i in matrix; P_{mi} is the pressure of phase i in matrix, MPa; ϕ_{f} is the porosity of micro-fracture system; S_{fi} is the saturation of phase i in micro-fracture system; δ_{f} is the coefficient for judging the intersection of a fracture segment and a micro-

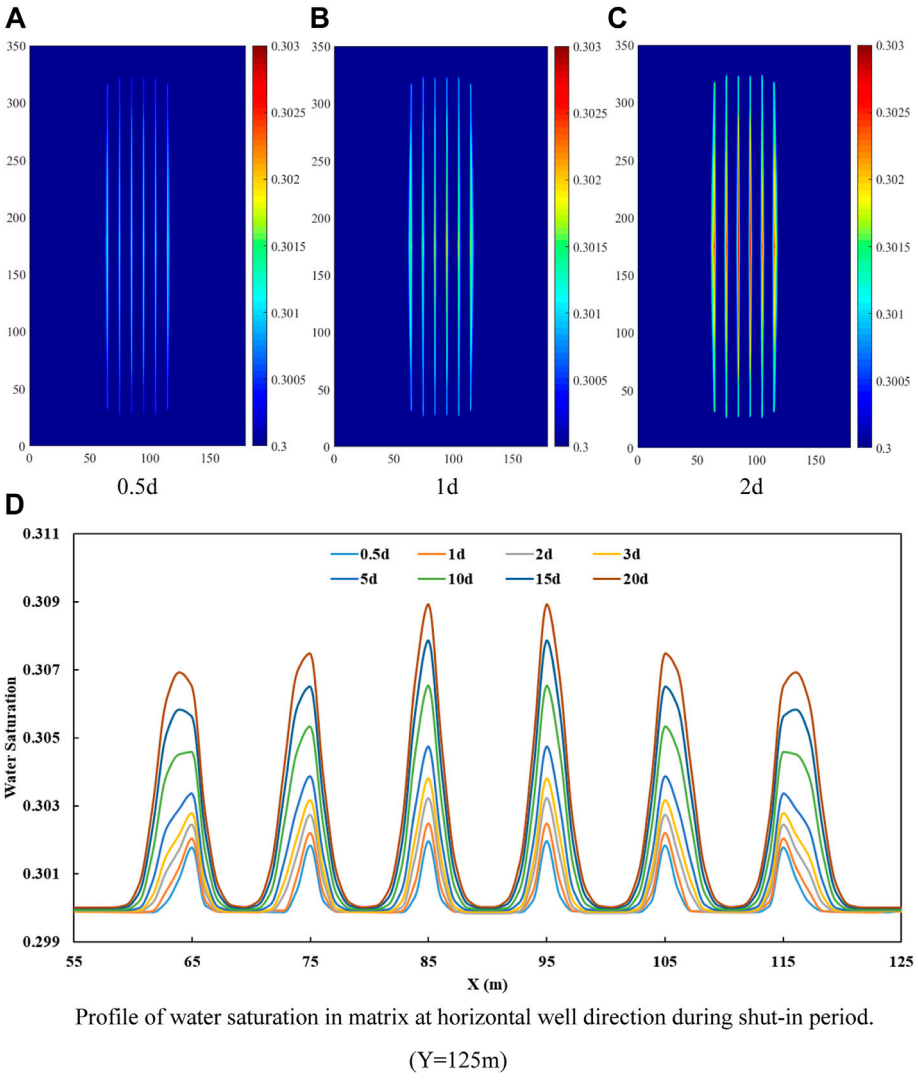

FIGURE 10
Distribution of water saturation in matrix during shut-in period. (In **(A–C)**, the range of water saturation is from 0.3 to 0.303. **(D)** is profile of water saturation which is drawn from the data in the figure of water saturation distribution in matrix during shut-in period (such as **(A–C)** and so on)).

fracture cell, if a fracture segment intersects a micro-fracture cell, then $\delta_f = 1$; if not, then $\delta_f = 0$.

The gas-water two-phase flow equation in matrix is

$$\nabla\left(\beta\frac{K_m K_{mri}}{\mu_i B_i}\nabla P_{mi}\right) - \alpha\frac{\beta K_m K_{mk}}{\mu_i B_i}\left(P_{mi} - P_{fi}\right) = \frac{\partial}{\partial t}\left(\frac{\phi_m S_{mi}}{B_i} + V_g\right) \tag{10}$$

where ϕ_m is the porosity of matrix; S_{mi} is the saturation of phase i in matrix; V_g is gas volume of adsorption, it exists only when describing gas flow, expressed as

$$V_g = \frac{\rho_s V_L P_{mg}}{P_{mg} + P_L} \tag{11}$$

where ρ_s is the rock density, kg/m^3; V_L is the Langmuir volume, m^3/kg; P_L is Langmuir pressure, MPa. In the gas-water two-phase seepage in shale pores, the effect of capillary pressure cannot be ignored. Capillary pressure could be expressed by Eq. 12:

$$\begin{cases} P_{mc}\left(S_{mw}\right) = P_{mg} - P_{mw} \\ P_{fc}\left(S_{fw}\right) = P_{fg} - P_{fw} \end{cases} \tag{12}$$

where P_{mc} is the capillary pressure in the matrix, MPa; P_{fc} is the capillary pressure in the micro-fracture system, MPa.

For shale gas reservoirs with low and ultralow permeability, the following apparent permeability model

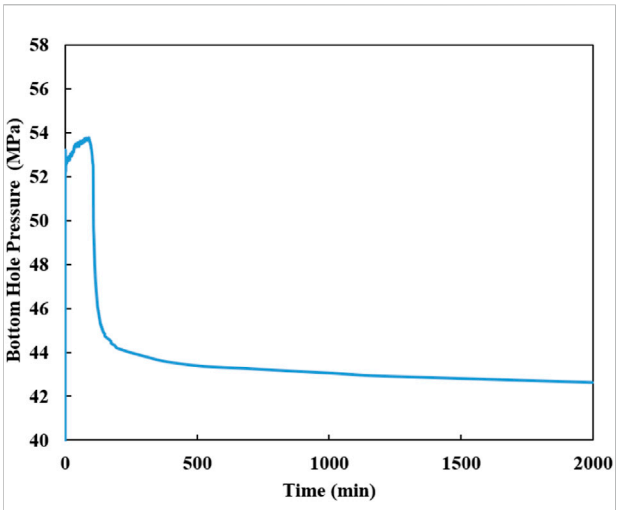

FIGURE 11
Bottom hole pressure curve from hydraulic fracturing to shut-in period.

proposed by Beskok and Karniadakis (1999) was employed to consider the gas slippage and diffusion effect:

$$K_m = K_{m0}(1 + aK_n)\left(1 + \frac{4K_n}{1 - bK_n}\right) \tag{13}$$

where K_{m0} is the initial matrix permeability, mD; a is the rarefaction parameter; K_n is the Knudsen number; b is the slip coefficient.

The hydraulic fracture permeability and micro-fracture permeability will decrease respectively with the decrease of fracture pressure and micro-fracture pressure, which is the stress sensitive effect. And exponential stress sensitivity formula is introduced into the model:

$$K_\varsigma = K_{\varsigma 0} e^{-c_\varsigma (P_{\varsigma 0} - P_\varsigma)} \tag{14}$$

where c is the stress sensitivity coefficient, 1/MPa and ς represents a fracture segment or micro-fracture cell.

Results

Basic parameters

We set up a reservoir model with dimensions of 350 m × 180 m, as shown in Figure 3A. A 180 m length hydraulic fracturing stage was selected and six initial fractures of 3 m length were placed in the reservoir intersecting with the

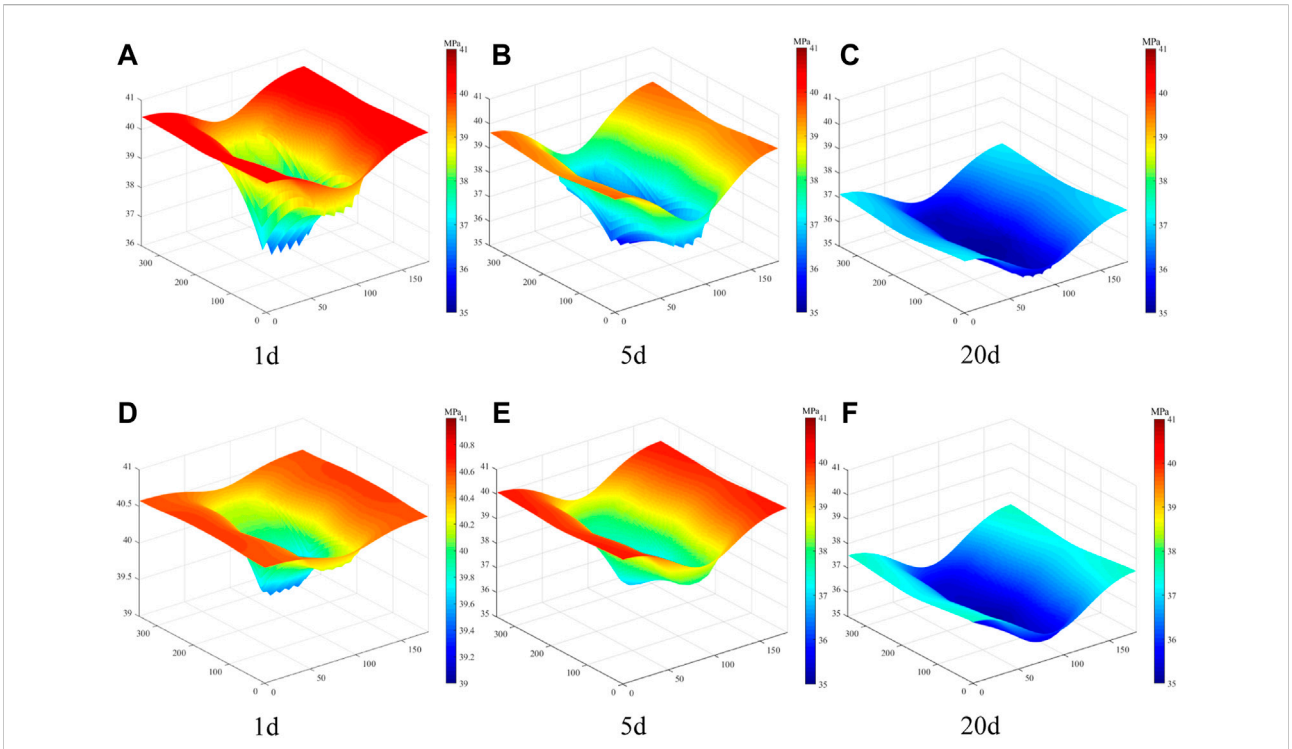

FIGURE 12
Distribution of pressure in micro-fracture system and matrix during production period. (In **(A–C)**, the range pressure in micro-fracture system is from 35 to 41 MPa. In **(D)**, the range of pressure in matrix is 39–41 MPa. In **(E,F)**, the range of pressure in matrix is from 35 to 41 MPa)

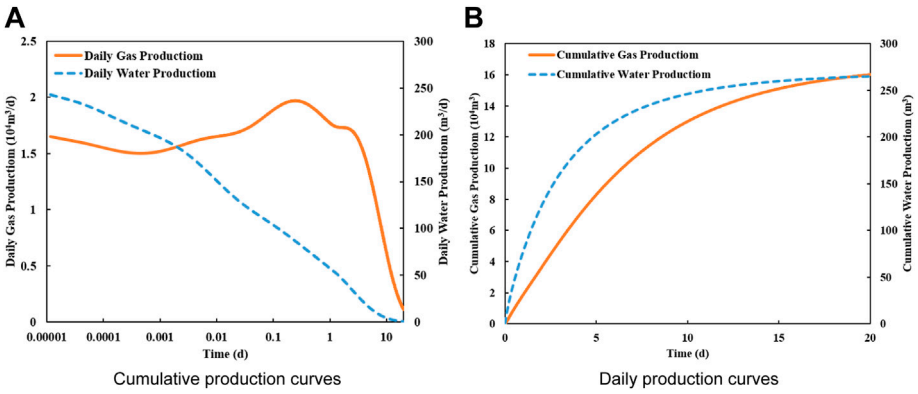

FIGURE 13
Curves of daily production and cumulative production of shale gas well. **(A)** is daily production curves. **(B)** is cumulative production curves.

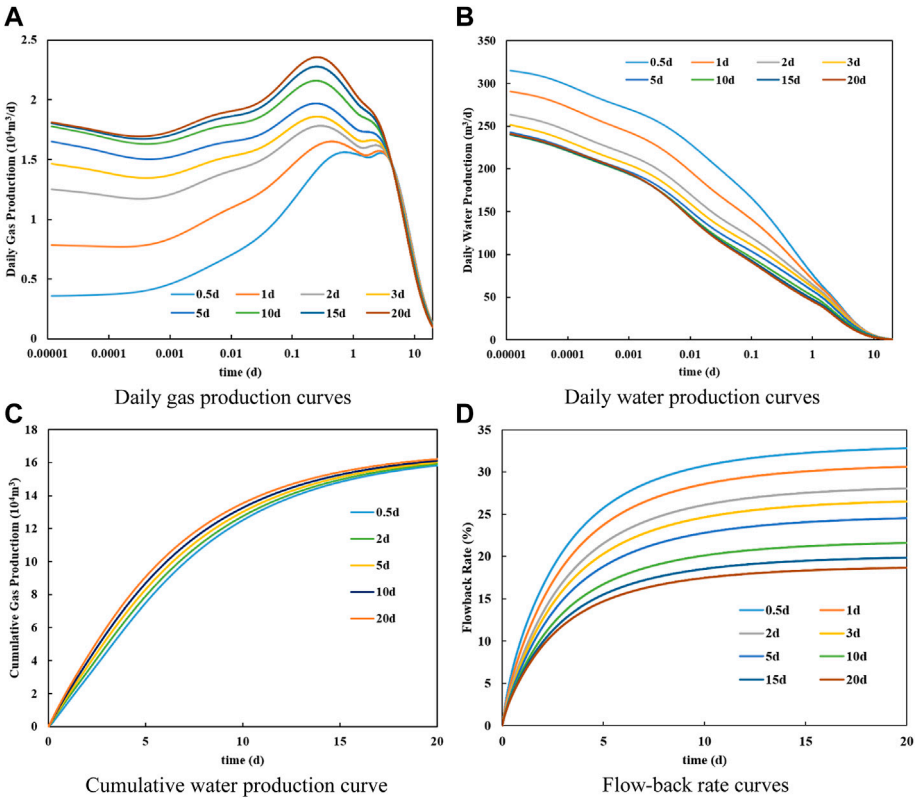

FIGURE 14
Production curves of shale gas well under different shut-in times. **(A)** Daily gas production curves. **(B)** Daily water production curves. **(C)** Cumulative water production curve. **(D)** Flow-back rate curves.

horizontal well. The Cartesian grids with grid size of 1 m × 1 m were used to divide the reservoir and fracture. And the initial fracture segments are three so that the fluid flow can be described by the EDFM. Table 1 lists the basic parameters of reservoir and fractures for a shale gas well in Sichuan Province, China. Fracture height is assumed to fully

TABLE 2 Parameters used for the simulations.

	K_f	SRV
Case 1	0.5 mD	280 m × 550 m × 30 m (Fig.37(a))
Case 2	0.05 mD	280 m × 550 m × 30 m (Fig.37(a))
Case 3	0.5 mD	180 m × 350 m × 30 m (Fig.37(a))
Case 4	0.05 mD	180 m × 350 m × 30 m (Fig.37(b))
Case 5	0.5 mD	70 m × 310 m × 30 m (Fig.37(c))
Case 6	0.05 mD	70 m × 310 m × 30 m (Fig.37(c))

penetrate reservoir thickness. Gas desorption is considered using Langmuir isotherm, which is widely used in shale gas reservoir simulators. Figure 3B shows relative permeability curves for the matrix, micro-fracture, and hydraulic fracture, respectively. Figures 3C,D show capillary pressure curves of matrix and micro-fracture system.

Model validation

Bottom hole pressure of shale gas well during hydraulic fracturing and shut-in period was obtained by the integrated model based on the parameters in Table 1. And the simulation results were compared with the bottom hole pressure during actual fracturing stimulation in Figure 4. It is evident that the simulated results are in good agreement with the actual data. Bottom hole pressure has a gradual upward trend during hydraulic fracturing. But the variation range of the actual data is larger, which is mainly caused by the instability of pumping rate. Therefore, the integrated model in this paper has a high accuracy.

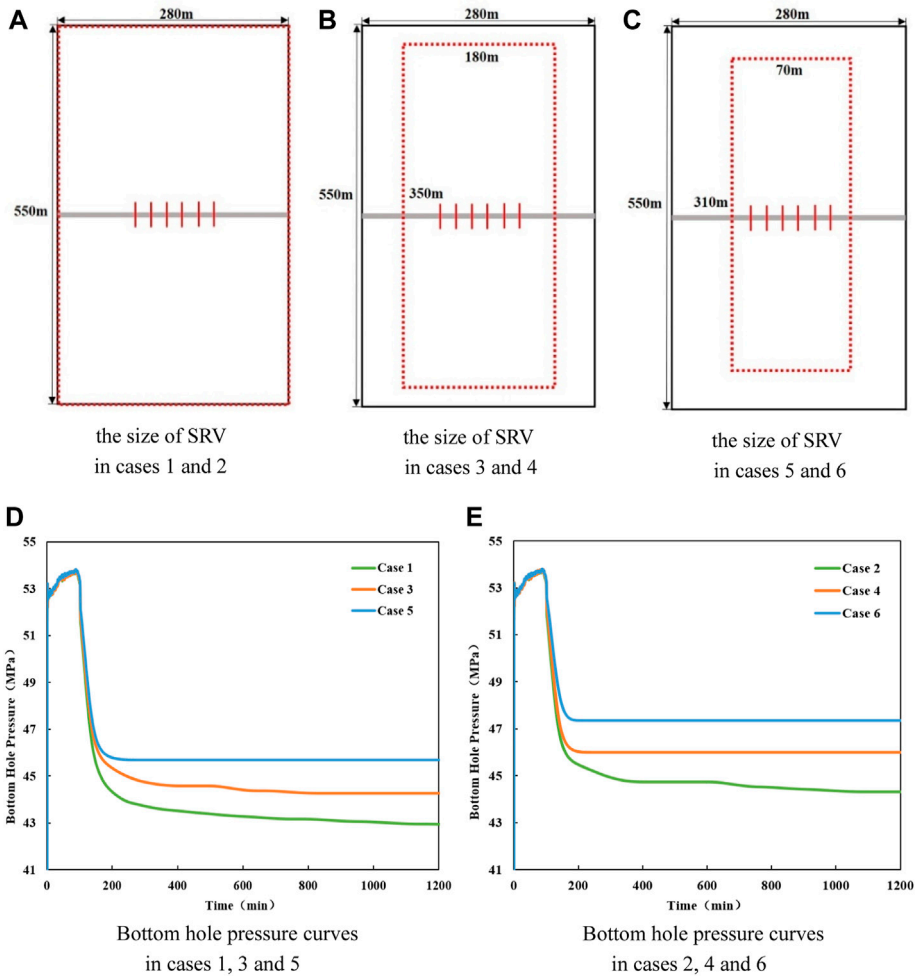

FIGURE 15
The size of SRV and bottom hole pressure curves in different cases. **(A)** The size of SRV in cases 1 and 2. **(B)** The size of SRV in cases 3 and 4. **(C)** The size of SRV in cases 5 and 6. **(D)** Bottom hole pressure curves in cases 1, 3 and 5. **(E)** Bottom hole pressure curves in cases 2, 4 and 6.

Distributions of pressure and water saturation in the micro-fracture system and matrix during fracturing period

The distributions of pore pressure and water saturation in reservoir during the hydraulic fracturing period were obtained based on the parameters in Table 1. The water saturation of the matrix changes little during hydraulic fracturing process due to low permeability. Therefore, the distribution of water saturation in matrix was not shown in the figures. Figure 5 shows the pore pressure distributions in micro-fracture system and matrix at different times, respectively. These simulation results show that the inner pressure of micro-fracture system and matrix around hydraulic fractures increases gradually with time during hydraulic fracturing stage. The pressure diffusion range in the micro-fracture system and matrix also expand with time gradually. The pore pressure of micro-fracture system and matrix between the first and sixth hydraulic fractures is much higher than that outside the above area. Because the flow of fracturing fluid in the reservoir between hydraulic fractures is hindered. The pore pressure in matrix increases slower than that in micro-fracture system, because there is a large seepage resistance between the matrix and the micro-fracture system.

Figures 6A–C show the variation of water saturation distribution in micro-fracture system during hydraulic fracturing. The variation of water saturation distribution in matrix is small during hydraulic fracturing due to the low permeability and shot stimulation time, so it is not shown. It is evident from these figures that water saturation of micro-fracture system around hydraulic fractures is positively correlated with time. And the influenced range of water saturation in micro-fracture system increases gradually with time. Moreover, the invasive range of fracturing fluid in micro-fracture system is significantly smaller than the spreading range of high pressure in micro-fracture system at the same time. The reason: relative permeability of water is much smaller than that of gas at the initial water saturation of micro-fracture system. Besides, gas has strong compressibility and expands more easily. The invasive range of fracturing fluid in micro-fracture system around different hydraulic fractures is shown in Figure 6D. It is found that the invasive ranges of the first and sixth hydraulic fractures far from other fractures are larger than those between first and sixth hydraulic fractures. This is a symptom of the inhibition of fluid flow in the reservoir area between hydraulic fractures.

Bottom hole pressure curves in Figure 7 show that hydraulic fracturing is a step-by-step process, which consists of fracture initiating, fluid filling, and fracture re-initiating. First, bottom hole pressure increases gradually with the pumping of fracturing fluid. When $K_I > K_{IC}$, hydraulic fracture is initiated and new fracture segments are generated. Then, the fracturing fluid enters new fracture segments and bottom hole pressure drops. After that, bottom hole pressure increases again with time until hydraulic fracture is initiated again. Meanwhile, Figure 7 shows that the variation of bottom hole pressure is not smooth during the fracture propagation process because the initiations of different hydraulic fractures are not simultaneous due to the different net pressure (Feng et al., 2016). And the bottom hole pressure has a general upward trend with the increase of pressure in micro-fracture system and matrix.

Distributions of pressure and water saturation in the micro-fracture and matrix during shut-in period

In the shut-in period, the pumping rate drops to zero. Figure 8 shows the distributions of pressure in micro-fracture system and matrix during the shut-in period, respectively. As shown in these figures, the high pressure of micro-fracture system and matrix brought by hydraulic fracturing gradually spreads to the deeper formation with the increase of shut-in time. Pressure spreads in the micro-fracture system slightly faster than the matrix due to the low permeability of matrix.

Figure 9 shows that the fracturing fluid, which invaded into micro-fracture, continues to flow into the deeper formation under the pressure gradient and capillary pressure. The invasive range of fracturing fluid increases with shut-in time. Fig.(d) shows the profile of water saturation in micro-fracture system during shut-in period. Micro-fracture water saturations around the first fracture and sixth fracture decrease fast. And the invasive ranges of fracturing fluid around the first fracture and sixth fracture are the largest. Moreover, locations of the maximum water saturation in micro-fracture system around the first fracture and sixth fracture are not the same as the locations of these fractures under the action of pressure gradient.

Figure 10 shows that capillary pressure and pressure gradient change the distribution of water saturation in the matrix during shut-in period. The matrix pressure around the middle hydraulic fractures is slightly higher than the micro-fracture pressure around the middle hydraulic fractures at the same shut-in time (Figure 8). But the strong capillary pressure in the matrix (Figure 3C) also guides fracturing fluid flow gradually into matrix from micro-fracture system. Figure 10 also shows that water saturation of matrix and the invasive range of fracturing fluid in matrix are positively correlated with the shut-in time.

Figure 11 shows the bottom hole pressure from fracturing to shut-in period. Bottom hole pressure is high during the hydraulic fracturing. When shut-in period begins, the pumping rate of fracturing fluid drops to zero and bottom hole pressure declines

rapidly. Moreover, bottom hole pressure becomes steady gradually with the increase of shut-in time.

Distributions of pressure and water saturation in the micro-fracture system and matrix during production period

The production of shale gas well begins after shut-in period. In this paper, bottom hole pressure is constant during production (P_{wf} = 35 MPa). Figure 12 shows the distributions of pressure in micro-fracture system and matrix during production period after 5 days shut-in. These figures show that the pressure of micro-fracture system and matrix continues to decrease during production process and the drop rates of pressure in micro-fracture system and matrix around fractures are the largest.

It is evident from Figure 13A that the shale gas well has a high initial gas production rate in the early stage of production (Luo et al., 2021) because water saturation of hydraulic fractures decreases gradually during shut-in period. Gas production of the initial stage mainly comes from hydraulic fractures and daily gas production also decreases slightly as the pressure in the fractures drops. Then gas in micro-fracture system flows into hydraulic fractures, which increases the gas saturation of hydraulic fractures and daily gas production. At the end of this event, daily gas production decreases gradually after reaching the peak. Figure 13B shows that the cumulative water production is 265.17 m^3 after producing 20 days. It is less than 30% of the total injection volume of fracturing fluid (the total injection volume of fracturing fluid is 1080 m^3). There is still a large amount of fracturing fluid retained in micro-fracture system and matrix after 20 days production.

Discussion

The impact of shut-in time on the production

The shale gas well productivities under different shut-in times were simulated by integrated model to analyze the relationship between shut-in time and production of shale gas well.

Figures 14A,B show daily gas production and daily water production under different shut-in times. Figure 14A shows that the daily gas production at the early period of production increases with the increase of shut-in time. The increase rate of daily gas production decreases gradually with the increase of shut-in time. The daily water production at the early period of production is negatively correlated with shut-in time, as shown in Figure 14B. It is evident that the invasive fracturing fluid gradually flows into the deeper formation with the increase of shut-in time. Water saturations of hydraulic fractures and micro-fracture system around hydraulic fractures decrease, which causes a high production capacity at the early period. The optimal shut-in time was suggested as 10 days combining Figures 14A–C.

Figure 14D shows that the flow-back rate was negatively correlated with the shut-in time. The volume of invasive fracturing fluid in the matrix gradually increases with the increase of shut-in time. And the invasion range of fracturing fluid in micro-fracture system and matrix gradually expands with the increase of shut-in time. It is difficult to bring the invasive fracturing fluid in micro-fracture system and matrix out of the formation.

The impact of the range of SRV and the permeability of micro-fracture system on the bottom hole pressure

A high permeability area is often formed around hydraulic fractures after hydraulic fracturing in the shale reservoir. And the volume of this area is Stimulated Reservoir Volume (SRV), which is the key index of hydraulic fracturing evaluation. In this paper, the micro-fracture system was used to describe the area of SRV in the reservoir. The range of SRV and the permeability of micro-fracture system influence the pressure transmission in the reservoir, which impacts the bottom hole pressure during shut-in period. Bottom hole pressures of different cases in Table 2 were simulated by the integrated model.

Figures 15D,E show that the range of SRV and the permeability of micro-fracture system are negatively correlated with the bottom hole pressure during the shut-in period. It is difficult for high pressure in micro-fracture system caused by hydraulic fracturing to spread to deeper formation when the range of SRV is small. Bottom hole pressures of cases 5 and 6 are still higher than that of other cases after a long time shut-in. When the micro-fracture permeability becomes higher (cases 1, 3, and 5), high pressure in micro-fracture system caused by hydraulic fracturing can spread to deeper formation conveniently. Bottom hole pressures of cases 1, 3, and 5 are lower than that of cases 2, 4, and 6 after a long time shut-in. The permeability of micro-fracture system determines the drop rate of bottom hole pressure and the size of SRV determines the amplitude of decreased pressure.

Conclusion

A model for simulating the integration process of hydraulic fracturing, shut-in period, and well production is developed. The distributions of pore pressure and water saturation varying in different periods and the production decline of shale gas well are obtained through the integrated simulation model. And the impact of shut-in time on production of shale gas well is also discussed. Moreover, the influences of the size of SRV and the

permeability of micro-fracture system on bottom hole pressure during shut-in period are analyzed.

1) In hydraulic fracturing process, the distributions of pore pressure and water saturation in micro-fracture system and matrix around hydraulic fractures are impacted by the fracturing fluid leak-off. The invasive range of fracturing fluid and the spreading ranges of high pressure in the reservoir around hydraulic fractures increase with time. The variation range of bottom hole pressure is not the same during the fracture propagation process because the initiations of different hydraulic fractures are not simultaneous.
2) During shut-in period, the high pressure in the reservoir brought by hydraulic fracturing spreads to the deeper formation with the increase of shut-in time. And the invasive range of fracturing fluid in the reservoir also increases with the shut-in time. The distribution of water saturation in matrix changes significantly during shut-in period due to the influences of capillary pressure and pressure gradient. The bottom hole pressure drops rapidly during shut-in period due to pressure transmission.
3) In production process, the pore pressure in the reservoir around hydraulic fractures drops rapidly. And daily gas production of shale gas well shows a falling-rising-falling trend. The flow-back rate of fracturing fluid is less than 30% of the total volume of fracturing fluid. And there is still a large amount of fracturing fluid retained in micro-fracture system and matrix after production.
4) With the increase of shut-in time, the daily gas production increases and the daily water production decreases gradually. A 10 days optimal shut-in time of the shale gas well in Sichuan Province, China was suggested by comparing the gas production under different shut-in times. The invasion range of fracturing fluid in micro-fracture system and matrix gradually expands with the increase of shut-in time. The flow-back rate is negatively correlated with the shut-in time.
5) The range of SRV and the permeability of micro-fracture system are negatively correlated with the bottom hole pressure during shut-in period. And the permeability of the micro-fracture system determines the drop rate of bottom hole pressure, and the size of SRV determines the amplitude of decreased pressure.

Data availability statement

The original contributions presented in the study are included in the article/supplementary material, further inquiries can be directed to the corresponding author.

Author contributions

YL, AL, and XC contributed to conception and design of the study. AL wrote the first draft of the manuscript. LC, CC, and WX wrote sections of the manuscript.

Funding

This study was supported by the Science and Technology Cooperation Project of the CNPC-SWPU Innovation Alliance, the National Natural Science Foundation of China (Grant no. U19A2043, U21B2071, and 52174033), and Natural Science Foundation of Sichuan Province (NSFSC) (No. 2022NSFSC0971).

Conflict of interest

Authors XC and LC was employed by PetroChina Xinjiang Oilfield Company. CC and WX PetroChina Southwest Oil & Gas Field Company.

The remaining authors declare that the research was conducted in the absence of any commercial or financial relationships that could be construed as a potential conflict of interest.

Publisher's note

All claims expressed in this article are solely those of the authors and do not necessarily represent those of their affiliated organizations, or those of the publisher, the editors and the reviewers. Any product that may be evaluated in this article, or claim that may be made by its manufacturer, is not guaranteed or endorsed by the publisher.

References

Beskok, A., and Karniadakis, G. E. (1999). Report: A model for flows in channels, pipes, and ducts at micro and nanoscales. *Microscale Thermophys. Eng.* 3 (1), 43–77. doi:10.1080/108939599199864

Cavalcante Filho, J. S. D. A., and Sepehrnoori, K. (2017). Simulation of planar hydraulic fractures with variable conductivity using the embedded discrete fracture model. *J. Petroleum Sci. Eng.* 153, 212–222. doi:10.1016/j.petrol.2017.03.049

Cavalcante-Filho, J. S. A., Shakiba, M., and Moinfar, A. (2015). *Implementation of a preprocessor for embedded discrete fracture modeling in an IMPEC compositional reservoir simulator*. Houston, Texas, Usa: The Spe Reservoir Simulation Symposium.

Dachanuwattana, S., Xia, Z., Yu, W., Qu, L., Wang, P., Liu, W., et al. (2018). Application of proxy-based MCMC and EDFM to history match a shale gas condensate well. *J. Petroleum Sci. Eng.* 167, 486–497. doi:10.1016/j.petrol.2018.04.025

Dong, Z., Li, W., Lei, G., Wang, H., and Wang, C. (2019). Embedded discrete fracture modeling as a method to upscale permeability for fractured reservoirs. *Energies* 12 (5), 812. doi:10.3390/en12050812

Du, S., Liang, B., and Lin, Y. (2017). *Field study: Embedded discrete fracture modeling with artificial intelligence in permian basin for shale formation*. San Antonio, Texas, Usa: The Spe Annual Technical Conference and Exhibition.

Fakcharoenphol, P., Torcuk, M., Kazemi, H., and Wu, Y. (2016). Effect of shut-in time on gas flow rate in hydraulic fractured shale reservoirs. *J. Nat. Gas Sci. Eng.* 32, 109–121. doi:10.1016/j.jngse.2016.03.068

Feng, Y., Jones, J. F., and Gray, K. E. (2016). A review on fracture-initiation and-propagation pressures for lost circulation and wellbore strengthening. *Spe Drill. Complet.* 31 (02), 134–144. doi:10.2118/181747-pa

Ghanbari, E., and Dehghanpour, H. (2016). The fate of fracturing water: A field and simulation study. *Fuel* 163, 282–294. doi:10.1016/j.fuel.2015.09.040

Li, L., and Lee, S. H. (2008). Efficient field-scale simulation of black oil in a naturally fractured reservoir through discrete fracture networks and homogenized media. *SPE Reserv. Eval. Eng.* 11 (04), 750–758. doi:10.2118/103901-pa

Liang, X., Liang, T., Zhou, F., Wang, C., Yang, K., Wei, D., et al. (2021). Impact of shut-in time on production after hydraulic fracturing in fractured shale gas formation: An experimental study. *J. Nat. Gas Sci. Eng.* 88, 103773. doi:10.1016/j.jngse.2020.103773

Liu, J., Sheng, J. J., Emadibaladehi, H., and Tu, J. (2021). Experimental study of the stimulating mechanism of shut-in after hydraulic fracturing in unconventional oil reservoirs. *Fuel* 300, 120982. doi:10.1016/j.fuel.2021.120982

Liu, Y., Leung, J. Y., Chalaturnyk, R., and Virues, C. J. J. (2017). Fracturing fluid distribution in shale gas reservoirs due to fracture closure, proppant distribution and gravity segregation. The Spe Unconventional Resources Conference. Calgary, Alberta, Canada. February 2017. IEEE.

Luo, A., Li, Y., Wu, L., Peng, Y., and Tang, W. (2021). Fractured horizontal well productivity model for shale gas considering stress sensitivity, hydraulic fracture azimuth, and interference between fractures. *Nat. Gas. Ind. B* 8 (3), 278–286. doi:10.1016/j.ngib.2021.04.008

Moinfar, A., Varavei, A., Sepehrnoori, K., and Johns, R. T. (2013). Development of a coupled dual continuum and discrete fracture model for the simulation of unconventional reservoirs. The Spe Reservoir Simulation Symposium. The Woodlands, Texas, Usa. February 2013. IEEE.

Peng, Y., Zhao, J., Sepehrnoori, K., Li, Z., and Xu, F. (2019). Study of delayed creep fracture initiation and propagation based on semi-analytical fractional model. *Appl. Math. Model.* 72, 700–715. doi:10.1016/j.apm.2019.03.034

Peng, Y., Zhao, J., Sepehrnoori, K., Li, Y., and Li, Z. (2020a). The influences of stress level, temperature, and water content on the fitted fractional orders of geomaterials. *Mech. Time. Depend. Mat.* 24, 221–232. doi:10.1007/s11043-019-09417-0

Peng, Y., Zhao, J., Sepehrnoori, K., and Li, Z. (2020b). Fractional model for simulating the viscoelastic behavior of artificial fracture in shale gas. *Eng. Fract. Mech.* 228, 106892. doi:10.1016/j.engfracmech.2020.106892

Salimzadeh, S., Paluszny, A., and Zimmerman, R. W. (2017). Three-dimensional poroelastic effects during hydraulic fracturing in permeable rocks. *Int. J. Solids Struct.* 108, 153–163. doi:10.1016/j.ijsolstr.2016.12.008

Shen, W., Xu, Y., Gu, J., Li, X., and Huang, W. (2016). Numerical simulation of gas and water flow mechanism in hydraulically fractured shale gas reservoirs. *J. Nat. Gas Sci. Eng.* 35, 726–735. doi:10.1016/j.jngse.2016.08.078

Sun, R., Yu, W., Xu, F., Pu, H., and Miao, J. (2019). Compositional simulation of CO2 Huff-n-Puff process in Middle Bakken tight oil reservoirs with hydraulic fractures. *Fuel* 236, 1446–1457. doi:10.1016/j.fuel.2018.09.113

Wang, F., Pan, Z., and Zhang, S. (2017). Impact of chemical osmosis on water leakoff and flowback behavior from hydraulically fractured gas shale. *J. Petroleum Sci. Eng.* 151, 264–274. doi:10.1016/j.petrol.2017.01.018

Wang, F., Chen, Q., and Ruan, Y. (2020a). Hydrodynamic equilibrium simulation and shut-in time optimization for hydraulically fractured shale gas wells. *Energies (Basel)* 13 (4), 961. doi:10.3390/en13040961

Wang, Q., Hu, Y., Zhao, J., Chen, S., Fu, C., and Zhao, C. (2020b). Numerical simulation of fracture initiation, propagation and fracture complexity in the presence of multiple perforations. *J. Nat. Gas Sci. Eng.* 83, 103486. doi:10.1016/j.jngse.2020.103486

Wang, T., Yang, Y., Peng, Y., Zhao, J., Qi, T., Zeng, J., et al. (2021). Simulation and evaluation for acid fracturing of carbonate reservoirs based on embedded discrete fracture model. *Nat. Gas. Ind. B* 8 (6), 637–649. doi:10.1016/j.ngib.2021.08.011

Xu, Y., Cavalcante Filho, J. S., Yu, W., and Sepehrnoori, K. (2017). Discrete-fracture modeling of complex hydraulic-fracture geometries in reservoir simulators. *SPE Reserv. Eval. Eng.* 20 (02), 403–422. doi:10.2118/183647-pa

Xu, Y., Fernandes, B. R. B., Marcondes, F., and Sepehrnoori, K. (2019). Embedded discrete fracture modeling for compositional reservoir simulation using corner-point grids. *J. Petroleum Sci. Eng.* 177, 41–52. doi:10.1016/j.petrol.2019.02.024

Yu, W., Xu, Y., Liu, M., Wu, K., and Sepehrnoori, K. (2018). Simulation of shale gas transport and production with complex fractures using embedded discrete fracture model. *AIChE J.* 64 (6), 2251–2264. doi:10.1002/aic.16060

Yue, H., Chang, H., Fan, Y., Chen, F., and Chen, P. (2020). Construction and prospect of China's shale gas technical standard system. *Nat. Gas. Ind. B* 7 (6), 664–670. doi:10.1016/j.ngib.2020.04.007

Zhang, H., Li, T., Han, D., Wang, D., Sun, D., and Yu, B. (2020). Study on a dual embedded discrete fracture model forFluid flow in fractured porous media. *Comput. Model. Eng. Sci.* 124 (1), 5–21. doi:10.32604/cmes.2020.09290

Zhang, J., Shi, M., Wang, D., Tong, Z., Hou, X., Niu, J., et al. (2022a). Fields and directions for shale gas exploration in China. *Nat. Gas. Ind. B* 9 (1), 20–32. doi:10.1016/j.ngib.2021.08.014

Zhang, L., He, X., Li, X., Li, K., He, J., Zhang, Z., et al. (2022b). Shale gas exploration and development in the Sichuan Basin: Progress, challenge and countermeasures. *Nat. Gas. Ind. B* 9 (2), 176–186. doi:10.1016/j.ngib.2021.08.024

Zhao, J., Peng, Y., Li, Y., and Xiao, W. (2015). Analytical model for simulating and analyzing the influence of interfacial slip on fracture height propagation in shale gas layers. *Environ. Earth Sci.* 73 (10), 5867–5875. doi:10.1007/s12665-015-4360-4

Zhao, J., Wang, Q., Hu, Y., Ren, L., and Zhao, C. (2019). Numerical investigation of shut-in time on stress evolution and tight oil production. *J. Petroleum Sci. Eng.* 179, 716–733. doi:10.1016/j.petrol.2019.03.087

Zhao, J., Zhao, J., Hu, Y., Huang, T., Zhao, X., and Liu, X. (2020). Non-planar fracture propagation model for fluid-driven fracturing based on fluid-solid coupling. *Eng. Fract. Mech.* 235, 107159. doi:10.1016/j.engfracmech.2020.107159

Zhao, J., Ren, L., Jiang, T., Hu, D., Wu, L., Wu, J., et al. (2022). Ten years of gas shale fracturing in China: Review and prospect. *Nat. Gas. Ind. B* 9 (2), 158–175. doi:10.1016/j.ngib.2022.03.002

Zhou, S., Dong, D., Zhang, J., Zou, C., Tian, C., Rui, Y., et al. (2021). Optimization of key parameters for porosity measurement of shale gas reservoirs. *Nat. Gas. Ind. B* 8 (5), 455–463. doi:10.1016/j.ngib.2021.08.004

Zhu, D., Hu, Y., Cui, M., Chen, Y., Liang, C., Cai, W., et al. (2020). Productivity simulation of hydraulically fractured wells based on hybrid local grid refinement and embedded discrete fracture model. *Petroleum Explor. Dev.* 47 (2), 365–373. doi:10.1016/s1876-3804(20)60053-2

frontiers | Frontiers in Energy Research

TYPE Methods
PUBLISHED 22 November 2022
DOI 10.3389/fenrg.2022.1003660

OPEN ACCESS

EDITED BY
Shuai Zhao,
Southwest Petroleum University,
Chengdu, China

REVIEWED BY
Yanchun Ling,
University of North Carolina at Chapel Hill, United States
Bing Hou,
China University of Petroleum, Beijing, China

*CORRESPONDENCE
Ji Zeng,
zj_516@outlook.com

SPECIALTY SECTION
This article was submitted to Advanced Clean Fuel Technologies, a section of the journal Frontiers in Energy Research

RECEIVED 26 July 2022
ACCEPTED 31 October 2022
PUBLISHED 22 November 2022

CITATION
Zeng J, Li W, Fang H, Huang X, Wang T, Zhang D and Yuan S (2022), The hydraulic fracturing design technology and application of geological-engineering integration for tight gas in jinqiu gas field.
Front. Energy Res. 10:1003660.
doi: 10.3389/fenrg.2022.1003660

The hydraulic fracturing design technology and application of geological-engineering integration for tight gas in jinqiu gas field

Ji Zeng*, Wenzhe Li, Hongming Fang, Xin Huang, Tao Wang, Dandan Zhang and Shuhang Yuan

Engineering Technology Research Institute, PetroChina Southwest Oil and Gas Field Company, Chengdu, China

Tight sandstone gas reservoir of Shaximiao formation in Jinqiu Gas field has the advantages of wide distribution and abundant resources. Due to its low porosity, low permeability and strong spatial heterogeneity, this reservoir puts forward high requirements for sweet spot identification, cluster design and hydraulic fracture morphology prediction. Since the conventional stimulation methods can not meet the requirement of economy, the geological-engineering integration model is established. This optimization model of multiple subjects could layout the relationship among engineering characteristics, hydraulic fracture shape and well productivity. Based on the simulation results, key controlling factors are identified and optimized. And the customized stimulation strategies are recommended for different reservoir quality and different channel sand. Through application of these methods, the average test well productivity in the target field increased from 50,500 cubic meter per day to 434,300 cubic meter per day, and it lay a solid foundation for the efficient development of tight gas in central Sichuan Basin.

KEYWORDS

tight sandstone gas, shaximiao formation, geological-engineering integration, hydraulic fracture, differentiation stimulation strategies

1 Introduction

In recent years, with the complexity of oil and gas exploration objects, tight sandstone gas reservoirs have become an important replacement field. Jinqiu gas field in Sichuan Basin is rich in resources and widely distributed. It is an important new block for oil and gas exploitation in Sichuan and Chongqing. And significant breakthrough in technique has been made in exploration and development. The tight sandstone reservoir of Shaximiao Formation in this area generally shows low porosity, ultra-low permeability and strong heterogeneity. The river channel is narrow. There are

23 sand groups developed longitudinally (Figure 1). There are great differences in reservoir mechanical properties, *in situ* stress distribution characteristics and natural fracture development of different sand groups. At the initial stage of the study block, an excessive stimulation technology is mainly used to ensure the full utilization of the reservoir, however, the pertinence and economy of this stimulation technique are not high. To solve these problem in unconventional oil and gas resources development, a geological-engineering integration method is introduced (Rutqvist et al., 2016; Teran 2017). This method aims to improve the productivity of single well, and requires a comprehensive analysis of Geology and reservoir (Ayatollahy et al., 2013). It is a combination of geology and engineering, which breaks the disciplinary barrier and realizes interdisciplinary cooperation (Maity 2013). Through a series of modelling, an optimized reservoir stimulation could be made in a specific field. The concept has been preliminarily applied in Sulige tight gas reservoir, stress sensitive tight reservoir in the west of Kuqa, dolomite reservoir in Tarim Basin, conventional low permeability reservoir in JinQiu Oilfield and other regions or reservoirs (Rafiq 2015; Zhao et al., 2015; Yousefzadeh et al., 2019; Sgher, 2021), and achieved good results (Jon et al., 2010).

This study summarizes the early stimulation filed tests in Jinqiu Gas field, then establishes geological model, fracture propagation model and productivity prediction model after hydraulic fracturing in Jinqiu Gas field. Through the coupling of these models, the integrated geological engineering reservoir stimulation design technology is realized in aiming gas field. This method effectively optimizes the fracturing parameters, realizes the differential stimulation technology, and supports the multi-stage stimulation and three-dimensional development of the river.

2 Geological characteristics and stimulation difficulties

Jinqiu gas field is located at the intersection of the middle paleo uplift and middle oblique gentle structural belt in Central Sichuan and the low gentle structural belt in the middle paleo depression in northern Sichuan. There are 23 sand groups developed in the tight gas of Shaximiao Formation in the study block. These sand groups have a burial depth of 1500–2200 m, a width of 400–900 m, a reservoir thickness of 10–25 m, an overburden permeability of 0.003–0.064mD, and a pressure coefficient of 0.3–1.2. It is highly heterogeneous, representing the characteristics of low porosity, ultra-low permeability and narrow channel.

In the early field tests, several rounds of technical research were carried out to form the multi fracture fracturing technology of *multi clusters in the stage + variable viscosity slick water + high-intensity continuous sand injection*. However, due to the influence of reservoir characteristics, tight gas has low porosity and permeability, and the influence range of single well, controlled reserve scale and cumulative production are limited. The main technical difficulties in improving the effect of regional implementation are reflected in two aspects.

1) The reservoir of Shaximiao formation is widely distributed, and the fault scale and natural fracture development degree vary greatly in different regions. Also, the lithologic boundary of channel sand body is complex, and the mechanical properties of sand and mudstone are quite different, therefore, it is difficult to carry out targeted stimulation. In the early practice, excessive transformation technology is adopted to ensure the stimulation effect. Because the permeability of tight sandstone reservoir is very low and the controlled reserves of single well are limited, the economic and efficient fracturing parameters need to be further optimized.
2) The brittleness index of the reservoir is low, the bedding of the reservoir is underdeveloped, and it is difficult to form a complex fracture network. In the early stage, the multi cluster process in the stage was mainly used to ensure the full utilization of the reservoir. However, due to the stress shadow effect, the small cluster spacing design led to the complexity of hydraulic fracture extension and the limited length of hydraulic fracture.

3 Geological-engineering integrated reservoir stimulation technology

In order to break through the difficulties in the stimulation of channel tight sandstone and improve the overall benefit, a geological-engineering integrated reservoir stimulation technology mode must be formed, which aims at benefit development and integrates multi-disciplinary and multi information. That is to say, it is necessary to carry out Fracturing and productivity simulation based on geological model in full combination with river channel distribution and reservoir physical properties, continuously optimize fracturing parameters and carry out targeted reservoir stimulation design guided by well productivity and expected rate of return.

3.1 Three-dimensional geological modeling

The three-dimensional geological model is an important foundation for fracturing design and numerical simulation, and a solid foundation for the research and application of geological engineering integration in this area. According to 3D seismic interpretation horizon, fault and well layered data, a regional 3D geological framework model is established, including fault model and layer model (Smart 2004).

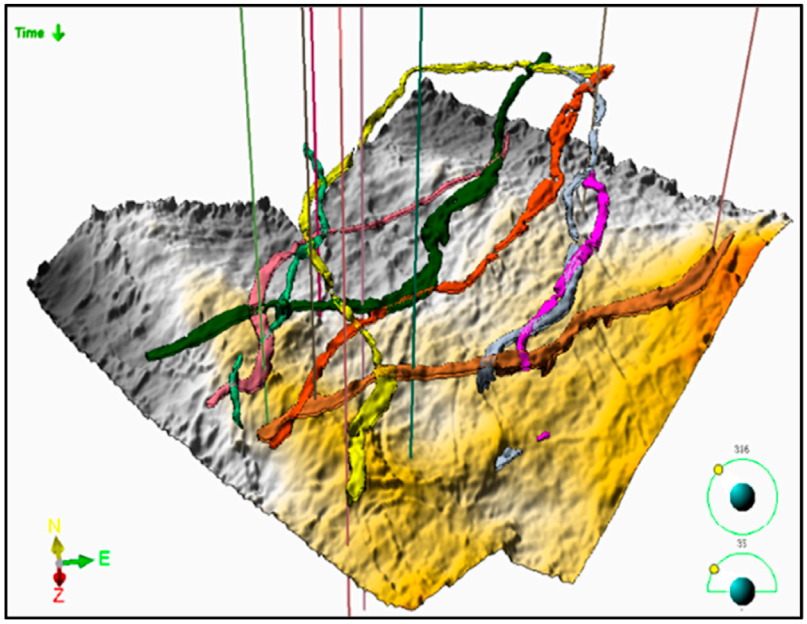

FIGURE 1
3D characterization of Shaximiao formation channel in Jinqiu gas field.

The model controls the trend of attributes in seismic inversion (Maity 2013). The model is corrected with logging interpretation results. The three-dimensional geological modeling technology is used to establish the reservoir attribute model and the three-dimensional model of rock elasticity and strength attributes. Different from the three-dimensional image display of reservoir, the three-dimensional regional geological model can quantitatively represent the data volume of underground geological characteristics and the three-dimensional spatial distribution of reservoir parameters, which lays a foundation for subsequent research (Figure 2).

3.2 Three-dimensional geomechanical modeling

The magnitude and direction of *in situ* stress affect the shape and trend of hydraulic fractures and are directly related to the effect of reservoir stimulation. In order to obtain the three-dimensional stress state of the reservoir, three-dimensional geomechanical modeling should be established firstly (Lark 2014). The core of modeling is to establish a three-dimensional geomechanical grid model based on the geological model. One-dimensional geomechanical model of single well and seismic inversion data are used to establish a static parameter model (Cao et al., 2001). Meanwhile, the model needs to consider the influence of the fault system on the stress field. And it is important to use the finite element simulator to calculate and simulate the current *in situ* stress field distribution.

3.2.1 Single well geomechanical modeling

One-dimensional geomechanical model of single well is established through processing logging data. Through sorting and analyzing the test results of single well core mechanics test, the transformation relationship of dynamic and static parameters is obtained, and the mechanical parameters of logging calculation are calibrated and checked (Figure 3). Single well rock mechanics modeling is mainly used to evaluate the rock mechanics properties and original field stress of single well, which provides an important data basis for three-dimensional geomechanics modeling.

3.2.2 Regional three-dimensional geomechanical modeling

On the basis of one-dimensional geomechanical modeling results of single well, a static parameter model is established by combining seismic inversion data (Yang et al., 2013). Considering the influence of the fault system on the stress field (Maerten et al., 2006), the regional three-dimensional geomechanical modeling work is carried out in the study area to evaluate the current *in situ* stress orientation, *in situ* stress field size and distribution law (Figure 4). At the same time, based on the three-dimensional *in situ* stress field, the limit stress state of the fault system is analyzed, and the fracture system in the limit stress state is selected to determine whether

the fault surface will be activated under the action of the corresponding shear stress and normal stress.

3.3 Three-dimensional geomechanical modeling

The regional model grid can not meet the needs of subsection and cluster design and hydraulic fracture simulation. And the layered three-dimensional geological modeling method must be used, which is more accurate in describing the structure and reservoir characteristics near the well platform. Combining with the deployment platform location and well location, the regional three-dimensional geological model is modified with controlling the structural details and subtle changes of reservoir parameters in both vertical and horizontal direction (Figure 5). The platform model has higher resolution and can reflect the spatial changes of reservoir attributes more finely. It can effectively support fracturing numerical simulation optimization and productivity prediction.

3.4 Three-dimensional model iteration update

Collecting new drilling data, including stratification, steering model and logging interpretation result data could help iterative updating of three-dimensional geological model and geomechanical model and deepen the understanding of structure, reservoir parameters and geomechanical characteristics (Wang et al., 2013; Han et al., 2019). And these updates lay a foundation for later fracturing design and optimization design (Figure 6).

3.5 The well productivity forecast model after hydraulic fracturing

The transport of natural gas in low-permeability reservoirs is complex (Friedel et al., 2006; Wang et al., 2017). The seepage of gas from the reservoir to the bottom hole is divided into two zones. One is the seepage in reservoir matrix. The other is the flow from the end of the fracture to bottom hole. Therefore, a new model of fracturing well capacity in tight gas reservoir considering the influence of multiple factors is established. The model is derived based on the following conditions.

① It is assumed that the reservoir is homogeneous and has equal thickness.
② The fracture is divided into n meshes, and the fracture height is equal to the thickness of the gas layer;
③ In the direction of fracture propagation, the fracture width and fracture permeability decrease gradually, and there is no pressure gradient in each unit;
④ The transport of natural gas is steady-state seepage flow, and single-phase isothermal seepage is considered.

The seepage model of the fracture is shown in Figure 7:

3.5.1 Radial seepage at the end of the fracture

Under the influence of the starting pressure gradient, stress sensitivity and slippage effect, this paper establish the differential equation of seepage flow.

$$\frac{Q_0}{2\pi rh} = \frac{PZ_{gsc}T_{gsc}k_g e^{\alpha(P-P_e)}\left(1+\frac{b}{p}\right)\left(\frac{d_p}{d_r}-\tau\right)}{\mu P_{gsc}ZT}. \tag{1}$$

Set the well bottom hole at origin of coordinate system. Within the steady-state seepage field, the relationship between the radius of the cross-section circle and the pressure follows the equation below.

$$r = \phi(p). \tag{2}$$

Substitute Eq. 2 into Eq. 1.

$$\int_{rwf1/2}^{r_e}\left[\frac{p_{gsc}T}{Z_{gsc}T_{gsc(2\pi rh)}K_g e-\alpha p_e(1+b/p)}Q_0\right]\mathrm{dr} = \int_{rwf1/2}^{p_e}\frac{pe^{\alpha p}}{\mu Z}\left(1-\tau\phi'(p)\right)\mathrm{d}p. \tag{3}$$

Pseudopressure function $m(p)$ is introduced.

$$m(p) = \int_0^p \frac{pe^{\alpha p}}{\mu Z}\left(1-\tau\phi'(p)\right)\mathrm{d}p, \tag{4}$$

And the ultimate seepage function in this zone can be obtained.

$$m(p_e) - m(p_{wf1}) = \left[\frac{p_{gsc}T}{Z_{gsc}T_{gsc}(2\pi h)k_g e-\alpha p_e(1+b/p)}ln\frac{2r_e}{r_{wf1}}\right]Q_0. \tag{5}$$

3.5.2 Linear seepage on both sides of the fracture

For the linear flow on both sides of the fracture, a differential equation for seepage flow is established as Eq. 6.

$$\frac{nQ_n}{2\pi r_{wf}h} = \frac{PZ_{gsc}T_{gsc}k_g e^{\alpha(P-P_e)}\left(1+\frac{b}{p}\right)\left(\frac{d_p}{d_r}-\tau\right)}{\mu P_{gsc}ZT}. \tag{6}$$

Substitute pseudopressure function into Eq. 6.

$$m(p) - m(p_{wfn}) = \left[\frac{p_{gsc}T}{Z_{gsc}T_{gsc}\left(\frac{2r_{wf}}{nh}\right)k_g e-\alpha p_e(1+b/p)}\left(r_e-R_{wf}\right)\right]Q_n. \tag{7}$$

3.5.3 Non-darcy seepage within hydraulic fracture

The permeability of hydraulic fractures is 50mD to 100mD, so the flow of gas in these fracture no longer

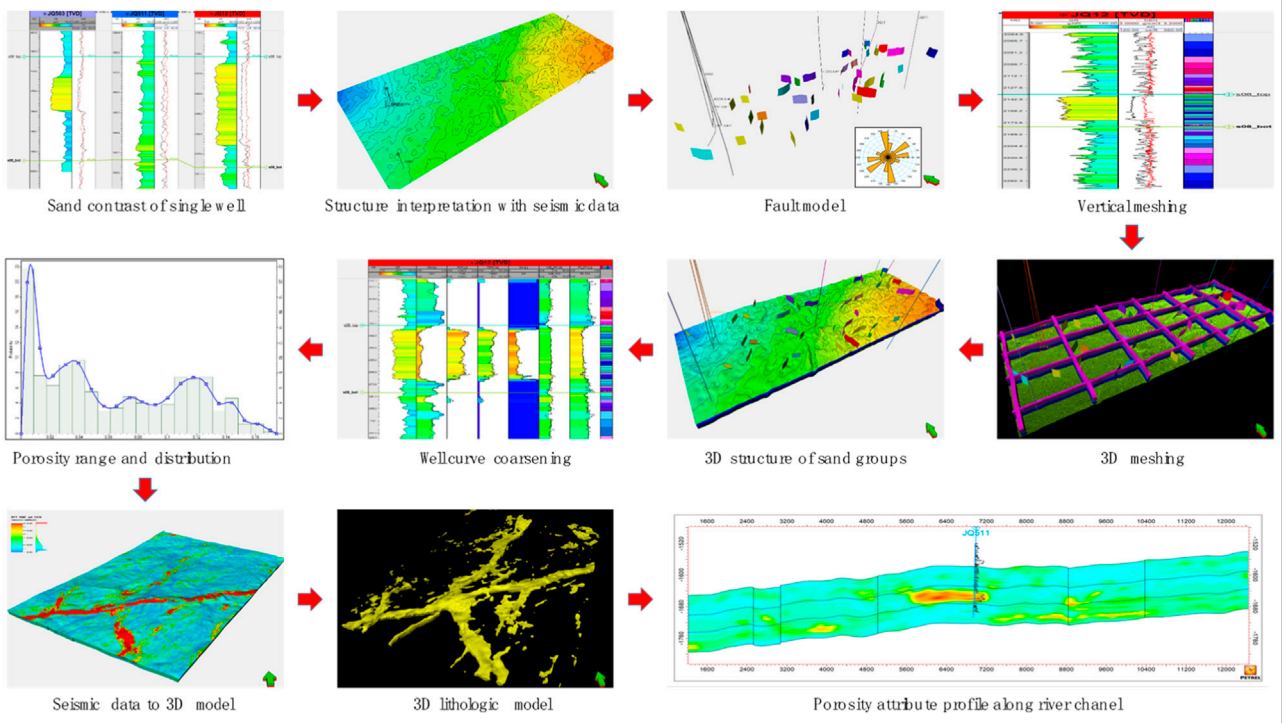

FIGURE 2
Technique flow.

meets the linear seepage of Darcy law (Shi et al., 2009; Pourafshary et al., 2015). Instead, the Fourier seepage differential equation should be more accurate in describing the seepage field.

$$\frac{\mathrm{d}p}{\mathrm{d}x} = \frac{\mu}{k_f} v_{fi} + \beta \rho v_{fi}^2. \tag{8}$$

The velocity of gas flow within hydraulic fracture v_{fi} is calculated by Eq. 9.

$$v_{f1} = \frac{p_{sc} T Z}{2 R_{wf} h T_{sc} Z_{sc} p} Q_{wf1}. \tag{9}$$

Introducing pseudopressure function (Lim et al., 1992) into Eq. 9, the ultimate seepage function in this zone can be derived as Eq. 10.

$$p_i - p_{i-1} = \frac{R_{wf1} \mu p_{sc} T Z}{\mathrm{n} k_{wf1} 2 R_{wf} h T_{sc} Z_{sc} p} Q_{wf1} + \frac{r_{wf} p_{sc} T Z \beta g_{sc}}{2\mathrm{n} R_{wf1} h T_{sc} Z_{sc} p} \rho_{gsc} Q_{wf1}^2. \tag{10}$$

3.5.4 Well productivity forecasting model

Define the number of fracture meshes as n, and name the mesh blocks from the bottom hole to the fracture front point from 1 to n:

$$\begin{bmatrix} k_{wf1} & k_{wf2} & k_{wf3} & \ldots & k_{wfn} \\ r_{wf1} & r_{wf2} & r_{wf3} & \ldots & r_{wfn} \\ p_{wf1} & p_{wf2} & p_{wf3} & \ldots & p_{wfn} \\ Q_{wf1} & Q_{wf2} & Q_{wf3} & \ldots & Q_{wfn} \\ Q_1 & Q_2 & Q_3 & \ldots & Q_n \end{bmatrix}. \tag{11}$$

The equation for the flow between the fracture grid and the matrix could be calculated by Eq. 12.

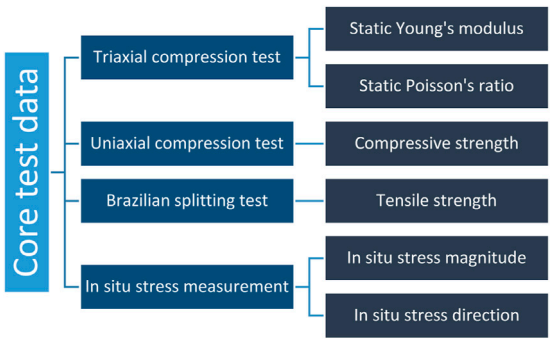

FIGURE 3
Core test and corresponding measured rock mechanical parameters.

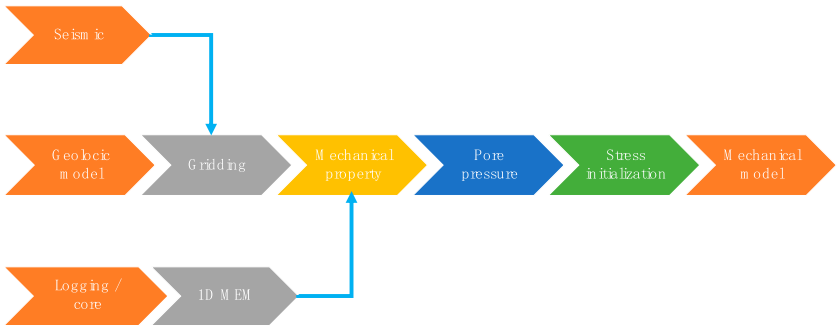

FIGURE 4
Regional 3D geomechanics modeling process.

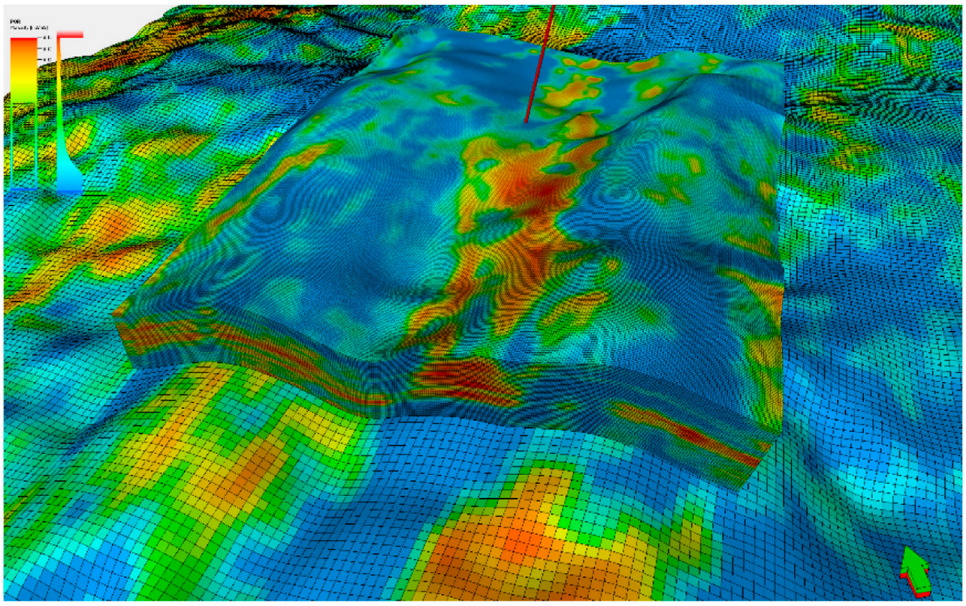

FIGURE 5
Comparison diagram of regional and platform models.

$$\begin{cases} m(p_e) - m(p_{wfn}) = \dfrac{p_{gsc}T}{Z_{gsc}T_{gsc}(2\pi h)k_g e^{-\alpha p_e}(1+b/p)} ln\dfrac{2r_e}{r_{wf}} Q_{(n),} \\ m(p_e) - m(p_{wf1}) = \dfrac{p_{gsc}T}{Z_{gsc}T_{gsc}\left(\dfrac{2r_{wf}}{nh}\right)k_g e^{-\alpha p_e}\left(1+\dfrac{b}{p}\right)} (r_e - r_{wf}) Q_{wf(i),} \\ p_{wf1} - p_{wf(i+1)} = \dfrac{\mu p_{gsc}TZ}{k_{wfi}2r_{wfi}hZ_{gsc}T_{gsc}p} Q_{i+1} + \dfrac{\mu p_{gsc}TZZ_{gsc}\beta}{2r_{wf1}hZ_{gsc}T_{gsc}p} Q^2_{i+1,} \\ Q_i = Q_{(i+1)} + Q_{wf(i),} \\ k_{wfi} = f(i), \\ i = 1、2...n. \end{cases} \tag{12}$$

The model is solved by iterative method. And the outflow of the mesh block Q_1 is the half-fracture yield.

3.6 Geological engineering integrated reservoir stimulation design

Previous fracturing design take induced stress (Taleghani et al., 2009; Dong et al., 2020) into consideration to recommend

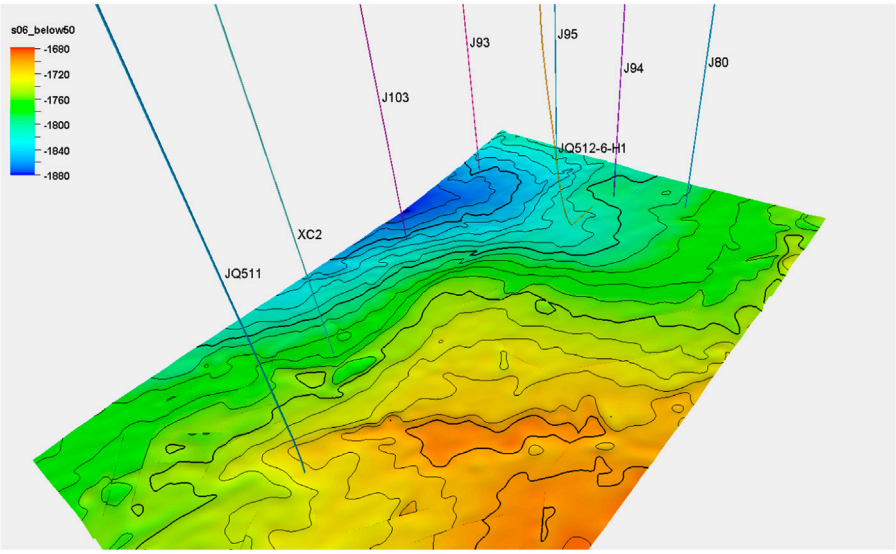

FIGURE 6
Correction of 3D structural plane by geological guidance comparison results.

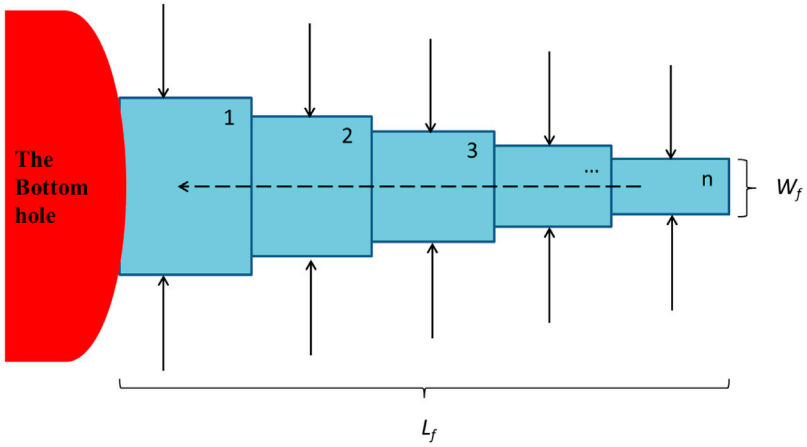

FIGURE 7
Simplified model of single-slit seepage flow.

cluster spacing. And it pays attention to the optimization relationship between fracturing execution parameters and post-fracturing productivity (Qiu et al., 2013). Being different from previous fracturing design, geological engineering integrated reservoir stimulation design aims at maximizing benefit of gas reservoir.

By simulating the extension of hydraulic fractures in the three-dimensional fine geological model, the proppant transport model is established to simulate the proppant placement law under different construction parameters and pumping procedures, then the shape of propped fractures could be more accurate. Besides, by carrying out post fracturing productivity prediction and analysis (Ren et al., 2014), the optimal fracture properties at different river channel locations, including fracture configuration and fracture conductivity, are recommended. Combined with the multi fracture competitive extension model (Liu et al., 2019) and proppant transport model, the fracturing construction parameters and pumping procedures are optimized to achieve higher economy (Figure 8).

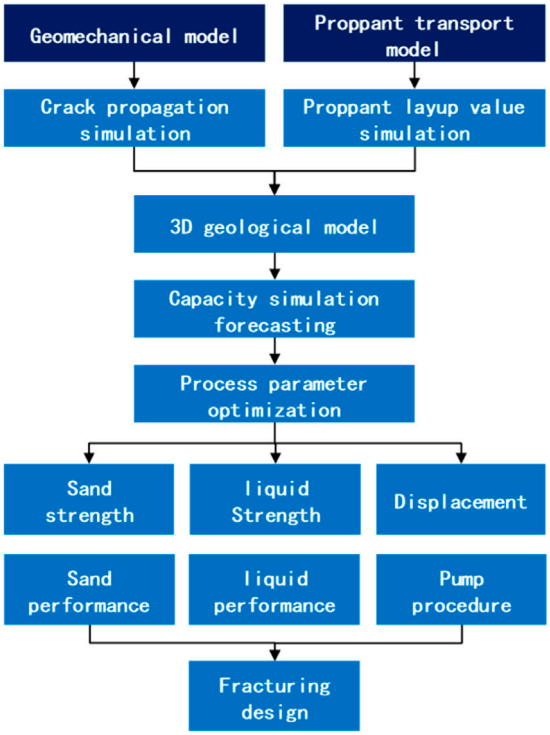

FIGURE 8
Fracturing design process.

4 Application of geological engineering integration

Taking JQ511 platform as an example, this paper analyzes the practice of geological engineering integration in platform wells in the study area. Well H1, Well H2, Well H3, and Well H4 are deployed on this platform. All these wells use geological engineering integration to optimize fracturing design. JQ511 platform is located at the intersection of two river courses. Affected by the river course trend, the included angle between the well trajectory of these three wells and the maximum horizontal principal stress of this platform is less than 60°. As a result, the control range of hydraulic fractures of these three wells should be limited. Using the integrated design idea of geological engineering, the reservoir is divided into three categories according to the reservoir quality, and customized design is carried out (Figure 9).

4.1 Productivity sensitivity model after hydraulic fracturing

Based on the fine geological model of this platform and in combination with the reservoir classification standard of Shaximiao Formation in Jinqiu gas field shown in Table 1, the distribution range and physical property distribution interval of different types of reservoirs are extracted, and the post fracturing productivity sensitivity model is established (Figure 10).

4.2 Well productivity sensitivity analysis after hydraulic fracturing

The single factor variable method is adopted to evaluate the influence law of engineering parameters such as cluster spacing, displacement and fracturing construction strength of different types of reservoirs under the guidance of stimulated productivity. This study figure out the main control engineering parameters of different types of reservoirs, and the optimization sequence of stimulation process and fracturing parameters. Affected by fluid filtration (Davletbaev, 2012) and inter fracture interference (Gorjian et al., 2021) during fracture propagation period, the fracture length of Class I reservoir is smaller than that of Class II and III reservoirs under the same fluid strength (Figure 11). The

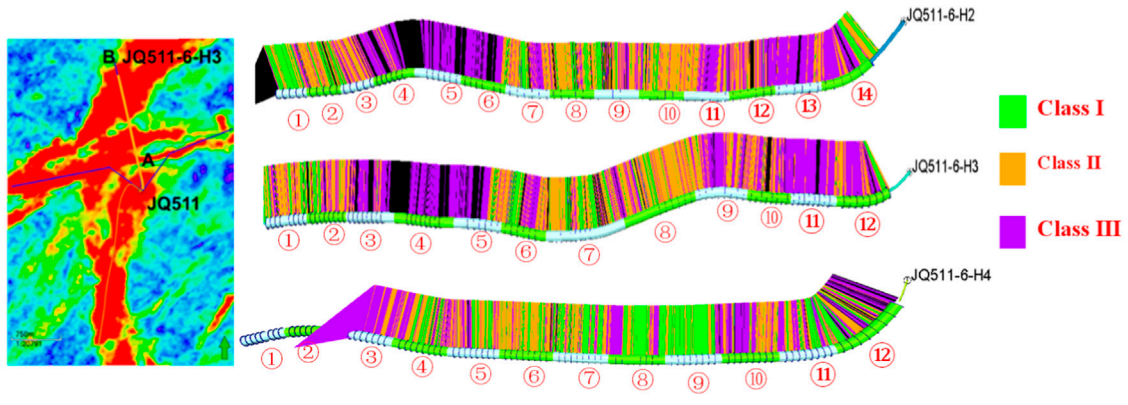

FIGURE 9
JQ511 platform geological model and reservoir quality classification of Well H2, Well H3 and Well H4.

FIGURE 10
Distribution of different types of reservoirs in JQ511 platform model.

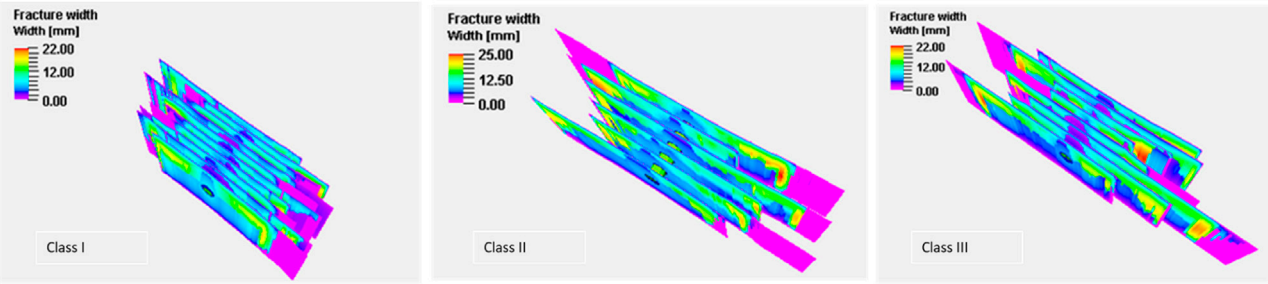

FIGURE 11
Simulated fracture length in various reservoirs of JQ511 platform at 14 m^3/min displacement.

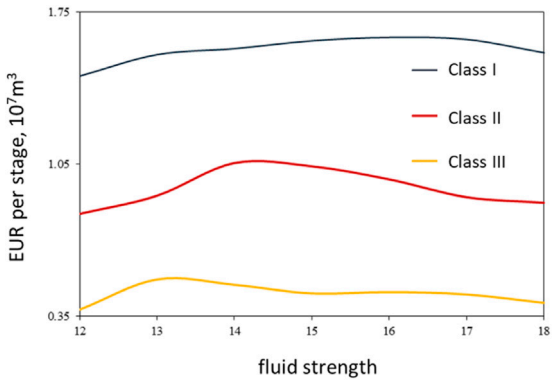

FIGURE 12
Simulated SRV in various reservoirs of JQ511 platform at 14 m^3/min displacement.

productivity and fluid strength of different reservoirs after fracturing climb up and then decline with the increase of fluid strength (Figure 12). Therefore, Class I reservoir of the platform considers to increase the liquid viscosity and reduce the liquid filtration. Class III reservoir selects the design range of liquid strength according to the inflection point principle to avoid over stimulation.

According to the fracture propagation and productivity simulation results (Figures 13, 14), the main engineering factor in JQ511 platform fracturing design is cluster spacing. Affected by the angle between the borehole trajectory and the direction of *in situ* stress, enlarging the cluster spacing is helpful to reduce the interference between artificial fractures. At the same time, for Class I reservoir, it is considered to increase the liquid viscosity, reduce the liquid filtration and increase the artificial fracture length.

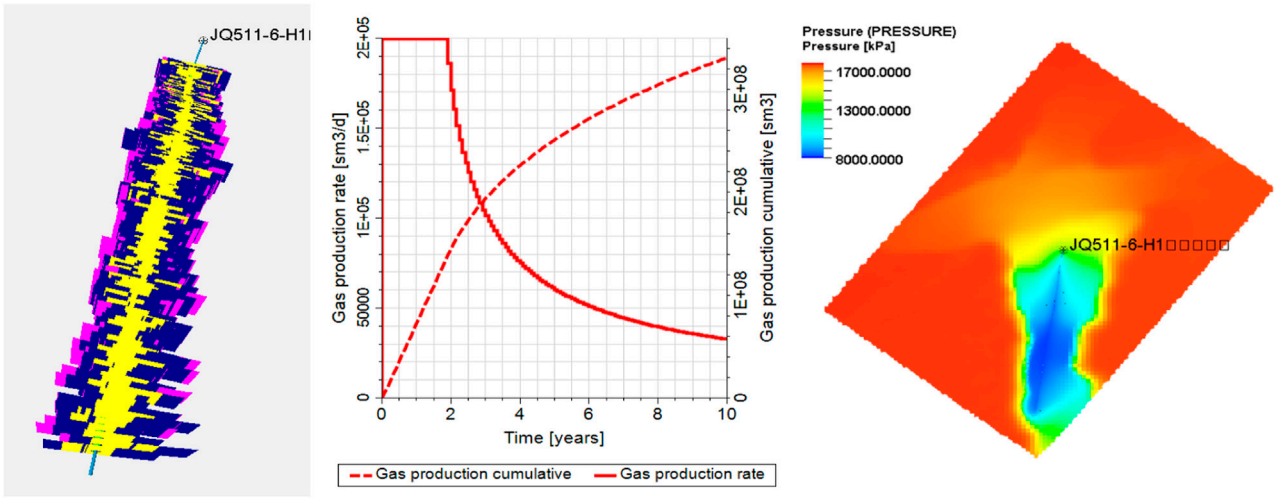

FIGURE 13
Optimization simulation results of Well H1.

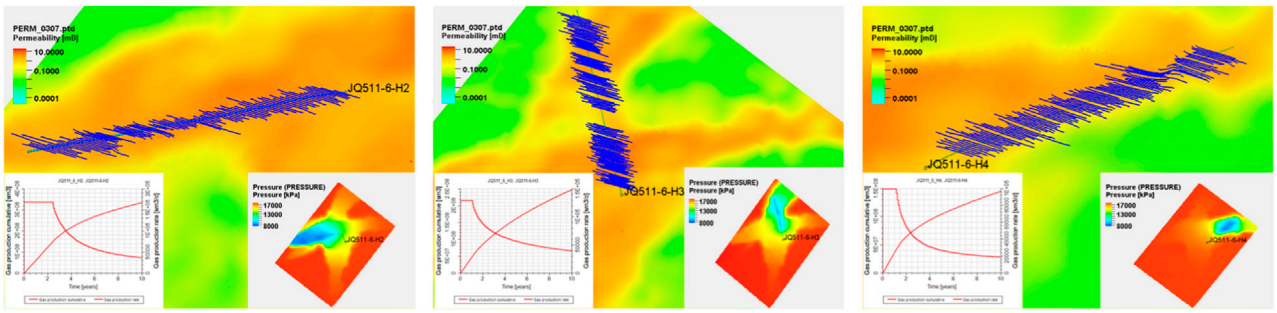

FIGURE 14
Simulation results of Well H2, Well H3, and Well H4 on JQ511 platform.

TABLE 1 Classification standard of Shaximiao Formation reservoir in Jinqiu gas field.

Type	Class I	Class II	Class III
lithology	Fine medium grained lithic arkose sandstone	Fine medium grained lithic arkose sandstone	Fine grained lithic arkose sandstone
Sedimentary microfacies	Lower distributary channel, distributary channel, distributary Bay, estuary dam and natural dike		
Porosity, %	≥12	10–12	7–10
Average air permeability, MD	≥1	0.4–1	0.02–0.4
Drainage pressure, MPa	<0.6	0.6–1	1–2
Median radius, μm	≥0.5	0.2–0.5	0.02–0.2
Nuclear magnetic spectrum characteristics	Two or three peaks, Low irreducible water saturation	Bimodal, Higher irreducible water saturation	Unimodal, High irreducible water saturation
Pore throat combination	Low pore micro throat	Low to ultra low pore micro throat	Ultra low pore micro throat

TABLE 2 Fracturing construction parameter optimization results.

Segment	Water, m^3		Sand, t		Perforation spacing m		Displacement m^3/min		Number of perforations	
	Before	After	Before	After	Before	After	Before	After	Before	After
21	1020	938	270	201		10		20.0	8	7
20	1660	1540	440	330		10		20.0	11	11
19	1660	1540	440	330		10		20.0	11	11
18	1660	1540	440	330		10		20.0	10	10
17	1660	1620	440	370		12.5		18.5	11	9
16	1580	1610	420	385		12.5		17.3	11	8
15	1480	1441	392	328		10		18.6	10	9
14	1360	1379	360	330		13.9		17.4	10	7
13	1320	1305	350	305		12.5		18.0	9	7
12	1400	1488	372	372		16.7		16.0	10	6
11	1400	1488	372	372	8–10	16.7	18	16.0	9	6
10	1380	1472	370	368		16.7		16.0	9	6
9	1440	1520	380	380		16.7		16.0	10	6
8	1440	1520	380	380		16.7		16.0	9	6
7	1380	1393	370	329		13.6		17.7	9	7
6	1500	1451	400	326		11.3		19.0	11	9
5	1620	1712	430	428		16.7		16.0	11	7
4	1620	1712	430	428		16.7		16.0	11	7
3	1480	1510	392	363		14.5		17.2	10	7
2	1480	1568	392	392		16.7		16.0	9	6
1	1440	1520	380	380		16.7		16.0	10	6

4.3 Platform fracturing design

Taking Well H1 as an example, according to the classification design results of reservoirs, the cluster spacing, fracturing fluid consumption, support amount and construction displacement are optimized (Table 2). Compare with original stimulation design, the amount of fracturing fluid used in Well H1 was reduced by 5.1%, proppant was reduced by 9.8%, the number of perforated clusters was reduced by 24.4%, and the average cluster spacing was increased by 40%.

Compared with previous design method, the optimized design method show advantages in the following aspects. The dynamic hydraulic length of Well H1 is increased by 23.8%. The propped fracture length increased by 22.6%. The effect of cluster spacing on SRV is not distinct. Use the same production system to forecast well productivity. The calculated stable production time of Well H1 with the optimized fracturing design could reach 1.9 years, which is 58.8% higher than that of the original fracturing design. Meanwhile, the 10-year end-of-term forecast cumulative gas production is 332 million cubic meters, showing an increase of 15.9% over before optimization.

According to the well productivity simulating model, the EUR of single gas well could be 156 million cubic meter to 210 million cubic meter.

5 Conclusion

1) With this geological engineering integrated simulation method of geology and engineering, the productivity prediction model of stimulated well in tight river sandstone gas reservoir is established. A more accurate fracture model is derived to describe fracture morphology and hydraulic fracture properties. Then, the horizontal well productivity prediction model is established in the unstructured meshes, which also take stress sensitivity influence into consideration.
2) The reservoirs in Jinqiu gas field are divided into three types according to their properties.

By means of integrated simulation, this paper defines the main engineering parameters of productivity in each type of reservoir, which includes cluster spacing, number of clusters in a single stage, fracturing strength, construction displacement, and proportion of pre-pad. And this set of parameters ultimately constitutes the optimal stimulation strategy. This horizontal well fracturing design process could be conductive to the field application of reservoir reconstruction in the future Maity et al., 2013.

Data availability statement

The raw data supporting the conclusions of this article will be made available by the authors, without undue reservation.

Author contributions

JZ contributed to the conception of the study WL performed the experiment HF contributed to the modeling XH performed the data analyses TW performed the simulation DZ helped perform the analysis SY helped perform the simulation.

Conflict of interest

JZ, WL, HF, XH, TW, DZ, SY, were empolyed by PetroChina Southwest Oil and Gas Field Company.

Publisher's note

All claims expressed in this article are solely those of the authors and do not necessarily represent those of their affiliated organizations, or those of the publisher, the editors and the reviewers. Any product that may be evaluated in this article, or claim that may be made by its manufacturer, is not guaranteed or endorsed by the publisher.

References

Ayatollahy, T. T. (2013). *Integrated workflow for characterizing and modeling fracture network in unconventional reservoirs using microseismic data*. Atlanta, GA, USA: Scholars' Press.

Cao, H., Claverie, M., Cao, D., Endo, T., and Yamamoto, H. (2001). Integrated interpretation of well logs and surface seismic. *J. De. Pediatr.* 1.

Davletbaev, A. Y. (2012). Fluid filtration in a porous medium with wells with vertical hydraulic fracture of the formation. *J. Eng. Phys. Thermophy.* 85 (5), 997–1003. doi:10.1007/s10891-012-0739-1

Dong, K. X., Wang, S. L., and Li, J. B. (2020). *Mechanism of fracture propagation turning induced by interfacial shear*. Singapore: Springer.

Friedel, T., and Voigt, H. D. (2006). Investigation of non-Darcy flow in tight-gas reservoirs with fractured wells. *J. Pet. Sci. Eng.* 54 (3-4), 112–128. doi:10.1016/j.petrol.2006.07.002

Gorjian, M., Hendi, S., and Hawkes, C. D. (2021). *An analytical framework for stress shadow analysis during hydraulic fracturing*. Saskatchewan, Canada: Applied to the Bakken Formation.

Han, G. Q., Xiao-Ming, G. E., Huang, R., Yang, H., and Guo, C. E. (2019). Seismic data application in horizontal well design of m oilfield in orinoco heavy oil belt. *Prog. Geophys.* 34.

Jon, Z., and Eolon, Z. (2010). *Estimating natural fracture producibility in tight gas sandstones: Coupling diagenesis with geomechanical modeling*. Ahmedabad, Gujarat, India: The Leading Edge.

Lark, R. M., Mathers, S. J., Thorpe, S., Arkley, S., Morgan, D. J., and Lawrence, D. (2013). A statistical assessment of the uncertainty in a 3-d geological framework model. *Proc. Geologists'. Assoc.* 124 (6), 946–958. doi:10.1016/j.pgeola.2013.01.005

Lim, K. T., Enedy, K. L., Bloomfield, K. K., and Aziz, K. (1992). "Application of a matrix-fracture transfer pseudofunction in geothermal reservoir simulation," in *Office of scientific & technical information technical reports*. Texas, USA: Unt digital library.

Liu, W., Liu, J., Hua, J., Wang, X., and Xiao, J. (2019). Friction types of hydraulic fracturing and measures for reducing friction. *Petrochem. Ind. Technol.* 10.

Maerten, L., Gillespie, P., and Daniel, J. M. (2006). Three-dimensional geomechanical modeling for constraint of subseismic fault simulation. *Am. Assoc. Pet. Geol. Bull.* 90 (9), 1337–1358. doi:10.1306/03130605148

Maity, D., Chen, Q., and Aminzadeh, F. (2013). "Integrated fracture characterization and associated error evaluation using geophysical data for unconventional reservoirs," in Proceedings of the Pacific Section AAPG, SEG and SEPM Joint Technical Conference, CA, USA, April 2013.

Maity, D. (2013). "Integrated reservoir characterization for unconventional reservoirs using seismic, microseismic and well log data,". Dissertations & Theses (Canada: Gradworks).

Pourafshary, P., Saboorian-Jooybari, L., and Hadi, F. (2015). Significance of non-Darcy flow effect in fractured tight reservoirs. *J. Nat. gas Sci. Eng.* 24, 132–143. doi:10.1016/j.jngse.2015.03.003

Qiu, X., Li, Z., and Liu, Y. (2013). Analysis of productivity equation and influence factors of horizontal wells in tight sand gas reservoir. *J. Southwest Petroleum Univ.* 15 (12), 2337–2350. Haidian, Beijing, and China.

Rafiq, A. (2015). *Integrated interpretation of microseismic with surface seismic data in a tight gas reservoir*. Central Alberta, Canada: Doctoral dissertation, University of Calgary.

Ren, J., Zhang, L., Ezekiel, J., Ren, S., and Meng, S. (2014). Reservoir characteristics and productivity analysis of tight sand gas in upper paleozoic ordos basin China. *J. Nat. Gas. Sci. Eng.* 19, 244–250. doi:10.1016/j.jngse.2014.05.014

Rutqvist, J., Jeanne, P., Dobson, P. F., Garcia, J., Hartline, C., Hutchings, L., et al. (2016). The northwest geysers egs demonstration project, California – part 2: Modeling and interpretation. *Geothermics* 63 (1), 120–138. doi:10.1016/j.geothermics.2015.08.002

Sgher, M. E., Aminian, K., and Ameri, S. (2021). "Evaluation of hydraulic fracturing treatment with microseismic data analysis in A marcellus shale horizontal well," in Proceedings of the SPE Western Regional Meeting, April 2021.

Shi, Y., Yang, Z., and Huang, Y. (2009). Study on non-linear seepage flow model for low-permeability reservoir. *Acta Pet. Sin.* 30 (5), 731–734.

Smart, K. J., Ferrill, D. A., Sims, D. W., Franklin, N. M., Ofoegbu, G. I., and Morris, A. P. (2004). "Integrated structural analysis and geomechanical modeling: An aid to reservoir exploration and development," in Proceedings of the 6th North America Rock Mechanics Symposium (NARMS), Houston, Texas, June 2004.

Taleghani, A. D. (2009). Analysis of hydraulic fracture propagation in fractured reservoirs : An improved model for the interaction between induced and natural fractures. *Diss. Theses - Gradworks* 5 (12), S58.

Teran, O. J. (2017). "Mapping unconventional reservoir stress conditions: An integrated workflow using geological, stimulation and microseismic data," in Proceedings of the Unconventional Resources Technology Conference, Austin, Texas, USA, July 2017.

Wang, D. D., Zhou, Y. B., Zhong-Zhen, M. A., Liu, Y. M., and Lin, J. C. (2013). Application of horizontal wells in geological statistical inversion. *Prog. Geophys.* 28 (3), 1522–1530.

Wang, X., and Sheng, J. J. (2017). Effect of low-velocity non-Darcy flow on well production performance in shale and tight oil reservoirs. *Fuel* 190, 41–46. doi:10.1016/j.fuel.2016.11.040

Yang, R. Z., Zhao, Z. G., Peng, W. J., Gu, Y. B., Wang, Z. G., and Zhuang, X. Q. (2013). Integrated application of 3d seismic and microseismic data in the development of tight gas reservoirs. *Appl. Geophys.* 10, 157–169. doi:10.1007/s11770-013-0374-4

Yousefzadeh, A., Li, Q., Aguilera, R., and Virués., C. (2019). Integrated interpretation of microseismic and petroleum-engineering data for comparison of gas production in two interfering adjacent wellpads in the horn river basin, Canada. *SPE Prod. operations* 35 (2), 255–271. doi:10.2118/197048-pa

Zhao, J., Peng, Y., Li, Y., and Xiao, W. (2015). Analytical model for simulating and analyzing the influence of interfacial slip on fracture height propagation in shale gas layers. *Environ. Earth Sci.* 73 (10), 5867–5875. doi:10.1007/s12665-015-4360-4

frontiers | Frontiers in Energy Research

TYPE Original Research
PUBLISHED 11 January 2023
DOI 10.3389/fenrg.2022.1031006

OPEN ACCESS

EDITED BY
Daoyi Zhu,
China University of Petroleum, Beijing, China

REVIEWED BY
Wei Sun,
Northeast Petroleum University, China
Bingyuan Hong,
Zhejiang Ocean University, China

*CORRESPONDENCE
Duo Xu,
xuduo95@126.com

†These authors contributed equally to this work and share first authorship

SPECIALTY SECTION
This article was submitted to Advanced Clean Fuel Technologies, a section of the journal Frontiers in Energy Research

RECEIVED 29 August 2022
ACCEPTED 21 September 2022
PUBLISHED 11 January 2023

CITATION
Xu D, Chen L, Zhan W, Zhang K, Lu J, Ji Y and Ma R (2023), Study on the leakage dispersion law of exposed high-pressure natural gas pipelines in the mountainous environment. *Front. Energy Res.* 10:1031006. doi: 10.3389/fenrg.2022.1031006

Study on the leakage dispersion law of exposed high-pressure natural gas pipelines in the mountainous environment

Duo Xu[1]*†, Liqiong Chen[1†], Wenwen Zhan[2], Kai Zhang[1], Jingyang Lu[1], Yongqiang Ji[3] and Rufei Ma[1]

[1]School of Petroleum Engineering, Southwest Petroleum University, Chengdu, China, [2]National Pipeline Research Center Conveyance Pipe Institute, Baoji Petroleum Steel Pipe Co.LTD, Baoji, China, [3]Petroleum Engineering Technology Research Institute, Sinopec North China Oil & Gas Branch, Zhengzhou, China

The pipelines in mountainous areas have complex terrain conditions and pass through many densely populated areas. Once a pipeline leakage accident occurs, it will cause serious damage to the surrounding people and the environment. In this article, a leakage diffusion model of a bare natural gas pipeline is established for the exposed leakage scenario, and a simulation scheme is established according to the characteristics of pipeline-laying processes and environmental characteristics in mountainous areas. Research has been carried out on the diffusion pattern and the influence range of exposed gas transmission pipeline leaks under four types of factors: different leak apertures, ambient wind speed, mountainous obstacle conditions, and mountainous laying environment. The dangerous range formed by the gas diffusing along the ground and high altitude under different scenarios and the influence law of different influencing factors on the dangerous range are obtained, and suggestions for emergency rescue focus areas and emergency response strategies have been given. The research conclusions can provide a theoretical basis for emergency response strategies for exposed leakage accidents of high-pressure natural gas pipelines in mountainous environments and are of great significance to the quantitative analysis of the risk consequences of natural gas pipelines.

KEYWORDS

natural gas pipeline in mountains, the law of leakage diffusion, exposed pipe leakage, safety management, emergency response strategies

1 Introduction

In recent years, the global demand for natural gas has continued to grow (Rui et al., 2017; Bu et al., 2021). Compared with other energy sources, natural gas can effectively reduce CO_2 emissions (Aguilera, 2014). The mileage and number of natural gas pipelines, the most important modes of natural gas transmission, are also soaring in China, which leads to more transmission pipelines passing through areas where populations gather and

buildings are concentrated. Due to the flammable and explosive nature of its transmission medium, the leakage failure of pipelines that carry natural gas often leads to environmental pollution, fire, and explosion accidents, which will cause great harm to the natural environment, social life, and public safety (Hoeks, 1975; Smith et al., 2005; Sklavounos and Rigas, 2006; Phillips et al., 2013; Jackson et al., 2014; Fan et al., 2018; Xiao et al., 2020; Zhang et al., 2020; Zhang et al., 2021; Zhu et al., 2021).

Gas pipeline leaks can be classified into two basic types based on the leak scenario: buried pipeline leaks and exposed pipeline leaks. Exposed gas pipeline leaks are usually caused by third-party damage and natural disasters, often leaking directly into the air over a large area, and according to the 2020 European Gas Pipeline Incident Data Group (EGIG) survey statistics, it was found that third-party damage caused up to 27% of pipeline incidents to occur within 2010–2019, which is the most significant pipeline failure factor (EGIG, 2020). Meanwhile, China has a complex geological landscape with many mountains and large drop-offs along some pipelines, and most of the pipelines are high-pressure natural gas pipelines. Since the mountainous terrain affects the gas leak diffusion pattern and makes it more difficult to predict the accident consequences and the environment in towering mountains and narrow valley bottoms is prone to the formation of confined spaces where gas leaks are more likely to occur in vapor cloud explosions, the complex topographic conditions dictate that the analysis of natural gas pipeline leak consequences should be different from that of plain areas and requires targeted research. Therefore, to avoid pipeline accidents resulting in casualties and property damage, the diffusion law of exposed gas pipeline leaks in mountainous environments should be clarified first to provide reliable theoretical support for emergency management after accidental gas pipeline leaks.

Since the 1970s and 1980s, theoretical and numerical simulations of gas diffusion processes have been studied, among which computational fluid dynamics and related techniques and methods have been more mature, based on which the current research has been conducted for the diffusion of bare gas leaks. Wilkening and Baraldi (2007) carried out a series of studies based on computational fluid dynamics for accidental leakage through small holes in high-pressure gas transmission pipelines and analyzed the effect of different properties of hydrogen and methane on the gas diffusion process and also the effect of different release scenarios, geometrical structures, and atmospheric conditions on the gas leakage pattern. Scargiali et al. (2011) conducted a numerical simulation study on the diffusion of heavy gas leaks and showed that the presence of buildings reduces the maximum concentration of heavy gas and increases the lateral diffusion of the gas. R.N. Meroney (2012) also studied the diffusion law of dense gas with finite volume based on computational fluid dynamics and analyzed the transient release diffusion of the gas on flat, sloping, and complex terrain surfaces under windless and windy conditions, respectively, providing data on the characteristics of transient plumes that are common in the field but difficult to accurately measure. B. Liu et al. (2016) carried out a study on the diffusion of carbon dioxide in complex environments, studied the CO_2 diffusion patterns in two complex situations, namely, flat terrain with symmetrical hills and urban areas with buildings, and investigated their effects on the diffusion profiles by varying the source intensity, wind speed, and building height. L. Soulhac et al. (2016) used the SIRANERISK model for the array obstacle situation to study the diffusion of steady and unsteady leakage sources in diffusion behavior inside and above the obstacle. Y. Dai et al. (2018) similarly investigated the gas diffusion dispersion under an array obstacle and analyzed the effect of four computational parameters and two physical parameters on the simulation results, the findings of which led to a further improvement in the quality of CFD simulations. A. Liu et al. (2018) carried out a study on the leakage dispersion of urban natural gas pipelines, which simulated the natural gas leakage and dispersion under three different pipeline scenarios, and the study showed that the closed scenario had the largest blocking effect on the ambient wind, the strongest vortex effect, and the widest range of high gas concentrations.

It can be seen from the existing research results that the application of the CFD theory to analyze the gas dispersion law has been relatively mature, which when applied to a variety of practical conditions showed good simulation performance. At present, there is some research on gas leakage and the dispersion law in various complex situations, but the research focus is generally on medium- and low-pressure pipelines or other types of gases; thus, research on leakage and the dispersion law of exposed high-pressure natural gas pipelines in mountainous terrain is still unexplored. Therefore, in this article, we will refine the obstacle scenarios for the actual conditions of pipelines laid in mountainous areas and the characteristics of pipeline laying and study the diffusion law of pipeline leaks in mountainous areas.

2 Materials and methods

2.1 Mathematical models

2.1.1 The basic equation followed by natural gas leaks

Natural gas is compressible, and when a leak occurs, the gas pressure inside the pipe is much higher than the external ambient pressure. Under the effect of pressure difference, the internal gas exchanges momentum with the external world and forms a velocity gradient. The leakage state can be described by combining the continuity equation, momentum equation, energy equation, and gas state equation (Liu et al., 2016; Liu et al., 2018).

The theoretical basis of the continuity equation is the law of mass conservation, the physical significance of which is the difference between the mass of the fluid inflow and outflow per unit time, and the unit volume is equal to the value of its internal mass change. The equation is shown in equation (1), where ρ denotes the density, (kg/m^3); u_x, u_y, and u_z denote the partial velocity of the gas in x, y, and z directions, respectively, (m/s); and T denotes time, (s).

$$\frac{\partial \rho}{\partial t} + \frac{\partial (\rho u_x)}{\partial x} + \frac{\partial (\rho u_y)}{\partial y} + \frac{\partial (\rho u_z)}{\partial z} = 0. \tag{1}$$

The momentum equation is based on Newton's second law, and the equation is shown in equation (2), where j denotes the three directions of the coordinate axes x, y, and z, u_j denotes the velocity in the direction of j (m/s), $\overline{u'}$ denotes the average pulse velocity over a certain period, (m/s), S_F is the source term of the conservation of the momentum equation, and p is the static pressure.

$$\frac{\partial \rho u_i u_j}{\partial x_j} = -\frac{\partial p}{\partial x_i} + \mu \frac{\partial^2 u_i}{\partial x_j \partial x_j} + \frac{\partial \left(-\rho \overline{u_i' u_j'} \right)}{\partial x_j} + \rho S_F. \tag{2}$$

The energy equation is based on the law of conservation of energy, and the equation is shown in equation (3), where E is the total energy of the fluid microcluster, (J/kg); h_j denotes the enthalpy of the component, j (J/kg); k_{eff} denotes the effective heat transfer coefficient, $(W/(m \cdot K))$; J_j denotes the diffusion component of the component j; and S_n denotes the source term including the heat of the chemical reaction with other volumetric heat.

$$\frac{\partial (\rho E)}{\partial t} + \nabla \cdot \left[\vec{u} (\rho E + P) \right] = \nabla \cdot \left(k_{eff} \nabla T - \sum_j h_j J_j + \tau_{eff} \cdot \vec{u} \right) + S_n. \tag{3}$$

For an ideal gas, the equation of the state of the gas is described as shown in equation (4), where p denotes the absolute pressure, (Pa); R denotes the gas constant, $(J/(kg \cdot K))$; and T denotes the thermodynamic temperature, (K).

$$p = \rho R T. \tag{4}$$

2.1.2 Turbulence model

The flow state at the gas leakage port of the high-pressure gas transmission pipeline is turbulent flow, and the turbulence model should be selected for conducting the simulation. In this article, the standard k – ε model is selected for turbulence modeling, which has been widely validated in diffusion simulations (Sini et al., 1996; Kiša and Jelemenský, 2009; Scargiali et al., 2011; Xing et al., 2013). The model is a two-sided equation consisting of the turbulent kinetic energy equation k and turbulent dissipative energy equation ε. The turbulent kinetic energy equation is shown in equation (5), and the turbulent dissipative energy equation is shown in equation (6).

$$\frac{\partial (\rho k)}{\partial t} = \frac{\partial}{\partial x} \left[\left(\mu + \frac{\mu_i}{\sigma_k} \right) \frac{\partial k}{\partial x_i} \right] + G_k + G_b - \rho \varepsilon Y_M, \tag{5}$$

$$\rho \frac{\partial \varepsilon}{\partial t} = \frac{\partial}{\partial x_i} \left[\left(\mu + \frac{\mu_i}{\mu_k} \right) \frac{\partial \varepsilon}{\partial x_i} \right] + C_1 \frac{\varepsilon}{k} (G_k + C_3 G_b) - C_2 \rho \frac{\varepsilon^2}{k}, \tag{6}$$

where μ denotes the fluid viscosity, μ_i denotes the turbulent viscosity, σ_k denotes the turbulent Prandtl number, G_b denotes the turbulent kinetic energy term generated by buoyancy, G_k denotes the turbulent kinetic energy term generated by the mean velocity gradient, Y_M denotes the dissipation term caused by compressible turbulent fluctuation expansion, and C_1, C_2, and C_3 are the empirical constants, which are taken as 1.44, 1.92, and 1, respectively.

2.1.3 Computational model of leakage diffusion

There are more mature theoretical models in gas diffusion, such as the Gaussian model, BM model, Sutton model, and box and similar model, each of which has different characteristics and adaptability (Slade, 1968; Ulden, 1974; Ermak et al., 1982; Pasquill and Smith, 1983; Britter and Mcquaid, 1988). Since the Gaussian model applies to light or neutral gases diffusing from a point source in a homogeneous atmospheric environment, the Gaussian model is chosen as the computational model for leakage dispersion in this article. The Gaussian model is divided into the Gaussian plume model and the Gaussian puff model. Among them, the Gaussian plume model applies to continuous leakage with a long leakage time and small leakage volume; the Gaussian puff model applies to transient leakage with a short leakage time and long diffusion time. The Gaussian model usually establishes the OXYZ coordinate system, where the leak point is the origin O, the downwind extension direction is along the x-axis, the *y*-axis is perpendicular to the x-z plane and intersects with the O point, and the *z*-axis is perpendicular to the x-y plane. Gaussian models are also based on the following assumptions:

- the gas leakage diffusion area is free of obstacles, and the ground is flat;
- mixed gas clouds have the same density as air and are not affected by buoyancy;
- the distributions of concentration and density inside the cloud cluster and on the cross section of the plume follow the normal Gaussian distribution;
- the moving speed of the cloud center or the axial spreading speed of the cloud plume is equal to the wind speed, and the wind speed is uniform and constant;
- the temperature of the gas cloud remains unchanged during the diffusion process.

When small-hole leaks occur in natural gas pipelines, they tend to be small and have a long leak time and can be considered a continuous leak source. The Gaussian plume model is shown in equation (7), where C denotes the natural gas concentration at any point in space, (kg/m^3); Q denotes the source strength, (kg/s); u denotes the average wind speed, (m/s); H denotes the effective source height, that is, the sum of the leak source height and the lift height, (m); σ_i denotes the diffusion coefficient; and when i is y, σ_i is the lateral diffusion coefficient, and when i is z, σ_i is the longitudinal diffusion coefficient.

$$C(x,y,z) = \frac{Q}{2\pi u\sigma_y\sigma_z}\exp\left(-\frac{y^2}{2\sigma_y^2}\right)\left\{\exp\left[-\frac{(z-H)^2}{2\sigma_z^2}\right] + \exp\left[-\frac{(z+H)^2}{2\sigma_z^2}\right]\right\}. \quad (7)$$

When a natural gas pipeline rupture or large bore leak occurs, the leak occurs rapidly and in a large volume, and the situation usually causes the activation of a pipeline shut-off valve to stop further gas leakage, which can be considered transient leak diffusion. The Gaussian puff model is shown in equation (8), where m is the total leakage volume, (kg); t is the leakage time, (s).

$$C(x,y,z,t) = \frac{Q}{(2\pi)^{3/2}\sigma_x\sigma_y\sigma_z}\exp\left\{-\frac{1}{2}\left[\frac{(x-ut)}{\sigma_x^2} + \frac{y^2}{\sigma_y^2}\right]\right\} \left\{\exp\left[-\frac{(z-H)^2}{2\sigma_z^2}\right] + \exp\left[-\frac{(z+H)^2}{2\sigma_z^2}\right]\right\}. \quad (8)$$

2.2 Physical model

2.2.1 Modeling and meshing

This article mainly discusses the diffusion law and the diffusion range in the horizontal and vertical directions of the exposed gas pipeline after leakage to provide a basis for relevant control measures. Considering the large pipe diameter, high transmission pressure, and large impact range after gas leakage, it is difficult to solve the calculation and requires a high computer system if a three-dimensional model is used for analysis, and the two-dimensional model can also meet the research requirements. The simulation results are more intuitive, so a two-dimensional model is used to analyze the concentration distribution of the leaking gas. The model mainly includes the natural wind inlet, diffusion area, and the location of the leak, and the simplified model of the pipeline leakage is shown in Figure 1.

In this article, a diffusion space of 200 m × 200 m is established, and the meshing is combined with both structural and non-structural grid forms. Considering the high methane concentration near the leak hole and the strict requirements on the mesh quality, local refinement is carried out, and a sparse mesh is used for the boundary locations of the diffusion area far from the leak hole to reduce the computational workload while satisfying the simulation calculation requirements and accuracy requirements.

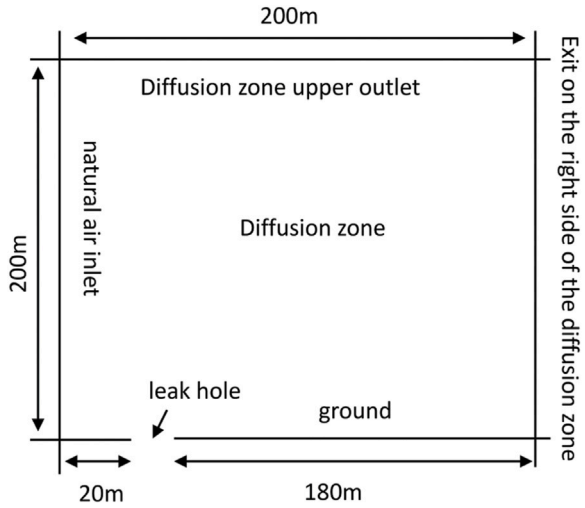

FIGURE 1
Schematic diagram of the leakage model of the exposed natural gas pipeline.

According to the aforementioned mesh division method, the mesh irrelevance verification is carried out for the default conditions as shown in Table 1, and the horizontal diffusion distance and vertical diffusion height after 60 s of leakage with different mesh numbers are shown in Figure 2. It can be seen that the simulation results tend to be stable when the number of grids exceeds 450,000. Therefore, based on the conclusion of the grid independence verification, the grid accuracy was tuned several times, and finally, a total of 445,784 grids were divided.

2.2.2 Setting of boundary conditions

Based on the analysis of the physical model of natural gas pipeline leakage and combined with the actual situation, the entrance boundaries set are mainly the velocity entrance of the natural wind on the left side and the velocity entrance of the gas from the leakage hole, and the exit boundaries set are mainly the pressure exit on the upper side and the right side, and the surface boundary is the ground on the lower side. At the same time, since the natural wind is not flowing at uniform velocity in all directions, but considering the operability of the simulation, the natural wind is considered to be flowing at uniform velocity.

2.2.3 Validation of the model

The article verifies the accuracy of the leakage dispersion model by comparing it with the experiment of Liu et al. (2018), which used an aluminum–plastic composite pipe with a diameter of 15 mm, an inner diameter of 12 mm, and an opening of 7 mm, set at a pressure of 0.2 MPa, a distance of 1.33 m between the buildings around the pipe, and a distance of 0.23 m between the leak point and the building. Six monitoring points with methane concentration sensors were installed near the location of the leak hole, and the data of each monitoring point were collected at

TABLE 1 Setting of simulation parameters.

Entry		Input data	
		Default	Variable
Leak hole diameter, k (m)		0.2	0.02; 0.1; 0.3
Ambient wind speed, v (m/s)		5	2; 8; 11
Obstacle	Height of the obstacle, h (m)	10	5; 20; 30
	Distance between the obstacle and leakage hole, l (m)	5	10; 20; 30
	Number of obstacles, n (pcs)	1	2; 3
Laying environment	Slope angle, α (°)	0	30; 60
	Laying position	Laying on a flat surface	Foot of the slope; surface of the slope

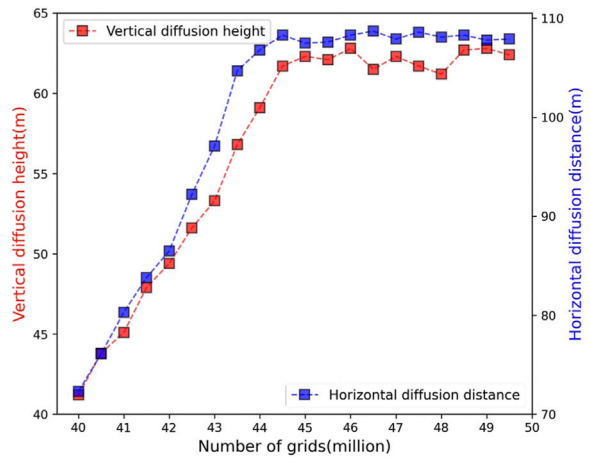

FIGURE 2
Grid independence verification.

120 s after the leak occurred. Comparing the numerical simulation data of monitoring point 2 (0, 0.93) and monitoring point 5 (0.23, 1.2) with the experimental data, the two have a high agreement with a maximum error of 8.3% and an average error of less than 6.5%, so the established model can be used for the study of leak dispersion in exposed natural gas pipelines. The comparison of numerical simulation and experimental results is shown in Figure 3.

2.3 Settings of variable parameters and monitoring points

The factors affecting the diffusion of gas leaks from exposed gas transmission pipelines are derived from the analysis as both internal and external factors. The internal factors mainly include the operational parameters such as transmission pipe diameter, pressure, and leak hole diameter, while the external factors mainly refer to the external environmental factors in the diffusion zone, such as wind speed and obstacle conditions. Since there are woods and mountains of certain height along the natural gas pipeline in mountainous areas, the analysis of gas diffusion needs to focus on the gas diffusion under different obstacles.

Based on a field study of a section of a mountainous natural gas pipeline in China, a pipe diameter of 1,016 mm, a delivery pressure of 10 MPa, and a temperature of 300 K were considered. Since leaks in exposed natural gas pipelines occur mainly in small and medium bore leaks, the leak bore diameter is mainly taken as the default variable of 200 mm. Considering that the top of the pipeline is under the greatest threat of damage, the direction of leakage is set vertically upward. The specific simulation variable parameters are set as shown in Table 1.

To grasp the natural gas concentration at different typical locations, some simulation scenarios set up concentration monitoring points for analysis. As shown in Figure 4, the coordinates at the midpoint of the leak mouth are (20, 0), and four monitoring points, namely, point A (20, 5), point B (25, 1.5), point C (25, 5), and point D (20, 10), are set near the leak hole to observe the changes of gas diffusion concentration at different heights from the leak mouth and at different horizontal distances from the leak hole, where points A and D studied the concentration at different height changes, points A and C studied the concentration changes at different horizontal distances, and point B studied the concentration changes at the respiratory layer of the personnel.

3 Result and discussion

Different methane concentrations cause different kinds of harm to the environment and people, and the article aims to study the diffusion law according to the methane concentration range corresponding to both fire explosion and poisoning. When the concentration ratio of methane in the air is within the range of

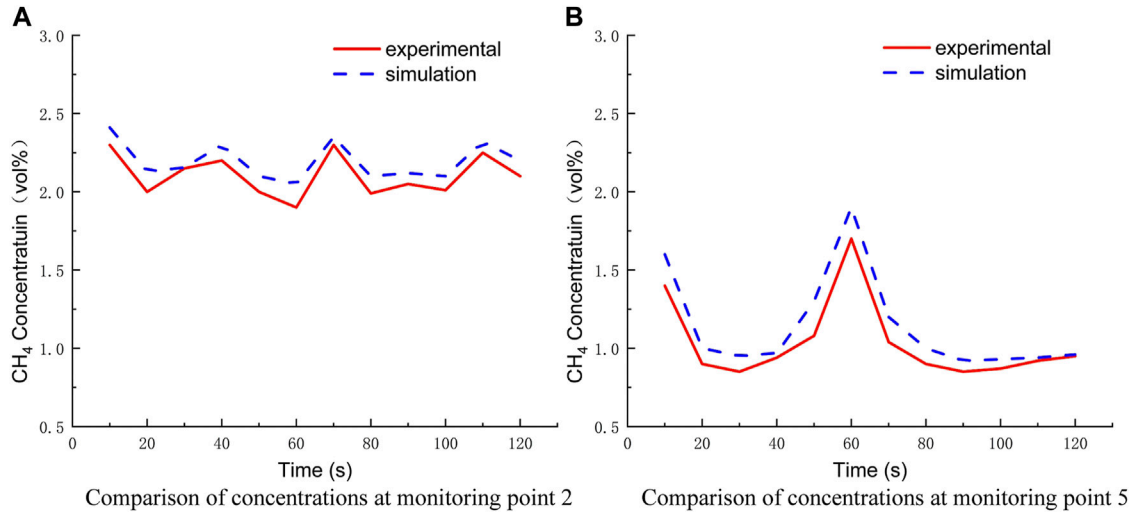

FIGURE 3
Comparison between numerical simulation and experimental results. **(A)** Comparison of concentrations at monitoring point 2. **(B)** Comparison of concentrations at monitoring point 5.

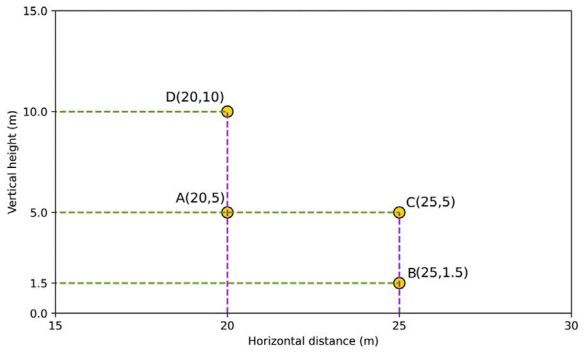

FIGURE 4
Location diagram of monitoring points.

5%–15%, the mixture is in the explosive concentration range; when the concentration ratio reaches 25%–30%, the mixture starts to cause harm to the human body. Therefore, using 5%, 15%, and 25% as methane observation concentration boundaries, we record the changes in the vertical height and horizontal distance of the lower limit of methane explosion under different working conditions with time, compare the differences in the danger range under each working condition, and also compare the changes in concentration at monitoring points under the same leakage time and then realize the analysis of the working condition diffusion process.

3.1 Leak diffusion process analysis

The simulation scenario was set up according to the constants in Table 1 and without surrounding obstacles. The transient model was selected, the time step was set to 0.2 s, and the number of time steps was set to 600. The gas dispersion clouds after 10 s, 30 s, 60 s, and 120 s of leakage were obtained as shown in Figure 5, and the concentration changes at monitoring points at different moments were obtained as shown in Figure 6, and the hazard distance of the lower limit of methane explosion at different moments was obtained as shown in Figure 7.

As can be seen from Figure 5, the exposed pipe is not affected by the soil resistance, and the gas is injected upward first with a large initial velocity at the beginning. With the increase in height, the kinetic energy of the gas decreases upward. At this time, the degree of influence of natural wind speed in the horizontal direction strengthens, and the gas starts to deflect to the right. The spread of natural gas and the extent of the danger zone increase with time.

From the concentration data of the monitoring points, it can be seen that the concentration change in the height direction is the largest and the fastest. When the height reaches a certain level, the concentration decreases due to the interference effect of the horizontal natural wind. Therefore, the concentration change at the monitoring point goes through three main stages: the gestation stage, the rapid growth stage, and the slow growth/stabilization stage. At the same moment, the closer to the leakage hole, the higher the gas concentration and the faster it reaches the steady state.

The lower limit of methane explosion at different moments of the change in the hazard distance can be found; the hazard distance first increases rapidly and then fluctuates at a certain interval, and finally, the boundary distance tends to stabilize. The reason for its fluctuations is

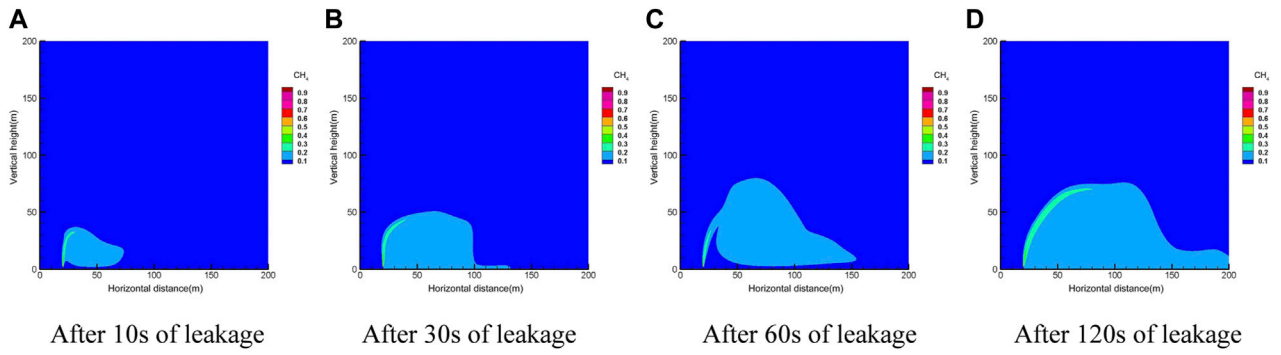

FIGURE 5
Time series of the diffusion process cloud diagram. **(A)** After 10 s of leakage. **(B)** After 30 s of leakage. **(C)** After 60 s of leakage. **(D)** After 120 s of leakage.

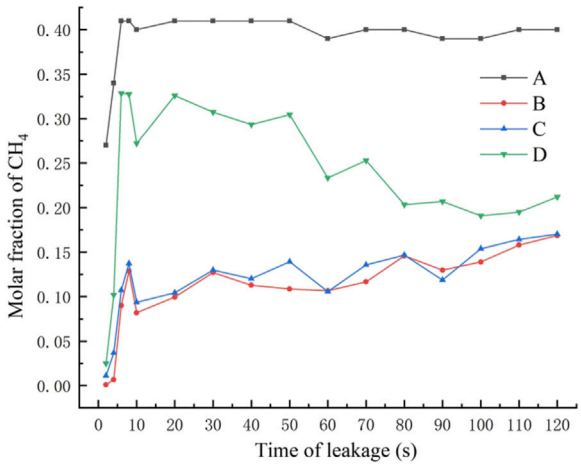

FIGURE 6
Concentration changes at monitoring points at different moments.

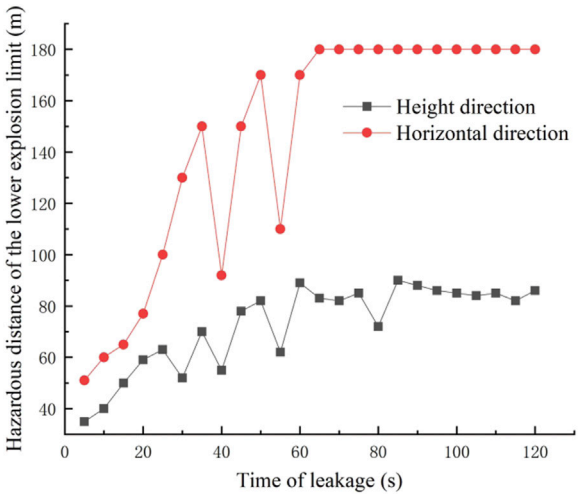

FIGURE 7
Hazard distance of the lower limit of methane explosion at different moments.

that the pipeline leakage hole is small, resulting in a small amount of gas leakage, in the role of wind speed—gas is too late to form a stable boundary.

3.2 Effect of leak hole diameter

Under different leak hole diameters, the pressure at the leak outlet will change, and the leak rate will be different. The study selected four leak hole diameters of 0.02 m, 0.1 m, 0.2 m, and 0.3 m. The rest of the relevant parameters were set to default values. The gas concentration distribution under different hole diameters after the leak occurred for 60 s is shown in Figure 8, the concentration at the monitoring point under different hole diameters after 120 s is shown in Figure 9, and the diffusion heights of different apertures at different times are shown in Figure 10.

As can be seen from Figure 8, under the effect of a certain wind speed, there is a large effect of different sizes of leak hole diameters on the concentration range of natural gas diffusion, but the diffusion shape is roughly the same in each case. In the case of the same leak time, the size of the diffusion range of natural gas after the occurrence of a leak is proportional to the size of the leak hole diameter. By observing the concentration distribution of different orifice diameters at each monitoring point after 120 s of leakage, it is found that the closer to the leakage hole, the higher

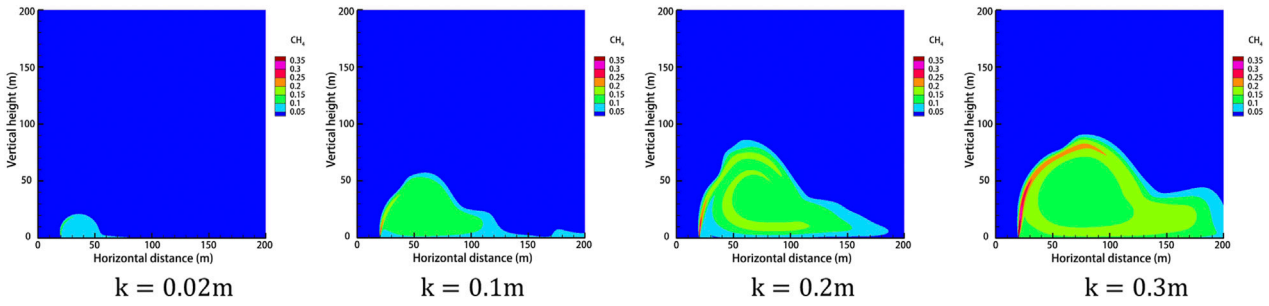

FIGURE 8
Cloud diagram of gas diffusion under different leakage apertures after 60 s of leakage. **(A)** k = 0.02 m. **(B)** k = 0.1 m. **(C)** k = 0.2 m. **(D)** k = 0.3 m.

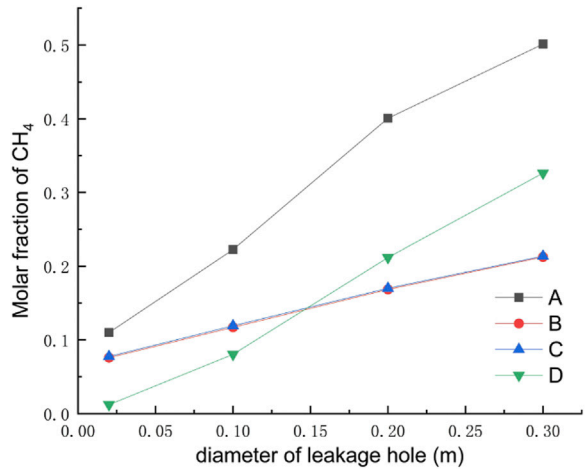

FIGURE 9
Concentration diagram of monitoring points under different leakage apertures after 120 s.

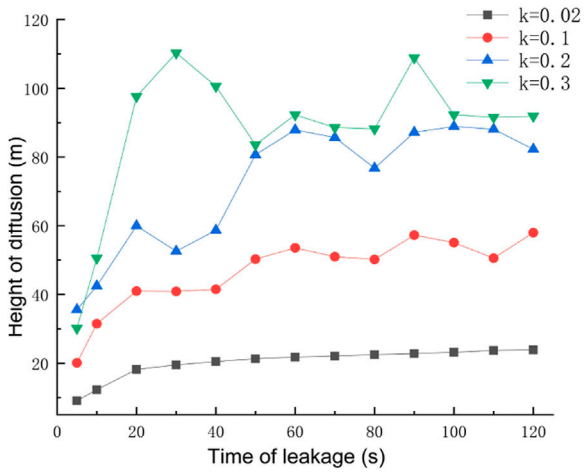

FIGURE 10
Diffusion height diagram of each leakage aperture at different times.

the concentration at the monitoring point. When the orifice diameter is small, the concentration at height monitoring point D is smaller than the concentration at horizontal monitoring point B/C, and as the leakage orifice diameter increases to 0.2 m, the concentration value at height monitoring point D exceeds the concentration value at the horizontal monitoring point B/C. Observation of the diffusion heights of different apertures at different moments reveals that when the leak aperture is larger, the turbulence effect is stronger, and the diffusion height of the gas is more volatile. As the leak aperture increases, the vertical diffusion height and horizontal diffusion distance of the gas increase, and the explosion hazard area range increases.

Therefore, the size of the leak hole is the most critical factor in determining the scope of the gas leak hazard, and the larger the leak hole, the wider the range of gas diffusion, resulting in more serious consequences of the accident, so the most effective emergency response is to block the leak or reduce the leak to prevent the scope of the hazard from becoming larger.

3.3 Effect of ambient wind speed

Through research on the meteorological situation along a section of a mountainous natural gas pipeline in China, the wind speed in the area is about 5 m/s for a long year, and four wind conditions of 2 m/s, 5 m/s, 8 m/s, and 11 m/s are selected considering individual extreme conditions. The rest of the relevant parameters are set to default values, and the gas

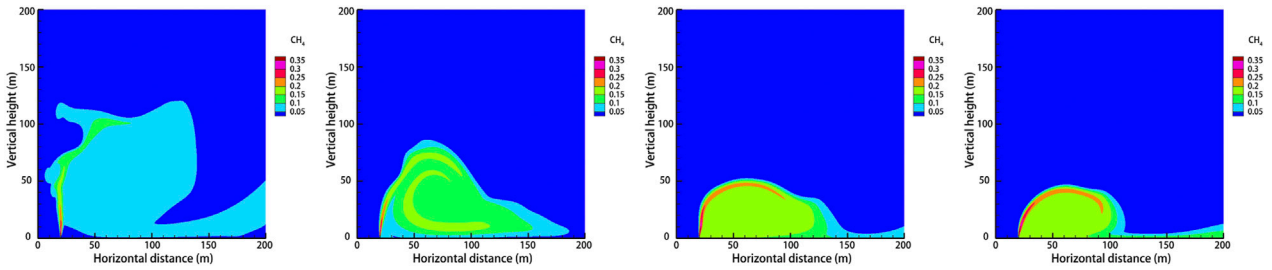

FIGURE 11
Cloud diagram of gas diffusion under different ambient wind speeds after 60 s of leakage. **(A)** v = 2 m/s. **(B)** v = 5 m/s. **(C)** v = 8 m/s. **(D)** v = 11 m/s.

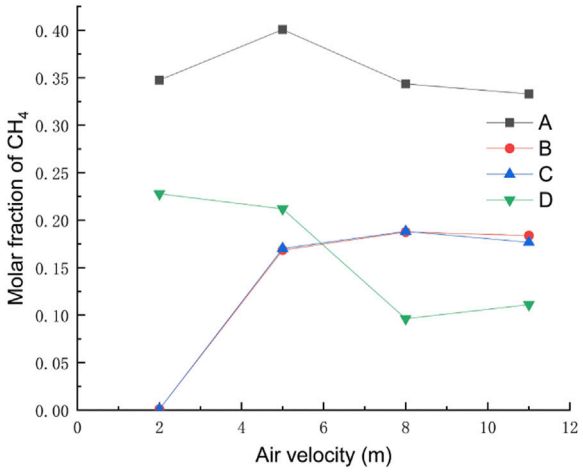

FIGURE 12
Concentration diagram of monitoring points under different ambient wind speeds after 120 s.

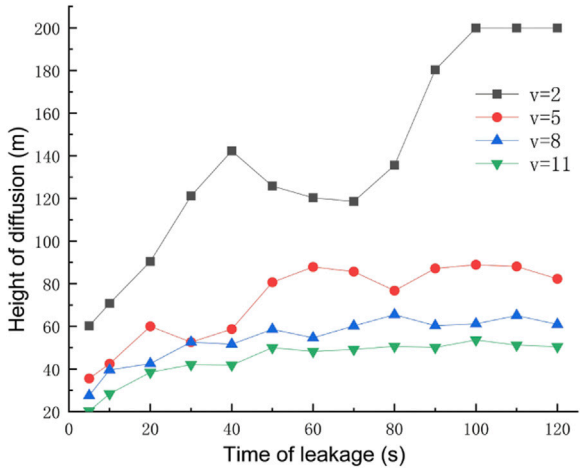

FIGURE 13
Diffusion height diagram of ambient wind speed at different times.

leakage under different ambient wind speeds at the same leakage time is shown in Figure 11. The concentrations at the monitoring points after 120 s at different wind speeds are shown in Figure 12, and the diffusion heights at different wind speeds at different moments are shown in Figure 13.

As can be seen from Figure 11, when the wind speed is small, the dominant effect of the gas leakage rate is obvious, and the distance of gas upward injection is larger. When the wind speed increases, the vertical diffusion height of the gas decreases and the horizontal diffusion distance increases because after the gas leak, the direction of its combined velocity shifts to the right, resulting in the gas leak being blown away by the horizontal wind speed before it has time to diffuse upward. By observing the concentration at each monitoring point under different wind speeds after the leakage occurred for 120 s, it can be concluded that when the wind speed is small, the concentration value of horizontal monitoring point B/C is very low, while the concentration of height monitoring point A/D is very high, and the gas mainly diffuses upward. As the wind speed increases, the concentration value of point B/C gradually increases, while the concentration value of point D decreases, and the gas mainly diffuses in the horizontal direction. By observing the diffusion height of each ambient wind speed at different moments, it is found that when the ambient wind speed is larger, the increase rate of vertical height decreases. As the wind speed increases, the vertical diffusion height of the gas decreases, while the horizontal diffusion distance increases, and the range of the explosion hazard area gathers near the surface.

The aforementioned analysis shows that the risk factor downwind of the leak is high, often forming a high-concentration zone, and an explosion will occur if there is an open fire in the area. Therefore, when designing pipeline lines, the local perennial wind direction should be taken into account, so that factories, residential areas, and other densely populated

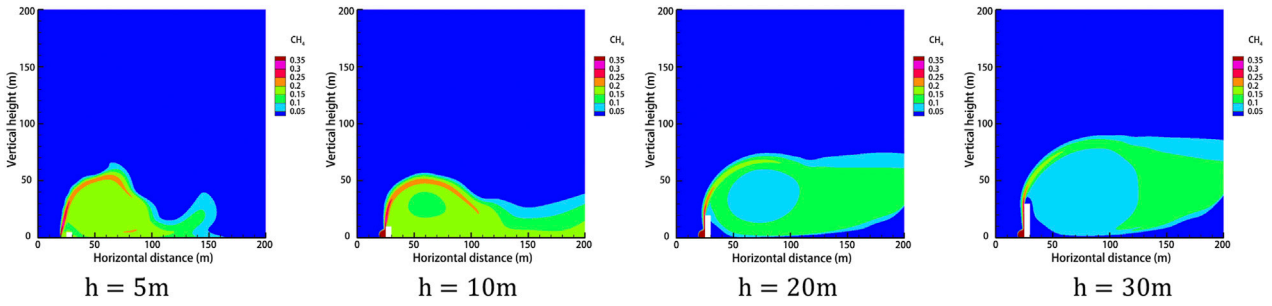

FIGURE 14
Gas dispersion clouds at different obstacle heights after 60 s of leakage. **(A)** h = 5 m. **(B)** h = 10 m. **(C)** h = 20 m. **(D)** h = 30 m.

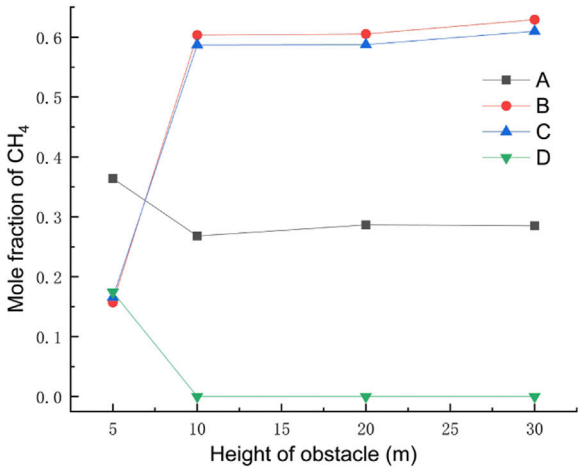

FIGURE 15
Concentration map of monitoring points under different obstacle heights after 120 s.

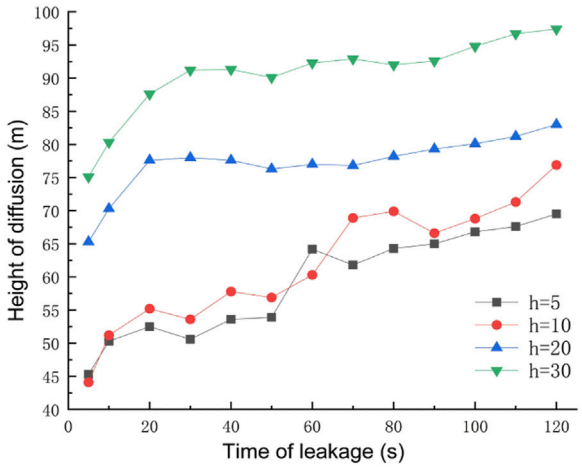

FIGURE 16
Diffusion height diagram for each obstacle height at different moments.

areas are as far away from the downwind direction of the pipeline as possible. When a natural gas leak occurs, people in the vicinity of the leak source and the downwind area should be quickly transferred to minimize casualties. When the wind speed is small, the rescue focus is on the high-altitude area. When the wind speed is large, natural gas is along the ground to form a high-concentration area, so the rescue focus is near the ground area. Wind speed can dilute the concentration of leaking gas, and emergency rescue, on the premise of eliminating the source of fire, should strengthen ventilation.

3.4 Effect of obstacles in mountainous areas

Since there are more trees and mountains in mountainous areas for natural gas pipelines, and it is found through field research that there are more densely populated high-consequence areas along the pipelines, and there are dense buildings around the pipelines, the gas dispersion pattern under various obstacle situations needs to be analyzed.

3.4.1 Effect of the obstacle height

The obstacle was set to 5 m away from the leak, the obstacle height was taken as 5 m, 10 m, 20 m, and 30 m for four working conditions, the rest of the relevant parameters were set to the default values, and the gas leakage under different obstacle heights is derived as shown in Figure 14. After 120 s of leakage, the concentration at each monitoring point under different obstacle heights is shown in Figure 15. The diffusion heights of different obstacle heights at different times are shown in Figure 16.

As can be seen from Figure 14, when the gas leak meets the obstacle, it will be subjected to the resistance effect, at which time

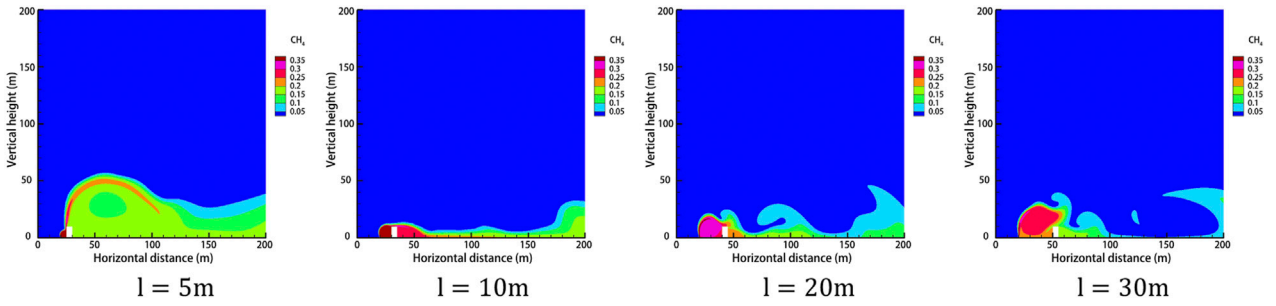

FIGURE 17
Gas dispersion clouds at different obstacle distances after 60 s of leakage. **(A)** l = 5 m. **(B)** l = 10 m. **(C)** l = 20 m. **(D)** l = 30 m.

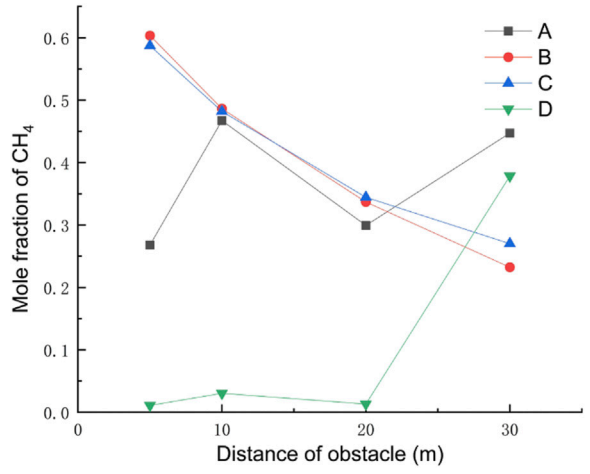

FIGURE 18
Concentration map of monitoring points at different obstacle distances after 120 s.

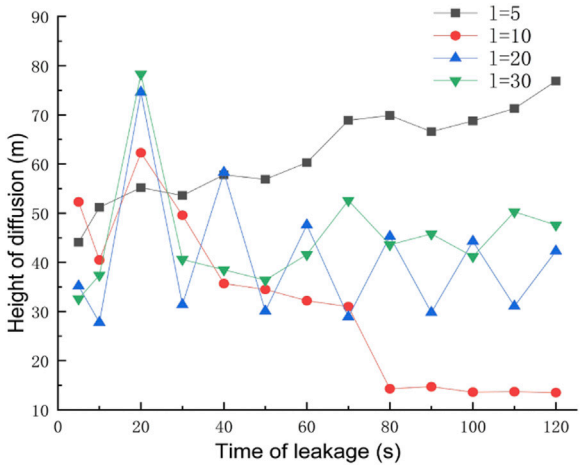

FIGURE 19
Diffusion height diagram of each obstacle distance at different moments.

point the part of the gas will move in the opposite direction, forming a vortex on the windward side of the obstacle, gathering a large amount of gas, and forming a high-concentration area, and the other part will cross the top of the obstacle and form a concentration, gathering area behind the obstacle. When the obstacle is too low, the leaking gas can easily cross the obstacle and form a high-concentration area both at the front and behind it. When the obstacle is high enough, the gas crosses the obstacle less and the gas concentration is lower near the surface of the leeward side of the obstacle, while when the height of the obstacle is greater, the gas will be moved higher and the leaking gas will blow away before it can fall back, resulting in a very low methane concentration in the area behind the obstacle. By observing the concentrations of each monitoring point under different obstacle heights after 120 s of leakage, when the obstacle is higher, under the effect of wind speed, a large amount of gas will be blown to the windward side of the obstacle. The gas will spread upward along the surface of the obstacle, which leads to very low concentrations at height monitoring point A/D and high concentrations at horizontal monitoring point B/C. Observation of different obstacle heights at different moments of gas diffusion height found that as the height of the obstacle increases, the vertical diffusion height of the gas increases, and the explosion hazard area range to the upper air layer gathered.

3.4.2 Effect of the obstacle distance

The height of the obstacle is set to 10 m, and the distance between the obstacle and the leak is taken as 5 m, 10 m, 20 m, and 30 m for four working conditions. The rest of the relevant parameters are set to the default values, and the gas leakage under different obstacle distances is obtained as shown in Figure 17. The concentration of each monitoring point under

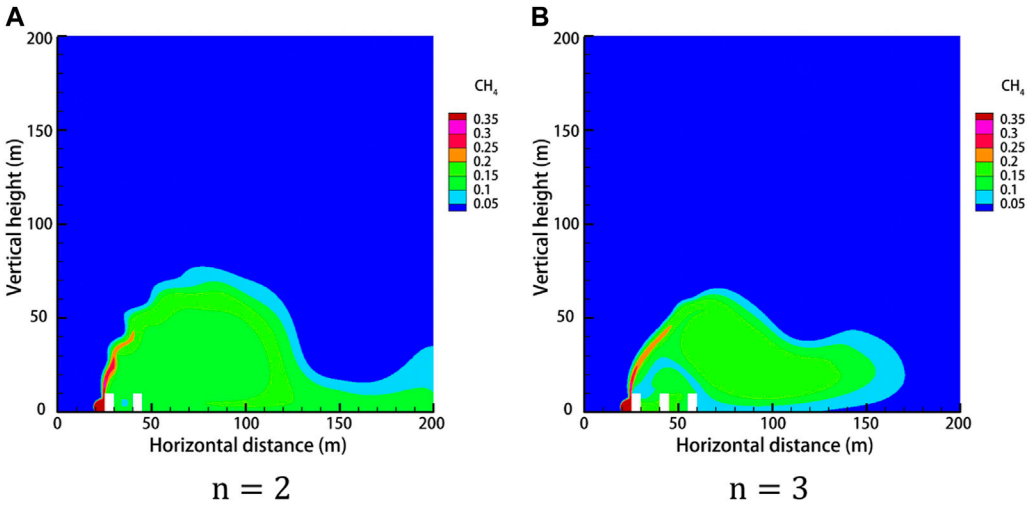

FIGURE 20
Gas dispersion clouds with different number of obstacles after 60 s of leakage. **(A)** n = 2 and **(B)** n = 3.

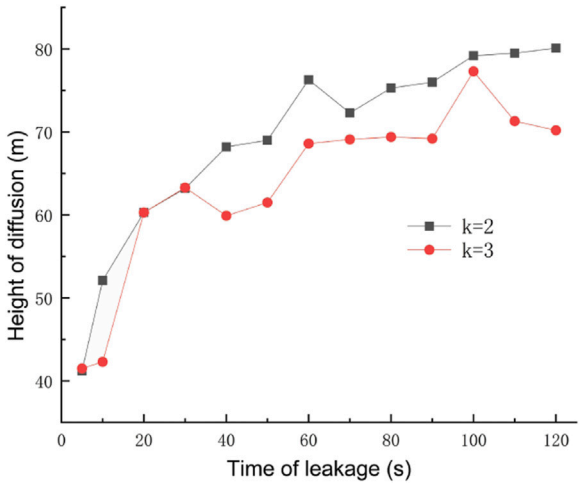

FIGURE 21
Diffusion height at different times for different number of obstacles.

different obstacle distances after 120 s of leakage is shown in Figure 18. The dispersion heights of different obstacle distances at different times are shown in Figure 19.

As can be seen from Figure 17, the gas ejected from the leak will form a vortex area on the windward side of the obstacle, which is easy to form a high-concentration area. As the distance between the obstacle and the leakage port becomes farther, the high-concentration area on the windward side of the obstacle becomes larger, after increasing to a certain distance. Although the high-concentration area will become larger, due to the dilution effect, its concentration has been reduced. As the distance between the obstacle and the leak becomes farther, the gas diffusion area on the leeward side of the obstacle becomes smaller, and the concentration decreases. Observation of the concentration of monitoring points under different distances of obstacles after 120 s of leakage reveals that when the distance of obstacles becomes farther, the concentration of horizontal monitoring point B/C decreases, and the concentration of height monitoring point D increases, which is because of the vortex formed on the windward side of obstacles becomes larger, and the concentration decreases. Also, at this time, the gas will not spread upward along the surface of obstacles; meanwhile, the concentration of height monitoring point D appears to increase. Observation of the diffusion height of different obstacle distances in different moments reveals that with the increase in the obstacle distance, the gas vertical diffusion height first increases and then decreases, and in the obstacle at a distance of 10 m from the leak located at the mouth, the gas diffusion height is the smallest, indicating that the gas diffusion height and the distance of the obstacle are not in a linear relationship.

3.4.3 Effect of the number of obstacles

When the pipeline is located in a densely populated high-consequence area, the buildings here must be dense, and the gas leakage dispersion will be different when there are multiple buildings. The distance between buildings is set to 10 m, the rest of the relevant parameters set to default values, and the gas diffusion law is studied when two buildings and three buildings exist side by side. The gas diffusion under a different number of obstacles is derived as shown in Figure 20. The diffusion height under a different number of obstacles at different moments is shown in Figure 21.

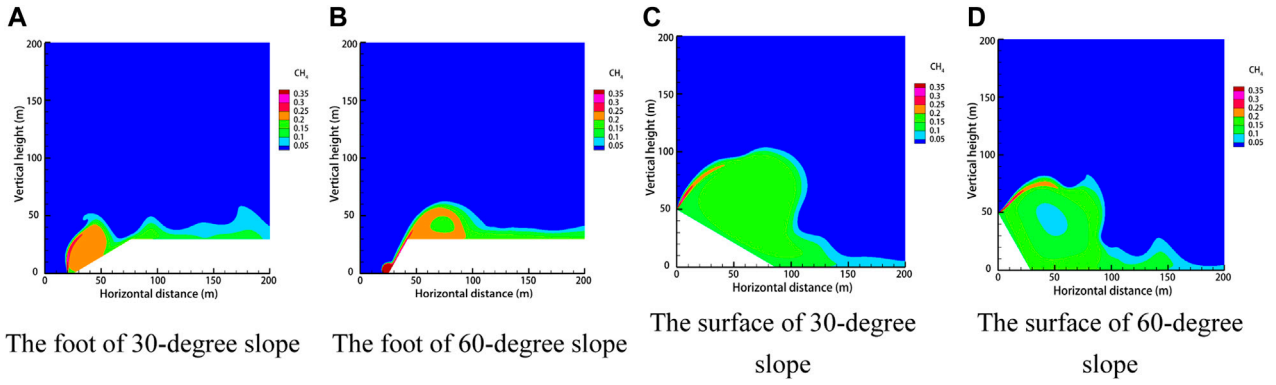

FIGURE 22
Dispersion clouds of different laying environments after 60 s of leakage. **(A)** Foot of 30-degree slope. **(B)** Foot of 60-degree slope. **(C)** Surface of 30-degree slope. **(D)** Surface of 60-degree slope.

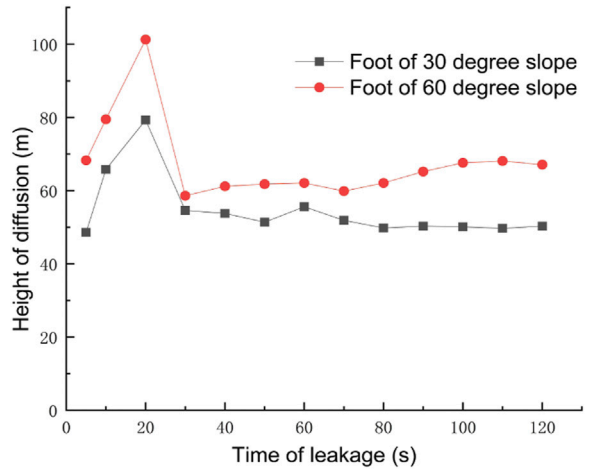

FIGURE 23
Diffusion height map of pipelines laid at the foot of the slope at different times.

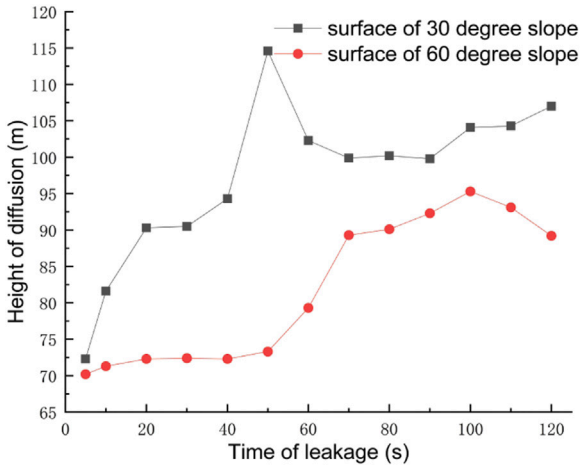

FIGURE 24
Diffusion height map of pipelines laid at the surface of the slope at different times.

From Figure 20, we can see that the number of obstacles changes the diffusion pattern after the gas leak. Two buildings side by side have a weaker blocking effect on the gas, and the concentration between buildings is lower, while the gas concentration in the area behind the buildings is higher, forming a larger concentration area. Three buildings side by side have a stronger blocking effect on the gas, and the concentration between buildings is higher, while the concentration in the area behind the buildings is lower. By observing the diffusion height at different moments with a different number of obstacles, it is found that the gas vertical diffusion height decreases with the increase in the number of obstacles.

Based on the law of the influence of different obstacle heights, distances, and quantities on gas diffusion, accident losses can be mitigated in the following ways:

1) The influence area is different with different obstacle heights. When the obstacle is low, the gas mainly converges near the surface, and when the obstacle is high, the gas diffuses to a high altitude. In the natural gas explosion accident, the main rescue area is the ground of low obstacles and high obstacles at high altitudes.
2) Because the higher the obstacle, the greater the barrier effect on the gas in the diffusion, under the conditions of

meeting the economy, as far as possible to build a high retaining wall.

3) When planning the location of the retaining wall, it is not better to be closer to the pipeline. When it is too close to the pipeline, the leaking gas will easily cross the retaining wall, while when it is too far from the pipeline, the high-concentration area on the windward side of the retaining wall is too large, exposing a large risk area and causing waste of resources such as land. When planning pipeline routes, the distance should be reasonably planned when there are buildings and other obstacles around.
4) For accident rescue after natural gas leakage, the windward side of the obstacle should be included in the emergency rescue area, this area may be poisoned shock, rescue personnel need to be fully equipped, and the first task is to cut off all sources of ignition in the area to avoid an explosion accident.

3.5 Effect of the pipe-laying environment

As the mountainous terrain is more complex and changeable, the pipeline-laying environment is also different from that of the plain area. Through the research, the laying environment is divided into four situations: the foot of a 30-degree slope, the foot of a 60-degree slope, the surface of a 30-degree slope, and the surface of a 60-degree slope. The diffusion law of gas leakage under different situations is shown in Figure 22. The diffusion heights of the pipes laid at the foot of the slope at different times are shown in Figure 23, and the diffusion heights of the pipes laid on the surface of the slope at different times are shown in Figure 24.

For the pipeline laid at the foot of the slope, when the slope is small, the gas will form a large high-concentration area at the slope surface, and its diffusion law is closer to the obstacle-free condition. When the slope is larger, a smaller high-concentration area will be formed at the foot of the slope, and a part of the gas will be diffused upward along the slope. Its diffusion law is closer to the vertical obstacle condition. After the gas pipeline leaks at the foot of the slope, the focus of emergency and rescue is on the slope surface of the small slope and the top of the large slope. Meanwhile, as the slope increases, the vertical diffusion height of the gas increases, and the horizontal diffusion rate decreases.

For the pipeline laid on the surface of the slope, when the slope is small, the gas mainly diffuses upward and mostly gathers on the slope surface. When the slope is large, the height of gas diffusion upward decreases, the horizontal diffusion distance becomes farther, and the gas mostly gathers at the foot of the slope and forms an area of higher concentration on the ground. At the same time, with the increase in the slope, the vertical diffusion height of the gas decreases, the gas reaches the foot of the slope faster, and the horizontal diffusion speed increases.

Therefore, the location of the laid pipeline is different, and the focus of emergency rescue is different. When a leak occurs in the pipeline at the foot of the slope, the gas spreads along the surface of the slope. When the slope is small, the focus of control should be placed on the surface of the slope. When the slope is large, the focus of control should be placed on the top of the slope. When the pipeline on the surface of the slope is leaking and the slope is small, the control focus should be on the surface of the slope. When the slope is large, the control focus should be on the bottom of the slope.

4 Conclusion

This article establishes a diffusion model of exposed natural gas pipeline leakage, analyzes the leakage diffusion process, and analyzes the diffusion law and danger area under different leakage apertures, ambient wind speeds, obstacle situations, laying positions, and other factors according to the injury concentration threshold of natural gas and finally puts forward the focus of emergency rescue and control measures development, mainly forming the following conclusions:

1) The exposed pipeline is different from the buried pipeline leakage because it is not affected by the soil resistance. The gas is injected upward first, and the starting speed is large, with the increase in height. The kinetic energy of the gas decreases upward. Also, at this time, the influence of the natural wind speed in the horizontal direction is strengthened, and the gas will be deflected to the right. The diffusion range of natural gas increases with time, and the area of the danger zone increases. The lower explosion limit of methane after gas leakage in the height direction and horizontal direction of the hazard distance changing with the leakage time is roughly the same law, and the hazard distance first increases rapidly and then fluctuates at a certain interval. Finally, the boundary distance tends to be stable. Therefore, the vicinity of the leak source and downwind area should be used as the focus area for personnel rescue.
2) As the diameter of the leak hole increases, the vertical diffusion height of the gas, the horizontal diffusion distance, and the range of the explosion hazard area will increase. When the leak hole diameter is larger, the turbulence effect is stronger, and the gas diffusion height is more volatile. The size of the leak hole diameter is the most critical factor in determining the hazard range of a gas leak, and the most effective emergency response is to block the leak or reduce the leak to prevent the hazard range from becoming further larger.
3) With the increase in wind speed, the gas vertical diffusion height decreases, while the horizontal diffusion distance increases, and the scope of the explosion hazard area to the surface near the gathering increases. When the wind speed is small, the focus of rescue is the high-altitude area. When the wind speed is larger, along the ground to form a high-concentration area, the focus of rescue is near the ground area. Wind speed can dilute the concentration of the leaking gas, and emergency rescue, on the premise of eliminating the source of fire, should strengthen ventilation.

4) Obstacles have a certain resistance effect. With the increase in the height of the obstacles, the gas vertical diffusion height increases, the explosion hazard area range to the upper air layer gathered, and the gas diffusion height and the distance of the obstacles are not in a linear relationship. With the increase in the number of obstacles, the gas vertical diffusion height decreases. In the natural gas explosion accident, the main rescue area location is the ground of low obstacles and high obstacles of high altitude. When planning the location of the retaining wall, not being closer to the pipeline is better, and when there are buildings and other obstacles around the pipeline, the distance should be reasonably planned.
5) The location of the laid pipeline is different, and the focus of emergency rescue is different. When a leak occurs in the pipeline at the foot of the slope, the gas spreads along the surface of the slope. When the slope is small, the focus of control should be placed on the surface of the slope. When the slope is large, the focus of control should be placed on the top of the slope. When the pipeline on the surface of the slope is leaking and the slope is small, the control focus should be on the surface of the slope. When the slope is large, the control focus should be on the bottom of the slope.

Data availability statement

The original contributions presented in the study are included in the article/Supplementary Material; further inquiries can be directed to the corresponding author.

Author contributions

DX: theoretical analysis, numerical simulation method study, and conclusion analysis; LC: theoretical analysis, establishment of simulation scenarios, and conclusion analysis; WZ: numerical modeling and validation; KZ: numerical simulation studies; JL: post-processing; YJ: pipeline-operating condition data collection and collation; and RM: literature research.

Conflict of interest

Author WZ was employed by Baoji Petroleum Steel Pipe Co., Ltd.

The remaining authors declare that the research was conducted in the absence of any commercial or financial relationships that could be construed as a potential conflict of interest.

Publisher's note

All claims expressed in this article are solely those of the authors and do not necessarily represent those of their affiliated organizations, or those of the publisher, the editors, and the reviewers. Any product that may be evaluated in this article, or claim that may be made by its manufacturer, is not guaranteed or endorsed by the publisher.

References

Aguilera, R. F. (2014). The role of natural gas in a low carbon Asia Pacific. *Appl. Energy* 113, 1795–1800. doi:10.1016/j.apenergy.2013.07.048

Britter, R. E., and Mcquaid, J. (1988). Workbook on the dispersion of dense gases. *Health & Saf. Exec.* 211, 656–661.

Bu, F., Liu, Y., Liu, Y., Xu, Z., Chen, S., Jiang, M., et al. (2021). Leakage diffusion characteristics and harmful boundary analysis of buried natural gas pipeline under multiple working conditions. *J. Nat. Gas Sci. Eng.* 94, 104047. doi:10.1016/j.jngse.2021.104047

Dai, Y., Mak, C. M., Ai, Z., and Hang, J. (2018). Evaluation of computational and physical parameters influencing CFD simulations of pollutant dispersion in building arrays. *Build. Environ.* 137, 90–107. doi:10.1016/j.buildenv.2018.04.005

EGIG (2020). 11th Report of the European gas pipeline incident data Group (period 1970 – 2019) Comprising. EGIG Report

Ermak, D. L., Chan, S. T., Morgan, D. L., and Morris, L. K. (1982). A comparison of dense gas dispersion model simulations with burro series LNG spill test results. *J. Hazard. Mater.* 6, 129–160. doi:10.1016/0304-3894(82)80037-x

Fan, Y. V., Perry, S., Klemeš, J. J., and Lee, C. T. (2018). A review on air emissions assessment: Transportation. *J. Clean. Prod.* 194, 673–684. doi:10.1016/j.jclepro.2018.05.151

Hoeks, J. (1975). Effect of leaking natural gas on soil and vegetation in urban areas. *Soil Sci.* 120, 317–318. doi:10.1097/00010694-197510000-00022

Jackson, R. B., Down, A., Phillips, N. G., Ackley, R. C., Cook, C. W., Plata, D. L., et al. (2014). Natural gas pipeline leaks across Washington, DC. *Environ. Sci. Technol.* 48, 2051–2058. doi:10.1021/es404474x

Kiša, M., and Jelemenský, L. (2009). CFD dispersion modelling for emergency preparadnes. *J. Loss Prev. Process Ind.* 22, 97–104. doi:10.1016/j.jlp.2008.09.013

Liu, A., Huang, J., Li, Z., Chen, J., Huang, X., Chen, K., et al. (2018). Numerical simulation and experiment on the law of urban natural gas leakage and diffusion for different building layouts. *J. Nat. Gas Sci. Eng.* 54, 1–10. doi:10.1016/j.jngse.2018.03.006

Liu, B., Liu, X., Lu, C., Godbole, A., Michal, G., and Tieu, A. K. (2016). Computational fluid dynamics simulation of carbon dioxide dispersion in a complex environment. *J. Loss Prev. Process Ind.* 40, 419–432. doi:10.1016/j.jlp.2016.01.017

Meroney, R. N. (2012). CFD modeling of dense gas cloud dispersion over irregular terrain. *J. Loss Prev. Process Ind.* 104-106, 500–508. doi:10.1016/j.jweia.2012.01.001

Pasquill, F., and Smith, F. B. (1983). *Atmospheric diffusion*. England: E. Horwood.

Phillips, N. G., Ackley, R., Crosson, E. R., Down, A., Hutyra, L. R., Brondfield, M., et al. (2013). Mapping urban pipeline leaks: Methane leaks across Boston. *Environ. Pollut.* 173, 1–4. doi:10.1016/j.envpol.2012.11.003

Rui, Z., Han, G., Zhang, H., Wang, S., Pu, H., and Ling, K. (2017). A new model to evaluate two leak points in a gas pipeline. *J. Nat. Gas Sci. Eng.* 46, 491–497. doi:10.1016/j.jngse.2017.08.025

Scargiali, F., Grisafi, F., Busciglio, A., and Brucato, A. (2011). Modeling and simulation of dense cloud dispersion in urban areas by means of computational fluid dynamics. *J. Hazard. Mater.* 197, 285–293. doi:10.1016/j.jhazmat.2011.09.086

Sini, J. F., Anquetin, S., and Mestayer, P. G. (1996). Pollutant dispersion and thermal effects in urban street canyons. *Atmos. Environ.* 30, 2659–2677. doi:10.1016/1352-2310(95)00321-5

Sklavounos, S., and Rigas, F. (2006). Estimation of safety distances in the vicinity of fuel gas pipelines. *J. Loss Prev. Process Ind.* 19, 24–31. doi:10.1016/j.jlp.2005.05.002

Slade, D. H. (1968). Meteorology and atomic energy, 1968. Technical Report.

Smith, K. L., Colls, J. J., and Steven, M. D. (2005). A facility to investigate effects of elevated soil gas concentration on vegetation. *Water Air Soil Pollut.* 161, 75–96. doi:10.1007/s11270-005-2833-x

Soulhac, L., Lamaison, G., Cierco, F. X., Ben Salem, N., Salizzoni, P., Mejean, P., et al. (2016). Siranerisk: Modelling dispersion of steady and unsteady pollutant releases in the urban canopy. *Atmos. Environ.* 140, 242–260. doi:10.1016/j.atmosenv.2016.04.027

Ulden, A. V. (1974). "On the spreading of a heavy gas released near the ground," in *Proceedings of First International Loss Prevention Symposium*, 221–226.

Wilkening, H., and Baraldi, D. (2007). CFD modelling of accidental hydrogen release from pipelines. *Int. J. Hydrog. Energy* 32, 2206–2215. doi:10.1016/j.ijhydene.2007.04.022

Xiao, J., Kong, W., Wang, X., and Li, M. (2020). Numerical modeling and assessment of natural gas pipeline separation in China: The data from henan province. *Pet. Sci.* 17, 268–278. doi:10.1007/s12182-019-00400-5

Xing, J., Liu, Z., Huang, P., Feng, C., Zhou, Y., Zhang, D., et al. (2013). Experimental and numerical study of the dispersion of carbon dioxide plume. *J. Hazard. Mater.* 256-257, 40–48. doi:10.1016/j.jhazmat.2013.03.066

Zhang, S., Wang, X., Cheng, Y. F., and Shuai, J. (2020). Modeling and analysis of a catastrophic oil spill and vapor cloud explosion in a confined space upon oil pipeline leaking. *Pet. Sci.* 17, 556–566. doi:10.1007/s12182-019-00403-2

Zhang, Z. W., Wang, J. C., Zhang, J. H., and Frank Cheng, Y. (2021). Modeling of the mechano-electrochemical effect at corrosion defect with varied inclinations on oil/gas pipelines. *Pet. Sci.* 18 (5), 1520–1529. doi:10.1016/j.petsci.2021.08.012

Zhu, D., Peng, S., Zhao, S., Wei, M., and Bai, B. (2021). Comprehensive review of sealant materials for leakage remediation technology in geological CO2 capture and storage process. *Energy fuels* 35 (6), 4711–4742. doi:10.1021/acs.energyfuels.0c04416

frontiers | Frontiers in Energy Research

TYPE Original Research
PUBLISHED 12 January 2023
DOI 10.3389/fenrg.2022.1008356

OPEN ACCESS

EDITED BY
Yibo Li,
Southwest Petroleum University, China

REVIEWED BY
Xiong Liu,
Xi'an Shiyou University, China
Yisheng Hu,
Southwest Petroleum University, China

*CORRESPONDENCE
Feng Xu,
xufeng01@cnpcint.com

SPECIALTY SECTION
This article was submitted to Advanced Clean Fuel Technologies, a section of the journal Frontiers in Energy Research

RECEIVED 31 July 2022
ACCEPTED 26 September 2022
PUBLISHED 12 January 2023

CITATION
Nie Z, Xu F, Ouyang J, Li X, Zhang J, Liu S, Han J and Li D (2023), Experimental tests and EDFM method to study gas injection in a fractured granite reservoir.
Front. Energy Res. 10:1008356.
doi: 10.3389/fenrg.2022.1008356

Experimental tests and EDFM method to study gas injection in a fractured granite reservoir

Zhiquan Nie[1], Feng Xu[1,2]*, Jingqi Ouyang[1], Xiangling Li[2], Juntao Zhang[1], Shiliang Liu[3], Jinqiang Han[3] and Da Li[3]

[1]China National Oil and Gas Exploration and Development Company Ltd. (CNODC), Beijing, China, [2]Research Institute of Petroleum Exploration and Development Co Ltd (RIPED) CNPC, Beijing, China, [3]Research Institute of Exploration and Development, Petrochina Yumen Oilfield Company, Jiuquan, China

The development of granite reservoirs with high dip fractures has many difficulties, such as a high decline rate, early water breakthrough, and numerous economic losses. Gas injection is usually used to maintain the formation pressure to increase single well productivity, and could be carried out in fractured reservoirs to enhance oil recovery. When injecting associated gas, it meets the environmental protection requirements of the local government to further eliminate the flare, implementing the concept of green and low-carbon development. In this study, both laboratory tests and reservoir simulation have been done to study the feasibility and the benefit of associated gas injection in the research target. For physical stimulation, it mainly includes experiments such as associated gas injection expansion, slim tube, long core displacement, and relative permeability. Through these experiments, the changes in the recovery factor after depletion development and gas displacement are systematically described and the key controls are revealed for improving the recovery ratio of fractured basement reservoirs. For the simulation part, the embedded discrete fracture model processor combining commercial reservoir simulators is fully integrated into the research. A 3D model with complex natural fractures is built to perform the associated gas injection performance of the fractured granite reservoir. Complex dynamic behaviors of natural fractures can be captured, which can maintain the accuracy of DFNs and keep the efficiency offered by structured gridding. Depletion development and gas injection development strategy are optimized in this research. The result shows that oil recovery by using gas injection is increased by 16.8% compared with depletion development by natural energy.

Abbreviations: IOC; International Oil Companies; NOC, National Oil Companies; NFR, Naturally Fractured Reservoir; DPDK, Dual Porosity Dual Permeability; DFM, Discrete Fracture Model; GOR, Gas Oil Ratio; PV, Pore Volume; PVT, Pressure-Volume-Temperature; MMP, Minimum Miscible Pressure; Swi, Irreducible Water Saturation; Sor, Residual Oil Saturation; So, Oil Saturation; kro/krg/krg, Relative Permeability of Oil/Gas/Water; Sgc, Critical Gas Saturation; EDFM, Embedded Discrete Fracture Model.

KEYWORDS

granite reservoir, associated gas injection, EDFM, natural fractures, depletion development

Introduction

In recent years, the low-carbon transformation has become an inevitable trend for the development of global energy companies (Ma et al., 2018; Vardon et al., 2022). Many IOCs and NOCs actively conduct researches on carbon peaking and carbon neutrality, comprehensively formulating a low-carbon strategic transformation path. Normally, oil companies generate a large amount of associated gas in the process of crude oil development, except for one part used to meet the demand of power generation for field daily production, most of it needs to be processed by direct venting or flare combustion, which not only emits a large amount of carbon dioxide into the air, but also wastes the associated natural gas to a large extent. To implement the concept of green and low-carbon development, and meet the environmental protection requirements of the local government to further eliminate the flare, the associated gas reinjection could be carried out in fractured reservoirs to enhance the oil recovery.

Fractured granite reservoirs were discovered in many countries, such as the United Kingdom, India, Egypt, Venezuela, Vietnam, Libya, China, and so on (Dang et al., 2001; Schechter 2002; Van Nguyen et al., 2016; Song et al., 2020; Delamaide et al., 2022). It is known that natural fractures have a great impact on flow properties, production, and ultimate recovery. Most of these reservoirs had high initial production rates and decline rates in the primary production stage. Usually, water and gas injection in fractured reservoirs were considered effective to maintain the reservoir pressure, as seen in Table 1. However, the presence of fractures would lead to rapid water channeling, and the major part of the oil would be trapped in the low permeability matrix blocks in most granite-NFRs. Compared with water flooding, gas can enter smaller microscopic fractures and pores, increasing the gas sweeping volume, and enhancing the oil recovery. Gas flooding could significantly reduce surface tension. The surface tension of oil and gas in immiscible flooding is also only 16%–25% of the oil-water interfacial tension in waterflooding. It is found that the fracture aperture that gas could enter in the gas flooding is 4–7 times smaller than that in water flooding, about 20 times smaller in some oil fields. What is more, it can make full use of the gravity difference between oil and gas in gas flooding, when gas is injected at the top of the reservoir and oil is recovered at the middle and lower parts of the reservoir.

Naturally fractured granite reservoirs are especially difficult to characterize, model, and simulate because of high static and dynamic heterogeneity (Nelson, 2001; Narr et al., 2006; Lonergan et al., 2007; Dipak, 2012; Peng et al., 2020). Researchers have been studying the behavior of fractured reservoirs to capture the physics of fluid flow in such systems (Warren and Root 1963; Cinco-ley and Samaniego-v 1981; Karimi-Fard and Firoozabadi 2003; Hoteit and Firoozabadi 2006; Zhou et al., 2014). To better understand the effect of fractures, several approaches have been proposed, most of which are grounded based on two classes of models, the dual porosity (or dual continuum) and the discrete fracture models. Each class of models has developed to answer some of the challenges associated with modeling and simulation of fractured reservoirs. In the dual porosity approach, an NFR model is represented by two collocated domains, the fracture domain, and the matrix domain. This method could be used in the reservoirs with densely distributed and highly connected fractures, which is very fast and efficient in computation time and has been successfully used in many real NFRs studies. However, there are many simplifications in the models, so they are not suitable for accurately simulating reservoirs with complex and large-scale fractures and fluids flowing along the fractures. In some fractured reservoirs, the fractures do not establish a

TABLE 1 Summary of fractured granite reservoirs.

No.	Reservoir	Country	Lithology	Reservoir Fluid	Development mode
1	Clair field	United Kingdom	Granite	Oil	Water injection
2	Dragon field	Vietnam	Granite	Oil	Water injection
3	La paz field	Venezuela	Limestone, granite	Oil	Water injection
4	Mara field	Venezuela	Granite and metamorphic	Oil	Water injection
5	Nafoora-Augila field	Libya	Granite	Oil	Water injection
6	PY-1 field	India	Weathered granite	Gas &Condensate	Natural energy
7	Shaim field	Russia	Granite and gneiss	Oil	Water injection
8	Sumatra-Beruk Northeast	Indonesia	Metaquartzites, weathered granite	Oil and gas	Natural energy
9	White Tiger field	Vietnam	Granite	Oil and gas	Water/Gas injection
10	Xinglongtai field	China	Metamorphosed granite	Oil and gas	Water/Gas injection
11	Zeit Bay field	Egypt	Fractured Granite	Oil	Gas injection

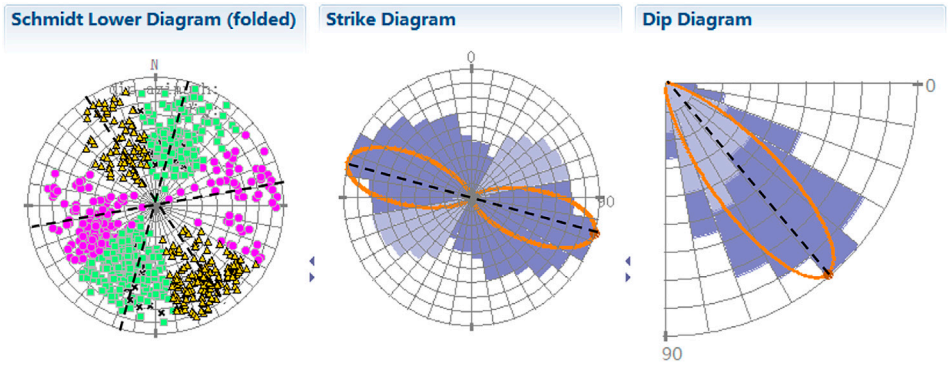

FIGURE 1
Global fracture analysis result.

connected network and thus the continuum assumption is no longer valid. Also, when fracture length is comparable to the size of the computational grid, upscaling and averaging the fracture's properties alter the realistic representation of the network (Long et al., 1982; Long and Witherspoon, 1985). To further eliminate such drawbacks in simulating fractured reservoirs, a new kind of model, called the Discrete Fracture Model (DFM), was proposed. In DFMs, each fracture is modeled explicitly through the application of unstructured gridding. Complex fracture geometry can be mostly represented by using this approach, and large quantities of small-scale grids are generated around the fractures. However, the DFM models have complicated gridding and time-consuming computation, so the models have great limitations in real field reservoir simulation. To solve the strait above, a 2D embedded discrete fracture model (EDFM) was proposed to keep the accuracy of DFMs while holding the efficiency presented by structured gridding (Lee et al., 2001; Li and Lee 2008; Hajibeygi et al., 2011). Last few years, many scholars spread the EDFM for 3D reservoir simulators (Moinfar et al., 2014; Cavalcante Filho et al., 2015; Xu et al., 2017, Xu F et al., 2018), making the EDFM method more useful in the fractured reservoirs.

In this study, both Lab tests and reservoir simulation have been done to study the feasibility and the benefit of associated gas injection in the research target. For physical stimulation, it mainly includes experiments such as associated gas injection expansion, slim tube, long core displacement, and relative permeability. Through these experiments, the changes in the recovery factor after water flooding and gas displacement are systematically described and the key controls are revealed for improving the recovery ratio of fractured basement reservoirs. For the simulation part, the EDFM processor combining commercial reservoir simulators is fully integrated into the research. A 3D model with complex natural fractures is built to perform the associated gas injection performance of the fractured granite reservoir.

TABLE 2 Composition of the associated gas.

Component	Composition, mol%
CO_2	0.3
N_2	5.7
C_1	62.2
C_2	11.0
C_3	13.0
iC_4	3.6
nC_4	2.9
iC_5	0.4
nC_5	0.2
C_{6+}	0.7

Reservoir characteristics

The research area is a brand-new oil field, the natural fractures play a major role in oil production for this specific granite reservoir. The reservoir thickness is about 150 m and could be separated into three layers vertically. The reservoir is composed of complex lithologies, which include metamorphic rocks and magmatic rocks. The structure characteristic of this reservoir is complicated by a basement fault system and long exposure history, complex natural fractures and vugs are well developed. The basement reservoir is characterized by low porosity and low permeability. Generally, the porosity is 2%–6%, and permeability is less than 10 mD. It is impossible to produce commercially without fracture communication. Fracture orientations are organized into three sets of fractures. One major trend (WNW-ESE), one secondary trend (ENE-WSW), and one minor trend (NS) are recognizable. Figure 1 shows the stereo plot of the 807 fractures interpreted in the reservoir units of the wells considered for the analysis. For each of the three sets of fractures, the average dip angle is computed

TABLE 3 Displacement efficiency at different pressures (96.8°C).

Pressure (MPa)	Displacement efficiency (%)
12.5	57.57
16	75.14
18	88.18
20	90.48
25	92.38

using the entire population of diffuse fractures and fracture clusters from all of the wells, ranging from 60° to 85°.

The wells completed in the area have high oil production, low water production, and low gas oil ratio (GOR). The effective fracture permeability interpreted based on the well testing method ranges from 118 to 3,410 mD, which revealed strong heterogeneity in the reservoir. Although the average well space is as far as 800 m, well interference between some wells is detected.

Experimental tests

The oil sample used in the experiment is from a typical well in the fractured granite reservoir, which belongs to a black oil system with low methane, low hydrocarbon intermediates, and high heavy hydrocarbon. The content of C_1+N_2 accounts for 9.56%, the content of C_2 ~ C6 + CO2 14.145%, and the content of C7+ 76.29%. The associated gas used in the experiment is from a high gas rate well in the main oilfield, with C1 + N2 accounting for 67.9%, C2 ~ C_6 + CO_2 32.1%, which is a rich gas with high methane content, as seen in Table 2. The formation temperature is 96.8°C the formation pressure is 12.3 MPa, and the gas/oil ratio is 15.9 m^3/m^3.

Phase behavior experiment

The gas/oil ratio is low, so the crude oil is under-saturated. The saturation pressure measured by the flash experiment is 2.55 MPa. The difference between the formation pressure and the bubble point pressure is so large that the elastic energy is weak, and therefore, it is necessary to inject water or gas to increase formation energy and produce the reservoir. Figure 2.

The P-V relationship curve shows that the increase of the gas-liquid relative volume is not significant after the crude oil is degassed. Affected by the low gas/oil ratio and under-saturation state, the PVT properties of the formation oil have minor changes during the process of multistage degassing while the formation pressure decreases due to the production.

The effects of injecting associated gas on increasing the dissolved gas volume in the crude oil and the expansion of the crude oil are studied. Multiple parameters are analyzed to determine the flow mechanism of associated gas in the fractured granite reservoir, such as the gas/oil ratio, saturation pressure, expansion factor, saturated oil density, viscosity, and shrinkage ratio.

The slim tube experiment is the main experimental method to determine the minimum miscible pressure (MMP) of a given injected gas. Related terms mainly refer to multiple-contact miscibility and MMP. Based on the measured data under experimental pressures, displacement efficiency to displacement pressures for all slim tube experiments at 1.2 PV of associated gas was plotted, and a linear correlation was fitted to the data. The MMP was predicted according to the fitted correlation. The results showed that when the injection pressure of associated gas was 18.45 MPa, the displacement efficiency at 1.2 PVs was able to be more than 90%, that is to say, 18.45 MPa could be regarded as the MMP, and when the pressure was higher, the characteristics of miscible flooding could appear (Table 3).

When the gas was injected at the formation pressure (12.3 MPa), the results of the back multiple-contact displacement experiment showed that the displacement process followed the mechanism of multiple-contact condensation gas displacement, and the injection of the associated gas at the original formation pressure is multiple-contact condensation near-miscible flooding. Figure 3.

When the pressure was increased to 16.9 MPa, the associated gas injection was able to achieve multiple-contact condensation miscible displacement. Figure 4.

TABLE 4 PVT data of injecting different volumes of the associated gas (96.8°C).

Gas injection rate, mol%	GOR, m3/m3	Expansion Coefficient	Bubble point Pressure, MPa	Surface oil density, g/cm^3	Saturated oil density, g/cm^3	Saturated oil viscosity, mPa·s
0	16.0	1.0000	2.5	0.8036	0.7216	8.8681
10	29.1	1.0350	4.0	0.8039	0.7069	6.2536
20	43.2	1.0800	5.6	0.8041	0.6898	4.1419
30	61.4	1.1370	7.3	0.8042	0.6695	2.6495
40	85.6	1.2150	9.2	0.8042	0.6449	1.5673
50	119.5	1.3260	11.2	0.8042	0.6146	0.8636
60	170.6	1.4950	13.4	0.8042	0.5761	0.4445

TABLE 5 Design for relative permeability experiments.

Type	No.	Porosity, %	Permeability, mD	Experiment Design
Matrix core	1	7.01	1.490	Gas/water flooding
	2	5.24	0.362	Gas/water flooding
	3	2.35	0.288	Gas/water flooding
Cores with Artificial Fractures	4	5.41	51.48	Gas/water flooding
	5	4.55	109.71	Gas/water flooding
	6	5.06	140.65	Gas/water flooding

TABLE 6 Statistics of characteristic values of oil/gas relative permeability curves of matrix cores and cores with artificial fractures.

Type	Core No.	Porosity %	Permeability, mD	Irreducible Water Saturation (S_{wi}) %	Residual Oil Saturation (S_{or}) %	S_o at which $k_{ro} = k_{rg}$	Two phage Flow Range (1- S_{gc}-S_{or}) %	Gas Flooding Efficiency %
Matrix Cores	1	7.01	1.490	33.18	30.93	56.70	35.89	53.71
	2	5.24	0.362	34.44	30.26	61.50	35.30	53.84
	3	2.35	0.288	34.35	27.31	54.40	38.34	58.40
	Total	4.87	0.713	33.99	29.50	57.53	36.51	55.32
Cores with Artificial Fractures	4	5.41	51.48	34.35	32.83	54.60	32.82	49.99
	5	4.55	109.71	32.4	24.32	61.50	43.28	64.02
	6	5.06	140.65	34.7	26.9	58.20	38.40	58.81
	Total	5.01	100.61	33.82	28.02	58.10	38.17	57.61

The expansion experiments of injecting associated gas were conducted at the formation temperature of 96.8°C in (Table 4). The results showed that gas injection had a good effect on increasing the dissolved gas volume in the crude oil and the expansion of the crude oil. The effects of different injected mediums and injected volumes were compared through experiments. It was proved that the associated gas had a good performance.

After the associated gas was injected into the reservoir oil, the saturation pressure of crude oil increased, and the greater the gas injection volume, the greater the saturation pressure, and the magnitude of the increase rose with the gas injection rate. Under the original formation pressure, the increased dissolved gas volume of associated gas injection was about 57% mol.

The expansion coefficients of crude oil and gas-oil ratios both increased with the gas injection rate because gas has certain solubility in crude oil and could expand the crude oil. For associated gas injection, the viscosity of crude oil at saturation pressure decreased significantly, and the viscosity of crude oil at saturation pressure decreased rapidly first and then slowly. However, the density of reservoir oil displayed first a slow and then a fast-decreasing trend.

The wax precipitation conditions were analyzed in the process of gas injection for the fractured basement reservoir. From the P-T phase diagram, the trajectory of the solid precipitation was close to a vertical line that decreased with pressure, and the solid phase precipitation temperatures of the oil were between 14 °C and 28 °C. What's more, the improved equation of state PR was used to calculate the wax precipitation for the composition distribution of the formation fluids in the NFR. The calculation pressure started with the formation pressure, and then the pressure was reduced successively, and the wax and other solids appearance temperature had little change, which was between 17 °C and 19°C, and the wax precipitation temperature was 18.6°C. Based on the P-T phase diagram and improved PR state equation, it is concluded that at the formation temperature (96.8°C) and pressure, the injection of associated gas into the reservoir will not cause wax solid precipitation in the formation. However, wax solid precipitation would occur in the wellbore, so it is needed to consider wax removal measures.

TABLE 7 Statistics of characteristic values of oil/water relative permeability curves of matrix cores and cores with artificial fractures.

Type	Core No.	Porosity %	Permeability, mD	Irreducible Water Saturation (S_{wi}) %	Residual Oil Saturation (S_{or}) %	S_w at which $k_{ro} = k_{rw}$	Two phage Flow Range (1- S_{wi}- S_{or}) %	Water Flooding Efficiency %
Matrix Cores	1	7.01	1.490	33.18	24.43	52.60	42.39	63.44
	2	5.24	0.36	34.08	29.35	48.30	36.57	55.48
	3	2.35	0.29	34.44	25.56	52.20	40.00	61.02
	Total	4.87	0.71	33.90	26.45	51.03	39.65	59.95
Cores with Artificial Fractures	4	5.41	51.48	34.35	32.75	52.20	32.90	50.11
	5	4.55	109.71	32.40	33.46	50.50	34.14	50.5
	6	5.06	140.65	34.70	28.95	52.20	36.35	55.66
	Total	5.01	100.61	33.82	31.72	51.63	34.46	52.09

TABLE 8 A summary of displacement efficiency for different injection methods.

Displacement method	Depletion drive (%)	Displacement at 7.7 MPa(%)	Displacement with shut-in (%)	Displacement efficiency (%)
Associated gas flooding	6.50	60.60	5.75	66.40
Water flooding	5.82	55.72	2.83	58.55

TABLE 9 Basic reservoir and fracture properties used for fractured reservoir simulations.

Parameter	Value
Model dimension (x×y×z)	1200 m × 1200 m × 90 m
Number of gridblocks (DX×DY×DZ)	100 × 100 × 10
Reservoir temperature	96.8 °C
Reservoir permeability	8 mD
Matrix porosity	6%
Rock compressibility	14.5×10^{-4} MPa^{-1}
Initial formation pressure	12.3 MPa
Reservoir mid-depth	1270 m
Reservoir GOR	15.9 m^3/m^3
K_v/K_H	0.10
Well radius	0.15 m
Fracture length	30–90 m
Dip angle	60°–85°
Fracture conductivity	30 mD·m

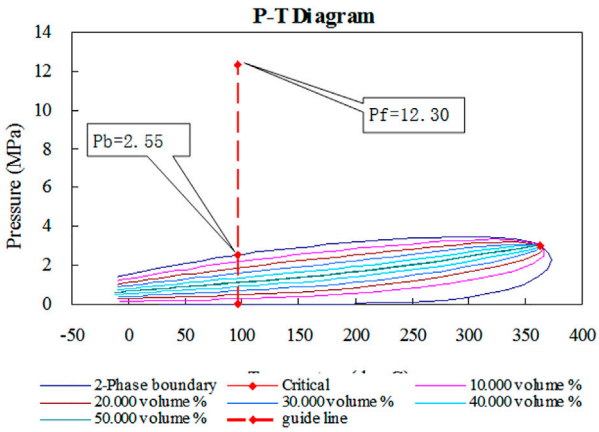

FIGURE 2
P-T Phase behavior of the flash experiment.

Relative permeability experiments

A standard testing workflow of the relative permeability of two-phase fluid (oil and gas) in rock is used to test the relative permeability curve of oil/gas in an unsteady status in gas flooding. The experimental process is that firstly the target rock sample is 100% saturated with water, then displaced water with oil to establish the irreducible water saturation, and in the following gas is used to drive oil to establish the residual oil saturation, the experimental data of oil/gas relative permeability and oil/gas relative permeability curve of each core in the process of gas flooding are determined and normalized.

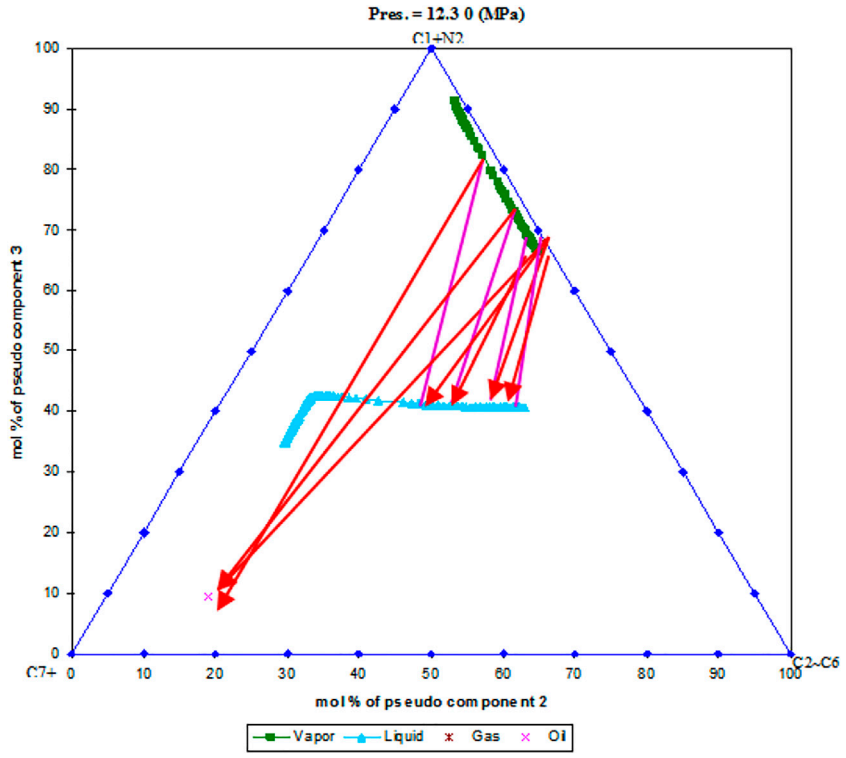

FIGURE 3
Triangle diagram of front multiple contact immiscible displacement of injecting associated gas (12.3 MPa).

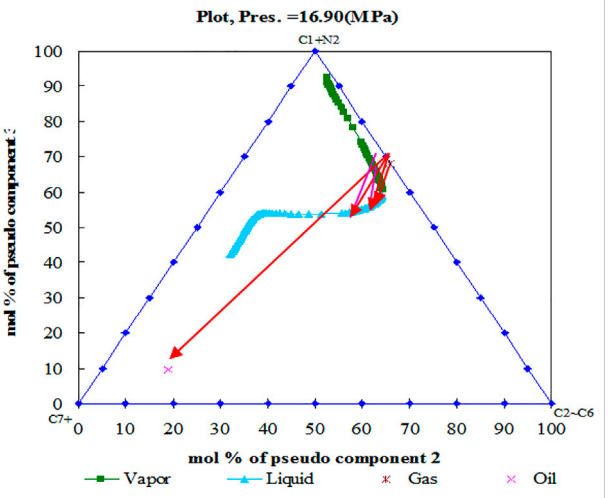

FIGURE 4
Triangle diagram of back multiple-contact immiscible displacement of injecting the associated gas (16.9 MPa).

The relative permeability experimental conditions in the process of gas flooding are: Temperature: 20 °C, Confining pressure: 15MPa, Displacement pressure: 12.3 MPa, Mineralization degree of saturated water: 1460 mg/L, Viscosity of injected gas/water: 0.021/1.03 mPa s, and the formulated oil for displacement with the viscosity of 3.85 mPa s.

In total, there are six relative permeability experiments for six cores divided into two groups, including three groups of gas/water flooding relative permeability experiments for matrix cores, and three groups of gas/water flooding relative permeability experiments for cores with artificial fractures (Table 5).

The relative permeability curve of oil/gas in the matrix core is as follows: the oil/gas flowing zone ranges from 35.3% to 38.34%, and the average two-phase flow range is about 36.51%. The average irreducible water saturation is about 33.99%, and the average residual oil saturation is about 29.5%. The irreducible water saturation at the intersection of the curve is about 57.53%, and the gas flooding efficiency of the rock is about 55.32%. The oil/gas relative permeability curve of cores with artificial fractures is as follows: the oil/gas flowing zone ranges from 32.82% to 43.28%, and the average two-phase flow range is about 38.17%, which is relatively wider. The average irreducible water saturation is about 33.82%, and the average residual oil saturation is about 28.02%. The irreducible water saturation at the intersection

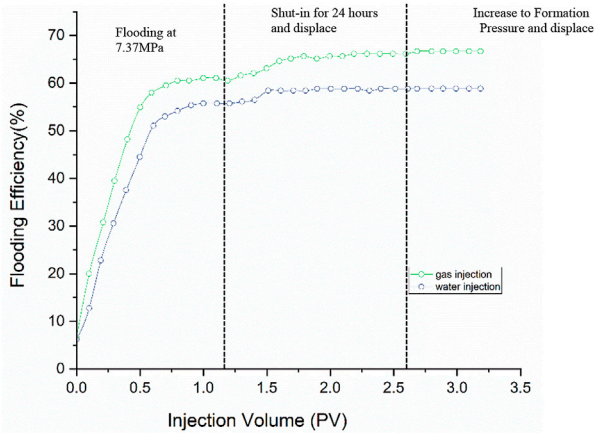

FIGURE 5
Injection PV vs oil flooding efficiency curve.

of the curve is about 58.1%, and the gas flooding efficiency of the rock is about 57.61% (Table 6).

Oil/water relative permeability curves of matrix and cores with artificial fractures are also tested. The characteristics are as follows: the irreducible water saturation of matrix core is higher (33.90%), and the residual oil saturation of matrix core is from 24.43% to 29.35% (26.45% on average), which is lower than that of cores with artificial fractures (31.72%). The range of two-phase (oil/water) flow of matrix core is 36.57%–42.39%, which is higher than 32.90%–36.35% of cores with artificial fractures. The oil recovery efficiency in the matrix core is 59.95% in water flooding, which is higher than that of the matrix core (52.09%) in gas flooding, because the water viscosity is higher than the gas viscosity. However, for the cores with artificial fractures, the efficiency of water flooding is about52.09%, which is lower than that of water flooding at 57.61% (Table 7).

Based on the above, oil/water relative permeability data and curves show that the water flooding efficiency of the matrix core is better than that of the fractured core. The main reason is that the injected water in the process of water flooding quickly broke through along the fractures, resulting in reduced swept area and eventually reduced oil recovery efficiency of cores with artificial fractures. What's more, the test results of the oil/gas relative permeability curve show that more gas can be diffused into more micro pores after cores with artificial fractures, and at the same time the surface tension between the oil and gas is reduced, resulting in a larger swept range, and the final oil recovery efficiency is higher.

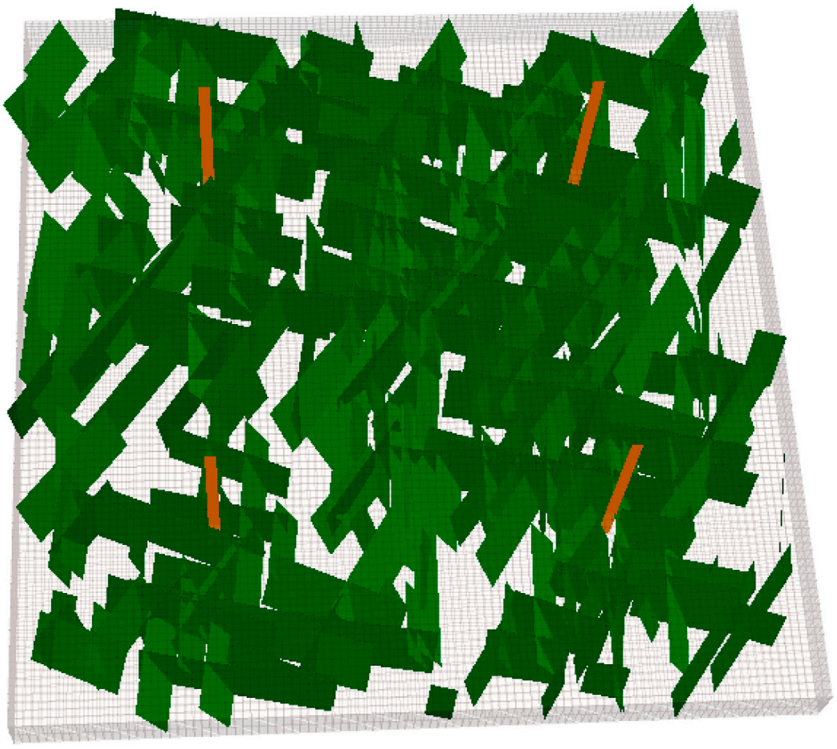

FIGURE 6
NFR simulation model with three sets of fractures.

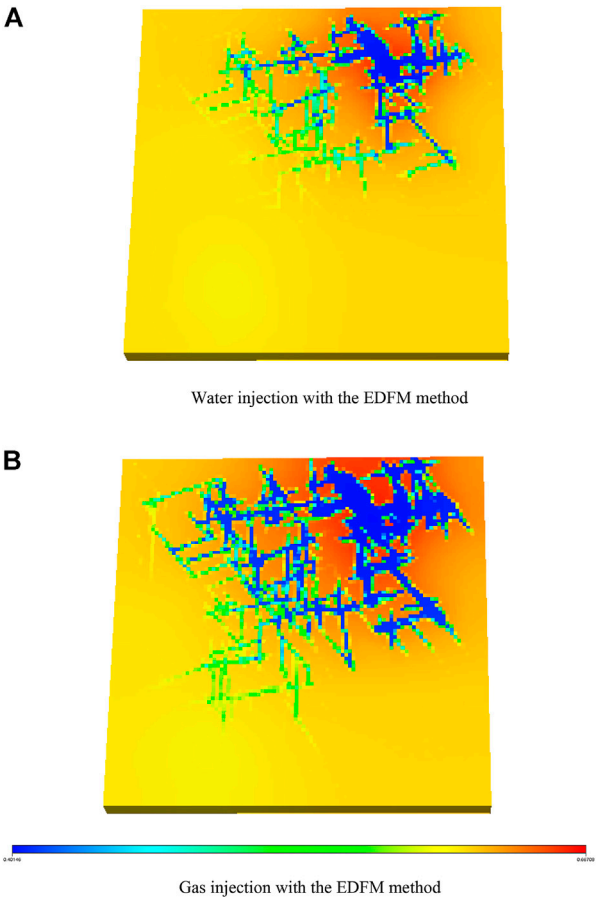

FIGURE 7
Comparison of oil saturation distribution map for water injection and gas injection **(A)** Water injection with the EDFM method **(B)** Gas injection with the EDFM method.

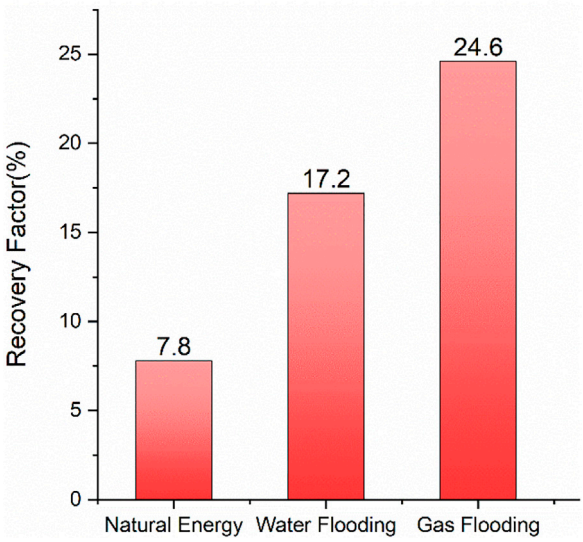

FIGURE 8
Comparison of oil recovery rate with different development mode.

Long core flooding tests

Through the long core displacement method, experimental research was carried out on the displacement efficiency, gas breakthrough, and regulations of gas displacement for the matrix and fractured cores by water/gas injection, and the influence was determined by gas flooding on displacement efficiency at the current reservoir pressure, which provided guidance and reference for the research on displacement mechanism and design of the future gas displacement development.

Water flooding and associated gas flooding were conducted, and it can be seen that (Table 8): 1) water flooding: When the system was produced at the experimental temperature of 96.8 °C from the original formation pressure of 12.3MPa–7.7 MPa by depletion drive, the recovery factor during the depletion process was 5.82%. Subsequently, water was injected until no more oil could be produced, and the displacement efficiency reached 55.72%. Under the current formation pressure, the system was displaced after 24 h of shut-in until no more oil was produced, and the displacement efficiency reached 58.43%. When the pressure was raised to the original formation pressure of 12.3 MPa, the system was displaced after 24-h of shut-in and the ultimate displacement efficiency was 58.55%. By comparing the results before and after shut-in, displacement efficiency was increased by 2.83%. The displacement efficiency with shut-in was improved to a limited extent, and the displacement efficiency with the high-pressure shut-in stage could be increased by 2%, which indicated that the diffusion dialysis ability of water was limited, and there was a little mass exchange with oil in the process of shut-in.

2) Associated gas flooding: With the same experimental process, the reserve recovery by depletion production in this experiment was 6.50%, and the displacement efficiency at the current formation pressure was 60.6%. Shut in for 24 h, the displacement efficiency at the current formation pressure was 65.8%. Shut in for 24 h, the ultimate displacement efficiency under the original formation pressure was 66.4%. Displacement efficiency was increased by 5.75% by shut-in. Figure 5.

Associated gas flooding has better displacement effects than water flooding, because the associated gas is lighter, which moves towards the upper part of the reservoir and causes gravity drainage and it is easy for the associated gas to dissolve in the oil, which would result in continuous mass transfer at the oil/gas contact, delay the breakthrough time and improve displacement efficiency. Shut-in can more intuitively

reflect the difference between gas and water injection because gas has much better diffusion ability while water has seepage ability. In the process of shut-in, the mass transfer between injected gas and oil is much larger, therefore shut-in well in the gas injection process has a much better effect and higher ultimate displacement efficiency.

Reservoir simulation using the EDFM method

To perform the associated gas injection performance of the fractured granite reservoir, a 3D reservoir model with complex natural fractures is built in a numerical-reservoir simulator. The dimensions of NFR are 4,000 ft × 4,000 ft×300 ft, and DX-DY-DZ is 100 × 100×10 in the matrix grid. Reservoir and fracture properties used in the simulation are summarized in Table 9. The relative permeability curve and other parameters are from the Relative Permeability Experiments above. Three sets of natural fractures are randomly generated with different orientations which are put into the NFR. Fracture orientations come from Borehole Imaging (BHI) logging, Set one is the major fracture (WNW-ESE), Set two is the secondary fracture (ENE-WSW), and Set three is the minor fracture (NS). The length of natural fractures ranges from 100 to 300 ft. Each set has about 100 fractures individually, which are randomly distributed in the fractured reservoir. The dip angle ranges from 60° to 80°. The fracture conductivity is 100 md ft from the well testing data.

A novel EDFM processor combining commercial reservoir simulators is fully integrated into the research. EDFM is a non-intrusive method, the calculations of the connection factors, including the NNC transmissibility factor and fracture well index, depend only on the gridding, reservoir permeability, and fracture geometries. Taking the reservoir and gridding parameters as inputs, the EDFM preprocessor provides information such as the number of extra grids, the equivalent properties of these grids, and the NNC pairs to help users make changes in the simulation input. Details of the calculations are discussed in many papers (Xu et al., 2019) Figure 6.

In this modeling method, firstly we have the EDFM model built (shown in Figure 6). EDFM is more accurate for fractured reservoir simulation, since it considers more about the big fractures' impact on fluid flow. All the three sets of fractures (WNW-ESE, ENE-WSW and NS) are used in the simulation model. Considering the fractured reservoir characteristics, four vertical wells are located in the dense fracture area, and producers are completed as open-hole about 180 feet as shown in Figure 6. The simulation time is about 20 years.

Use numerical simulation with EDFM methods to optimize and compare the following two development methods: 1) Natural energy development: three new wells and use natural energy for oil production; 2) Gas injection: Make full use of the difference between oil and gas gravity to inject gas into the reservoir to quickly supplement formation energy and improve the ratio of the total oil produced to OOIP under the condition of overall production from matrix and fracture system.

When the NFR is developed by natural energy, the recovery factor of depletion is about 7.8% after 20 years. In Figure 7, the production performance of water injection and gas injection is observed. Water flooding has a smaller flooding area, and gas flooding has a larger flooding area. Compared with the above two schemes, the recovery factor of water flooding is lower, about 17.2%. The numerical simulation predicts that the recovery factor of associated gas injection is 24.6%, shown in Figure 8. It is seen that associated gas can enter smaller microscopic fractures and pores, increasing the gas sweeping volume, and enhancing the oil recovery. Therefore, the development mode of gas injection is recommended.

Conclusion

1) Associated gas flooding has better displacement performance. Associated gas development has a higher recovery ratio than N_2 because the associated gas is lighter, which moves towards the upper part of the reservoir and causes gravity drainage and because it is easy for the associated gas to dissolve in the oil, which would result in continuous mass transfer at the oil/gas contact, delay the breakthrough time and improve displacement efficiency.
2) The tests of the oil/gas relative permeability curve show that more gas can be diffused into more micro pores after cores with artificial fractures, resulting in a larger swept range, and the final oil recovery efficiency is higher.
3) Compared with natural energy development and associated gas injection, the recovery factor of associated gas flooding is 24.6%, about 16.8% higher than that of depletion development. So the development mode of associated gas injection is recommended in the fractured granite reservoir.

Data availability statement

The original contributions presented in the study are included in the article/supplementary material further inquiries can be directed to the corresponding author.

Author contributions

FX, NZ, and JQ contributed to conception and design of the study. FX organized the database. XL performed the statistical analysis. FX wrote the first draft of the manuscript. JZ, SL, JH, and DL wrote sections of the manuscript. All contributed to

manuscript revision, read, and approved the submitted authors version.

Acknowledgments

The authors would like to acknowledge support from China National Oil and Gas Exploration and Development Company Ltd.

Conflict of interest

Authors FX, NZ, JO, and JZ were employed by the China National Oil and Gas Exploration and Development Company Ltd. (CNODC); Author XL was employed by the Research Institute of Petroleum Exploration and Development Co Ltd (RIPED) CNPC; Authors SL, JH, and DL were employed by the Research Institute of Exploration and Development, Petrochina Yumen Oilfield Company.

The remaining authors declare that the research was conducted in the absence of any commercial or financial relationships that could be construed as a potential conflict of interest.

Publisher's note

All claims expressed in this article are solely those of the authors and do not necessarily represent those of their affiliated organizations, or those of the publisher, the editors and the reviewers. Any product that may be evaluated in this article, or claim that may be made by its manufacturer, is not guaranteed or endorsed by the publisher.

References

Cavalcante Filho, J. S. D. A., Xu, Y., and Sepehrnoori, K. "Modeling fishbones using the embedded discrete fracture model formulation: Sensitivity analysis and history matching," in Proceedings of the Paper SPE 175124 presented at the SPE Annual Technical Conference and Exhibition, Houston, Texas, September 2015, 28–30.

Cinco, L. H., Samaniego, V. F., and Dominguez, A. N. (1978). Transient pressure behavior for a well with a finite-conductivity vertical fracture. *Soc. Petroleum Eng. J.* 18 (04), 253–264. doi:10.2118/6014-pa

Dang, C. T. Q., Chen, Z. J., Nguyen, N. T. B., Bae, W., and Phung, T. H. (2011). Lessons learned and experiences gained in developing the waterflooding concept of a fractured basement-granite reservoir: A 20-year Case study. *J. Can. Petroleum Technol.* 50 (09), 10–23. doi:10.2118/137561-pa

Delamaide, E., Batôt, G., Alshaqsi, A., Alkindy, A., and Al-Mejni, R. "Enhanced oil recovery in naturally fractured reservoirs: State of the art and future perspectives," in Proceedings of the Paper SPE 200076 presented at the SPE Conference at Oman Petroleum & Energy Show, Muscat, Oman, March 2022, 21–23.

Dipak, S. R., Adnan, A., Naveen, K., Saad, M., Laurent, G., De Joussineau, G., et al. (2012). Characterizing and modeling natural fracture networks in a tight carbonate reservoir in the Middle East: A methodology. *Bull. Geol. Soc. Malays.* 58 (3), 29–35. doi:10.7186/bgsm58201205

Hajibeygi, H., Karvounis, D., and Jenny, P. (2011). A hierarchical fracture model for the iterative multiscale finite volume method. *J. Comput. Phys.* 230 (24), 8729–8743. doi:10.1016/j.jcp.2011.08.021

Hoteit, H., and Firoozabadi, A. (2005). Multicomponent fluid flow by discontinuous Galerkin and mixed methods in unfractured and fractured media. *Water Resour. Res.* 41 (11), 1–15. doi:10.1029/2005wr004339

Karimi-Fard, M., and Firoozabadi, A. (2003). Numerical simulation of water injection in fractured media using the discrete-fracture model and the galerkin method. *SPE Reserv. Eval. Eng.* 6 (02), 117–126. doi:10.2118/83633-pa

Lee, S. H., Lough, M. F., and Jensen, C. L. (2001). Hierarchical modeling of flow in naturally fractured formations with multiple length scales. *Water Resour. Res.* 37 (3), 443–455. doi:10.1029/2000wr900340

Li, L., and Lee, S. H. (2008). Efficient field-scale simulation of black oil in a naturally fractured reservoir through discrete fracture networks and homogenized media. *SPE Reserv. Eval. Eng.* 11 (04), 750–758. doi:10.2118/103901-pa

Lonergan, L., Jolly, R. J. H., Rawnsley, K., and Sanderson, D. J. (2007). *Fractured reservoirs*. London, UK: Geological Society.

Long, J. C. S., Remer, J. S., Wilson, C. R., and Witherspoon, P. A. (1982). Porous media equivalents for networks of discontinuous fractures. *Water Resour. Res.* 18 (3), 645–658. doi:10.1029/wr018i003p00645

Long, J. C. S., and Witherspoon, P. A. (1985). The relationship of the degree of interconnection to permeability in fracture networks. *J. Geophys. Res.* 90 (B4), 3087. doi:10.1029/jb090ib04p03087

Ma, J., Yang, Y., Wang, H., Li, L., Wang, Z., and Li, D. (2018). How much CO2 is stored and verified through CCS/CCUS in China? *Energy Procedia* 154 (2018), 60–65. doi:10.1016/j.egypro.2018.11.011

Moinfar, A., Varavei, A., Sepehrnoori, K., and Johns, R. T. (2013). Development of an efficient embedded discrete fracture model for 3D compositional reservoir simulation in fractured reservoirs. *SPE J.* 19 (02), 289–303. doi:10.2118/154246-pa

Narr, W., Schechter, D. S., and Thompson, L. B. (2006). *Naturally fractured reservoir characterization*. Richardson, Texas: Society of Petroleum Engineers.

Nelson, R. A. (2001). *Geologic analysis of naturally fractured reservoirs*. Houston, Texas: Gulf Professional Publishing.

Nguyen, T. V., and Tran, X. V. (2016). Gas-assisted gravity drainage process for improved oil recovery in Bao Den fractured basement reservoir. *Sci. Tech. Dev. J.* 19 (1), 161–168. doi:10.32508/stdj.v19i1.514

Peng, Y., Zhao, J., Sepehrnoori, K., and Li, Z. (2020). Fractional model for simulating the viscoelastic behavior of artificial fracture in shale gas. *Eng. Fract. Mech.* 228, 106892. doi:10.1016/j.engfracmech.2020.106892

Schechter, D. (2002). Waterflooding and CO2 injection in the naturally fractured spraberry trend area. *J. Can. Petroleum Technol.* 41 (10), 10–15. doi:10.2118/02-10-das

Song, Z.-J., Li, M., Zhao, C., Yang, Y.-L., and Hou, J.-R. (2020). Gas injection for enhanced oil recovery in two-dimensional geology-based physical model of tahe fractured-vuggy carbonate reservoirs: Karst fault system. *Pet. Sci.* 17 (2), 419–433. doi:10.1007/s12182-020-00427-z

Vardon, D. R., Sherbacow, B. J., Guan, K., Heyne, J. S., and Abdullah, Z. (2022). Realizing 'net-zero-carbon' sustainable aviation fuel. *Joule* 6 (1), 16–21. doi:10.1016/j.joule.2021.12.013

Warren, J. E., and Root, P. J. (1963). The behavior of naturally fractured reservoirs. *Soc. Petroleum Eng. J.* 3 (03), 245–255. doi:10.2118/426-pa

Xu, F., Li, X., Gong, Y., Lei, C., Li, X., Yu, W., and Ding, Y. (2019). "A powerful and practical workflow for a naturally fractured reservoir with complex fracture geometries from modeling to simulation," in Proceedings of the SPE Paper URTEC-2019-1043-MS presented at the SPE/AAPG/SEG Unconventional Resources Technology Conference, Denver, Colorado, USA, July 2019, 22–24.

Xu F, F., Yu, W., Li, X., Miao, J., Zhao, G., Sepehrnoori, K., and Wen, G. (2018), "A fast EDFM method for production simulation of complex fractures in naturally fractured reservoirs," in Proceedings of the SPE Paper SPE-191800-18ERM-MS presented at the SPE/AAPG Eastern Regional Meeting, Pittsburgh, PA, USA, October 2018, 7–11.

Xu, Y., Cavalcante Filho, J. S. A., Yu, W., and Sepehrnoori, K. (2017). Discrete-fracture modeling of complex hydraulic-fracture geometries in reservoir simulators. *SPE Reserv. Eval. Eng.* 20 (02), 403–422. doi:10.2118/183647-pa

Zhou, W., Banerjee, R., Poe, B. D., Spath, J., and Thambynayagam, M. (2013). Semianalytical production simulation of complex hydraulic-fracture networks. *Soc. Petroleum Eng. J.* 19 (01), 06–18. doi:10.2118/157367-pa

frontiers | Frontiers in Energy Research

TYPE Original Research
PUBLISHED 24 January 2023
DOI 10.3389/fenrg.2022.1002053

OPEN ACCESS

EDITED BY
Yibo Li,
Southwest Petroleum University, China

REVIEWED BY
Guodong Zhang,
Qingdao University of Science and Technology, China
Weirong Li,
Xi'an Shiyou University, China
Jianguang Wei,
Northeast Petroleum University, China

*CORRESPONDENCE
Hongda Hao,
haohongda90@126.com
Jirui Hou,
houjirui@126.com

SPECIALTY SECTION
This article was submitted to Advanced Clean Fuel Technologies, a section of the journal Frontiers in Energy Research

RECEIVED 24 July 2022
ACCEPTED 01 December 2022
PUBLISHED 24 January 2023

CITATION
Hao H, Hou J, Qu M, Guo W, Deng S and Liu H (2023), Using a well-to-well interplay during the CO_2 huff-n-puff process for enhanced oil recovery in an inclined oil reservoir: Experiments, simulations, and pilot tests.
Front. Energy Res. 10:1002053.
doi: 10.3389/fenrg.2022.1002053

Using a well-to-well interplay during the CO_2 huff-n-puff process for enhanced oil recovery in an inclined oil reservoir: Experiments, simulations, and pilot tests

Hongda Hao[1]*, Jirui Hou[2]*, Ming Qu[1,2], Wenmin Guo[1], Song Deng[1] and Huaizhu Liu[3]

[1]School of Petroleum and Natural Gas Engineering, School of Energy, Changzhou University, Changzhou, China, [2]Research Institute of Unconventional Oil and Gas Science and Technology, China University of Petroleum, Beijing, China, [3]Research Institute of Drilling and Production Technology, PetroChina Jidong Oilfield Company, Tangshan, China

A well-to-well interplay of CO_2 huff-n-puff is proposed as a novel gas injection strategy for displacing interwell-remaining oil in a well pair in an inclined oil reservoir. The well-to-well interplay mechanisms for enhanced oil recovery (EOR) are first studied in the laboratory using a three-dimensional (3D) physical model. Different CO_2 injection schemes are designed according to different well locations, and the production performance including oil, water, and gas rates is used for the EOR evaluation. A sensitivity analysis of the well-to-well interplay is then studied using a numerical model, and geological, developmental and fluidic factors are considered in the simulations. The experimental results show that, when CO_2 is injected into a lower well, a higher well always benefits with an oil increment. Under the effects of gravity segregation and edge-water driving, the injected CO_2 at the lower position can move upward to a higher position, where a large proportion of crude oil remains between wells after natural edge-water flooding. Oil recovery from the well-to-well interplay is 2.30% higher than conventional CO_2 huff-n-puff in the laboratory. Numerical results show that CO_2 injection mass, stratigraphic dip, horizontal permeability, and interwell spacing are the factors that most influence the well-to-well interplay; an application criterion for the well-to-well interplay is then proposed based on the simulations. Pilot tests using the well-to-well interplay of CO_2 huff-n-puff have been widely applied in C2-1 Block, Jidong Oilfield, China, since 2010. A total of 2.27×10^4 m^3 crude oil was recovered to the end of 2018, and the oil/CO_2 exchange ratio was as high as 3.92. The well-to-well interplay not only effectively extracted the interwell-remaining oil but also achieved higher CO_2 utilization efficiency. The findings of this study can lead to a better understanding of the EOR mechanisms used in the well-to-well interplay during the CO_2 huff-n-puff process in an inclined oil reservoir.

KEYWORDS

CO_2 huff-n-puff, well-to-well interplay, enhanced oil recovery, inclined reservoir, interwell remaining oil

1 Introduction

Given the continuous consumption of conventional reservoir reserves, unconventional resources have been of wide interest in recent years. Heavy oil reservoirs as one unconventional resource face challenges in oil production due to low oil mobility within the porous media (Babadagli, 2003; Huang et al., 2019; Shilov et al., 2019). Thermal methods, including steam injection and *in situ* combustion, are the most widely used techniques for enhanced heavy oil recovery; however, their applications are limited in thin or deep layers because of massive heat loss and the high investment necessary (Wang et al., 2018; Alajmi, 2021). Solvent-based non-thermal methods, including cyclic solvent injection and vapor extraction, are proving suitable for enhanced oil recovery (EOR) in these kinds of reservoirs (Jiang et al., 2014; Ma et al., 2017). Among such methods, the CO_2 huff-n-puff process is considered a promising technique for these complicated oil reserves (Ahadi & Torabi, 2018; Zhou et al., 2019). When CO_2 is injected into heavy oil reservoirs, the main EOR mechanisms include viscosity reduction, oil swelling, IFT reduction, and light/medium components extraction, greatly enhancing heavy oil production during the CO_2 huff-n-puff process (Kavousi et al., 2014; Cui et al., 2017; Li et al., 2018; Kashkooli et al., 2022; Zhou et al., 2022).

C2-1 Block in the Jidong Oilfield, China, is a heavy oil reservoir with a viscosity of 289 mPa·s under formation conditions (60, 16.24 MPa); it is an inclined reservoir with a stratigraphic dip of 15° (Figure 1). The block was initially developed by natural edge-water flooding from 2003, obtaining oil recovery of 4.79% by the end of 2010. During this operation, several wells faced severe water channeling problems, with water-cut values as high as 99%, and little oil was recovered. Several CO_2 huff-n-puff processes were conducted to enhance this oil recovery between 2008 and 2010. After CO_2 was injected into a single well, the oil production rate was enhanced from less than 2 t/d to more than 10 t/d, and the water cut also dropped to as low as 20–30%. Although the oil increases were obtained with a CO_2 injection, they sharply dropped to small values for the second cycle of CO_2 huff-n-puff—as observed by Ma et al. (2015). Furthermore, since CO_2 huff-n-puff is just a stimulation method for single wells with a limited range (Li et al., 2017), it can only extract the oil near the wellbore area: a quantity of crude oil still remained between the wells after CO_2 huff-n-puff in the C2-1 Block. Although a variety of chemicals including viscosity reducer, foaming agent, and gel have been proposed to further enhance CO_2 huff-n-puff oil recovery (Hao et al., 2021; Hao et al., 2022; Qu et al., 2022), they are still single-well stimulation methods, and novel techniques or gas injection strategies need to be studied to extract interwell-remaining oil during the CO_2 huff-n-puff process.

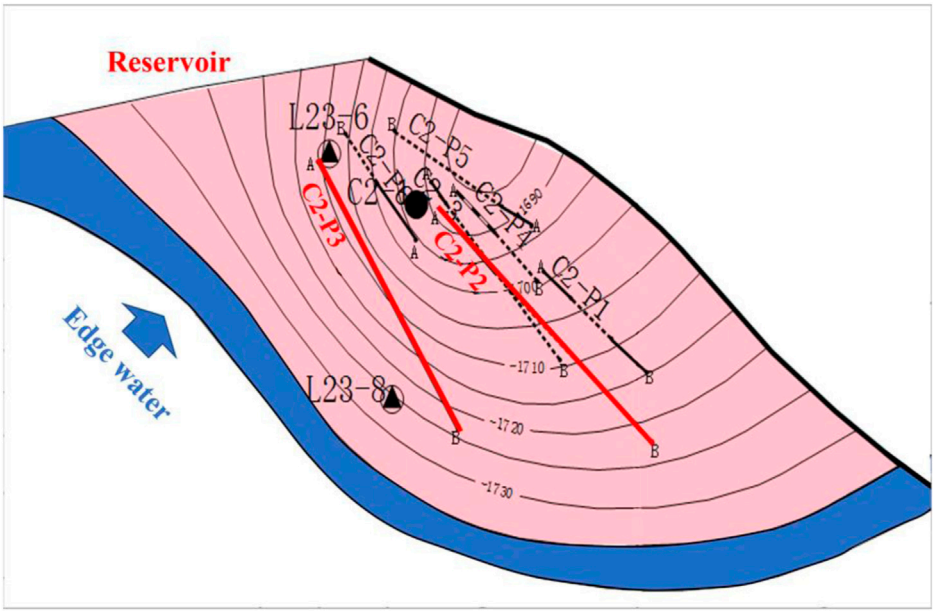

FIGURE 1
Top structure map of C2-1 Block, Jidong Oilfield, China.

When gas and water are injected into a formation, the gas will move to the top of the reservoir while the water will move to the bottom due to gravity—this is called "gravity segregation". In a horizontal reservoir, gravity segregation is usually a negative factor since the injected gas and water will override the oil (Fayers & Zhou, 1996). For example, the water-alternating-gas (WAG) technique is considered the most useful for EOR when CO_2 is mixed with oil; however, the gas–oil mixture will be separated by gravity as the mixture moves further away from the injector. As a result, the WAG process provides an unsatisfactory sweep efficiency with gravity segregation, leading to an early gas breakthrough in the producer (Afzali et al., 2018; Khan & Mandal, 2020). The gas-assisted gravity drainage (GAGD) technique has recently been proposed as an effective EOR method because it takes full advantage of gravity segregation, and a higher formation dip is favorable for its EOR (Chen et al., 2021). During a GAGD process, the oil is usually driven by CO_2 down-dip from the pores toward the wells. With a properly designed gas injection strategy, the gas breakthrough can be significantly delayed, with recovery of more than 30% in the laboratory (Rezk et al., 2019; Al-Obaidi et al., 2022).

Although, GAGD could achieve remarkable oil recovery in the inclined oil reservoirs, most GAGD processes are operated in a model without edge water. In the presence of an active aquifer, conditions could be completely different because the water coning could severely affect EOR. The treatment of edge water should be considered a primary task when applying an EOR method to this kind of reservoir. CO_2 has proven to be an effective method for water treatment (Wang et al., 2021; Tian et al., 2022); when it is injected into a lower location in an inclined oil reservoir, it will first delay the edge-water coning. Then, the CO_2 will move upward with the assistance of edge-water driving and gravity segregation, where the oil remaining between a well pair is just right at the higher position. As a result, a well-to-well interplay will occur with the interwell-remaining oil produced from the higher position. Gravity segregation is typically affected by developmental, geological, and fluidic factors. For example, Stone (1982) observed that the injection rate, vertical permeability, and density difference between water and gas are the main parameters that affect gravity segregation. The study conducted by Rogers & Grigg (2001) revealed that the increase in the vertical-to-horizontal permeability ratio (K_v/K_h) will reduce oil recovery during the WAG process, due to the dominant effect of gravity segregation. Al-Mudhafar et al. (2018) believe that reservoir heterogeneity is the most crucial factor that strongly affects hydrocarbon recovery during GAGD. Thus, as a CO_2–EOR method governed by gravity segregation, the influencing factors of well-to-well interplay during the CO_2 huff-n-puff process proposed in this paper should also be studied to achieve a better CO_2–EOR effect.

In order to study the mechanisms of interwell-remaining oil displacement using a well-to-well interplay of CO_2 huff-n-puff in an inclined oil reservoir, a well pair was established in a three dimensional (3D) inclined physical model. CO_2 was injected into the model through the lower well only, the higher well only, and the lower and higher wells simultaneously. The production performances, including oil, water, and gas rates, were used to evaluate the interplay mechanisms between the wells. A sensitivity analysis of the well-to-well interplay was then studied using a base reservoir model, and geological, developmental, and fluidic factors including CO_2 injection mass, interwell spacing, stratigraphic dip, horizontal and vertical permeability, and oil viscosity were considered in the simulations. EOR tests using the well-to-well interplay of CO_2 huff-n-puff were conducted in the pilot, and the oil recovered by the well-to-well interplay is also introduced in this paper.

2 Materials and methods

Theoretical analysis, physical experiments, numerical simulation, and field tests were utilized to study the EOR mechanisms, influencing factors, and its application to the well-to-well interplay of CO_2 huff-n-puff; the technical route of this study is shown in Figure 2.

2.1 Scaling groups for physical and numerical models

The inclined oil reservoir of C2-1 Block is in a geological reserve of 4.51×10^5 m^3. The average porosity and permeability of the reservoir is 25.9%, 667×10^{-3} μm^2, respectively, the depth of water/oil contact (WOC) is 1735 m, and the aquifer size is 100 times that of the oil reservoir. Since the purpose of this paper is mainly to discover the well-to-well interplay mechanisms and its influencing factors, the actual oil reservoir was simplified to an equivalent model with an effective radius of 316.23 m and an effective thickness of 26.8 m; Wells C2-P3 and C2-P2 were selected to form a typical well pair. The basic parameters of the equivalent model were the same as the actual oil reservoir (Table 1).

Scaling groups of the geometrical parameters derived by Shook et al. (1992) were then used to establish the 3D physical and numerical models, which were proven to be an effective method for CO_2–EOR by Li et al. (2015) and Zhao et al. (2018). An aspect ratio of the model (R_{model}) was used to ensure the similarity of the model; aspect ratios of well-length and spacing (R_{well} and $R_{spacing}$) and an aspect ratio of WOC (R_{WOC}) were used to ensure the similarity of the well pair. The permeability ratio (K_{mn}) was used to simulate a heterogeneity similar to the reservoir. Since the basic parameters of the equivalent model are given, the dimensionless group values were calculated (Table 2). Thence, the unknown parameters of the physical and numerical models were determined with the dimensionless values, with the final results listed in Table 1.

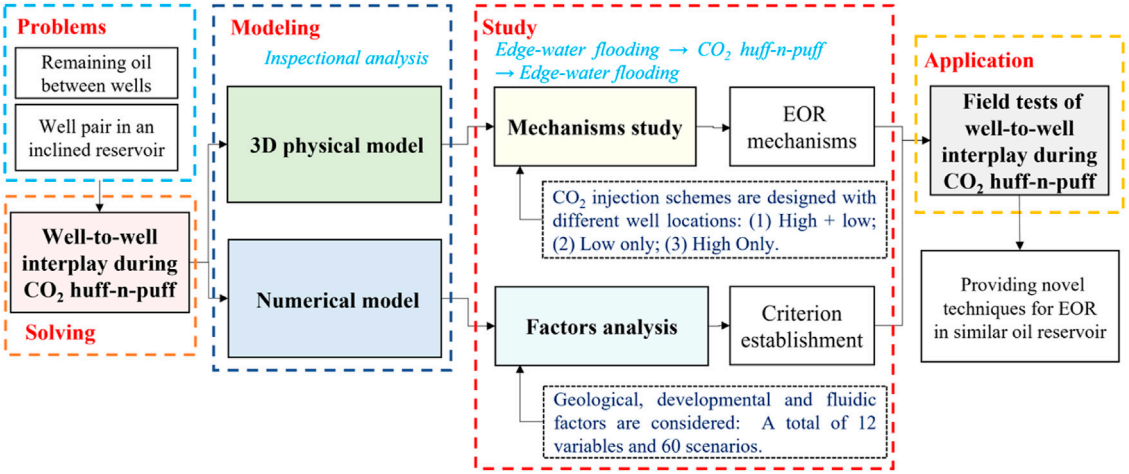

FIGURE 2
Technical route and major steps used in the study of well-to-well interplay of CO_2 huff-n-puff.

TABLE 1 Basic parameters for the equivalent reservoir, physical model, and numerical model.

Basic parameter	Equivalent model	3D physical model	Numerical model
Equivalent model radius (L)/m	316.23	0.400	316.23
Effective model height (H)/m	26.8	0.053	26.8
Stratigraphic dip (α)/°	15	15	15
Well length (L_{well})/m	102.72	0.130	100
Well spacing ($L_{spacing}$)/m	50	0.060	50
Distance between the lower well and WOC (L_{WOC})/m	96.60	0.17	100
Average horizontal permeability (K_h)/×10^{-3}μm^2	667	750	667
Average vertical permeability (K_v)/×10^{-3}μm^2	271.27	750	271.27
Highest permeability (K_{max})/×10^{-3}μm^2	1258.03	1200	1258.03
Lowest permeability (K_{min})/×10^{-3}μm^2	313.18	300	313.18
Average porosity/%	0.259	0.30	0.259

TABLE 2 Dimensionless group values calculated from the equivalent reservoir.

Dimensionless scaling group	
Aspect ratio of the model $R_{model} = (L/H)\sqrt{K_v/K_h}$	7.5246
Aspect ratio of the well length $R_{well} = (L_{well}/L)$	0.3248
Aspect ratio of the well spacing $R_{spacing} = (L_{spacing}/L)$	0.1581
Aspect ratio of WOC $R_{woc} = (L_{woc}/L)$	0.3055
Permeability ratio $K_{mn} = (K_{max}/K_{min})$	4.0170

According to the calculations, the 3D physical model used for well-to-well interplay during the CO_2 huff-n-puff process had a diameter of 400 mm, a thickness of 53 mm, and a stratigraphic dip of 15° (Figure 3A). The horizontal well pair including P1H and P2H was established in the middle of the core. The lengths of P1H and P2H were both 130 mm, the spacing between P1H and P2H is 65 mm, and the distance between P1H and WOC was 120 mm (Figure 3B). The model was a heterogeneous core with an average permeability of 750 × 10^{-3} μm^2, upper layer permeability of 300 × 10^{-3} μm^2, and bottom layer permeability of 1200 × 10^{-3} μm^2. In order to achieve the different

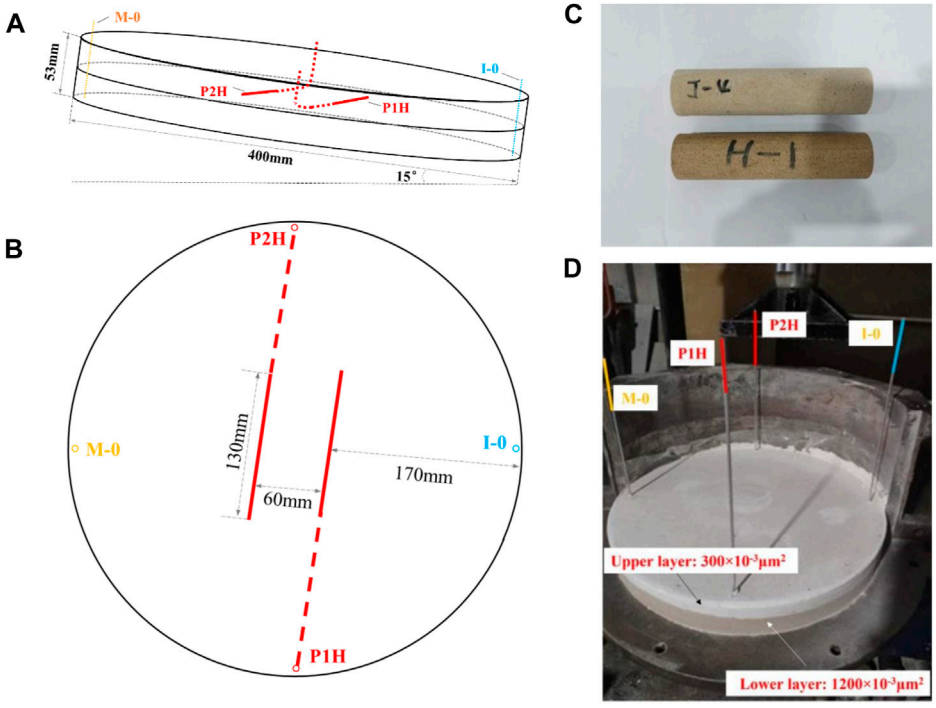

FIGURE 3
3D physical model used for the well-to-well interplay of CO2 huff-n-puff. **(A)** Side view and **(B)** top view of the designed model. **(C)** Picture of the 1D core. **(D)** Picture of the 3D core.

TABLE 3 Sand formula used to fabricate different permeabilities for 3D cores (measured from 1D cores).

Mesh range of sand	Core 1	Core 2
	Proportion/wt%	Proportion/wt%
40–80	28.9	6.2
80–100	66.4	62.3
100–150	3.7	24.9
200–300	1.0	6.6
Measured permeability/$\times10^{-3}\mu m^2$	300	1200

permeabilities of the upper and lower layers, 1D homogenous cores were first fabricated with different mesh ranges of sand in the laboratory Figure 3C). The proportions of different sands were determined after the permeability tests of 1D cores, with the results listed in Table 3. The sand formulas were then used to fabricate the 3D physical model (Figure 3D).

The numerical model was designed to be 500 m × 200 m × 30 m using a CMG-GEM simulator, and the value of the net gross ratio (NTG) was set at 0.9. With the same effective thickness of 26.8 m, the effective radius (L) was equal to 316.23 m in a circular equivalent model (Table 1). A Cartesian grid was used in the modeling—51 grids with a length of 9.8039 m were set in the x direction, 41 grids with a length of 4.8780 m were set in the y direction, and 15 grids with a length of 2 m were set in the z direction. The reservoir dip was set at 15°, and the depth of WOC was 1735 m. The sand body was normal rhythmic with an average permeability of 667 × 10^{-3} μm^2 and an average porosity of 25.9%. The initial oil saturation was set as 0.65, and the geological reserve was calculated to be same as the reserve in the real reservoir. An edge-water aquifer was connected to the bottom of the reservoir, which was 100-times the model size. P1H and P2H with the same horizontal length of 100 m were set as the lower and the higher wells, respectively. The spacing between P1H and P2H was set at 50 m, and the distance between P1H and

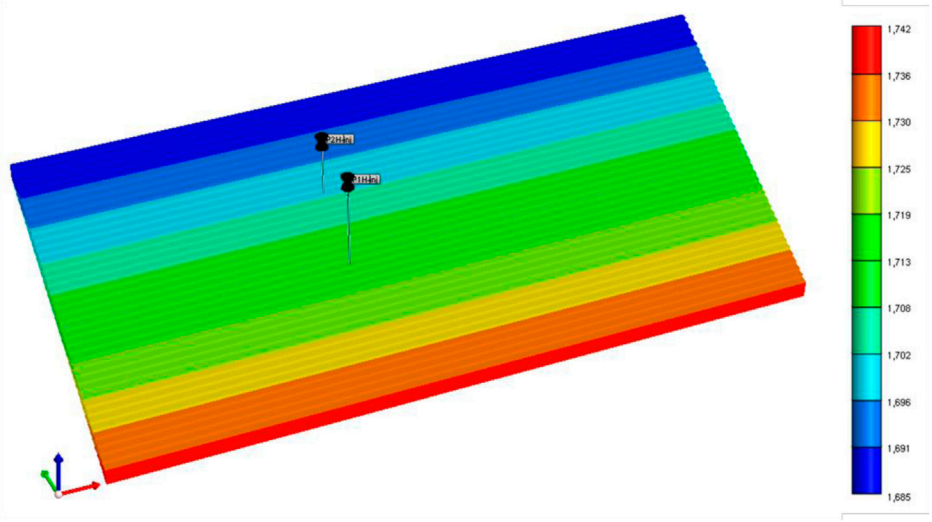

FIGURE 4
Numerical model used for the well-to-well interplay during CO2 huff-n-puff (grid top).

TABLE 4 Basic parameters of 3D physical models.

Scenario	Experimental scheme	Apparent volume/mL	Pore volume/mL	Porosity/ %	Permeability/ $\times10^{-3}\mu m^2$	Initial oil saturation/%
1	P1H_Lower Well 50 ml(RC) CO_2 + P2H_Higher Well 50 ml(RC) CO_2	6656.8	1755.2	26.37	300/1200	63.26
2	P1H_Lower Well 100 ml(RC) CO_2	6644.2	1700.9	25.60		66.32
3	P2H_Lower Well 100 ml(RC) CO_2	6669.4	1726.0	25.88		64.30

WOC was set at 100 m. The grid top of the numerical model is shown in Figure 4.

2.2 3D physical experiments for well-to-well interplay of CO_2 huff-n-puff

The oil and water samples used for the 3D physical experiments were collected from the block. The density of the formation oil was 0.97×10^3 kg/m^3, the viscosity was 289 mPa·s, and the gas/oil ratio was 18.9 m^3/m^3 under formation conditions (60°C, 16.24 MPa). The salinity of the formation water was 2.83×10^3 mg/L, and the injected CO_2 with a purity of 99.99 mol% was from Beijing, China. The basic parameters of the 3D physical models are listed in Table 4. The experimental setup consisted of six sub-systems: an injection system, an edge-water system, a displacement system, a production system, a temperature control system, and a data-acquisition system. In the injection system, the formation water, formation oil, and CO_2 were stored in cylinders and then injected into the model by a pump. In the edge-water system, formation water was stored in the cylinder and then injected into the model through Well I-0 (Figure 3). The 3D physical model was placed in the coreholder with a dip of 15°. In the production system, backpressure regulars (BPRs) were connected to the horizontal wells to control the production pressure. The produced oil and water were recorded by test tubes, while the gas was measured by using a gas flow meter. The thermostat was used to maintain the reservoir temperature, and the pressure monitored by M-0 was obtained by the data-acquisition system.

Several 3D experiments were designed in the laboratory to study the well-to-well interplay mechanisms of CO_2 huff-n-puff. The models were first displaced by the edge water and then by the CO_2 huff-n-puff process. Different injection schemes were designed with different injection wells and CO_2 volume allocations (Table 4). The bulk volume of the core was first measured before the 3D experiment. The core was then evacuated and saturated with formation water. The porosity was determined as the ratio of water saturation volume to bulk volume. The core was then displaced by formation oil to reach an initial oil saturation—calculated as the ratio of produced oil volume to the pore volume.

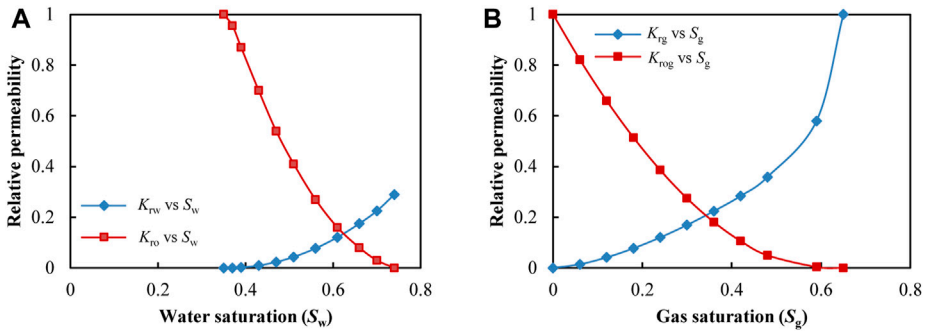

FIGURE 5
Relative permeability used for the numerical simulation. **(A)** Oil–water relative permeability. **(B)** Oil–gas relative permeability.

Edge-water driving was conducted first in the model according to these detailed procedures: 1) The formation temperature was set to 60°C, and the production pressures of the horizontal wells (P1H and P2H) were set to 16.40 MPa using BPRs. 2) Water was then injected through I-0 under a constant rate of 0.4 Ml/min to simulate the natural edge-water driving. 3) P1H and P2H were opened for production and then shut in simultaneously when the composite water cut of the well pair reached 98%.

CO_2 huff-n-puff was then conducted after edge-water driving. In Scenario 1, CO_2 was injected into the model through both the lower well P1H and the higher well P2H. The detailed procedures were 1) 50 Ml (reservoir conditions, RC) CO_2 and 50 Ml (RC) CO_2 were injected through P1H and P2H, individually, and then, these wells were shut in. 2) After a soaking time of 12 h, P1H and P2H were re-opened again for production. Simultaneously, the edge water was re-injected into the model through I-0. 3) The experiment was terminated when the composite water cut again reached 98%. The pressure, oil production, water production, and gas production were measured, and the oil recovery enhanced by CO_2 huff-n-puff was then calculated.

Scenarios 2 and 3 were designed with an equal total CO_2 volume of 100 Ml (RC) but different injection wells and gas allocations. In Scenario 2, 100 Ml of CO_2 was injected into the model only through the lower well P1H. In Scenario 3, 100 Ml of CO_2 was injected into the model only through the higher well P2H. Other procedures were the same as mentioned previously. After the experiments were finished, the production performances of the three scenarios were compared to study the interplay mechanisms during the CO_2 huff-n-puff process.

2.3 Numerical simulations for well-to-well interplay of CO_2 huff-n-puff

A sensitivity analysis of well-to-well interplay during CO_2 huff-n-puff was then conducted using the numerical model shown in Figure 4. Seven pseudo-components—CO_2, C_1+N_2, C_2~C_4, C_5~C_6, C_{7+}, C_{11+}, and C_{28+}—were set to simulate the formation oil, with proportions of 0%, 0%, 1.65%, 5.69%, 18.24%, 29.93%, and 44.49%, respectively. The viscosity of formation oil was tested at 289.25 mPa·s with a density of 0.974 × 10^3 kg/m^3—similar to the real oil sample under formation conditions. Figure 5 shows the oil–water and oil–gas relative permeabilities used for the numerical simulation.

As with the laboratory experiments, natural edge-water flooding was first conducted in the numerical model, and the liquid production rates of P1H and P2H were set equally at 18.42 m^3/d. Figure 6 gives the fitting curves of the daily production oil rates obtained from C2-P2 in the real reservoir and P2H in the numerical model. The daily oil rate was more than 16 m^3/d at the initial production stage (less than 18 days), dropping sharply to about 8 m^3/d within 50 days, and then gradually dropping to about 1 m^3/d. The average oil rate was 4.06 m^3/d within 500 days in the numerical model—similar to the average rate of 4.08 m^3/d obtained from C2-P2. Thus, the built model can be used to reflect the production performances of the real reservoir. The edge-water flooding process was conducted until the composite water-cut of the well pair reached 98%. Then, the CO_2 huff-n-puff process was conducted with CO_2 injected only through the lower well P1H. A total CO_2 mass of 400t was injected at a rate of 100 t/d. After 30 days of soaking time, P1H and P2H were reproduced until the composite water cut of the well pair again reached 98%. The oil production of the well pair enhanced by well-to-well interplay was obtained after the simulation.

Sensitivity analysis was then conducted, considering the developmental, geological, and fluidic factors used in the base model. A total of 12 variables and 60 scenarios were designed using the base model (as listed in Table 5). The oil production recovered by CO_2 puff-n-huff (ΔQ_o) was used to evaluate the well-to-well interplay for the well pair. Since five values were set for each variable, several values of ΔQ_o can be obtained after the simulations, and then, an average oil production ($\Delta \bar{Q}_o$) can be calculated as $\Delta \bar{Q}_o = \sum_{i=1}^{n} \Delta Q_{o-i}/n$, where ΔQ_{o-i} is the ith value of oil production (i = 1,2, . . . ,n.). The standard deviation of oil

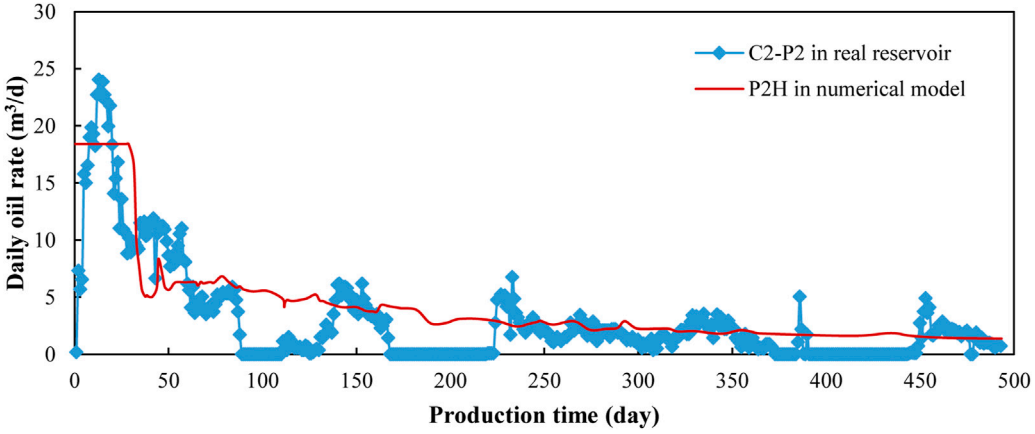

FIGURE 6
Fitting curves of daily oil rates obtained from the real reservoir and numerical model.

TABLE 5 Sensitivity analysis designed for the well-to-well interplay of CO_2 huff-n-puff.

Type	Influencing factor	Value	Default value
Developmental factors	CO_2 injection mass (t)	100, 200, 300, 400, and 500	400
	CO_2 injection rate (t/d)	25, 50, 100, 200, and 400	50
	Liquid production rate (m^3/d)	9.21, 13.82, 18.42, 27.63, and 36.85	18.42
	CO_2 soaking time (d)	15, 30, 60, 90, and 120	30
	Interwell spacing/m	40, 50, 60,70, and 80	50
	Height from WOC/m	6.31, 11.36, 16.41, 21.46, and 26.51	21.46
Geological factors	Horizontal permeability K_x/($\times10^{-3}\mu m^2$)	50, 100, 300, 667, and 1000	667
	Vertical permeability K_z/K_x	0.1, 0.2, 0.3, 0.4, and 0.5	0.4
	Lorentz coefficient of permeability (L_K)	0.1, 0.2, 0.3, 0.4, and 0.5	0.2
	Net gross ratio (NTG)	0.6, 0.7, 0.8, 0.9, and 1	0.9
	Stratigraphic dip (°)	0, 5, 10, 15, and 20	15
Fluidic factor	Oil viscosity (mPa·s)	10, 50, 100, 289.25, and 1000	289.25

production factor ($S_{\Delta Q_o}$) can also be calculated as $S_{\Delta Q_o} = \sqrt{\sum_{i=1}^{n}(\Delta Q_{o-i} - \Delta\bar{Q}_o)^2/n}$. Then, a coefficient of variation (C_v) was introduced as an evaluation index for the comparison of influencing factors for well-to-well interplay. The coefficient of variation (C_v) was defined as the ratio of the standard deviation to the average value of oil increase ($C_v = S_{\Delta Q_o}/\bar{Q}_o$). A higher value of C_v represented that the involved factor is more sensitive to the well-to-well interplay. After a comparison of C_v for each factor, the controlling factors for the well-to-well interplay during CO_2 huff-n-puff can be screened out.

3 Results and discussion

3.1 EOR mechanisms of the well-to-well interplay in 3D experiments

Before the CO_2 huff-n-puff operations, edge-water driving experiments were first conducted in the 3D physical models to form a similar remaining oil saturation; the results are compared in Table 6. Since the lower well P1H was closer to the edge water, the oil recovery of P1H was always the lowest with 6.84%–8.07%. The higher well P2H obtained a higher oil recovery of 11.21%–13.69%. When the composite water-cut of the well pair reached

TABLE 6 Experimental results of CO_2 huff-n-puff conducted in 3D physical models.

Scenario	Experimental scheme	Production well	Oil recovery/%		
			Edge-water driving	CO_2 huff-n-puff	Total
1	P1H_Lower Well 50 ml CO_2 + P2H_Higher Well 50 ml CO_2	P1H	7.48	2.18	9.66
		P2H	12.27	5.21	17.48
		Pair	19.75	7.39	27.14
2	P1H_Lower Well 100 ml CO_2	P1H	8.07	3.56	11.63
		P2H	13.69	6.13	19.82
		Pair	21.76	9.69	31.45
3	P2H_Higher Well 100 ml CO_2	P1H	6.84	2.27	9.11
		P2H	11.21	4.77	15.98
		Pair	18.05	7.04	25.09

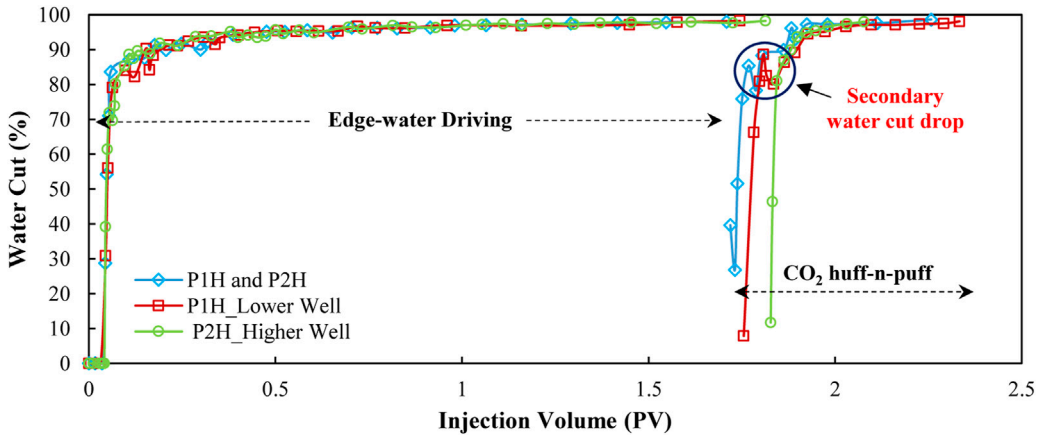

FIGURE 7
Comparison of composite water cuts for different CO_2 huff-n-puff scenarios.

98%, the total injection volume of edge water was around 1.70–1.80 PV, and the total oil recovery for the well pair was 18.05%–21.76%.

In order to study the mechanisms of well-to-well interplay during the CO_2 huff-n-puff process, different CO_2 injection schemes were designed according to the wells' locations. For the conventional CO_2 huff-n-puff conducted in Scenario 1, a total oil recovery of 7.39% was obtained for the well pair. The lower well P1H obtained an oil recovery of 2.18%, and the higher well P2H obtained an oil recovery of 5.21%. However, when CO_2 was injected only through the lower well P1H (Scenario 2), the highest oil recovery was achieved among the three scenarios. Not only did the operation well P1H obtain an oil recovery of 3.56%, but the higher well P2H also obtained an oil recovery of 6.13%., indicating an interplay between P1H and P2H during the CO_2 huff-n-puff process. When CO_2 was injected only through the higher well P2H (Scenario 3), the lowest oil recovery was obtained, with only 2.27% oil recovery obtained from P1H and 4.77% oil recovery from P2H.

Figure 7 compares the composite water cuts for different CO_2 huff-n-puff scenarios. At the initial production stage of CO_2 huff-n-puff, it can be observed that the lowest water-cut drop was obtained when CO_2 was injected only through lower well P1H (Scenario 2). CO_2 is soluble in the water phase, which is beneficial for treatment through water invasion. After comparing Scenarios 1 and 2, it is evident that a larger volume of CO_2 injected into the

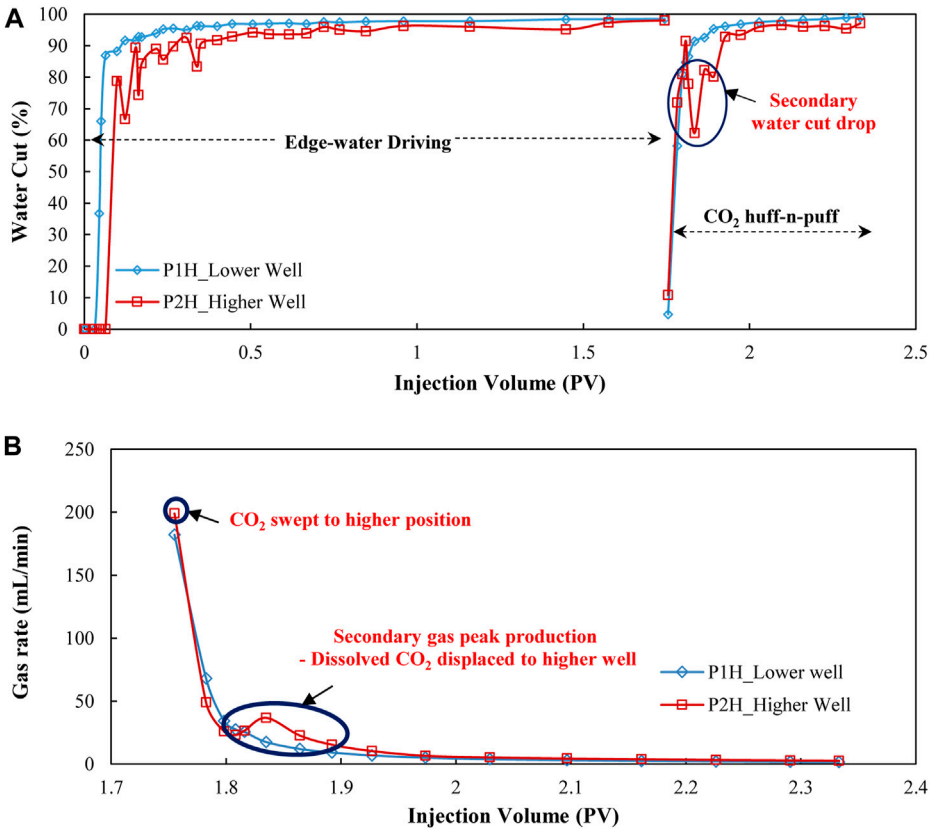

FIGURE 8
Production performance for single wells in Scenario 2 with CO_2 injected only through the lower well P2H. **(A)** Water cut curves. **(B)** Gas rate curves.

lower well allows better edge-water control. In addition to the lowest water-cut drop, production life can also be prolonged to 0.58 PV when the water cut again reaches 98% in Scenario 2. It can be observed that a secondary water cut drop formed in the successive production stage in Scenarios 1 and 2. Since CO_2 was injected though the lower well, it could be soluble in the remaining oil between P1H and P2H. With the assistance of edge-water driving, the dissolved CO_2 was displaced to a higher position, which then brought the amount of interwell-remaining oil to the higher well P2H. When CO_2 was injected only through the higher well P2H (Scenario 3), the water cut drop was mainly due to the oil recovered from P2H. Since no gas was injected through the lower well, the edge-water invasion was severe with the shortest production life of only 0.25 PV, and the water cut increased sharply with no period of secondary water-cut drops.

Figure 8A shows the water cut curves of individual wells in Scenario 2. When the composite water cut reached 98.27%, the water cut of P1H and P2H was 98.54% and 98.10%, respectively. After CO_2 was injected into the lower well P1H, the invasive edge water was treated first by CO_2, with the water cut of P1H and P2H dropping to as low as 4.73% and 10.80%, respectively. A large amount of crude oil was produced from P1H and P2H as long as CO_2 was produced—revealing it as the main contributor to the oil recovery increase. As the production process continued, the water cut of the lower well P1H increased gradually to around 90%; however, a secondary water cut drop was observed in the higher well P2H. The water cut of P2H again dropped from 91.55% to 62.26% during an injection volume of 1.81 PV to 1.83 PV, which can be attributed to the interwell-remaining oil displaced by the dissolved CO_2 and edge water. The injected CO_2 not only extracted the oil remaining around P1H and P2H but also displaced the oil remaining between P1H and P2H. Consequently, the oil recovery of the well pair can be maximized by injecting CO_2 into the lower position of the model.

Figure 8B provides the gas production rates for individual wells during the CO_2 huff-n-puff process in Scenario 2. Since CO_2 was injected only through the lower well P1H, an amount of CO_2 was produced from P1H immediately when the well was opened for production. However, it is interested to note that a larger amount of gas was also immediately produced from the higher well P2H. Since the model had a dip of 15°, part of the injected CO_2 in the lower position could migrate upward under

gravitational differentiation, and then sweep the near-wellbore area of P2H. The remaining oil around P2H could be effectively extracted by the migrated CO_2, which then caused a remarkable water drop and oil increase for P2H. As the production process continued, the gas rate of the lower well P1H decreased gradually; however, another peak appeared on the gas rate of the higher well P2H. Since the edge water was being continuously injected into the model, part of the CO_2 in the lower position was displaced into the interwell area and then dissolved with the remaining oil. The remaining oil, dissolved CO_2, and invasive edge water were then produced successively from the higher well P2H. The duration of the secondary gas production peak for P2H was the same as that of the secondary water cut drop (as shown in Figure 8A), confirming that the oil increase in this period was due to the interwell remaining oil being displaced by CO_2 and edge water.

In summary, when CO_2 huff-n-puff is conducted in a well pair located in an inclined reservoir, an interplay can be formed between wells with a CO_2 injection into the lower position. Not only can water drop and oil increase be obtained from the lower well after the gas injection but also a more remarkable water drop and oil increase can also be obtained from the higher well. On one hand, the injected CO_2 in the lower position can migrate upward under gravitational differentiation in the inclined reservoir. On the other hand, dissolved CO_2 can be displaced into the interwell area with the assistance of edge-water flooding. Under the influence of migrated CO_2, dissolved CO_2, and edge water, the oil remaining between the wells can be effectively extracted through the higher well. The oil recovery of the well pair enhanced by CO_2 conducted in Scenario 2 is 2.3% better than the conventional CO_2 huff-n-huff, indicating that using the well-to-well interplay during a CO_2 huff-n-puff process for enhanced oil recovery is a promising gas injection strategy for the inclined oil reservoir.

3.2 Sensitivity analysis on the well-to-well interplay in simulations

Although the formation mechanisms of well-to-well interplay during the CO_2 huff-n-puff process were revealed using laboratory experiments, the influencing factors still need to be discussed before enlarging its application in field tests. A base reservoir model was built using a CMG-GEM simulator. As in the laboratory experiments, natural edge-water flooding was also first conducted in the base model, and CO_2 huff-n-puff was then conducted after the composite water cut reached 98%. For the default model, the liquid production rates of P1H and P2H were set at 18.42 m^3. CO_2 was injected through the lower well P1H at a rate of 100 t/d, a total CO_2 volume of 400t, and CO_2 soaking time of 30 days. After the composite water cut of the well pair reached 98%, 175.4t of crude oil was recovered from the lower well P1H, while a significant increase of 1197.24t of crude oil was obtained from the higher well P2H, accounting for 87.16% of the total oil increments for the well pair. Figure 9 shows the oil saturation before and after CO_2 huff-n-puff. The edge water mainly flowed through the higher permeable layers at the bottom of the reservoir, and an amount of crude oil remained between P1H and P2H. After the CO_2 huff-n-puff process was operated at the well pair, the oil saturation between P1H and P2H dropped notably due to the occurrence of well-to-well interplay. The injected CO_2 through the lower well P1H migrated upward with the displacement of edge water; the remaining oil between the wells was then effectively displaced from the higher well P2H. The simulation result was consistent with the experimental result, confirming that the well-to-well interplay of CO_2 huff-n-puff is an effective EOR method for the well pair in the inclined oil reservoir.

Sensitivity analysis was then conducted using the base model, with the simulation results shown in Table 7 and Figure 10. The calculated coefficient of variation (C_v) ranged from 0.0553 to 0.7287, with an average value of 0.2103. The C_v values of four factors— CO_2 injection mass, stratigraphic dip, horizontal permeability (K_x) and interwell spacing—were higher than its average. These four are considered the factors of most influence for the well-to-well interplay during CO_2 huff-n-puff. CO_2 injection mass is the primary factor in the well-to-well interplay, and Figure 11 shows the production performance of different CO_2 injection masses for the well pair. When the mass was less than or equal to 200t, the amount of CO_2 was mostly produced through the lower well P1H, with little CO_2 migrating up to the higher well P2H (Figure 11B). No interplay occurred between P1H and P2H; thus, the oil increment was less than 200t with the operation of CO_2 huff-n-puff. When the injected CO_2 mass exceeds 200t, the oil increase increased sharply to more than 1000t, a produced gas rate was observed from the higher well P2H, and the composite water cut also showed a secondary drop during the production stage. Thus, the injection mass of CO_2 should be more than 200t in order to enhance oil recovery using the well-to-well interplay.

The stratigraphic dip was the secondary influencing factor for the well-to-well interplay, and Figure 12 shows the production performance of different stratigraphic dips during CO_2 huff-n-puff. It can be observed that the oil increase is less than 850t when the dip is less than or equal to 5° and that little gas was produced from the higher well P2H. The dip was so small that the injected CO_2 could not migrate up to the higher position during one cycle of CO_2 huff-n-puff (Figure 12B). When the dip was higher than 5°, the oil increment increased to more than 1000t, a produced gas rate was observed from the higher well P2H, and the composite water cut also showed a secondary drop during the production stage. It can also be observed that a higher stratigraphic dip can recover more oil for the well pair, which is beneficial for the displacement of interwell-remaining oil achieved by CO_2 upward migration.

Horizontal permeability is the third influencing factor for well-to-well interplay, and Figure 13 shows the production performance of different horizontal permeabilities during CO_2 huff-n-puff. It can be observed that the oil increase was less than 500t when the

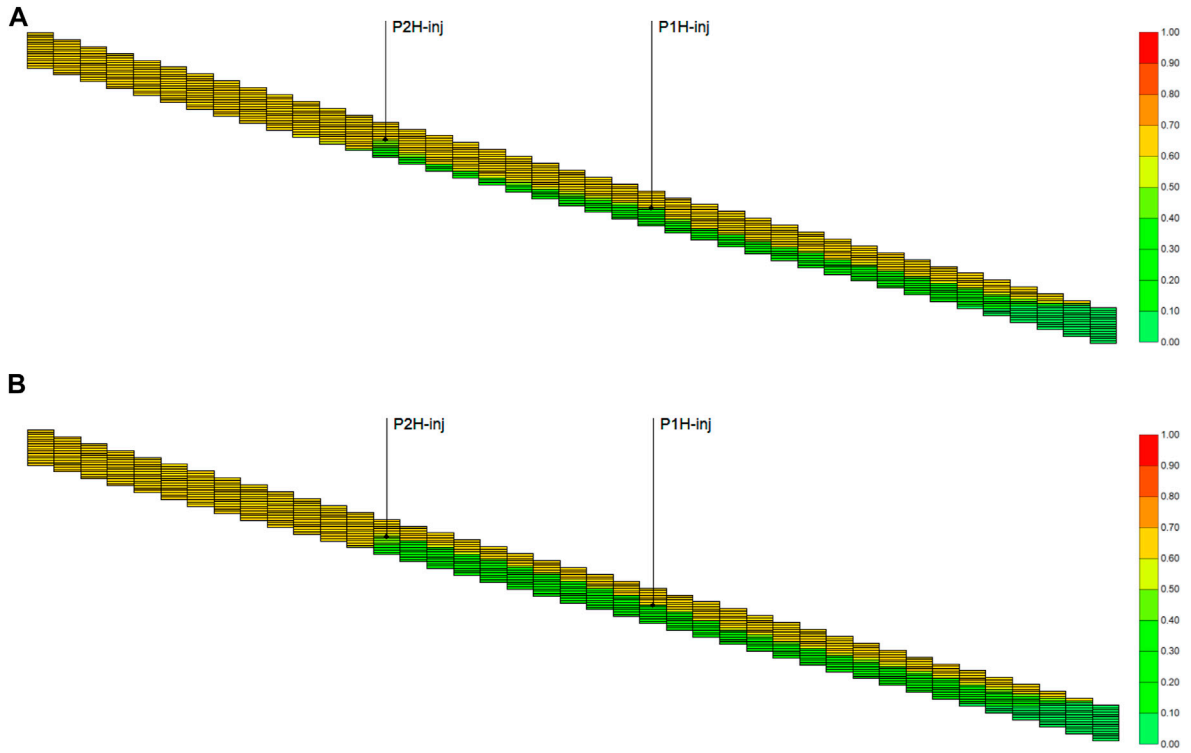

FIGURE 9
Oil saturation before and after the well-to-well interplay of CO_2 huff-n-puff. **(A)** Before and **(B)** after the well-to-well interplay of CO_2 huff-n-puff.

permeability was less than or equal to 100×10^{-3} μm^2, and that little gas was produced from the higher well P2H. The permeability was so small that the injected CO_2 could not migrate up to the higher position (Figure 13B). When the permeability was higher than 100×10^{-3} μm^2, the oil increase increased to more than 1000t, a produced gas rate was observed from the higher well P2H, and the composite water cut also showed a secondary drop during the production stage. Thus, the horizontal permeability should be more than 100×10^{-3} μm^2 when using well-to-well interplay for EOR.

The interwell spacing is the fourth influencing factor for well-to-well interplay, and Figure 14 shows the production performance of different interwell spacings during CO_2 huff-n-puff. It can be observed the oil increase increased as interwell spacing increased, which can be more than 2000t when the spacing exceeds 70 m. As the interwell spacing increased, more crude oil remained between P1H and P2H after edge-water driving. When CO_2 was injected into the lower well P1H, oil could be continuously produced from the higher well P2H under CO_2 gravitational differentiation and edge-water displacement (Figure 14B). As a result, the composite water cut remained at a level of less than 98% for more than 800 days, and considerable remaining oil was effectively recovered from the reservoir using the well-to-well interplay during CO_2 huff-n-puff.

In summary, a successful CO_2-EOR operation using well-to-well interplay mostly depends on both geological and developmental factors. The oil reservoir should be inclined with a stratigraphic dip of more than 5°, and horizontal permeability should be more than 100×10^{-3} μm^2. The CO_2 injection mass is the primary influencing factor; it should be more than 200t, and CO_2 should be injected through the lower position of the reservoir. A larger interwell spacing can allow the injected CO_2 to fully dissolve with the crude oil and then displace the remaining oil upward to a higher position. With an elaborate design of gas injection in this inclined oil reservoir, a considerable oil increase of more than 1000t can be recovered using the well-to-well interplay during the CO_2 huff-n-puff process.

3.3 Pilot tests using well-to-well interplay during the CO_2 huff-n-puff process

Pilot tests using well-to-well interplay of CO_2 huff-n-puff were widely applied after natural edge-water flooding in C2-1 Block, Jidong Oilfield, China, from 2010; a total of 2.27×10^4 m^3 of crude oil was recovered until the end of 2018. Figure 15 shows five typical well pairs using well-to-well

TABLE 7 Simulation results and sensitivity analysis of well-to-well interplay during CO_2 huff-n-puff.

Influence factors	Value of ΔQ_o (t)	Average value ($\Delta\bar{Q}_o$) (t)	Standard deviation ($S_{\Delta Q_o}$)	Coefficient of variation (C_v)
CO_2 injection mass	64.09, 133.66, 1154.27, 1373.58, and 1436.47	832.41	606.62	0.7287
CO_2 injection rate	1383.43, 1341.14, 1372.58, 1443.72, and 1626.54	1433.48	102.10	0.0712
Liquid production rate	1446.69, 1397.29, 1371.58, 1272.00, and 1176.97	1332.91	96.55	0.0724
CO_2 soaking time	1237.14, 1371.58, 1427.42, 1496.49, and 1510.72	1408.67	99.27	0.0705
Interwell spacing	1149.90, 1371.58, 1816.29, 2160.07, and 2391.64	1777.90	465.55	0.2619
Height from WOC	1561, 1507.56, 1423.63, 1371.58, and 1352.22	1443.20	79.76	0.0553
Horizontal permeability K_x	401.92, 424.41, 1420.17, 1371.58, and 1338.05	991.23	472.76	0.4769
Vertical permeability K_z/K_x	1030.79, 1254.71, 1334.89, 1371.58, and 1499.93	1298.38	155.45	0.1197
Lorentz coefficient of permeability (L_K)	1511.87, 1371.58, 1264.38, 1220.25, and 1167.27	1307.07	122.48	0.0937
Net gross ratio (NTG)	1155.73, 1170.87, 1302.01, 1371.58, and 1587.19	1317.48	157.21	0.1193
Stratigraphic dip	778.74, 827.62, 1205.74, 1371.58, and 1625.67	1161.87	322.34	0.2774
Oil viscosity	2063.50, 1773.80, 1563.30, 1371.58, and 1278.58	1610.15	283.32	0.1760

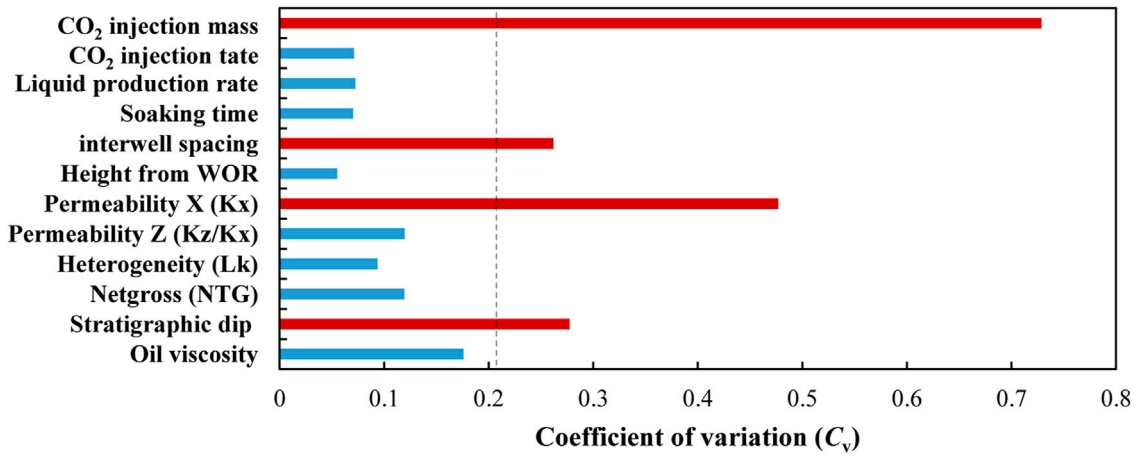

FIGURE 10
Sensitivity analysis results of the well-to-well interplay during the CO_2 huff-n-puff process.

interplay where CO_2 was injected into the reservoir through the lower wells. After the CO_2 injection, the same phenomena were observed with the oil recovered from both the lower and higher wells. Moreover, the oil increases of the higher wells were always higher than those of the lower wells, indicating that the interwell-remaining oil had been successfully displaced using the well-to-well interplay of CO_2 huff-n-puff.

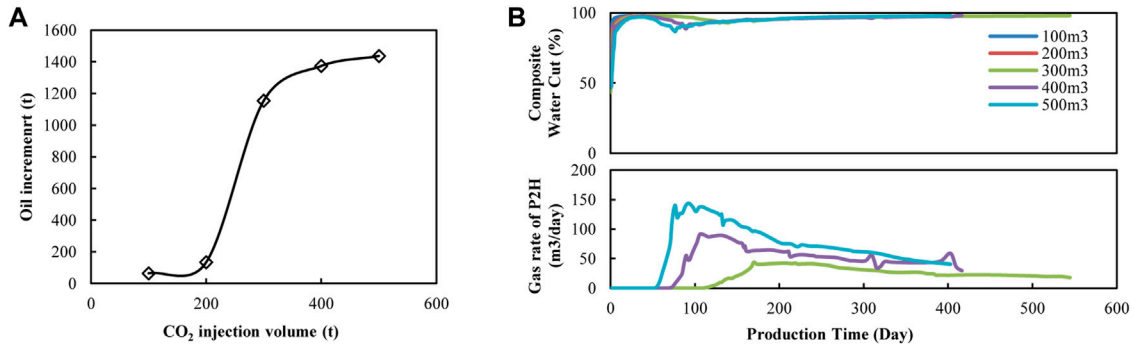

FIGURE 11
Production performance of different CO_2 injection volumes for the well-to-well interplay of CO_2 huff-n-puff. **(A)** Oil increment *vs.* CO_2 injection volume. **(B)** Composite water cut and production gas rate *vs.* time.

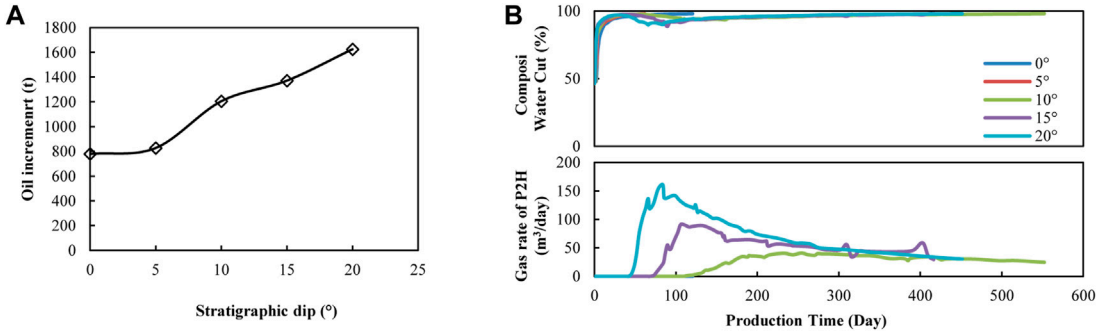

FIGURE 12
Production performance of different stratigraphic dips for well-to-well interplay of CO_2 huff-n-puff. **(A)** Oil increase vs. interwell spacing. **(B)** Composite water cut and production gas rate *vs.* time.

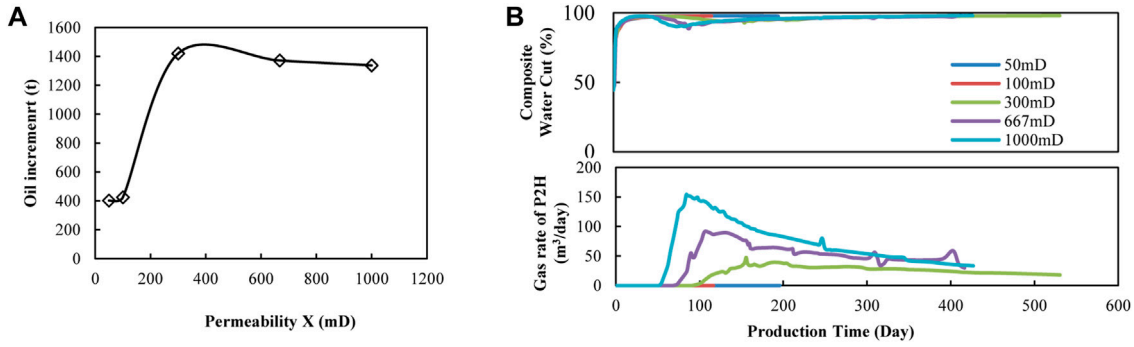

FIGURE 13
Production performance of different horizontal permeabilities for the well-to-well interplay of CO_2 huff-n-puff. **(A)** Oil increase *vs.* interwell spacing. **(B)** Composite water cut and production gas rate *vs.* time.

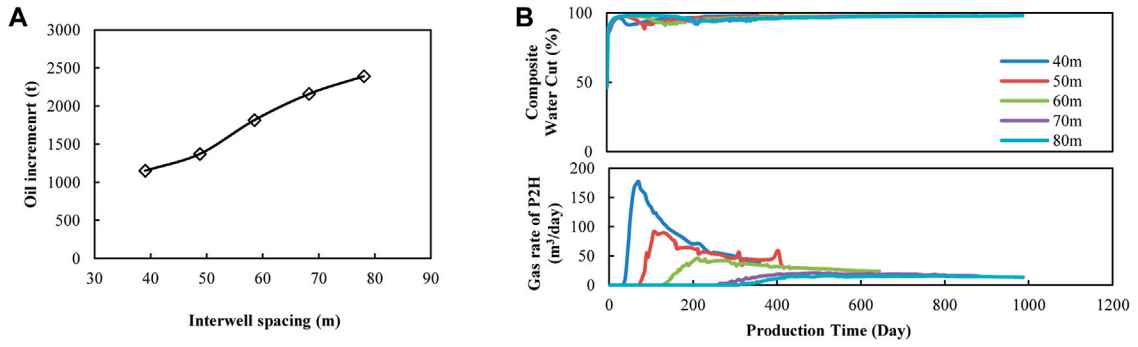

FIGURE 14
Production performance of different interwell spacings for the well-to-well interplay of CO_2 huff-n-puff. **(A)** Oil increase *vs.* interwell spacing. **(B)** Composite water cut and production gas rate *vs.* time.

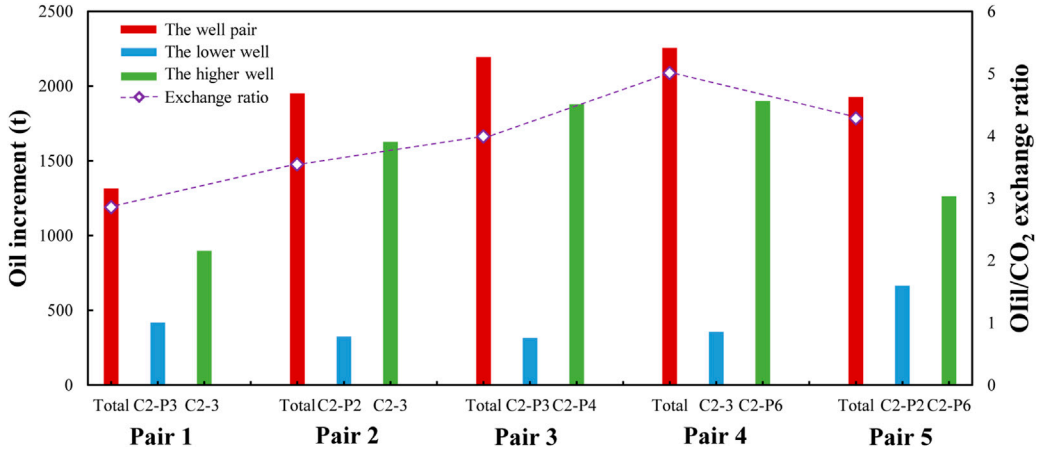

FIGURE 15
Oil increase and oil–CO_2 exchange ratio for five well pairs using the well-to-well interplay of CO_2 huff-n-puff in pilot tests.

The oil–CO_2 exchange ratio is defined as the oil increment enhanced by per unit CO_2, which can be used to reflect CO_2 utilization efficiency. The higher the value of the oil–CO_2 exchange ratio, the more efficient the CO_2 utilization is. Figure 15 also shows the total oil increases and the oil–CO_2 exchange ratio for these five well pairs. Using well-to-well interplay, the total oil increase for a well pair was more than 1300t during CO_2 puff-n-huff; the oil increases for pairs 4 and 5 in particular were more than 2000t. The oil–exchange ratio ranged from 2.85 to 5.01, which means that a small mass of CO_2 can recover plenty of crude oil from the reservoir. The total CO_2 mass operating in these five pairs was 2460t, the total oil increase was 9642.1t, and the average oil–CO_2 exchange ratio was 3.92. The well-to-well interplay not only achieved considerable EOR but also showed great potential for improving the CO_2 utilization efficiency during CO_2 huff-n-puff.

Although the successful utilization of well-to-well interplay during the CO_2 huff-n-puff process has brought great profits to the oil company, there are still some problems to be resolved during its operation. For example, several operations of the well-to-well interplay were failures because of the presence of fractures; however, some were much better than the EOR effects conducted in areas with no fractures. These may lead to completely different EOR mechanisms during the well-to-well interplay, which we will further investigate and report in a future study.

4 Conclusion

The well-to-well interplay of CO_2 huff-n-puff is proposed as a novel gas injection strategy for enhanced oil recovery (EOR) in

an inclined oil reservoir. Laboratory experiments, numerical simulations, and pilot tests are reported in this paper, and these are some conclusions:

1) When CO_2 is injected into a lower well of a well pair in an inclined oil reservoir, not only can water drop and oil increase be obtained from the lower well, but a more remarkable water drop and oil increase can also be obtained from the higher well. The interplay between wells can dramatically enhance oil recovery for the well pair.
2) The displacement of interwell-remaining oil is the main contribution for EOR using well-to-well interplay. Under gravitational differentiation and edge-water flooding, CO_2 and edge water can migrate upward to displace the oil between wells. Physical experimental results show that oil recovery enhanced by a well-to-well interplay is 2.30% higher than recovery using conventional CO_2 huff-n-huff.
3) Sensitivity analysis results show that CO_2 injection mass, stratigraphic dip, horizontal permeability, and interwell spacing are the factors that most influence well-to-well interplay. To realize a better oil increment, the reservoir dip should be more than 5°, the permeability should be more than 100×10^{-3} μm^2, the CO_2 injection mass should be more than 300t, and greater interwell spacing is beneficial for achieving a better CO_2–EOR effect.
4) A total of 2.27×10^4 m^3 of crude oil was recovered using well-to-well interplay in the pilot between 2010 and 2018. The results of five typical well pairs show that the oil–CO_2 exchange ratio was as high as 3.92. The well-to-well interplay not only achieved a considerable EOR effect but also showed great potential for improving efficient CO_2 utilization during the CO_2 huff-n-puff process.

Data availability statement

The original contributions presented in the study are included in the article/Supplementary material; further inquiries can be directed to the corresponding authors.

Author contributions

HH contributed to the conception of the study. JH provided the funding for the study. MQ performed the experiment. WG performed the simulation. SD performed the data analyses obtained in the experiment and simulation. HL provided the data operated in the pilot test.

Funding

The project is supported by the National Natural Science Foundation of China (52174046).

Acknowledgments

The authors wish to acknowledge all involved colleagues at Changzhou University, China University of Petroleum (Beijing), and the Drilling and Production Technology Research Institute, PetroChina Jidong Oilfield Company.

Conflict of interest

HL was employed by PetroChina Jidong Oilfield Company.

The remaining authors declare that the research was conducted in the absence of any commercial or financial relationships that could be construed as a potential conflict of interest.

Publisher's note

All claims expressed in this article are solely those of the authors and do not necessarily represent those of their affiliated organizations, or those of the publisher, the editors, and the reviewers. Any product that may be evaluated in this article, or claim that may be made by its manufacturer, is not guaranteed or endorsed by the publisher.

References

Afzali, S., Rezaei, N., and Zendehboudi, S. (2018). A comprehensive review on enhanced oil recovery by water alternating gas (WAG) injection. *Fuel* 227, 218–246. doi:10.1016/j.fuel.2018.04.015

Ahadi, A., and Torabi, F. (2018). Effect of light hydrocarbon solvents on the performance of CO2-based cyclic solvent injection (CSI) in heavy oil systems. *J. Pet. Sci. Eng.* 163, 526–537. doi:10.1016/j.petrol.2017.12.062

Al-Mudhafar, W., Rao, D., and Srinivasan, S. (2018). Reservoir sensitivity analysis for heterogeneity and anisotropy effects quantification through the cyclic CO2-Assisted Gravity Drainage EOR process - a case study from South Rumaila oil field. *Fuel* 221, 455–468. doi:10.1016/j.fuel.2018.02.121

Al-Obaidi, D., Al-Mudhafar, W., and Al-Jawad, M. (2022). Experimental evaluation of Carbon Dioxide-Assisted Gravity Drainage process (CO2-AGD) to improve oil recovery in reservoirs with strong water drive. *Fuel* 324, 124409. doi:10.1016/j.fuel.2022.124409

Alajmi, A. (2021). Heat loss effect on oil bank formation during steam flood. *J. Pet. Sci. Eng.* 199, 108262. doi:10.1016/j.petrol.2020.108262

Babadagli, T. (2003). Evaluation of EOR methods for heavy-oil recovery in naturally fractured reservoirs. *J. Pet. Sci. Eng.* 37 (1-2), 25–37. doi:10.1016/s0920-4105(02)00309-1

Chen, X., Li, Y., Tang, X., Qi, H., Sun, X., and Luo, J. (2021). Effect of gravity segregation on CO2 flooding under various pressure conditions: Application to CO2 sequestration and oil production. *Energy* 226, 120294. doi:10.1016/j.energy.2021.120294

Cui, M., Wang, R., Lv, C., and Tang, Y. (2017). Research on microscopic oil displacement mechanism of CO2 EOR in extra-high water cut reservoirs. *J. Pet. Sci. Eng.* 154, 315–321. doi:10.1016/j.petrol.2017.04.006

Fayers, F., and Zhou, D. (1996). On the importance of gravity and three-phase flow in gas displacement processes. *J. Pet. Sci. Eng.* 15 (2-4), 321–341. doi:10.1016/0920-4105(96)00010-1

Hao, H., Hou, J., Zhao, F., Huang, H., and Liu, H. (2021). N2-foam-assisted CO2 huff-n-puff process for enhanced oil recovery in a heterogeneous edge-water reservoir: Experiments and pilot tests. *RSC Adv.* 11, 1134–1146. doi:10.1039/d0ra09448j

Hao, H., Yuan, D., Hou, J., Guo, W., and Liu, H. (2022). Using starch graft copolymer gel to assist the CO2 huff-n-puff process for enhanced oil recovery in a water channeling reservoir. *RSC Adv.* 12, 19990–20003. doi:10.1039/d2ra01812h

Huang, K., Zhu, W., Sun, L., Wang, Q., and Liu, Q. (2019). Experimental study on gas EOR for heavy oil in glutenite reservoirs after water flooding. *J. Pet. Sci. Eng.* 181, 106130. doi:10.1016/j.petrol.2019.05.081

Jiang, T., Zeng, F., Jia, X., and Gu, Y. (2014). A new solvent-based enhanced heavy oil recovery method: Cyclic production with continuous solvent injection. *Fuel* 115, 426–433. doi:10.1016/j.fuel.2013.07.043

Kashkooli, S., Gandomkar, A., Riazi, M., and Tavallali, M. (2022). The investigation of gas trapping and relative permeability alteration during optimization of CO2-EOR and sequestration. *Int. J. Greenh. Gas Control* 113, 103529. doi:10.1016/j.ijggc.2021.103529

Kavousi, A., Torabi, F., Chan, C., and Shirif, E. (2014). Experimental measurement and parametric study of CO2 solubility and molecular diffusivity in heavy crude oil systems. *Fluid Phase Equilib.* 371, 57–66. doi:10.1016/j.fluid.2014.03.007

Khan, M., and Mandal, A. (2020). Analytical model for gravity segregation in WAG displacement recovery of inclined stratified reservoirs. *J. Pet. Sci. Eng.* 286, 106722. doi:10.1016/j.petrol.2019.106722

Li, B., Zhang, Q., Li, S., and Li, Z. (2017). Enhanced heavy oil recovery via surfactant-assisted CO2 huff-n-puff processes. *J. Pet. Sci. Eng.* 159, 25–34. doi:10.1016/j.petrol.2017.09.029

Li, L., Khorsandi, S., Johns, R., and Dilmore, R. M. (2015). CO2 enhanced oil recovery and storage using a gravity-enhanced process. *Int. J. Greenh. Gas Control* 42, 502–515. doi:10.1016/j.ijggc.2015.09.006

Li, S., Li, B., Zhang, Q., Li, Z., and Yang, D. (2018). Effect of CO2 on heavy oil recovery and physical properties in huff-n-puff processes under reservoir conditions. *J. Energy Resour. Technol.* 140, 072907. doi:10.1115/1.4039325

Ma, H., Yu, G., She, Y., and Gu, Y. (2017). A parabolic solvent chamber model for simulating the solvent vapor extraction (VAPEX) heavy oil recovery process. *J. Pet. Sci. Eng.* 149, 465–475. doi:10.1016/j.petrol.2016.10.036

Ma, J., Wang, X., Gao, R., Zeng, F., Huang, C., Tontiwachwuthikul, P., et al. (2015). Enhanced light oil recovery from tight formations through CO2 huff 'n' puff processes. *Fuel* 154, 35–44. doi:10.1016/j.fuel.2015.03.029

Qu, M., Liang, T., Hou, J., Liu, Z., Yang, E., and Liu, X. (2022). Laboratory study and field application of amphiphilic molybdenum disulfide nanosheets for enhanced oil recovery. *J. Pet. Sci. Eng.* 208, 109695. doi:10.1016/j.petrol.2021.109695

Rezk, M., Foroozesh, J., Zivar, D., and Mumtaz, M. (2019). CO2 storage potential during CO2 enhanced oil recovery in sandstone reservoirs. *J. Nat. Gas. Sci. Eng.* 66, 233–243. doi:10.1016/j.jngse.2019.04.002

Rogers, J., and Grigg, R. (2000). "A literature analysis of the WAG injectivity abnormalities in the CO2 process," in *SPE/DOE improved oil recovery symposium* (Oklahoma, OK, USA.

Shilov, E., Cheremisin, A., Maksakov, K., and Kharlanov, S. (2019). Huff-n-puff experimental studies of CO2 with heavy oil. *Energies* 12, 4308. doi:10.3390/en12224308

Shook, M., Li, D., and Lake, L. (1992). Scaling immiscible flow through permeable media by inspectional analysis. *Int. Rock Mech. Min.* 16 (4), 311–349.

Stone, H. (1982). "Vertical, conformance in an alternating water-miscible gas flood," in *SPE annual technical conference and exhibition* (Louisiana, LA, USA.

Tian, C., Pang, Z., Liu, D., Wang, X., Hong, Q., Chen, J., et al. (2022). Micro-action mechanism and macro-prediction analysis in the process of CO2 huff-n-puff in ultra-heavy oil reservoirs. *J. Pet. Sci. Eng.* 211, 110171. doi:10.1016/j.petrol.2022.110171

Wang, C., Liu, P., Wang, F., Atadurdyyev, B., and Ovluyagulyyev, M. (2018). Experimental study on effects of CO2 and improving oil recovery for CO2 assisted SAGD in superheavy-oil reservoirs. *J. Pet. Sci. Eng.* 165, 1073–1080. doi:10.1016/j.petrol.2018.02.058

Wang, P., Zhao, F., Huang, S., Zhang, M., Feng, H., Li, Y., et al. (2021). Laboratory investigation on oil Increment and water cut control of CO2, N2, and gas mixture huff-n-puff in edge-water fault-block reservoirs. *J. Energy Resour. Technol.* 143, 083001. doi:10.1115/1.4048862

Zhao, F., Hao, H., Lv, G., Wang, Z., Hou, J., Wang, P., et al. (2018). Performance improvement of CO2 flooding using production controls in 3D areal heterogeneous models: Experimental and numerical simulations. *J. Pet. Sci. Eng.* 164, 12–23. doi:10.1016/j.petrol.2018.01.036

Zhou, X., Li, X., Shen, D., Shi, L., Zhang, Z., Sun, X., et al. (2022). CO2 huff-n-puff process to enhance heavy oil recovery and CO2 storage: An integration study. *Energy* 239, 122003. doi:10.1016/j.energy.2021.122003

Zhou, X., Yuan, Q., Rui, Z., Wang, H., Feng, J., Zhang, L., et al. (2019). Feasibility study of CO_2 huff 'n' puff process to enhance heavy oil recovery via long core experiments. *Appl. Energy* 236, 526–539. doi:10.1016/j.apenergy.2018.12.007

Frontiers in
Energy Research

Advances and innovation in sustainable, reliable and affordable energy

Explores sustainable and environmental developments in energy. It focuses on technological advances supporting Sustainable Development Goal 7: access to affordable, reliable, sustainable and modern energy for all.

Discover the latest Research Topics

See more →

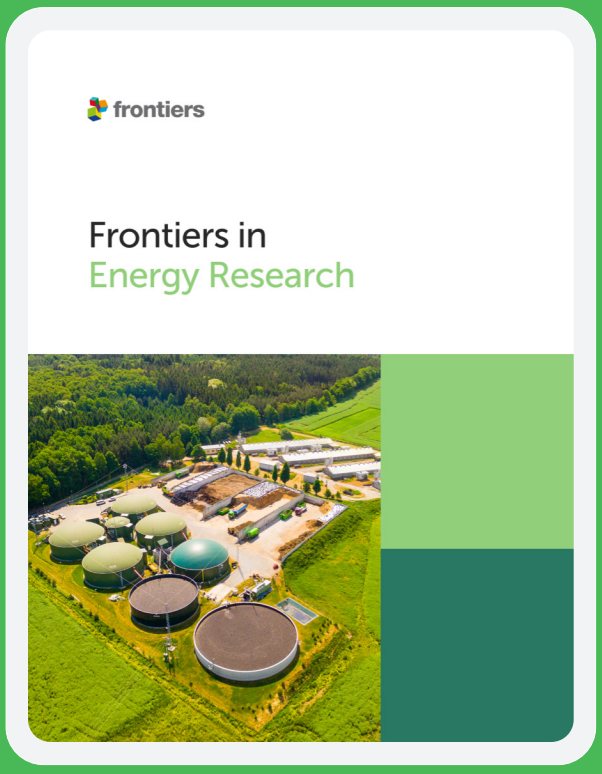

Frontiers

Avenue du Tribunal-Fédéral 34
1005 Lausanne, Switzerland
frontiersin.org

Contact us

+41 (0)21 510 17 00
frontiersin.org/about/contact